UNIVERSITY OF CALIFORNIA, SAN DIEGO

The role of collagen on the structural response of dermal layers in mammals and fish

A dissertation submitted in partial satisfaction of the

requirements for the degree of Doctor of Philosophy

in

Materials Science and Engineering

by

Vincent Robert Sherman

Committee in charge:

Professor Marc A. Meyers, Chair
Professor Shengqiang Cai
Professor Xanthippi Markenscoff
Professor Joanna McKittrick
Professor Jan Talbot

2016

The Dissertation of Vincent Robert Sherman is approved, and is acceptable in quality and form for publication on microfilm and electronically:

_____

_____

_____

_____

_____

Chair

University of California, San Diego

2016

TABLE OF CONTENTS

LIST OF FIGURES

LIST OF TABLES

ACKNOWLEDGEMENTS

I would like to gratefully acknowledge my advisor, Professor Marc Meyers, for his intellectual guidance and financial support. Your exuberant teaching style while teaching "Elements of Materials Science" kindled my interest in the subject, and by welcoming me to join your research group as an undergraduate I became inspired to pursue the research of which this dissertation is composed. I would also like to thank my committee members, Shengqiang Cai, Xanthippi Markenscoff, Joanna McKittrick, and Jan Talbot for their suggestions and support. I am grateful to all of my coauthors, collaborators, and colleagues who have contributed to the success of my work, especially Maribel Lopez, Robert Ritchie, Bin Wang, Mason Mackey, and Wen Yang.

I would also like to thank all of my friends and family for their continued encouragement and support throughout my education, especially my parents, Jim and Kathy, my sister, Tara, and my girlfriend, Sarah Calara. The bike rides, camping trips, happy hours, and all the other time we spent together provided me the rest and recuperation I needed to succeed.

Financial support is key to the success of this work. The work presented in this dissertation was supported principally by a Multi-University Research Initiative through the Air Force Office of Scientific Research of the United States (AFOSR-FA9550-15-1-0009). Additional funding sources include the National Science Foundation, Division of Materials Research, Ceramics Program Grant 1006931; X-ray scattering data was collected at beamline 7.3.3 of the Advanced Light Source through the Mechanical Behavior of Materials Program at the Lawrence Berkeley National Laboratory, which is supported by the Director of the Office of Science, Office of Basic Energy Sciences of the U.S.

Department of Energy under Contract No. DE-AC02-05CH11231; μ-CT imaging was performed at the National Center for Microscopy and Imaging Research at the University of California, San Diego, and funded by National Institutes of Health Grant P41GM103412 to Mark H. Ellisman.

Chapter 2, in full, is a reprint of the material as it appears in "The materials science of collagen" Journal of the Mechanical Behavior of Biomedical Materials, vol 52, pp 22-50, 2015. This work was coauthored by W. Yang and M. A. Meyers. The dissertation author is the first and corresponding author of this work.

Chapter 3, in part, is published as "Microstructural and geometric influences in the protective scales of *Atractosteus spatula*" Journal of The Royal Society Interface, in press, 2016. This work was coauthored by N. A. Yaraghi, D. Kisailus and M. A. Meyers. The dissertation author is the first author of this work.

Chapter 3, in part, is published as "Protective role of *Arapaima gigas* fish scales: Structure and mechanical behavior" Acta Biomaterialia, vol 10, pp 3599-3614, 2014. This work was coauthored by W. Yang, B. Gludovatz, M. Mackey, E. Zimmermann, E. Chang, E. Schaible, Z. Qin, M. Buehler, R. Ritchie and M. Meyers. The dissertation author is the second author of this work.

Chapter 3, in part, is published as "A comparative study of piscine defense: The scales of *Arapaima gigas*, *Latimeria chalumnae* and *Atractosteus spatula*" Journal of the Mechanical Behavior of Biomedical Materials, in press, 2016. This work was coauthored by H. Quan, W. Yang, R. Ritchie and M. Meyers. The dissertation author is the first author of this work.

Chapter 4, in part, is under peer review for publication with coauthors Y. Tang, S. Zaho, W. Yang and M. Meyers. The dissertation author is the first author of this work.

Chapter 4, in part, is published as “On the tear resistance of skin” Nature Communications, vol 6, 2015. This work was coauthored by W. Yang, B. Gludovatz, E. Schaible, P. Stewart, R. Ritchie and M. Meyers. The dissertation author is the second author of this work.

VITA

2016 Ph.D. Materials Science and Engineering

University of California, San Diego, La Jolla, CA

Dissertation: The role of collagen on the structural response of dermal layers in mammals and fish

Advisor: Professor Marc A. Meyers

2013 M.S. Materials Science and Engineering

University of California, San Diego, La Jolla, CA

2012 B.S. Mechanical Engineering

University of California, San Diego, La Jolla, CA

PUBLICATIONS

Sherman VR, Yaraghi N, Meyers MA, Kisailus D. Microstructural and geometric influences in the protective scales of *Atractosteus spatula*. Journal of The Royal Society Interface, in press, 2016.

Sherman VR, Quan H, Yang W, Ritchie RO, Meyers MA. A comparative study of piscine defense: The scales of *Arapaima gigas*, *Latimeria chalumnae* and *Atractosteus spatula*. Journal of the Mechanical Behavior of Biomedical Materials, in press, 2016.

Wang B, Yang W, Sherman VR, Meyers MA. Pangolin armor: overlapping, structure, and mechanical properties of the keratinous scales. Acta Biomaterialia, vol 41 pp 60-74 2016.

Jung J-Y, Naleway S, Yaraghi N, Herrera S, Sherman VR, Bushong EA, Ellisman MH, Kisailus D, McKittrick J. Structural analysis of tongue and hyoid apparatus of a woodpecker. Acta Biomaterialia, vol 37, pp 1-13, 2016.

Sherman VR, Yang W, Meyers MA. The materials science of collagen. Journal of the Mechanical Behavior of Biomedical Materials, vol 52, pp 22-50, 2015.

Yang W, Sherman VR, Gludovatz B, Schaible E, Stewart P, Ritchie RO, Meyers MA, On the tear resistance of skin. Nature Communications, vol 6, 2015.

Liu D, Guo C, Chai L, Sherman VR, Qin X, Ding Y, Meyers MA. Mechanical properties and corrosion resistance of hot extruded Mg–2.5Zn–1Ca alloy. Materials Science and Engineering: B, vol 195, pp 50-58, 2015.

Wang B-F, Sun J-Y, Zou J-D, Sherman V, Li J. Mechanical responses, texture and microstructural evolution of high purity aluminum deformed by equal channel angular pressing. Journal of Central South University, vol 22, pp 3698-3704, 2015

Yang W, Sherman VR, Gludovatz B, Mackey M, Zimmermann EA, Chang EH, Schaible E, Qin Z, Buehler MJ, Ritchie RO, Meyers MA. Protective role of Arapaima gigas fish scales: Structure and mechanical behavior. Acta Biomaterialia, vol 10, pp 3599-3614, 2014.

Sherman VR, Tang Y, Zaho S, Yang W, Meyers MA. Structural characterization and viscoelastic constitutive modeling of skin. Submitted.

Hahn EN, Sherman VR, Pissarenko A, Meyers MA. The remarkable strength of nature's technical ceramic: the eggshell. Submitted.

ABSTRACT OF DISSERTATION

The role of collagen on the structural response of dermal layers in mammals and fish

by

Vincent Robert Sherman

Doctor of Philosophy in Materials Science and Engineering

University of California, San Diego, 2016

Professor Marc André Meyers, Chair

We study in depth the role of collagen in the protective layers of mammals (skin) and fish (scales) in depth to reveal its contribution to their mechanical performance. In order to gain an understanding of the structure property relations, we investigate its hierarchical arrangement and how it results in a specialized response.

For rabbit skin, chosen as a model material for the dermis of vertebrates, deformation is expressed in terms of four mechanisms of collagen fibril activity that

virtually eliminate the possibility of tearing in notched samples: fibril straightening, fibril reorientation towards the tensile direction, elastic stretching, and interfibrillar sliding. A model reflecting the in vivo shape of collagen is derived. The model incorporates the effects of its elasticity, viscoelasticity, and orientation.

For arapaima and alligator gar scales, we investigate their protective function and identify key features which result in their resistance to failure. For the elasmoid scales of the arapaima, we show that the scale has a *Bouligand*-like arrangement of collagen layers which stretch, rotate, and delaminate to dissipate energy and arrest cracking prior to catastrophic failure. Atop the foundation are mineral ridges; this arrangement provides high toughness and resistance to penetration by predator teeth. We show that the ganoid scales of the alligator gar have a boney composite foundation of collagen and hydroxyapatite as well as an external surface of pure hydroxyapatite. Failure averting features of the gar scale include: crack inhibiting mineral decussation in the external ganoine layer; mineral crystals and tubules which deflect cracks in the bony region; and saw-tooth ridges along the interface between the two scale layers which direct cracks away from the weak interface. Furthermore, the scale's geometry is optimized to provide full coverage while accommodating physiological motion. Key features of the scale morphology are replicated in a bioinspired model which retains protection and flexibility.

CHAPTER 1: INTRODUCTION AND OBJECTIVES

1.1 Introduction to biological materials science

Materials science is one of the oldest forms of science. Eras throughout history have been defined by the materials of the day; beginning with the Stone Age, followed by the Bronze Age, the Iron Age, the Silicon Age, and now the Material Design Age. This timeline is shown in Figure 1.1, beginning before 9000 BC. The evolution of this timeline is driven by the development of superior materials. The original material, the stone, was overshadowed by bronze and iron, with superior strength, processability, and toughness. In the 20th century, the semiconductors, produced by silicon, drove the tech boom. Our current era, the Material Design Age, is a time during which scientists and engineers precisely tailor the composition and microstructure of materials in order to maximize performance. Crucial components of the material design age include polymers, nanomaterials, composites, and bioinspired materials.

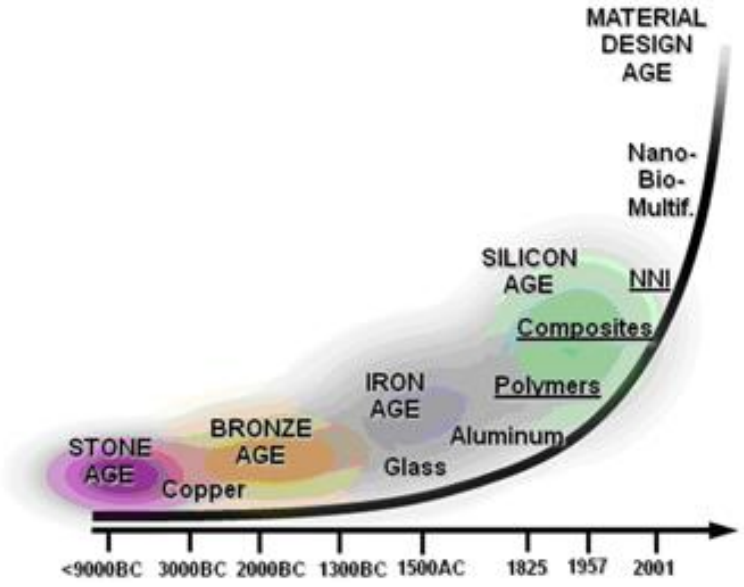

Figure 1.1: The evolution of materials from <9000 BC to modern day [1].

Advances in science and technology are driven by a desire to improve quality of life. These advances have resulted in a plethora of contemporary materials of great complexity and variety, which represent thousands of years of material development. Natural structures, however, have been refined and improved for hundreds of millions of years through the process of natural selection and evolution, where the most successful structural forms survive and propagate. Recognizing the contributions and complexity of nature, in 1917, Thompson [2] published "On Growth and Form", which broadened the field of Materials Science and incorporated biology as one of the main elements of materials science. Today, scientists and engineers have built on Thompson's idea, and biomimicry and bioinspiration have emerged as interdisciplinary research fields which combine the fields of materials science and biology. Figure 1.2 shows a schematic representation of the three main constituents of modern materials science. Biomimicry aims to precisely replicate and utilize the structures found in nature, while bioinspiration has the goal of identifying the crucial elements which make a superior natural material and then reproducing these essence of these features to make a superior manmade product.

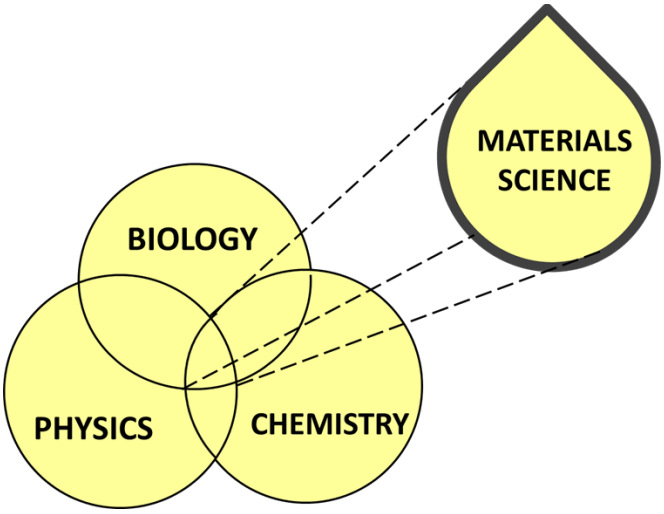

Figure 1.2: Biological materials science at the intersection of physics, chemistry, and biology.

Biological and bioinspired materials are represented by a heptahedron (Figure 1.3), which contains unique features of natural materials which we hope to incorporate, through biomimetics, and bioinspiration, into synthetic systems. Each of the seven components are unique characteristics, crucial to the full understanding and exploitation of biological systems.

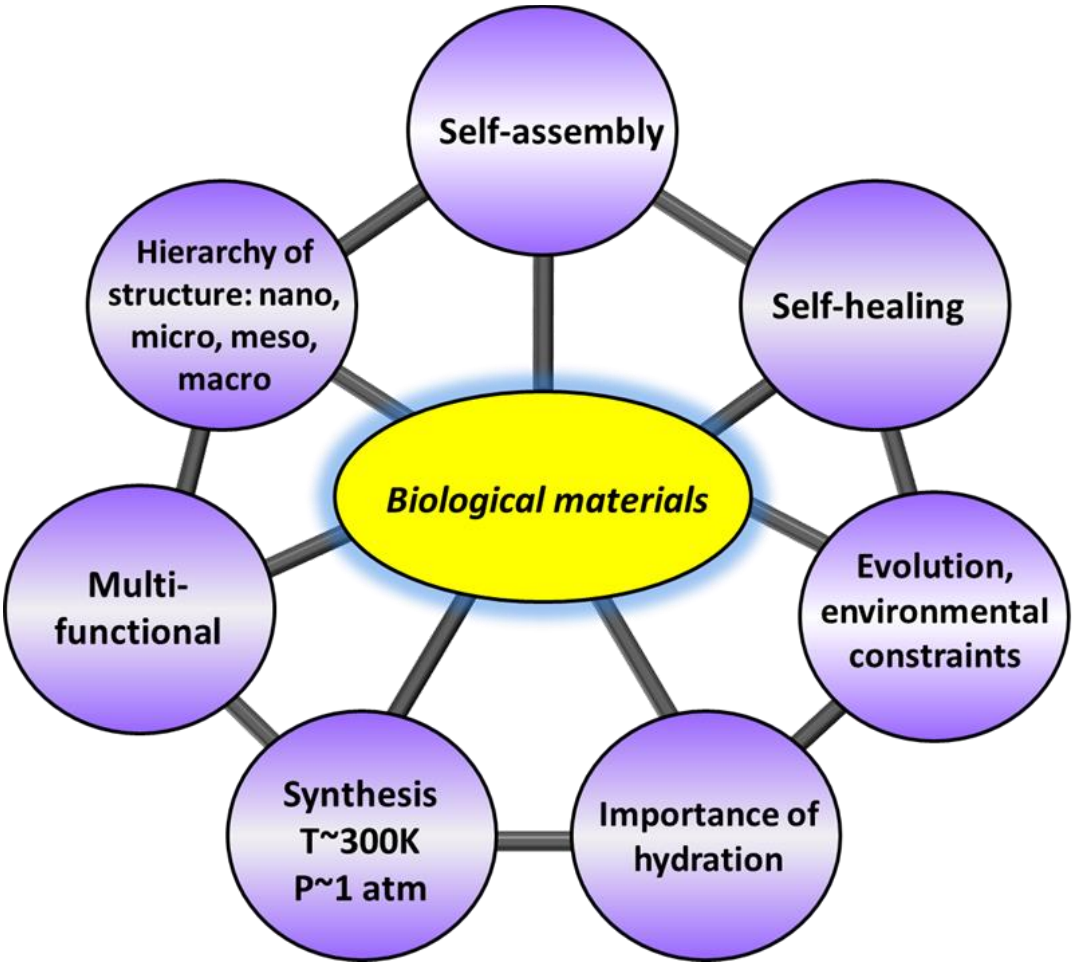

Figure 1.3: Fundamental and unique components of biological materials [3].

1.2 Objective of studying skin

Skin is a multifunctional organ which covers vertebrates, providing protection from the environment, temperature regulation, camouflage, thermal energy collection, and is a

host for embedded sensors. It is crucial in terms of defense, as the failure of skin will quickly lead to death due to infection. Therefore, the skin must possess damage minimization strategies in order to aid in its effectiveness. The objectives of studying skin are:

1. Investigate the mechanical properties of skin, paying special attention to its unique tensile response, and its extreme tearing resistance.
2. Develop a hierarchical model which accurately defines the structure of skin from the molecular to the macroscopic level.
3. Define the failure averting properties of the skin which lead to its tear resistance.
4. Develop an accurate model of collagen in skin based on its physical structure while accounting for elasticity, viscosity, and anisotropy.

The results from these studies will provide an improved understanding of the important characteristics of collagen based dermal protection. This new knowledge will aid in the further development of lead to new opportunities to create more robust bio-inspired materials and designs.

1.3 Objective of studying scales

Scales accomplish many of the same functions as skin, in addition to providing protecting from impact and penetration due to predatory attack. Scales perform their protective role while maintaining a full coverage and conforming to the locomotive requirements of the fish they protect. The objectives of studying scales are:

1. Investigate the mechanical properties and hierarchal structure of the scales of the arapaima and the alligator gar.

2. Understand how the two scales achieve the function of protection from predatory impact and penetration, and describe the relationship between the properties of the fish's scales and predatory threats.
3. Produce an armor prototype inspired by the hierarchal structure of the alligator gar, utilizing 3d additive manufacturing and other techniques.

Understanding the key protective features of scales opens the possibility for incorporation of natural designs into superior synthetic armors. In particular, a scale inspired armor which allows for improved flexibility of joints and accommodation of strain would improve the protection of both human and machine.

CHAPTER 2: BACKGROUND OF COLLAGEN

2.1 Types of collagen and its ubiquity in nature

Collagen is a structural biological polymer of upmost importance. Over 200,000 articles have been written about collagen, divulging the intricacies of this biopolymer which is the key ingredient of connective tissues. It is prevalent in tendons, skin, blood vessels, cornea, and fish scales, and creates composites with minerals to make bones, teeth, and cartilage. Collagen makes up to 30% of the mass of vertebrates and lays their structural framework. Due to its ubiquity and importance, collagen has been nicknamed the "steel of biological materials".

Collagen comes in many forms throughout nature. Each polypeptide molecule is a left-handed chain (Figure 2.1a); three polypeptide molecules form a right handed triple helical structure (Figure 2.1b). Each helical structure is called tropocollagen [4]. Each polypeptide chain (also called procollagen) contains a region characterized by a repeating amino acid motif: Gly-X-Y where Gly is a glycine and X or Y can be any amino acid. Glycine is at the core of the protein, while the X and Y amino acids are exposed at the surface.

The triple helical region is a major part of most collagens, but in some cases it can be only a minor part with other large non-collagenous domains of the molecule. In humans, there are 28 proteins known as collagens, as well as many other proteins which are considered part of the collagen superfamily. Collagens are classified into several general groups: fibril collagens, FACIT (Fibril Associated Collagens with Interrupted Triple Helices) and FACIT-like collagens, beaded filament collagens, basement membrane

collagens, short chain collagens, transmembrane collagens, as well as some unclassified collagens. The most common form of collagen is type I, which is a fibril collagen [5]. However, a brief description of the various classes is presented below.

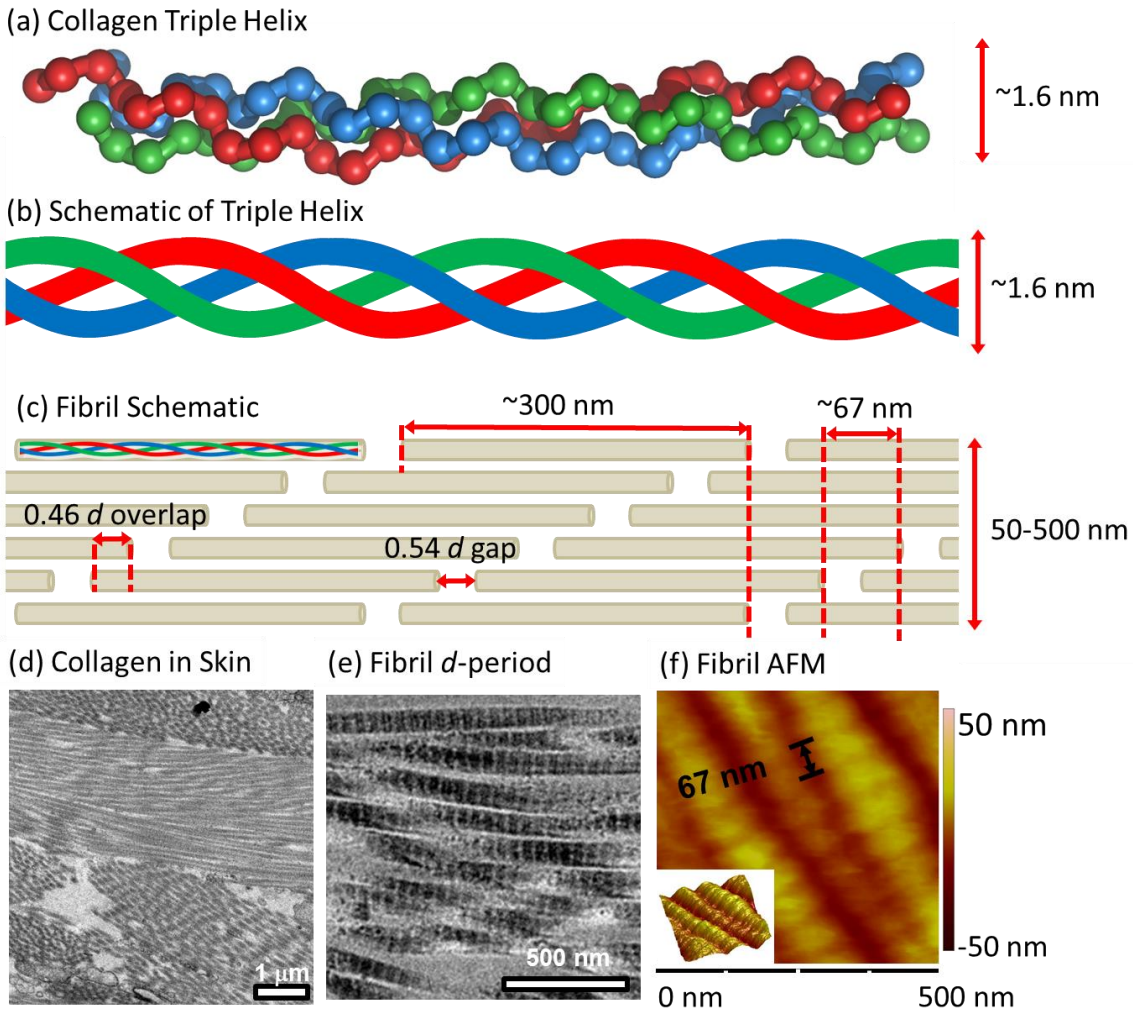

Figure 2.1: Structural hierarchy of fibril collagen. (a) In collagen formations, helical left-handed procollagen chains (Red, Green, Blue) form a right-handed triple helix of roughly 300 nm in length. (b) Schematic representation of triple helix formed by three procollagen chains. (c) Arrangement of triple helices into fibrils. Triple helices are arranged in a staggered manner, leading to a gap (0.54 *d*) and an overlap (0.46 *d*) region. The gap region has less triple helices across the section, and the overlap region has more. This gap and overlap has a periodicity, or *d*-period, of ~67 nm, and is the cause of the visible banding in collagen fibrils. (d) Layers of collagen fibrils in a cross-section of skin. (e) Collagen fibrils of 100 nm diameter imaged by TEM. Fibrils clearly display the characteristic banding feature. Due to the viewing angle of the fibrils, *d*-period measurements decrease proportionally to the cosine of the viewing angle. A 90° viewing angle would lead to perfectly accurate measurements. (f) AFM of hydrated collagen fibrils in an arapaima scale. 67 nm *d*-period is measured.

2.2 Fibril collagens

Fibril collagens are characterized by a characteristic *d*-banding pattern, where a staggered collagen arrangement creates visible bands on the fibrils produced. Highly organized fibrils and fibers provide structural support throughout the body including in bones, skin, tendons, cartilage, dentin, blood vessels, nerves, intestines, and in the fibrous capsules of organs.

The structural hierarchy is illustrated in Figure 2.1c. Hydrated collagen molecules of ~1.6 nm [6] diameter and ~299 nm length (as packed within fibrils) are staggered by integral multiples of ~67 nm, or one *d*-period [7]. The two-dimensional version of this is shown, but in three dimensions it becomes impossible to maintain equal staggering with all adjacent molecules [8]. In order to maximize the number of quarter staggered molecules, Smith [6] proposed a collagen filament composed of five molecules in cross-section where each molecule is staggered by one *d*-period. These five-molecule arrangements, called microfibrils, correspond to the observation of 2-3 nm diameter collagenous structures and is the only reasonable geometric arrangement to reflect these observations [6, 9]. Each molecule is 4.46 *d* long, and a gap of 0.54 *d* (~36 nm) lies at the ends of non-overlapping molecules. There is also an overlap of 0.46 *d*, or 31 nm between adjacent molecules. The 0.54 *d* length empty period along with the 0.46 *d* overlap lead to the full 67 nm *d*-period. This overlapping pattern is called the quarter-staggered assembly [10].

A full crystallographic description of type I fibrillar collagen supermolecular structure was presented by Orgel et al. [11] and is shown in Figure 2.2. The electron density map of Figure 2.2a shows the collagen molecules forming a helicoid around the axis; the microfibril has a supermolecular right-handed twist. This is also shown in Figure 2.2c.

Thus, there are three helices: polypeptide chains (left handed), collagen chains (right handed), and microfibrils (right handed) consisting of five collagen chains. The molecules have a quasi-hexagonal packing pattern, and the maps confirm that each microfibril consists of five molecules in the overlap region. This detailed description of the packing of molecular collagen is a powerful tool for the understanding and modeling of the collagen fibril.

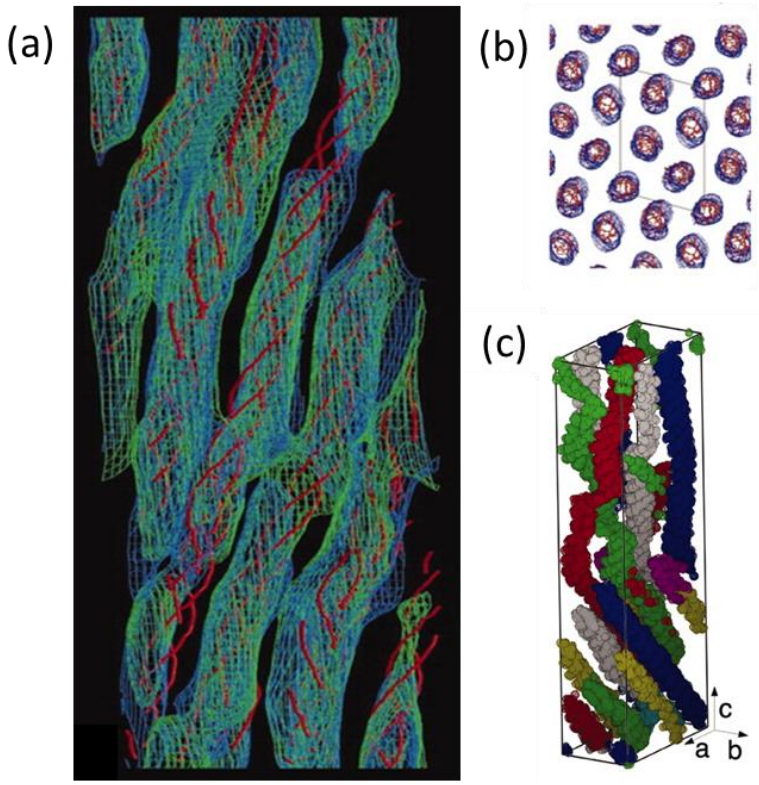

Figure 2.2: Collagen structure as presented by Orgel et al. [11] (a) Electron density map of a collagen microfibril consisting of five collagen molecule segments, and showing the right-handed supermolecular twist. (b) Unit cell marked around fibril cross-sections, showing the quasihexagonal packing of the molecular segments. (c) Molecular path of a collagen molecule through multiple unit cells.

2.2.1 FACIT collagens

Fibril Associated Collagens with Interrupted Triple Helices are abbreviated FACIT collagens. FACIT collagens are thus named due to their associations and interactions with collagen fibrils. They have collagenous domains which are interrupted by non-helical

domains, and associate with the surface of collagen fibrils. Type IX collagen, for example, is a FACIT collagen which lies anti-parallel along type II fibrils [12]. A hinge region provides flexibility between the collagen cross-linked with type II fibrils and a terminal domain which is available for interactions with matrix constituents [13]. However, some FACITs are not actually known to interact with collagen fibrils; these collagens are classified based on the primary sequence which is similar to that of type IX, XII and XIV collagen, which have been shown to interact directly with fibril collagen molecules [4, 14, 15].

2.2.2 Beaded filament collagen

There is only one beaded filament collagen, type VI. Type VI collagen is composed of beaded filaments with short triple helical regions, and is about one third the length of fibrillar collagens. Type VI collagen plays an important role in maintaining tissue integrity. The beaded filament collagens have large N and C terminal regions, and molecules assemble into filaments with a periodicity of 110 nm. However, the terminal regions are not cleaved during assembly. These uncleaved terminal regions cause a periodic bead region throughout the collagen filament [14].

2.2.3 Basement membrane collagens

The basement membrane is a matrix under the cavities of the epithelium lining and surfaces of organs including skin, and the endothelium in the interior of blood vessels. Basement membrane collagen (type IV) creates specialized structures found at tissue boundaries. It forms relatively thin sheets of 40-50 nm thick interlaced networks, which aid in molecular filtration. The network is a fine meshwork structure of many branches, about 20 nm between branching points [5, 14, 16]. Other collagens found in the basement

membrane zone include collagen VII, which creates anchoring filaments of about two molecules in length, and collagens XVIII and XV, which are crucial to eye and muscular development, respectively.

2.2.4 Short chain collagens

Short chain collagens (VIII and X) are meshwork forming collagens. The triple helical region is short: about half the length of fibrillar collagen. Type VIII collagen forms a hexagonal meshwork of thin fibrils, and functions as an enhancer of growth factor induced proliferation of cells. Type X collagen localizes in the hypertrophic zone of mineralizing cartilage [14].

2.2.5 Transmembrane collagens

Transmembrane collagens span the plasma membrane of cells, binding to extracellular and sometimes intracellular ligands. They are subject to shedding *in vivo* and *in vitro*, and are multifunctional, serving as a matrix receptor when membrane-bound and a signaling factor when soluble [17]. Additionally, transmembrane collagens play an important role in adhesion [5]. In this overview we focus on the most abundant type of collagen, fibril collagens.

2.3 Genesis and formation of fibril collagen

Collagen biosynthesis is a complex and deeply explored process. While it was once believed that the organization of collagen was a “self-assembly” process, where secreted collagen molecules would be ejected into intercellular space and self-assemble, this idea is no longer fully accepted [18, 19]. What is clear is that the formation of collagen fibrils does not occur in one step, but requires intracellular and extracellular stages which lead to the production of the common fiber [20]. Birk and Trelstad [21] identified pockets in the

membranes of collagen producing fibroblasts which suggested that the fibroblast coordinated collagen assembly. The fibril formation process in a simplified manner is outlined in Figure 2.3, beginning with the synthesis of procollagen chains on ribosomes (Figure 2.3a). These polypeptide procollagen chains are imported into the rough endoplasmic reticulum (ER) (Figure 2.3b) where, after a series of posttranslational steps, three chains combine to make a triple helical procollagen molecule. Stabilization of this molecule is due largely to hydroxylation of proline and hydroxyproline which, combined, make up about 20% of the total amino acids in human fibrillary collagens; hydroxylation of these amino acids leads to hydrogen bonding and the electron withdrawing effect [22].

Procollagen molecules transit via the Golgi complex (Figure 2.3c) where they are packaged into secretory vesicles, called Golgi to Plasma Membrane Carriers. During this packaging and transportation in the vesicles (Figure 2.3d), C- terminal processing, or removal of the procollagen propeptides by proteinases begins. Although procollagen processing was believed to be a completely extracellular event, N- and C- proteinases have been identified in the Golgi network, and the C-proteinases have been shown to be active [23, 24]. Canty et al. [25] showed that in embryonic tendon fibroblasts, some Golgi to plasma membrane carriers contain fibrils. Once formed, fibrils are subsequently stabilized by the formation of covalent crosslinks based on the reactions of aldehydes which are generated enzymatically from lysine or hydroxylysine side-chains [26]. Golgi to plasma membrane carriers then push out of the plasma membrane, creating a protrusion called a fibripositor (fibril depositor, Figure 2.3e). Fibripositors have thus far been identified in tendon [25], fibrohistiocytic tumors [27], and corneal structures [21], and have become a common model used to explain the production of the fibril architecture in highly

anisotropic, load bearing collagen arrays [28]. An alternative model suggests that fibrils condense from highly concentrated liquid crystalline solutions of tropocollagen monomer. Trelstad [29] concluded that physical forces lead to the alignment of collagen structures, and Ruberti and Zieske [30] have produced supporting evidence of this model by the creation of aligned collagen structures by simply confining monomer solutions between two featureless surfaces. Assembly from a liquid crystalline solution would simplify the collagen matrix assembly, and is consistent with some observations [31, 32].

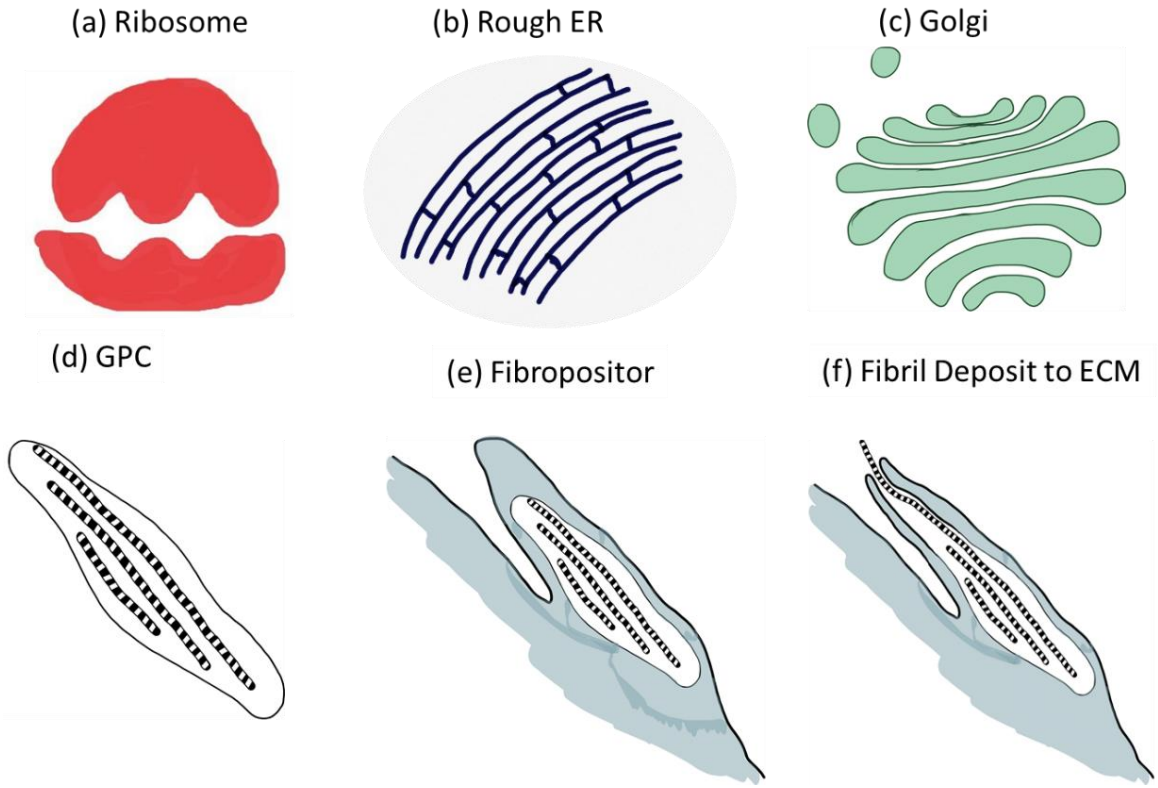

Figure 2.3: Formation of a collagen fibril. (a) The formation of a collagen fibril begins where the Ribosome synthesizes procollagen chains. (b) The ribosome imports new procollagen chains into the rough endoplasmic reticulum. Posttranslational modifications result in assembly of procollagen molecules. (c) The Golgi pack procollagen molecules into secretory vessels, called Golgi to Plasma Membrane Carriers (GPCs). (d) GPC package after separating from Golgi apparatus. (e) A fibripositor (fibril depositor) is formed as the GCPs pushes out of the plasma membrane of the cell, preparing to deposit a fibril. (f) The fibripositor opens and deposits a fibril into the ECM.

2.4 Mechanical response of fibril collagen

The mechanical response of fibril collagen can be evaluated at different scales including: the molecular scale, the response of an individual molecule; the fibril scale, the response of the individual fibril; the microscale, the response of a collagen fiber; and the macroscale, the response of a collagenous tissue. Over time, many investigations have been performed at these different scales, and in some cases there are large variances in results across the same hierarchal level. Additional hierarchical levels have been described such as the microfibril, subfibril, and fascicle [33], but the majority of research regarding the mechanical response of collagen has focused on the following levels: molecule, fibril, fiber, and tissue. Table 2.1 compares the response of collagen at multiple hierarchical levels. One aspect that is significant is that the elastic modulus decreases as one marches up the hierarchical spatial scale. This is due to interfibrillar sliding at the lower scale and interfiber sliding at the larger scale as well as the straightening and reorientation of the fibrils/fibers.

Molecular dynamics simulations have become a key tool used to further the understanding of collagenous-based tissues. In order to effectively simulate collagen, it is crucial to have a good understanding of the molecular structure and packing arrangement of collagen molecules within the fibril. The earliest simulations were based on short, ~10 nm collagen-like peptides based on information from X-ray crystallography [34]. Knowledge of the collagen molecular structure has expanded, and now molecular packing data of type I collagen by Orgel et al. [11] provide molecular resolution packing information. Combined with high resolution crystallography of collagen model peptides [22, 35], a whole molecule and tri-dimensional understanding of the structure of collagen is attained [7].

Table 2.1: Comparison of Young's Modulus of collagen at multiple hierarchal levels

Molecular	
Single molecule stretching, Atomistic modeling [36]	4.8 GPa
Single molecule stretching, reactive atomistic modeling [37]	7 GPa
Single molecule stretching, Atomistic modeling [38]	2.4 GPa
Coarse grain modeling [39]	4 GPa
Atomistic modeling [40]	4 GPa
Atomistic modeling [41]	4.5-6.2 GPa (long, short molecule)
X-ray diffraction [42]	3 GPa
Brillouin Light Scattering [43]	9 GPa
Brillouin Light Scattering [44]	5.1 GPa
Estimate from persistent length [45]	3 GPa
Estimate from persistent length [46]	4.1 GPa
Estimate from persistent length [47]	0.35-12 GPa
Microfibril and Fibril	
MEMS stretching [48]	0.4-0.5 GPa low strain, 12 GPa high strain
MEMS stretching [49]	0.86 GPa low strain
X-ray diffraction [50]	1 GPa
X-ray diffraction [51]	0.43 GPa
AFM testing [52]	0.2-0.8 GPa aqueous, 2-7 GPa ambient
Bead and String based mesoscale modeling [53, 54]	4.4 GPa low strain, 38 GPa high strain
Atomistic modeling [34]	0.3 GPa low strain, 1.2 GPa high strain
Fiber	
Crosslinked Rat tail Tensile testing [55]	1.10 GPa
Non-Crosslinked Rat tail Tensile testing [55]	50-250 MPa
Extruded, crosslinked fiber [55]	260-560 MPa
Rat tail tendon [33]	960-1570 MPa
Rat tail tendon [56]	480-540 MPa
Extruded, crosslinked fiber [56]	170-550 MPa
Rabbit patellar tendon [57]	30-80 MPa
Tissue	
Skin [58]	0-50 MPa
Tendon [59]	1 GPa
Cornea [60]	0.2-1.0 MPa
Mitral Valve [61]	0-50 MPa

2.4.1 The molecular scale

Multiple atomistic and coarse grain modeling simulations as well as a number of experimental methods have led to a variety of estimates of the molecular modulus of the collagen molecule. Figure 2.4a shows a molecule being pulled in tension. Sasaki and Odajima [42] used X-ray diffraction to measure the helical pitch of collagen molecules, and deduced the strain from the molecular pitch; this lead to an estimate of the modulus of 3.0 GPa. In separate studies, Cusack and Miller [44] and Harley et al. [43] used Brillouin light scattering to vibrate tendons, and extrapolated molecular moduli of 5.1 and 9 GPa, respectively. Atomistic modeling by Lorenzo and Caffarena [36], Buehler [37], Gautieri et al. [40], and Vesentini et al. [38], and coarse grain modeling by Gautieri et al. [39] predicted moduli similar to experimental measurements, between 2.4 and 7 GPa [34]. Figure 2.4 highlights several important results of testing at the molecular scale; Figure 2.4b presents the results of simulations by Gautieri et al. [39] relating the elastic modulus at the molecular scale to the strain rate and showing that only above a certain rate there is a strong relationship between them. This critical rate helps determine an upper limit on strain rates during simulations in order to minimize computation time, which may be large due to the number of atoms in a collagen molecule [34]. Pradhan et al. [41] highlighted the importance that the length of the molecule plays, and simulated the modulus of short (8.5 nm) and long (300 nm) collagen molecules: 6.2 and 4.5 GPa. Figure 2.4c-d shows that the short molecules have a saw-tooth like force-displacement curve due to the large proportion of hydrogen bonds being broken and reformed, while a longer molecule shows a much smoother curve; these results highlight the important considerations which must be accounted for when simulating the molecular response of collagen.

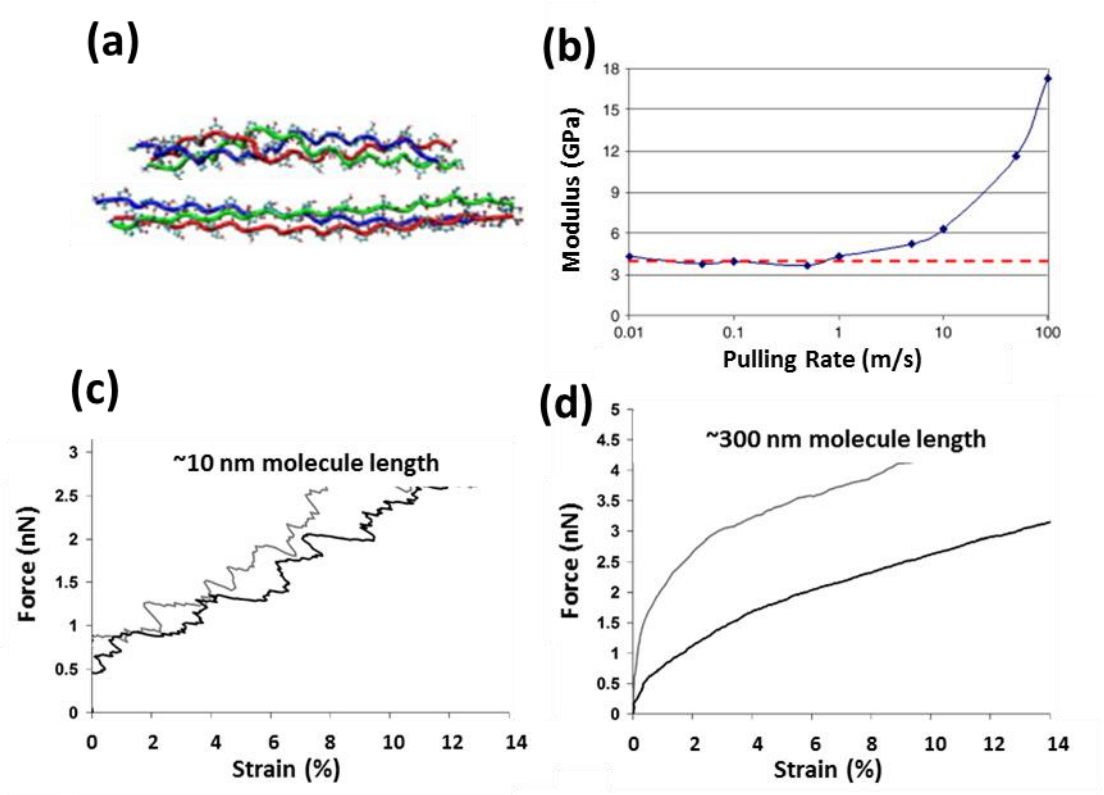

Figure 2.4: Mechanical response of molecular scale collagen. (a) A collagen triple helix subjected to extension. (b) Simulations by Gautieri et al. [40] predict the mechanical response of the collagen triple helix. The modulus (increasing from 4 to 17 GPa) and its relationship to strain rate is illustrated. (c-d) Simulations of short and long molecules by Pradhan et al. [41] show the importance of molecule length in the tensile response; short molecules lead to a sawtooth like force-displacement curve due to the breaking and recreation of hydrogen bonds.

2.4.2 The fibril scale

The elastic modulus of collagen at the fibril scale is lower than the modulus at the molecular scale. Similar to tests of the individual molecule, the results of different fibril tests have produced a variety of results. Among wet fibrils, chosen due to their relevance to the in vivo condition, reported values of fibril modulus have a range from 0.2 GPa to 0.8 GPa at small strains. Testing methods used to test fibril modulus include X-ray diffraction by Sasaki and Odajima [42], where measured fibril strain is compared to tissue stress values (0.43 GPA), and AFM testing by Van Der Rijt et al. [52], who pulled an individual hydrated fibril and recorded a modulus 0.2-0.8 GPa (increasing with strain). MEMS stretching of a

single fibril by Eppell et al. [48] and Shen et al. [49] recorded moduli of 0.76 to 0.82 GPa. The experimental setup and results for nanoscale testing are shown in Figure 2.5; AFM and MEMS testing is shown in Figure 2.5a-b and the AFM measured tensile response by Van Der Rijt et al. [52] is shown in Figure 2.5c. Atomistic and mesoscale modeling has been conducted by Buehler [53, 54] who estimated a range of 4.36-38 GPa, and more recently by Gautieri et al. [34] who predicted 0.3-1.2 GPa, making note of the extreme importance of geometry, scale of observation, deformation state, and hydration level during simulations.

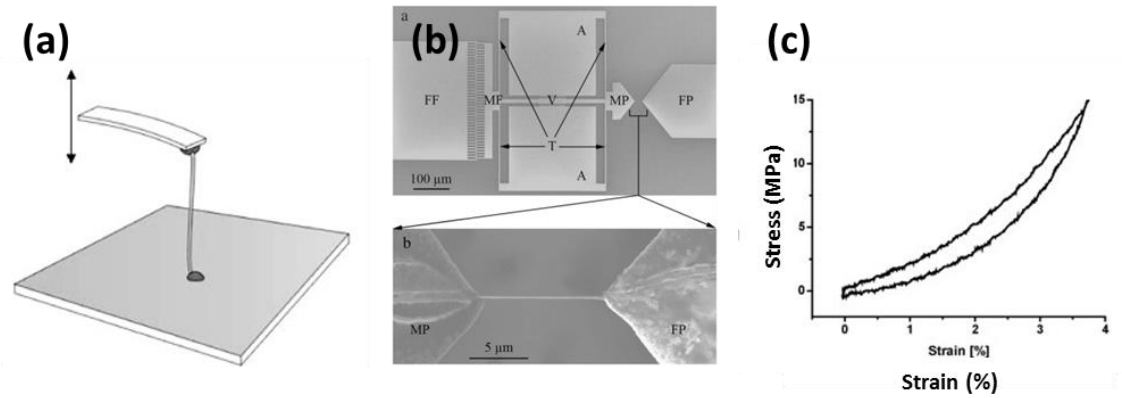

Figure 2.5: Mechanical response of collagen at fibril scale. Multiple tests have been done on collagen fibrils. (a) A test using AFM by Van Der Rijt et al. [52], using glue to attach the fibril to the AFM tip and a base plate. (b) MEMS stretching of collagen fibril by Eppell et al. [48] (c) Stress strain curve of wet collagen fibril by Van Der Rijt et al. [52]; dry measurements were also recorded, but the wet curve is shown because collagen fibrils are hydrated in the in vivo environment.

A degree of the variance in the results of mechanical testing can be understood based on Buehler's [53] simulation of the effects of crosslink density on collagen fibrils. Crosslinks can be visualized as areas of increased adhesion between collagen molecules, seen in Figure 2.6a. By varying the crosslink density from zero to approximately 3 per molecule, the stress which the fibril can support increases from less than 0.5 GPa to over 6 GPa. Additionally, the failure changes from a more gradual sliding to a brittle one as the

density increases (Figure 2.6b). The first regime is characterized by the breaking of hydrogen bonds and a lower modulus compared to the second region which becomes relevant at ~30% strain, and corresponds to the stretching of the molecular backbone of the collagen triple helix. It is only with sufficient molecular cross-linking that sliding can be averted, and this second regime is pertinent. One can conclude that the elastic modulus and fibril strength are dependent on the density of bonds between the molecules.

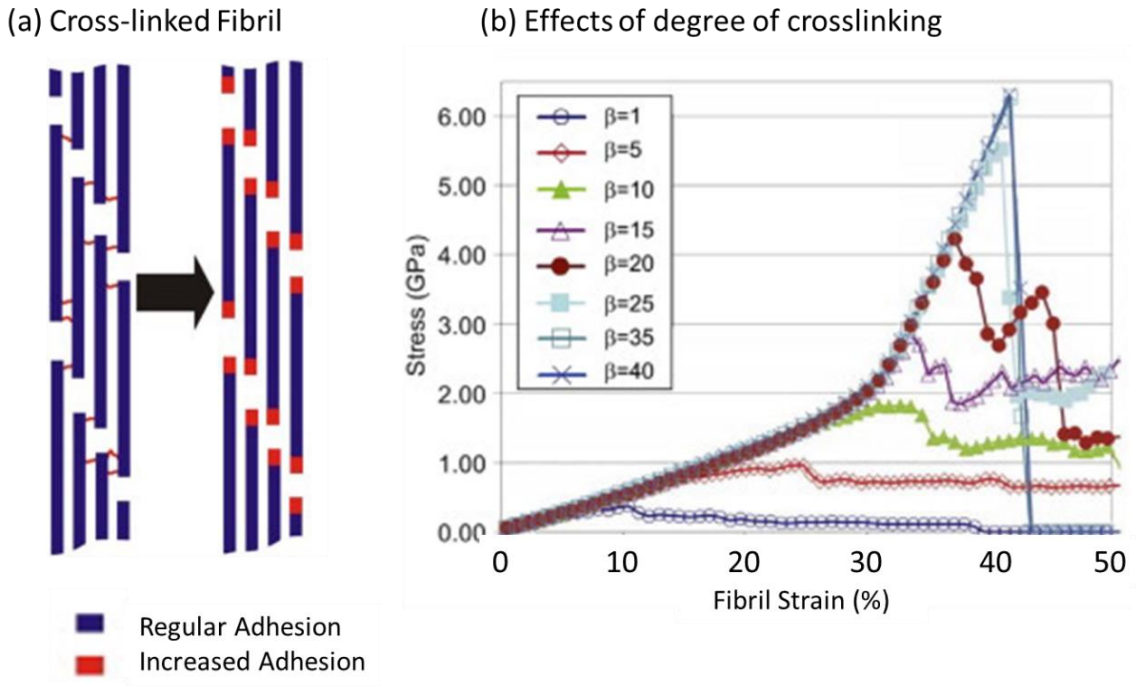

Figure 2.6: Crosslinking and mechanical response of fibril collagen. β is a parameter which is a linear representation of the degree of crosslinking; β=15 corresponds to one cross link per molecule, β=30 corresponds to two, etc. (a) Schematic showing schematic of cross-linked fibril with an average of one cross-link per molecule (corresponding to β=15.) (b) Simulations showing the effects of degree of crosslinking on a collagen fibril. At higher crosslink densities, there is a higher degree of adhesion between molecules; this leads to sufficient adhesion to enter the second elastic regime of increased modulus which corresponds to the stretching of the backbone of the collagen helix. The first elastic regime corresponds to breaking of hydrogen bonds between the helices of the collagen molecules. Schematic and simulation are results of Buehler [53].

Molecular simulations are a crucial tool at the fibril level but computationally difficult because a single solvated collagen fibril contains billions of atoms [34]. Even a single collagen molecule is computationally expensive due to the length of ~300 nm. In

order to effectively model larger fibrils, atoms are assembled into large groups of up to 100 pseudo atoms; this is called coarse graining. The Martini model provides a more modest level of coarsening, where generally four atoms are grouped [62].The resulting reduction in the number of particles also allows for a larger time step, and ultimately speeds up atomic simulations by 200-400 times [63]. Over time, the modeled structure of collagen has improved, as available computational power has increased. Combined with advances in the methods of evaluating and incorporating the collagen molecular structure, the quality of simulations has continually improved. These advances continue to open many possibilities for future studies of collagen at the full fibril or even fiber level, and beyond. Section 2.7 shows how this method is applied to the elucidation of the mechanical response of the *Bouligand*-like structure of the Arapaima scale.

2.4.3 The microscale

Microscale tests are performed on the collagen fiber, which is a bundle of fibrils. A rather limited number of investigations have been performed at the microscale. Fibers have been extracted from rat tail tendon and tested by Gentleman et al. [55] and Haut [33]. A tensile test of a collagen fiber is shown in Figure 2.7a, and results are presented in Figure 2.7b-c. Gentleman et al. [55] concluded that modulus of fibers increases with strain rate (consistent with the MD predictions of Gautieri et al. [40], shown in Figure 2.4b), and increases with initial length, ranging from 50 to 250 MPa. It is also interesting to note that upon exposing these fibrils to a cross-linking agent, the modulus increases to ~1 GPa, on the order of the fibril strength. It is possible that by cross-linking the fiber and eliminating the interfibrillar sliding, the fibril stiffness may be realized at the fiber level. These tests were performed on rat tail fibers, which display properties changing with age and maturity.

Throughout tissues, collagen fibers will inevitably display different properties due to natural differences such as shape, orientation, mineralization, and degree of cross-linking. Tendon is often chosen as an ideal material to study, because it is close to a pure and aligned collagen structure.

Collagen fibers are not present in all collagen-based structures. Structures which do include this hierarchal level include skin, tendon, and arteries. For example, the cornea does not have fibers, but rather fibrils which are organized in a highly ordered manner in order to allow transparency. Dentin consists of many mineralized fibrils. However, there are many instances where authors refer to collagen fibers in both the cornea and dentin, but this is due to discrepancies in the definition of fibrils and fibers. To further confuse the situation, a fibril may be described physically as a small fiber. But this should not confuse the fact that in the hierarchical structure of collagen, a fiber and fibril are unique levels which are not interchangeable and should not be confused. Other structures, such as the nails, hooves, and feathers do not have collagen at all.

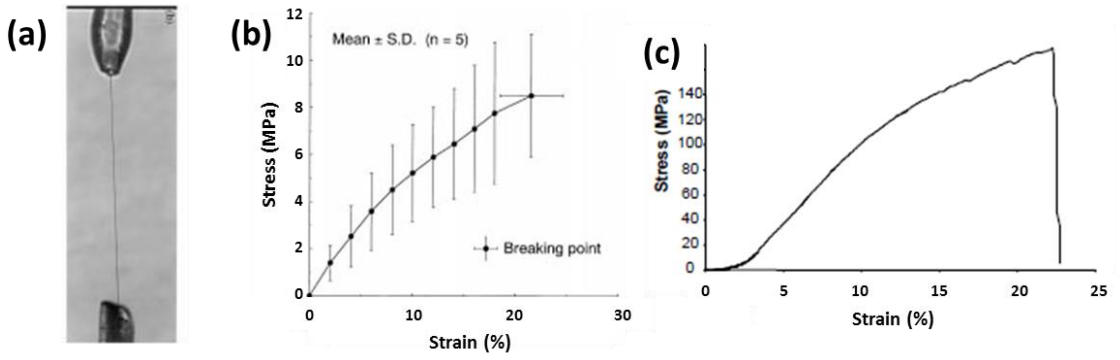

Figure 2.7: Mechanical response of collagen at the fiber scale. (a) Microscale tests of a collagen fiber. (b) Stress strain relations from the rabbit patellar tendon by Miyaziki [57]. (c) Stress strain relations from the rat tail collagen fibers from Gentleman et al. [55].

2.4.4 The macroscale

At the macroscale, collagen fibrils and fibers may be arranged into a vast number of structures with extremely variable properties. Skin, tendon, and the cornea are all nearly exclusively collagen, yet specialized hierarchal organization generates properties which are vastly different.

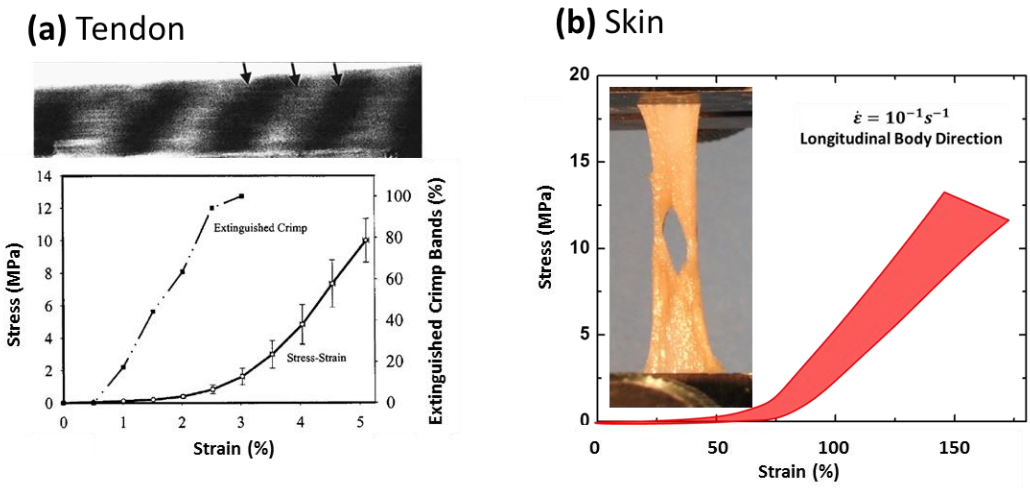

Figure 2.8: Mechanical response of collagen at the macroscale. (a) Macroscale tests of a tendon. The visible crimp in the tendon is extinguished in the toe region of the curve, followed by a stiffening. (b) Macroscale tests of skin, showing a much larger toe region of the curve do to the extreme curvature of the collagen fibers.

Tendon has parallel and slightly wavy fibrils, with a very small low load extension of 2-3%, followed by a linear modulus and near failure a slightly decreased modulus. As strain increases, the crimp bands are extinguished (Figure 2.8a). The modulus of tendon can be as high as 1 GPa [59] and ultimate strength reaches 250 MPa [64].

Rabbit skin is made of a net of wavy collagen fibers, and may experience greater than 50% extension before sizeable load is carried, and a modulus which begins at zero, increasing with strain to ~50 MPa, and an ultimate strength of ~15 MPa. This unique response is shown in Figure 2.8b. In order to visualize the extreme differences and range of mechanical behavior, the tensile responses of tendon and skin are shown in Figure 2.9.

The strength of tendon reaches values of ~90 MPa [65], while skin has a typical strength of 10-20 MPa (raccoon skin shown, with a strength of 10 MPa). Accordingly, the maximum strain of skin is much higher (ε_{max} ~ 0.5-1.5) than tendon (ε_{max} ~ 0.1).

Another example is the cornea which is comprised of lamellae of highly ordered straight fibrils with identical size and spacing. This structure is optimized for transparency, but at a cost: a much lower strength than tendon at only ~20 MPa [66]. The vast differences in mesoscale properties of collagen -based tissues are due to the hierarchical organization and configuration of the molecules, fibrils, and fibers.

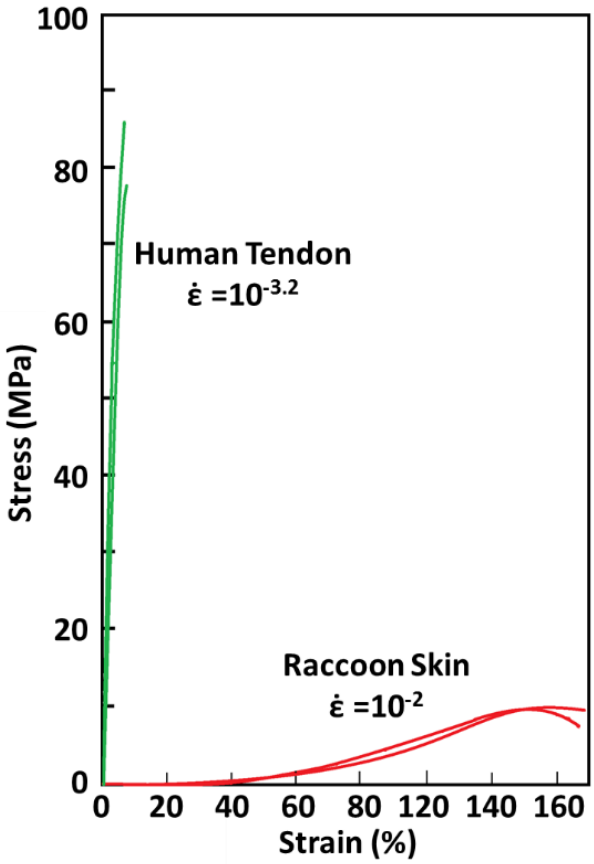

Figure 2.9: Illustration of the great variation in the mechanical response of collagen structures. A human tendon strains to less than 10% before rupture, at a stress of nearly 90 MPa [65]. Raccoon skin, in contrast, only supports ~10 MPa, but fails at a strain of nearly 150%. These vast differences of two collagen based structures show the extreme importance of the geometric organization of collagen fibrils.

2.4.5 Effects of mineralization

Mineralized collagen structures are designed to carry compressive load, as mineral crystals minimize sliding and deformation of the collagen. Figure 2.10a shows in a schematic manner the arrangement of minerals in the bone. Mineral particles are deposited within (intrafibrillar) and on the surface (interfibrillar) of collagen fibrils, which leads to a fully mineralized composite matrix of protein and mineral components [67, 68]. Structures made of this composite, such as bone, dentin, and fish scales, all experience altered mechanical properties compared to non-mineralized tissues. Both the mineral and collagen form a continuous network. The most important differences are that the mineralized structures are much stiffer and much less extensible than non-mineralized structures in tension, and have a much higher compressive strength [69]. This mineral is commonly referred to as hydroxyapatite, but in fact has a stoichiometrically deficient amount of hydroxyl [70, 71]. Carbonate ions substitute hydroxyl and make up a large portion of the stoichiometric deficiency [72]. However, this is only one of a large number of possible substitutions, which include Na^{+} or Mg^{2+} replacing Ca^{2+} ions, HPO_4^{-2} replacing phosphate ions, Cl^{-1} and F^{-1} replacing OH^{-1}, and CO_3^{-2} replacing phosphate and hydroxyl [73]. These substitutions are responsible for a lack of consistency in the literature as bone mineral may be referred to as apatite, hydroxyapatite, carbonated hydroxyapatite, and hydroxylapatite, among others. For the purpose of this review and to avoid confusion, the apatite-based component of bone will be referred to simply as mineral.

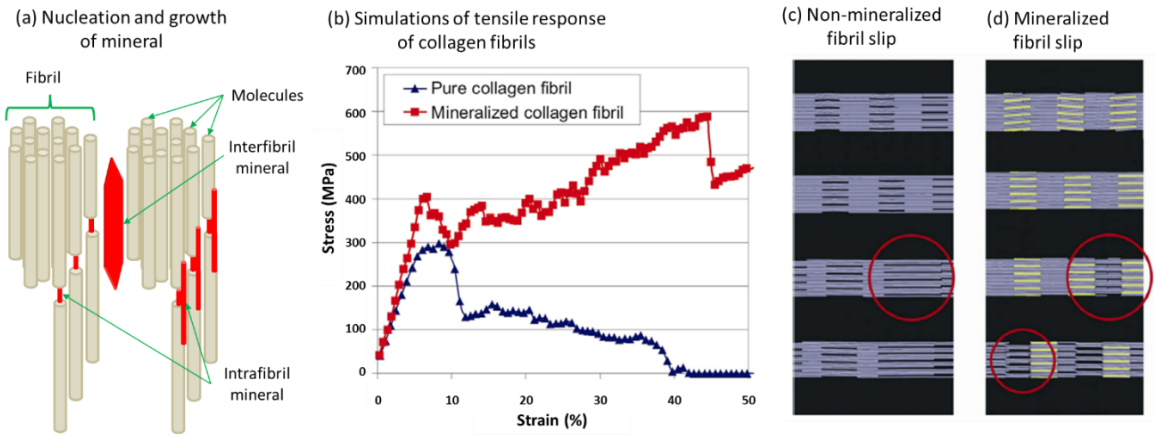

Figure 2.10: The effects of mineral on the collagen fibril. (a) Arrangement of mineral within and around collagen fibrils. Left: mineral nucleates in the gap region of fibrils. Right: nucleated mineral grows to form plate like crystals. Interfibrillar mineral grows between the two fibrils. (b) Simulations of the tensile stress-strain curves of non-mineralized and mineralized collagen fibrils. (c) Location of intermolecular slip of non-mineralized collagen. (d) Location of slip between mineral and collagen molecules. (b-c) from Buehler [74].

The result of the mineralization process is that collagen fibrils are impregnated with plate -shaped mineral particles which have dimensions of ~2 nm thickness and ~40 nm diameter [75]. In the gap regions of collagen fibrils, minerals nucleate to form intrafibrillar crystals, with the c-axis aligned with the molecule direction. These mineral particles grow and form plate-like crystals [76], as illustrated in Figure 2.10a. These mineral particles undergo less strain than the fibrils; the fibril to mineral strain ratio is 5:2, and the collagen matrix must absorb the remaining three-fifths of strain [77, 78]. Figure 2.10a also shows interfibrillar minerals (between collagen fibrils) oriented with their c-axis perpendicular to the molecular direction. The mineralization on the outer surface of the fibrils forms a continuous network. Thus, both the mineral and the collagen form interpenetrating networks. This is only addressed by current models in a superficial manner. For instance, the Fratzl [73] model assumes platelets which are not interconnected. More research is needed, both experimental and computational, to develop a full understanding of the synergy between the two components. Buehler [74] shows that, after initial slipping,

mineralized collagen continues to carry a significant load compared to non-mineralized fibrils (Figure 2.10b). The differences arise because non-mineralized collagen fibrils yield primarily by intermolecular slip (Figure 2.10c). The slip leads to the deformation of the region with lower material density, initiating at the interface between mineral particles and collagen molecules, thus reducing the density of the material and inducing nanoscale voids (Figure 2.10d). Via this nano-mechanism, the mineralized collagen fibrils are able to tolerate a large fraction of microcracks, without causing any macroscopic failure of the bone. In a way, the bone is remodeling itself [74]. Additionally, the formation of microcracks generates the mechanisms of ‘crack meandering’ and ‘crack bridging’ which enhance its toughness. The toughening mechanisms will be further discussed in Section 2.8.

2.4.6 Effects of hydration

The cross-linking of collagen fibrils is extremely important in establishing the mechanical response. In this regard, hydration plays a major role; in hydrated collagen, hydrogen bonds form between collagen and water, which allows for slipping and movement. However, as the collagen is dried, bonds form directly between collagen molecules and fibrils, preventing sliding and stiffening the structure. Skin is a suitable material to observe the effects of hydration; as the skin is dehydrated, its mechanical response is drastically changed, because of the reduction of interfibrillar sliding. The effect of dehydration was evaluated [58] by recording the stress-strain curves of skin after drying. The hydrated curve displays a long toe region; with dehydration, it becomes progressively shorter and stiffer. Four levels of hydration are shown in Figure 2.11 [58], corresponding to the percentages of initial weight: 100, 80, 60 and 35%,. The first corresponds to fresh

skin which has a water content of approximately 65-70%. The skin containing 35% of the original weight has very little moisture content since, as noted earlier, collagen represents approximately 30% of the body weight in vertebrates.

The toe region of the stress-strain curve of skin shown in Figure 2.11 is caused by the sliding and reorienting of collagen fibrils, which allows for large extension without high stress. The stress-strain curve of the most severely dried skin in this work (35 wt.% of the fresh skin, or 65% weight reduction from fresh skin) does not show an initial toe region because the sliding between the collagen fibrils is highly limited due to the lack of water molecules. A plateau can be seen at 8 MPa, where the internal stress is sufficient to break the interfibrillar bonds and at which point fibril reorientation can occur. Therefore, an elevated stress toe-like region exists as the interfibrillar bonds begin to break. Modeling by Gautieri et al. [79] predicts a decrease of the intermolecular separation from 1.6 to 1.1 nm with dehydration and, similarly, decreased intermolecular sliding in the collagen. In their computations, the force to pull a molecule from a microfibril increased from 4 nN to 30 nN. This calculated eight-fold increase is reflected in the higher stress levels measured with decreasing hydration.

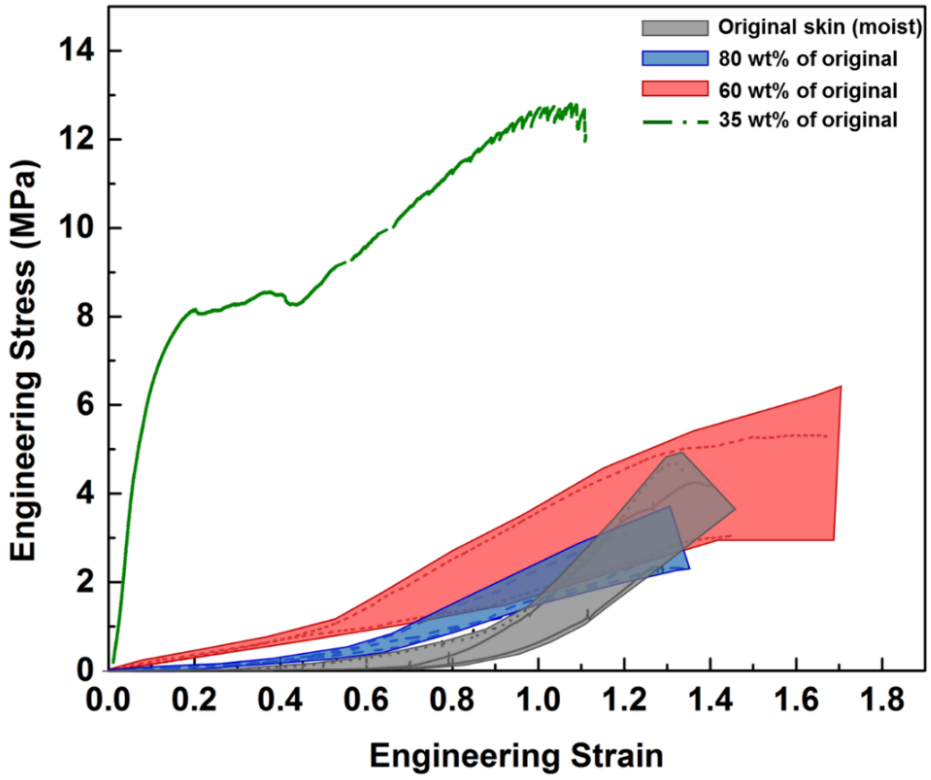

Figure 2.11: Stress-strain curves of original moist skin and dehydrated skin of different amounts. As skin becomes dehydrated, the toe region becomes shorter and stiffer due to increased adhesion between fibrils which prevents sliding and reorientation. After losing 65% of its weight to dehydration, the characteristic toe region of skin has vanished and been replaced with a higher stress quasi-toe region, which occurs when the internal stress is sufficient to break the bonds between dry fibrils and the fibrils proceed to reorient.

2.5 Models for collagen extension (tensile response)

The mechanical properties of collagen and collagen-based tissues have been modeled using several approaches: (a) hyperelastic macroscopic models based on strain energy in which strain energy functions are developed and lead to mechanical behavior calculations, (b) macroscopic mathematical fits where a nonlinear constitutive equations are used, and (c) structurally and physically based models where a constitutive equation of a linear elastic material is modified by geometric characteristics. These models are necessary for collagen-based materials which undergo large deformations in order to

capture their unusual mechanical behavior, which differs from the typical linear response of engineering metals and ceramics.

2.5.1 Hyperelastic macroscopic models based on strain energy

Strain energy models calculate stress in a material by taking the derivative of W, the strain energy, which is a function of the strain. Several models have been developed for biological tissues including one by Fung [80], developed specifically for skin; and more general models by Blatz et al. [81] and Veronda and Westmann [82]. Stress vs. strain relationships can be derived from these models using assumptions such as incompressibility (Equation 1), assumed boundary conditions, and the relationship between stress and the strain energy (Equation 2). σ_1, σ_2, σ_3 represents the stresses, and λ_1, λ_2, λ_3 are the stretch ratios in the principal directions OX_1, OX_2, and OX_3.

The constancy in volume hypothesis is:

$$\lambda_1\lambda_2\lambda_3 = 1 \tag{1}$$

The difference in Cauchy stresses in principal directions is the derivative of the strain energy with respect to the direction of extension (the derivation is presented in the Appendix A.2). This relationship results from a simplification of the Cauchy stress and strain energy relationship [83]. The result is Equation 2.

$$\sigma_1 - \sigma_3 = \lambda_1 \frac{\partial W(\lambda_1, \lambda_2)}{\partial \lambda_1} \tag{2}$$

Tong and Fung [84] developed a relationship between the strain energy and stress state, specifically for skin, as follows in Equation 3. This “biphasic” function has two parts: the second term expresses the response at higher stress levels, while the first term

represents the lower stress levels. Constants $\alpha, a,$ and c are used, and E_{ij} is the Green strain tensor.

$$W = f(\alpha, e) + c \exp\left[F(a, e)\right] \tag{3}$$

$$f(\alpha, e) = \alpha_1 E_{11}^2 + \alpha_2 E_{22}^2 + \alpha_3 E_{12}^2 + \alpha_3 E_{21}^2 + 2\alpha_4 E_{11} E_{22} \tag{4}$$

$$F(\alpha, e) = a_1 E_{11}^2 + a_2 E_{22}^2 + a_3 E_{12}^2 + a_3 E_{21}^2 + 2a_4 E_{11} E_{22} \tag{5}$$

where $E_{11} = E_1 = 0.5\left(\lambda_1^2 - 1\right)$ and $E_{22} = E_2 = 0.5\left(\lambda_2^2 - 1\right)$

Blatz et al. [81] suggested the relationship shown in Equation 6, by modifying an equation originally proposed by Valanis and Landel [85] and specifically applying it to soft tissues:

$$W = \sum_{i=1}^{3} C\left[e^{\alpha\left(\lambda_i^2 - 1\right)} - 1\right] \tag{6}$$

where C and α are constants.

Veronda and Westmann [82] developed the relationship for strain energy of the incompressible material shown in Equation 7. However, this expression presupposes isotropy, limiting the generality. C_1, C_2, and β are constants used.

$$W = C_1\left[e^{\beta(I_1 - 3)} - 1\right] + C_2\left(I_2 - 3\right) \tag{7}$$

where $I_1 = \lambda_1^2 + \lambda_2^2 + \lambda_3^2$ and $I_2 = \lambda_1^2\lambda_2^2 + \lambda_2^2\lambda_3^2 + \lambda_3^2\lambda_1^2$. I_1 and I_2 are the first and second strain invariants.

2.5.2 Macroscopic mathematical fits

Mathematical models make use of nonlinear constitutive equations to represent the extension of the skin. These models are not reduced to a strain energy form and do not

represent the anisotropic three-dimensional stress state. Over the years, many relationships have been developed, using a variety of fitting parameters including *a*, *b*, *d*, *k*, *C*, *n*, β, α, and some physically based parameters such as σ^* (reference stress) and ε^* (reference strain), and physical inputs ε (strain) and σ (stress). Hyperbolic, exponential, and power equations have been used to describe the non-linear behavior. The first relationship was developed by Wertheim in 1847 [86] who proposed Equation 8, a hyperbolic relationship between stress and strain:

$$\varepsilon^2 = a\sigma^2 + b\sigma \tag{8}$$

This expression gives a slope that monotonically increases with strain. Thus, over 150 years ago the response triggered the imagination of researchers. Figure 2.12a shows the graphical representation of Wertheim's equation, given here because of its historical value. The parameters a and b are experimentally matched to the data.

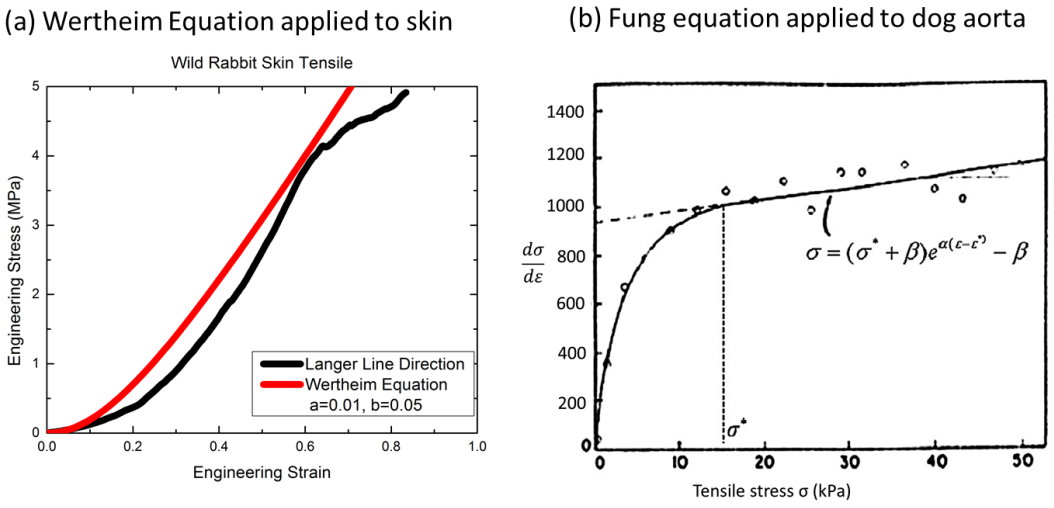

Figure 2.12: Wertheim and Fung equations applied. (a) Wertheim equation is applied to the skin extension curve along the Langer lines of a wild rabbit, or transverse to the direction of the body. (b) Representation of mechanical response of a dog aorta (circumferential strip) in terms of tangent modulus (slope of stress-strain curve) vs. tensile stress; slope and intercept provide parameters for Fung equation. (Reproduced based on Fung 1993 [87])

Morgan in 1960 [88] and Ridge and Wright in 1964 [89] both proposed power relationships, Equations 9 and 10, respectively:

$$\sigma = \varepsilon^{d} \tag{9}$$

$$\varepsilon = C + k\sigma^{b} \tag{10}$$

An exponential stress strain relationship was specifically developed for biological materials, by Fung in 1967 [90]:

$$\sigma = \left(\sigma^{*} + \beta\right)e^{\alpha\left(\varepsilon-\varepsilon^{*}\right)} - \beta \tag{11}$$

Fung [90] suggested that the increase in slope experienced at higher strains is due to full extension of collagen and elastin fibers, and effectively applied his model to the rabbit mesentery. Figure 2.12b shows the application of the Fung equation to dog aorta.

In general, the power law relationship is more effective at describing tissues with a larger toe region, as presented by Doehring et al. [91]. Recently, Chen et al. [92] implemented a combined power law and linear equation using a Heaviside function, as shown in Equation 12. The unfurling and straightening of the polymer chains is described by the power law, followed by a linear region initiated by a Heaviside function and corresponding to the stretching of the polymer chain backbones:

$$\sigma = k_1\varepsilon^{n+1} + H(\varepsilon_c)E(\varepsilon - \varepsilon_c) \tag{12}$$

k, n, and ε_c are parameters and E is the slope of the linear portion. This equation shows a small discontinuity in slope at ε_c.

2.5.3 Structurally and physically based models

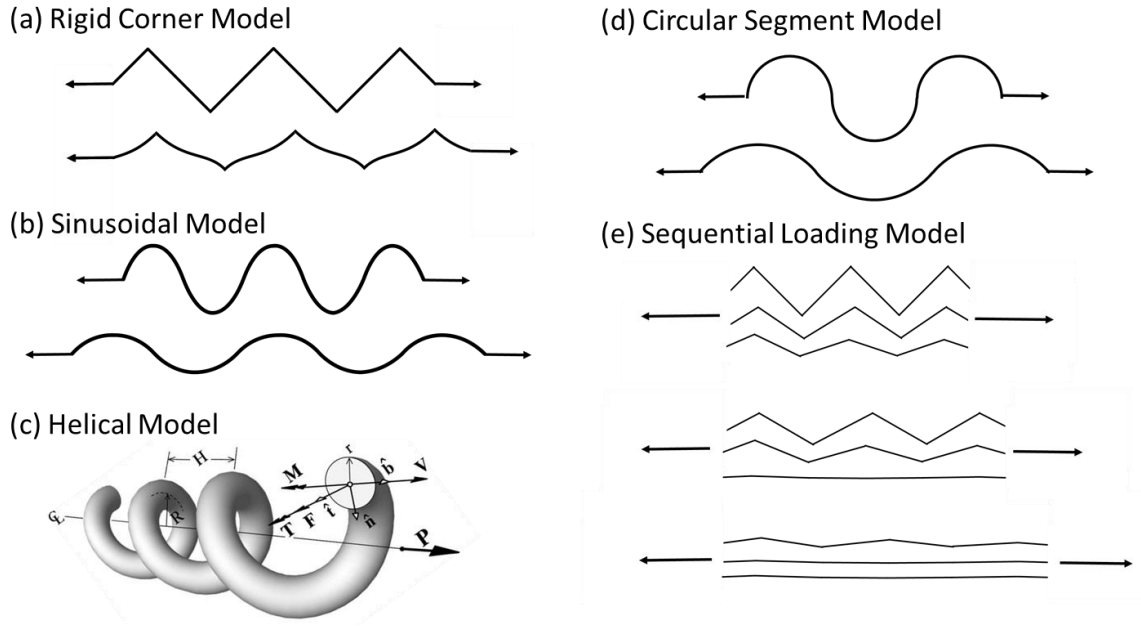

Figure 2.13: Structural collagen models and deformation. (a) The rigid corner model, assuming apexes of infinite rigidity. These apexes maintain their original angle under extension, while the beams in-between deform [93]. (b) The sinusoidal model, originally developed by Comninou and Yannas [94], but later simplified by Lanir [95]. (c) The helical model, originally developed by Beskos and Jenkins [96], and later modified for finite modulus at full extension by Freed et al. [61]. (d) Circular segment model, developed by Yang et al. [58]. (e) The sequential loading model developed by Kastellic et al. [97], which assumes stiffness only due to fully straightened fibers.

Structural models have been developed in order to describe the mechanical response of collagen as its configuration evolves under an applied strain. These models require the ability to observe how the structure of the fibers and fibrils evolves during extension. Some argue that the crimp structure of collagen has a two-dimensional wavy shape, while others state that it is a three-dimensional helix. Structural models have been developed to represent both assumptions. Due to the complexity of the collagen arrangements, the equations for these models are rather involved. The earliest model was proposed by Diamant et al. [93] in 1972, and is shown in Figure 2.13a. Fibrils were modeled as in-plane zig-zag shaped beams, with fixed (and not jointed) apexes of infinite rigidity. Using the bending modulus of the beams between the apexes, the relationship

between stress and strain takes the form of Equation 13 where ε_∞ is the length of the fully extended fiber, E is the Young's modulus of the fiber, and λ is the total stretch ratio:

$$\varepsilon - (\sigma / E) = \varepsilon_\infty - \lambda \sqrt{(E / \sigma)} \tag{13}$$

In 1976, Comninou and Yannas [94] developed a sinusoidal model for fibril shape, which was simplified in 1978 by Lanir [95]. The model is illustrated in Figure 2.13b. Upon stretching, the energy of the system changes due to the tensile and bending deformation of fibers, matrix-fiber interactions (modeled as a beam on an elastic foundation) and the strength of elastin fibers. Lanir's equation is designed to include the elastic component of matrix fiber interactions, and takes into account both elastic and geometric strain of fibers, in the form of Equation 14, where F_c is a horizontal component of force on the collagen fibers, ε_e is elastic strain of the fiber under extension (which is calculated using further equations), γ and α are geometric parameters, and K_e is the spring constant incorporating the cross sectional area:

$$F = F_c \varepsilon_e + K_e \left(\varepsilon_e + \gamma \Delta (\Delta + 2) / (1 + \Delta)^2 \right) \tag{14}$$

where $\Delta = \alpha \varepsilon_e$.

A helical model was first developed in 1975 by Beskos and Jenkins [96], but assumed fiber inextensibility—leading to an infinite stiffness at full extension. Therefore, this model was modified by Freed [61] to incorporate a piecewise function, allowing for a linear modulus at full fiber extension (denoted as $\overline{\lambda}$). The helical model is illustrated in Figure 2.13c, and takes the form of Equations 15 and 16. Freed et al. [61] used a strain energy function to calculate stresses prior to full fiber extension, taking into account axial

force, shear force, bending moment, and torque. $\overline{E}$ is a modulus based on the geometry of the helix, and ξ is a geometric parameter.

$$For\ \lambda < \bar{\lambda} \qquad \sigma = \xi \bar{E}\left(\lambda - 1\right) \tag{15}$$

$$For\ \lambda > \bar{\lambda} \qquad \sigma = \bar{E}\left(\bar{\lambda} - 1\right) + E\left(\lambda / \bar{\lambda} - 1\right) \tag{16}$$

Yang et al. [98] developed a model assuming that fibrils are circular segments of various radii and degrees of curvature, with the goal of most accurately reflecting the configuration of highly crimped fibril structures, as shown in Figure 2.13d. Stresses are calculated through Equation 17, while strains are obtained using Equation 18. *E'* is a pseudo-modulus determined from the geometric shape, *r* is the radius of the circular segments, θ_0 is the initial angle of the circular segments, and r_c is the initial circle radius.

$$\frac{\sigma_0}{E} = \frac{1}{E} \cdot \int_{r_c}^{r} E' \left\{ \frac{\csc(\theta_0)}{r_c \cdot r} \left[r \sin\left(\frac{r_c}{r} \theta_0 \right) - r_c \theta_0 \cos\left(\frac{r_c \theta_0}{r} \right) \right] \right\} dr \tag{17}$$

$$d\varepsilon = \left\{ \frac{\csc(\theta_0)}{r_c \cdot r} \left[r \sin\left(\frac{r_c}{r} \theta_0 \right) - r_c \theta_0 \cos\left(\frac{r_c \theta_0}{r} \right) \right] \right\} dr \tag{18}$$

In 1980 Kastelic et al. [97] took a different approach, suggesting that the variation in modulus is due to an assumption that resistance only arises from the elasticity of completely straight fibrils. Different degrees of crimp and variances in crimp angle affect the size of the toe and heel region. θ represents crimp angle of the outermost collagen fibrils in a fiber, $\theta(\rho)$ crimp angle at relative radius, ρ inside the fiber, R^* is fibril radius, and *b* represents a blunting factor, to reduce the sharpness of the crimps in the model which is shown in Figure 2.13e and represented by Equation 19.

$$\sigma / E = \varepsilon \left(R^* \right)^2 - 2(1-b) \int_0^{R^*} \left(\frac{1}{cos\theta(\rho)} - 1 \right) \rho d\rho \tag{19}$$

The worm-like chain model derives a nonlinear constitutive equation based on a continuously flexible isotropic rod. One example of a rod like this is a noodle; an important parameter, the persistence length, is the length for which the correlations in the orientation of the two ends are lost. The worm-like chain model takes into account an entropic term (due to changes in configuration) as well as an enthalpic term (due to elongation of the polymer). Inputs into the model include force, F; the Boltzmann constant, K_b; the absolute temperature, T; the persistence length, L_p; the contour (total) length of the fibers, L; and z, the extension (displacement) [3, 99].

$$F = \frac{k_b T}{L_p}\left(\frac{1}{4\left(1-z/L\right)^2} - \frac{1}{4} + \frac{z}{L}\right) \tag{20}$$

Four of the physically-based structural models presented can be compared to experimental observations, as shown in Figure 2.14. It is clear that for the tendon to which these models are being compared, the sine wave and circular segment are the most plausible ones. It is important to consider that these curves are plotted under the assumption that sliding between fibrils does not occur and does not contribute to strain. In fact, any sliding will shift the curve towards the right. If sliding does occur during extension (and this is treated in section 2.5.4), the circular segment model may be the most accurate representation of the in vivo fibril shape. This is also the most physically plausible configuration because the curvature is constant along the fiber length.

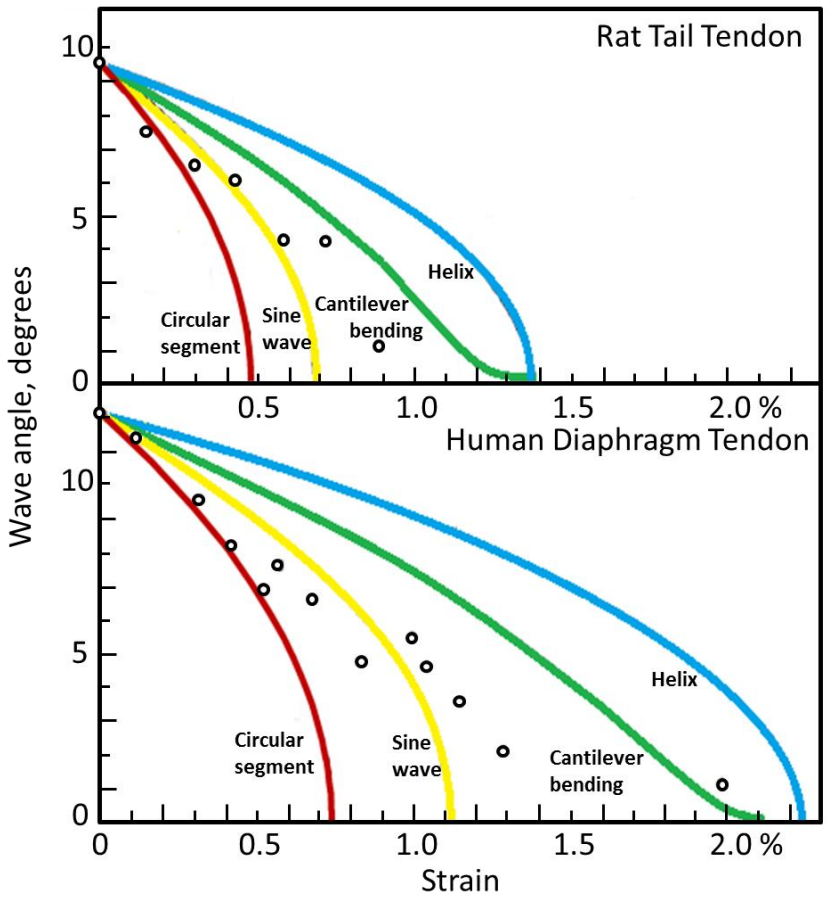

Figure 2.14: Comparison of wave angle under tension in different structural models. Experimental data points from tendon under tension (open circles) are compared to a calculated decrease in wave angle of structural models. In calculations, strictly geometric changes are accounted for; there is no inclusion of elastic strain or sliding, both of which are known to occur. Any elastic strain or sliding would add to the amount of strain at a particular stress level; the curves would be shifted towards the right. Adapted from Dale et al. [100].

2.5.4 Viscoelasticity in collagen structures

The theory of viscoelasticity is well established, the simplest representation of a viscous component being the dashpot. There are three principal models used to represent different viscoelastic materials, which consist of arrangements of springs and dashpots. These models are the Maxwell, Kelvin, and the Standard models. For the complete derivations, see, for instance, Meyers and Chen [3].Figure 2.15 shows the three models with their governing constitutive equations.

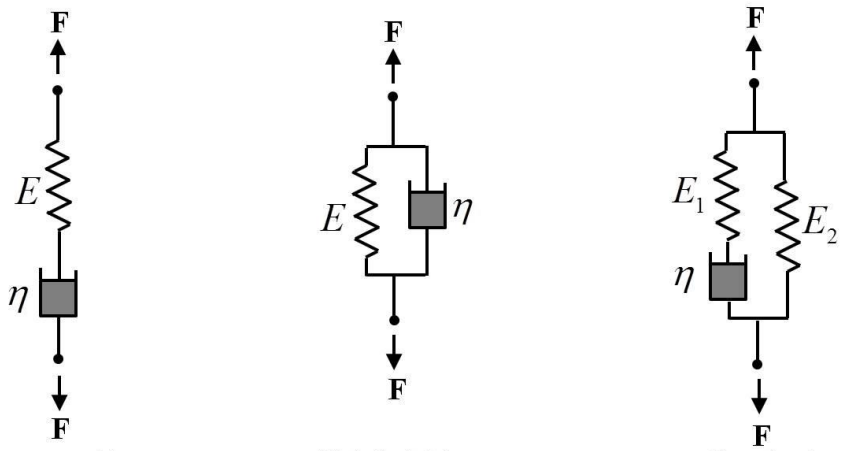

$$\frac{d\varepsilon_{total}}{dt} = \frac{\sigma}{\eta} + \frac{1}{E}\frac{d\sigma}{dt} \qquad \sigma(t) = E\varepsilon(t) + \eta\frac{d\varepsilon(t)}{dt} \qquad \frac{d\varepsilon}{dt} = \frac{\frac{E_2}{\eta}\left(\frac{\eta}{E_2}\frac{d\sigma}{dt} + \sigma - E_1\varepsilon\right)}{E_1 + E_2}$$

Figure 2.15: Viscoelastic models. Three common models for viscoelastic behavior, and corresponding equations in terms of stress and strain [3].

The amount of research on the viscous component of biological materials is rather limited. Recently, Puxkandl et al. [101] modeled the collagen fiber as two Kelvin models in series. The first element in the series represents the fibril, with the viscous effects caused by molecular friction and the elastic component derived from molecular cross links. The second in the series represents the proteoglycan-rich matrix, with the viscous effects caused by proteoglycan viscous relaxation and the elastic component caused by matrix shearing. This in series Kelvin arrangement is described by Equation 21, where α, β, and γ are defined material properties, ε_D is fibril strain, and ε_T is total strain.

$$\frac{d\varepsilon_T}{d\varepsilon_D} = \alpha + (\beta - \alpha)e^{-\gamma\varepsilon_T/\dot{\varepsilon}_T} \tag{21}$$

Using *in situ* X-ray diffraction, the elongation of collagen fibrils and the tendon as a whole were simultaneously measured [101], and the viscous effects caused the ratio of

fibril strain to tendon strain to increase with increased strain rates. Figure 2.16a shows the model used, and the increasing ratio of fibril to total strain measured during tests.

The storage modulus (*E'*) and loss modulus (*E''*) of articular porcine cartilage were measured using dynamic indentation in the range of 1-250 Hz by Franke et al. [102]; this frequency is representative of loading conditions in gait. *E'* describes the in-phase elastic response of a given material, and *E''* is a measure for the damping/energy being dissipated throughout the experiment. In this experiment, both were measured from the oscillations in the loading of a nanoindenter. The contact damping, D_c, frequency, ω, and contact stiffness, C are related to the storage and loss modulus through Equation 22. The resulting measurements are shown in Figure 2.16b; both storage and loss moduli are related to the loading frequency, reflective of the strain-rate dependence of collagenous materials. The trend is for both to increase with increasing loading frequency.

$$\frac{E'}{E''} = \frac{D_c \omega}{S} \tag{22}$$

Single human collagen fibrils were extracted from the patellar tendon by Svensson et al. [103]. Using AFM, tests were performed at multiple strain rates to distinguish the viscous and elastic components of the tensile response. The results, shown in Figure 2.16c, is well fitted by a second order polynomial. Additionally, the results show that viscosity is a decreasing function of the strain rate. This is in agreement with results of self-assembled fibers tested by Silver et al. [104], who suggested that the thixotropic effects are due to interstitial water molecules which hydroplane on subfibrillar elements at increasing strain rates.

Yang et al. [58] expressed the time-dependent component using the Maxwell model, with the elastic spring (Equation 23) and a dashpot in series. The viscous contribution is due to the time-dependent sliding between fibrils. The viscous term can be represented by a simple Newtonian response: $\sigma = \eta \dot{\varepsilon}_t$, where η is the Newtonian viscosity, such that the viscous strain is given by:

$$\varepsilon_\eta = \frac{1}{\eta}\int \sigma dt \tag{23}$$

For simplicity, a polynomial fit to the elastic constitutive equation of the form $\sigma = A\varepsilon_{el} + B\varepsilon_{el}^2 + C\varepsilon_{el}^3 + D\varepsilon_{el}^4$ is used, where A, B, C and D are fitting constants, which leads to:

$$\varepsilon_\eta = \frac{1}{\eta}\int \left(A\varepsilon_{el} + B\varepsilon_{el}^2 + C\varepsilon_{el}^3 + D\varepsilon_{el}^4 \right)\dot{\varepsilon}^{-1} d\varepsilon \tag{24}$$

where $\dot{\varepsilon}$ is the strain rate. The viscous component comes from interfibrillar bonds, the breaking of which results in sliding between fibrils. Thus, the fractional area where viscous flow takes place is small; as such the viscosity used in Equation 24 is an 'effective' viscosity. The elastic response is modified as a function of viscosity (at a constant strain rate) and strain rate (at a constant viscosity) in Figure 2.16d. These calculations show in schematic fashion how the viscosity influences the mechanical response. As the samples dry, the viscosity increases and the overall response is altered.

The three cases above illustrate the incorporation of viscosity into the constitutive response. The sliding component is very important and cannot be ignored.

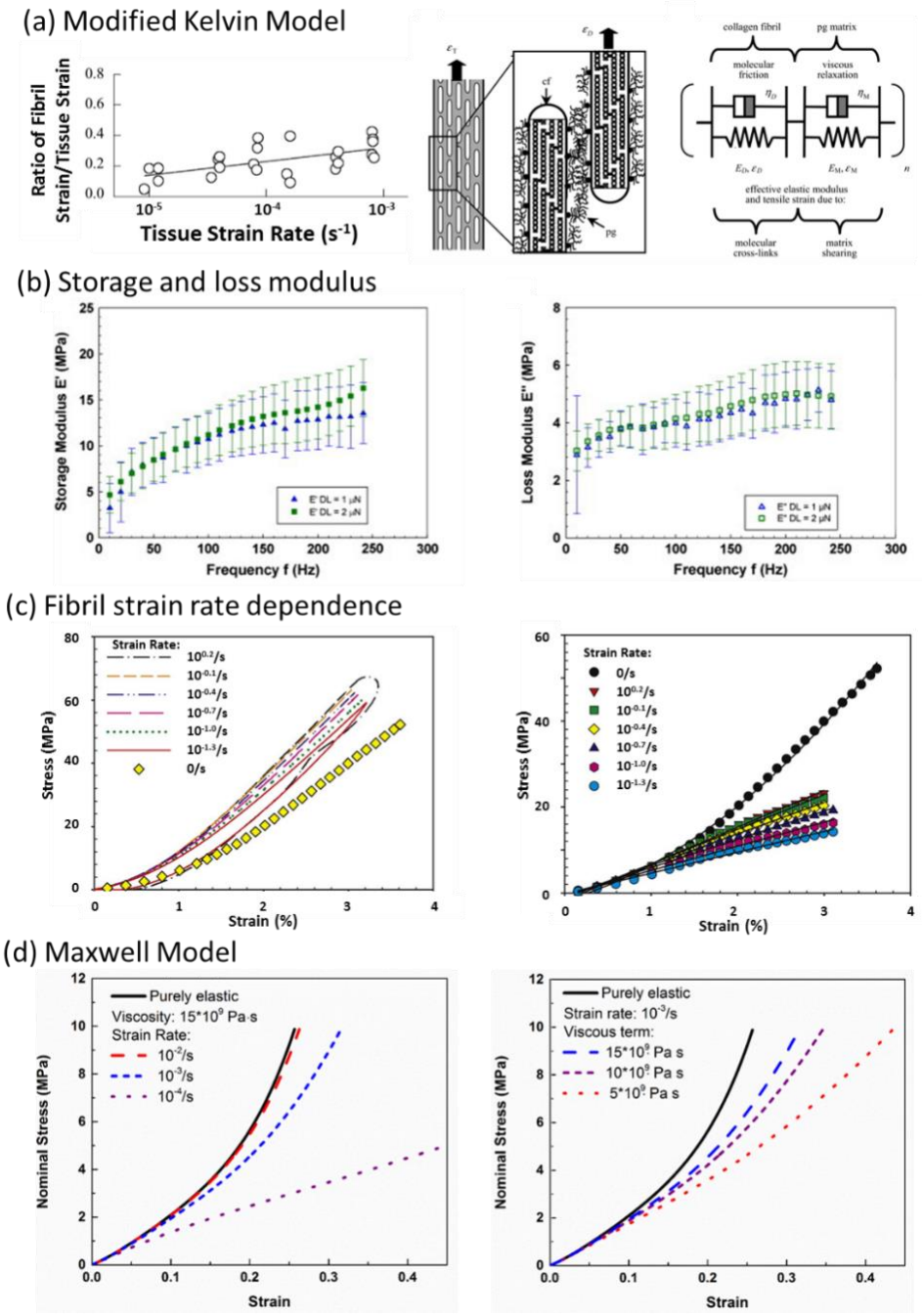

Figure 2.16: Modeling of viscoelasticity in collagen structures. (a) Puxkandl et al. [101] used two Kelvin models, and showed that increased strain rate increased fibril strain relative to tissue strain. (b) Nanoindentation tests from Franke et al. [102] show increase of storage and loss modulus with increased frequency. (c) Strain rate dependence of a collagen fibril by Svensson et al. [103]. Left: fibril pulled at different strain rates show effects of viscosity. Right: Elastic curve (black) taken from near zero strain rate is subtracted from dynamic curves to show viscous component of fibril extension (all other colors). (d) Incorporation of viscosity and strain rate by Yang et al. [58], holding representative viscosity constant (left) and holding strain rate constant (right).

2.6 Collagen in skin

Collagen has a specialized hierarchical structure in skin. The structure of skin varies greatly between different species, because of the functional requirements of the specific species of animal. However, skin is generally regarded as an anisotropic, nonlinear elastic material. By investigating the skin of various animals, we can observe important differences in the structures due to evolutionary constraints, which lead to unique mechanical properties. The structural features and mechanical response of the skin of three widely different vertebrates, the rhinoceros, rabbit, and chicken are summarized in Figure 2.17 -Figure 2.19.

2.6.1 Rhinoceros (*Ceratotherium simum*)

The rhinoceros is a fighting animal, and its skin is adapted accordingly. A tightly woven structure (Figure 2.17a) of collagen fibers creates a thick dermis which, due to the abnormally straight collagen fibers (Figure 2.17b), lacks the large toe region typical of most mammalian skin (Figure 2.17c). This arrangement leads to a response which is directionally isotropic, and lacks the extreme tear resistance common to most skins. While this may first seem to be a disadvantage for a fighting animal, it is not the case. Were the skin to be punctured (as is inevitable in a fight) but not tear, the energy of the blow would focus on the penetration region, and put the major organs of the animal at risk. By tearing, the rhinoceros is subjected to superficial gashes but the energy from the blow is dissipated across a larger area while avoiding deeper penetration which could lead to lethal damage. This design is different from other mammalian skin, which has a larger toe region in order to absorb strain energy and prevent fracture altogether. For comparison, the response of the rhinoceros skin alongside the response of cat skin is shown in Figure 2.17d. The skin of

the rhinoceros is highly cross-linked and stronger than most, with a failure strength of ~35 MPa and relatively low fracture strains of ~0.2 on most of the body, and slightly over 0.3 on the belly [105].

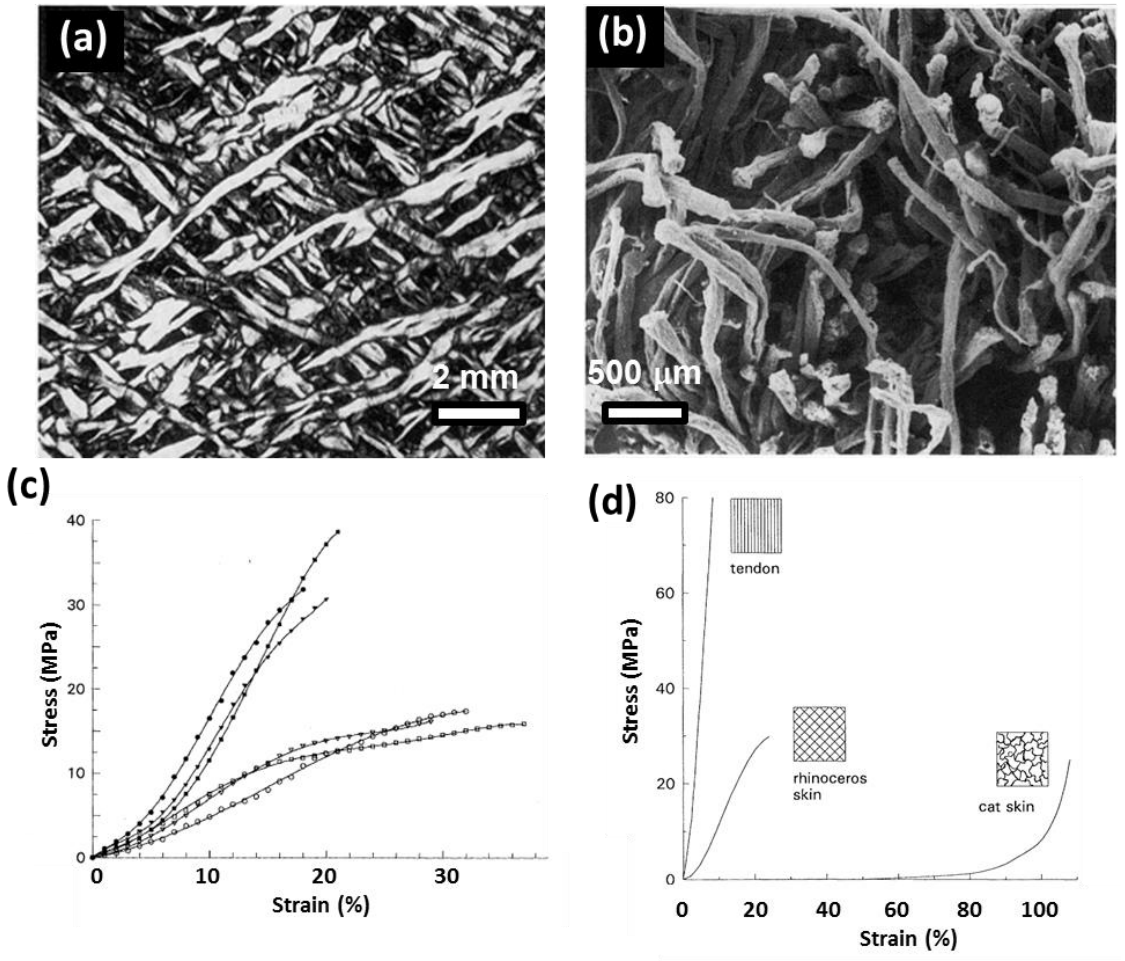

Figure 2.17: Microstructure and tensile response of a rhinoceros skin. (a) The rhinoceros skin displays a woven structure of collagen fibers. (b) Fracture of the rhinoceros skin reveals minimal waviness of the collagen fibers. (c) Tensile tests of three orthogonal directions of dorsolateral (stiffer, closed circles) and belly (open circles). Dorsolateral skin is substantially stiffer than belly skin, but orientation effects are insignificant. Due to the straight collagen fibers, rhinoceros skin exhibits a unique tensile response with a minimal toe region. (d) Tensile response of rhinoceros skin plotted next to cat skin in order to illustrate the relative inextensibility of rhinoceros skin.

2.6.2 New Zealand white rabbit (*Oryctolagus cuniculus*)

In opposition to the rhinoceros, the New Zealand (NZ) white rabbit has a skin with radically different mechanical response. This small creature needs skin which will not tear

as it crashes through sticks and branches. Therefore, it has a microstructure which is much different than that of the rhinoceros; the NZ white rabbit's skin is a vast meshwork of wavy collagen fibers (Figure 2.18a-b), which TEM reveals to lie in-plane with the skin (Figure 2.18c). This is a transmission electron micrograph of a thin section showing a fiber horizontally bisecting the picture with fibrils close to parallel to the foil plane, while the top and bottom portions reveal the cross sections of the fibrils and fibers. This shows that the fibers have a range of different orientations, consistent with Figure 2.18b. A large dermis and a comparatively thin epidermis cause the mechanical properties to be dominated by the dermis. Upon extension, the fibers undergo significant straightening and reorientation, allowing the skin to experience large strains with very little stress. This response is captured well by the model of Yang et al. [58] in which the radius of the circular section gradually increases. Under further extension, all fibers become straight and aligned, at which point the slope of the stress strain curve increases rapidly, and stresses begin to rise linearly with strain (Figure 2.18d). Throughout the extension process, fibril straightening, reorientation, stretching and sliding all contribute to a skin which sacrifices some strength compared to that of the rhinoceros, but is demonstrated to be extremely tear resistant. Additionally, as seen in Figure 2.18d, the rabbit skin is highly anisotropic; this is due to geometric effects and initial fiber orientations in the skin structure. The fracture strength of rabbit skin is ~12 MPa, at strains in excess of 0.5 and up to 1.5, parallel and perpendicular to the Langer lines [58, 106]. These lines define the stiffest direction in the skin.

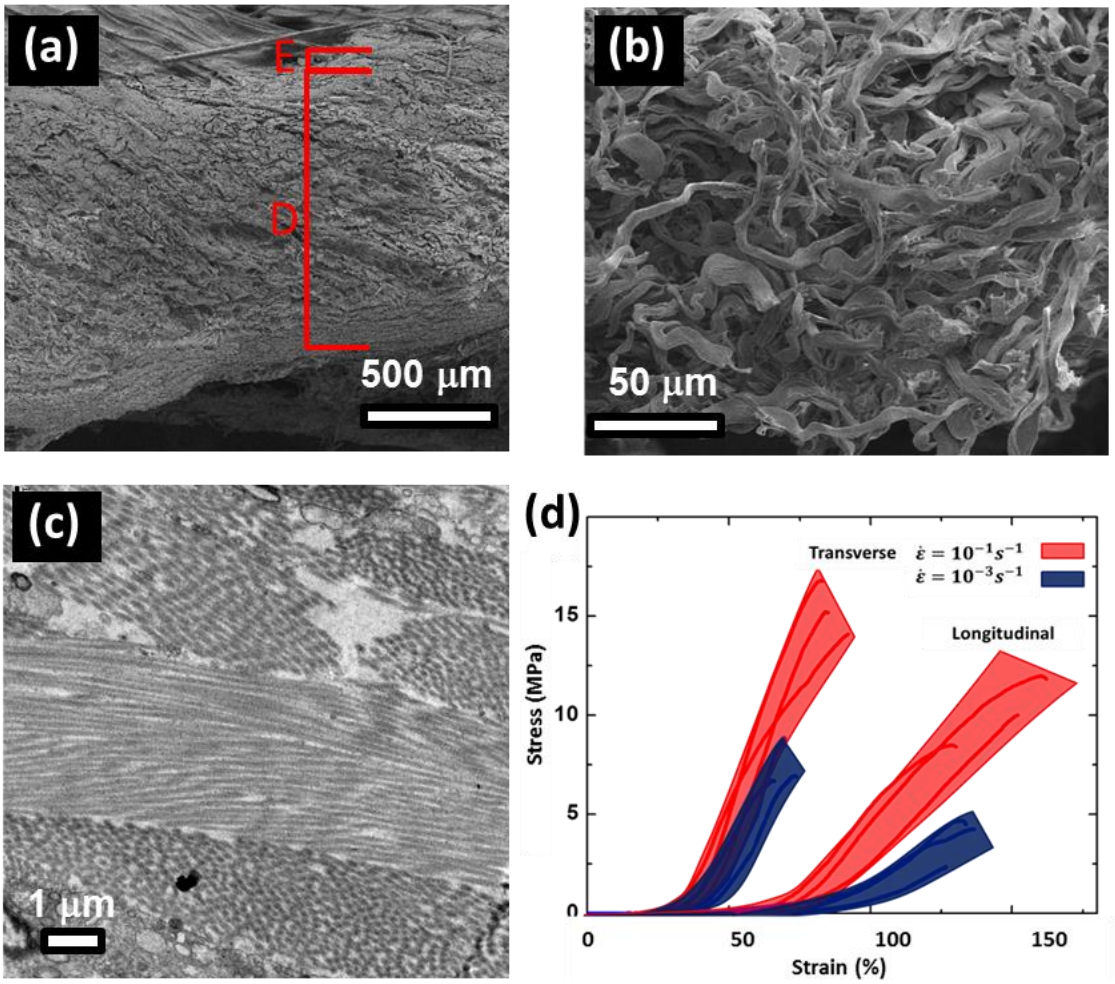

Figure 2.18: Microstructure and tensile response of rabbit skin. (a) Rabbit skin epidermis (E) and dermis (D). Compared to epidermis, dermis is much thicker and made of a network of intertwined wavy collagen fibers. (b) Close examination of a fracture surface reveals an extremely wavy structure. (c) TEM of rabbit skin cross section shows several fibers in different orientations. (d) The wavy structure of rabbit skin collagen leads to a large toe region under tension. Additionally, the skin shows highly anisotropic testing results, suggesting that the collagen fibers lie principally in certain preferred orientations.

2.6.3 Chicken (*Gallus gallus*)

The skin of the brown chicken has another type of unique structure and function. Chicken skin supports the feathers, which also protect it from predators. The chicken neck skin was observed in these experiments. While in most animals the dermis is thick and compact, in the chicken a thick spongy layer provides the site for anchoring the roots of the feathers (calamus). Beneath the spongy dermis lies a compact dermis which consists of

two distinct layers of densely packed collagen fascicles, each with a clearly visible preferred orientation (Figure 2.19a). Fascicles consist of wavy fibers, which contribute to the large toe region of chicken skin in tension (Figure 2.19b-c). The thicker layer of the dermis is oriented in the direction along which strength is more crucial for the support of the feathers. This structure of multiple layers with minimal interactions, as well as a large epidermis sacrifices the strength of the skin; the fracture strength of the skin is orientation dependent (according to whether the thicker or thinner layer of the dermis is aligned with the tensile stress) and ranges from ~0.5-1.0 MPa, at strains of ~0.8-1.0 (Figure 2.19d).

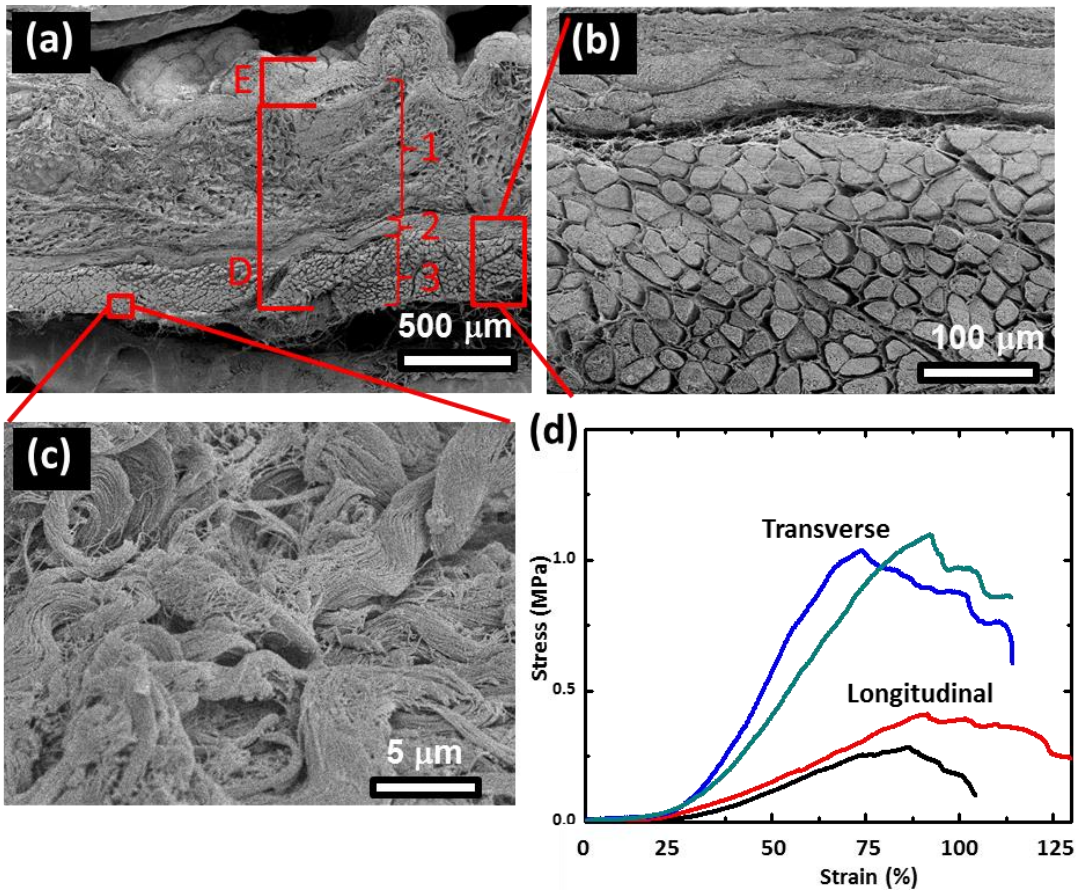

Figure 2.19: Microstructure and tensile response of chicken skin. (a) Chicken skin epidermis (E) and dermis (D). The dermis consists of three distinct layers (1, 2, 3 in figure); layer 1 is a spongy arrangement of collagen fibers, while layers 2 and 3 consist of densely packed collagen fibers which are packed into fascicles. (b) The fascicles in layers 2 and 3 viewed at higher magnification. (c) Fracture surface showing wavy fibers which fascicles are made of. (d) Tensile response in the transverse and longitudinal directions is drastically different due to the minimal interaction between the two layers of fascicles.

2.7 Collagen in fish scales

The refined structural design of collagen in fish scales facilitates a robust armor tailored to the needs of the particular species. Fish with unique requirements have evolved different types of scales and mechanisms in order to provide protection from predators. Scales can be classified into several distinct types: ganoid, elasmoid, placoid, cycloid, cosmoid and ctenoid. Three chosen scales are described here: the ganoid scale of the alligator gar, the elasmoid scale of the arapaima, and the cosmoid scale of the coelacanth.

2.7.1 Alligator gar (*Atractosteus spatula*)

The ganoid scales of the alligator gar are thick and have a highly mineralized exterior surface with a tough, boney foundation (Figure 2.20a-b). In Figure 2.20a, the ganoid surface layers is white, whereas the bone is darker. The cross-section, shown in Figure 2.20b, shows a serrated interface between the two layers whose function is possibly to increase adhesion and crack deflection ability. These penetration-resistant scales are necessary to provide protection from the alligator, as well as from self-predation. To achieve this, a mineralized matrix of collagen fibrils with parallel tubules throughout provides a tough, crack impeding foundation (Figure 2.20c) of ~3.5 mm thick in adult fish. An outer mineralized surface of ~1.5 mm, called ganoine, is nearly pure hydroxyapatite and covers a large percent of the scale. The ganoine provides a hard (2.5 GPa microhardness) barrier against penetration by teeth; beneath it, the softer (400 MPa microhardness) but tougher bone-like base consisting of a hydroxyapatite and collagen composite provides flexural strength. This robust scale is highly protective, but not flexible. Due to mineral protein interactions which reduce collagen sliding, hydration (or lack thereof) has minimal effects on the modulus of the gar scale. However, hydration does

cause a large degree of post-yield plasticity (Figure 2.20d). In order for the fish to remain flexible at a low weight penalty there is a small overlap, ~30% across scales. The scales are able to move with hinge like interfaces, allowing flexing in the required directions for propulsion. This unique tridimensional arrangement provides a protective layer of constant thickness [107]. The Senegal bichir, although a fraction of the size (2-3 meters vs. 0.1-0.5 meters length), has scales with a similar architecture and materials structure.

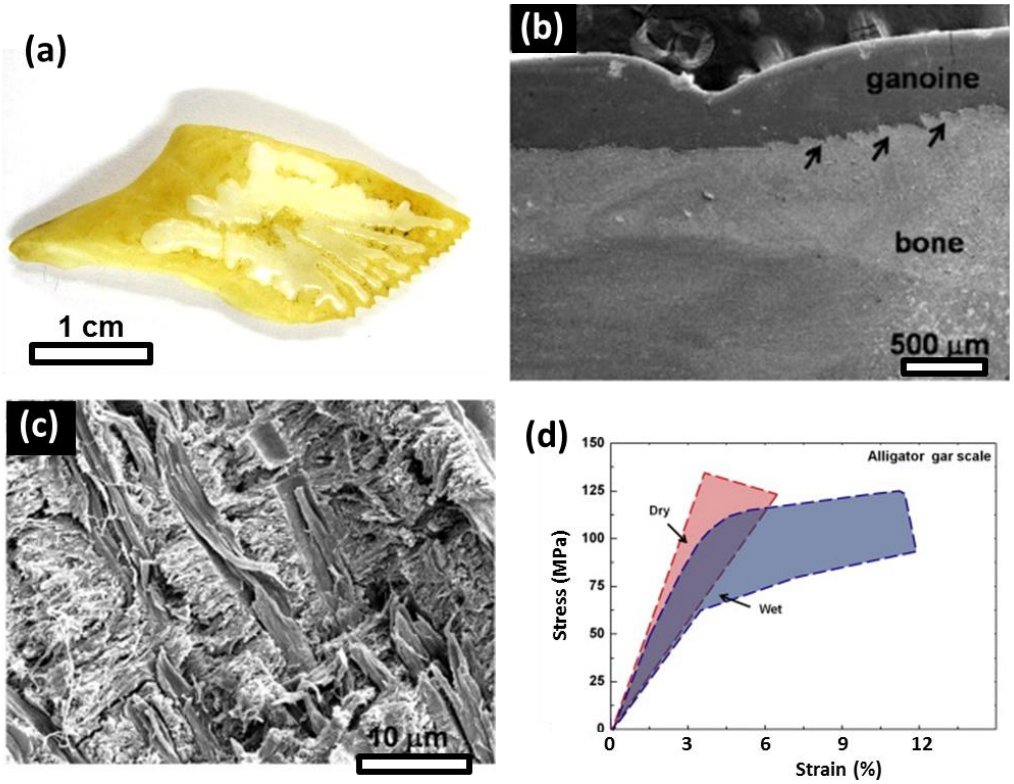

Figure 2.20: Microstructure and tensile response of alligator gar scale. (a) The entirety of the ganoid type alligator gar scale. Lighter area is exposed ganoine, while darker area is boney base. (b) Cross-section of gar scale. Two distinct layers; highly mineralized external ganoine layer, and boney base layer. (c) Fracture surface of boney layer of gar scale made up of hydroxyapatite crystals and mineralized collagen, with small tubules which run from the scale base to the ganoine layer. (d) Tensile testing of gar scale. High degree of mineralization minimizes effects of hydration, prior to yielding. However, a large amount of deformation is attainable post yield when testing hydrated samples, due to the large elasticity of wet collagen fibrils.

2.7.2 Arapaima (*Arapaima gigas*)

The arapaima is a teleost fish which has elasmoid scales specialized for protection against the piranha [108]. Similar to the gar and most other fish species [109], the arapaima

scale (Figure 2.21a-b) has an external layer (microhardness: 550 MPa) is harder than the internal layers (200 MPa) [110]. However, these values are much lower than the ones of ganoid scales. In the arapaima, lamellae of parallel collagen fibrils beneath the hard mineral external layer form a *Bouligand*-like structure, shown in Figure 2.21c. These lamella slide across each other to allow flexibility. Due to the high collagen content of the arapaima scale, the hydration levels are crucial to their function.

Figure 2.21d shows that without hydration, the collagen layers cannot slide, the elastic modulus is much higher, and the scale toughness (area under the stress-strain curve) decreases. For the arapaima, a flexible scale is necessary due to the large degree of overlap, which is in excess of 60% [108]. With large scales ~8 cm in length and a large degree of overlap, scale flexibility is required. Otherwise, the scales would be unable to conform to the fish's body as it flexes during motion, and the protective nature of the scales would be compromised. In the natural hydrated state, the outer mineral layer provides hardness, minimizing local plasticity and promoting fracture of the piranha tooth. During deformation, the inner collagen is able to bend, deform, and rotate while averting failure.

The *Bouligand*-type structure of the teleost fish renders propagation of a crack very difficult for two principal reasons: a) A crack cannot propagate along a simple path because successive layers of collagen have different orientations and therefore the front is delocalized. b) The delamination of fibers and their defibrillation at the front of a crack creates a process zone, since fibrils connecting the opposite sides generate compressive stresses at the crack tip. Figure 2.22a-d shows images of the opening of a notch viewed in a scanning electron microscope with a tensile attachment. It was not possible to propagate the crack since the layers of collagen (four imaged) separated, stretched, rotated, and

defibrillated. Dastjerdi and Barthelat [111] developed a fracture toughness testing setup (Figure 2.22e) for the scales of *Moronis saxitilis* (striped bass) and obtained values of 15-18 kJ/m2. This places scales, at the top of the Wegst-Ashby toughness chart, above all other biological materials [111]. The intricate mechanism by which a process zone develops is shown in Figure 2.22f and drawn schematically in Figure 2.22g. The bony layer contributes little to the toughness and fractures readily, as was also shown by Yang et al. [112]. The delamination of fibers and their separation into fibrils creates a process zone at the tip of the cracks and effectively impedes its propagation.

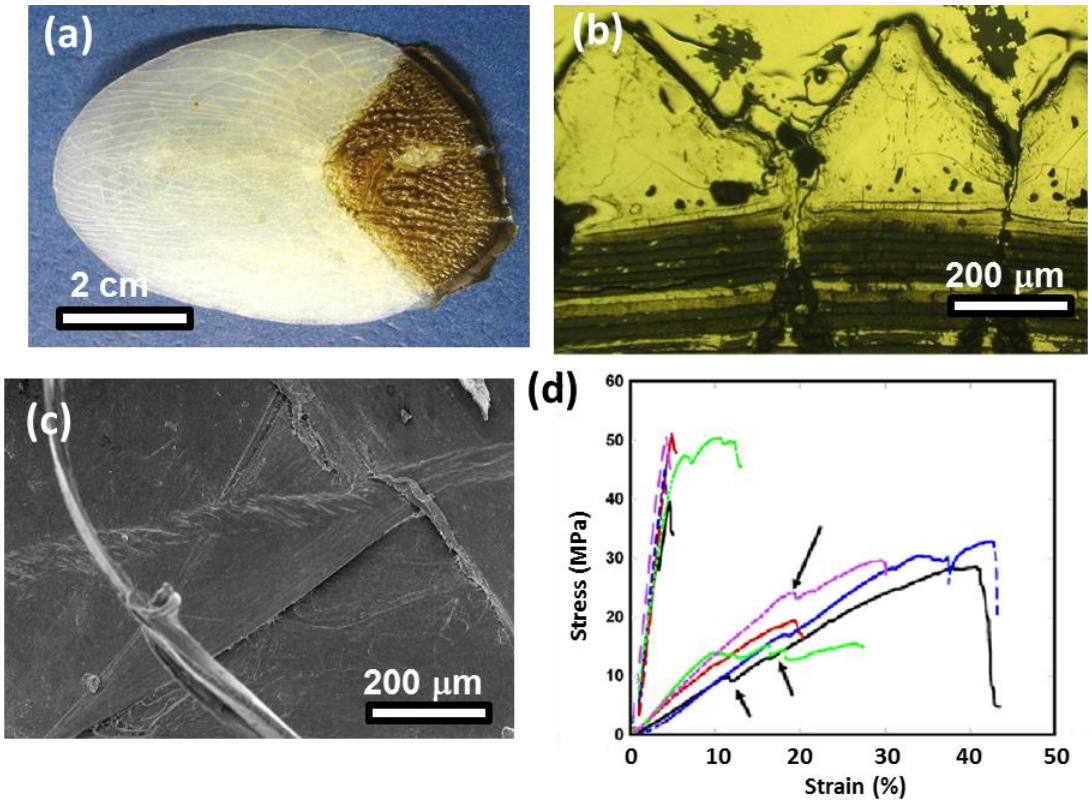

Figure 2.21: Microstructure and tensile response of arapaima scale. (a) The entirety of the arapaima scale, and its arrangement in relation to other scales. (b) Cross-section of arapaima scale; there are many layers including a thick ridged external mineral layer, and many thinner collagen layers beneath. (c) View of the multiple orientations of several internal collagen layers. View is perpendicular to the surface of scale. (d) Testing of arapaima scale. Due to low degree of mineralization, hydrated fibrils easily slide across one another. Therefore, wet scales are much more ductile than dry scales. Additionally, it is clear that the wet scales fail in stages, as individual layers of collagen fail. Previous studies by Yang et al. [112] have illustrated a complex process of failure avoidance, including stretching, rotation and delamination of collagen layers.

The mechanism of fibril, stretching, rotation, and delamination can be modeled by molecular dynamics, using the coarse graining methodology which allows larger molecules to be simulated. The molecular dynamics model, based on a simple elastic network model [113, 114], was used to theoretically investigate the mechanisms of the deformation and delamination in the Arapaima scales under uniaxial tension. This model does not take the fibrils as elements but rather considers the larger collagen fibers to better simulate the response of the lamellae.

Molecular dynamics methods were applied to a scale consisting of 3 lamellae, which is shown in Figure 2.23. In order to determine the correct surface energy of the collagen fibers in the scale, multiple simulations were run. These simulations, shown in Figure 2.23b reveal that 1 J/m^2 provides the best approximation to the stress-strain curve of the scales shown in Figure 2.21d. The deformation of the individual lamellae during the simulation reveal collagen bridging, delamination, and sympathetic lamella rotation.

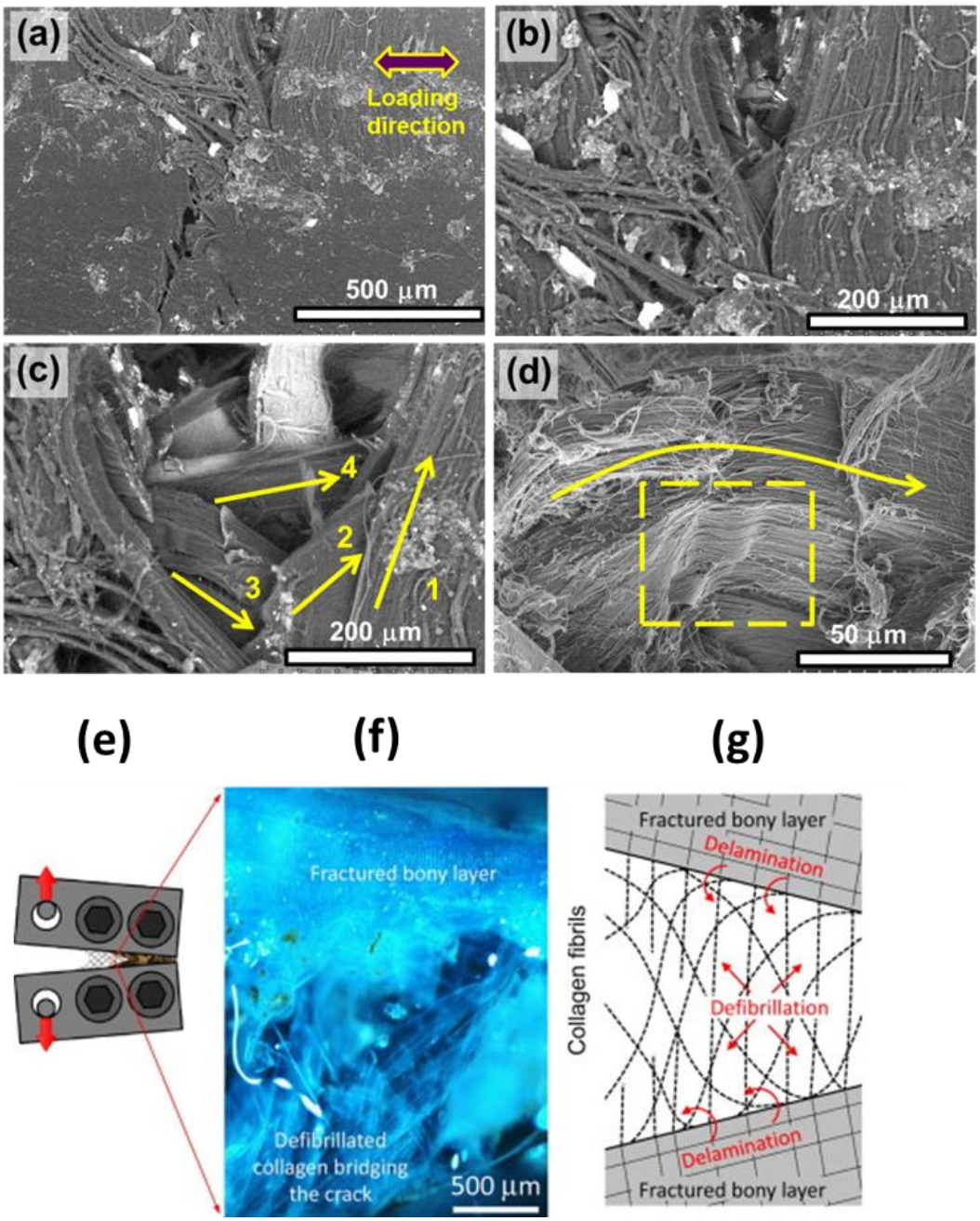

Figure 2.22: Extraordinary resistance to damage propagation in scale of teleost fish. (a-d) *Arapaima gigas*; (e-g) *Moronis saxitilis* (a) Initial configuration of notch at the onset of loading (the notch is in the center of the image with the notch root pointing towards the bottom); (b) the collagen fibrils separate when the samples are being loaded; (c) four orientations of lamellae are being exposed (shown by the individual arrows); (d) the collagen fibrils bend and stretch as shown by the arrow; some of the collagen fibrils relax when the test stopped [112] (e) fracture toughness testing configuration; (f) defibrillated collagen fibrils; (g) schematic mechanism showing how delamination and defibrillation of fibrils leads to formation of extensive process zone (from Dastjerdi and Barthelat [111]).

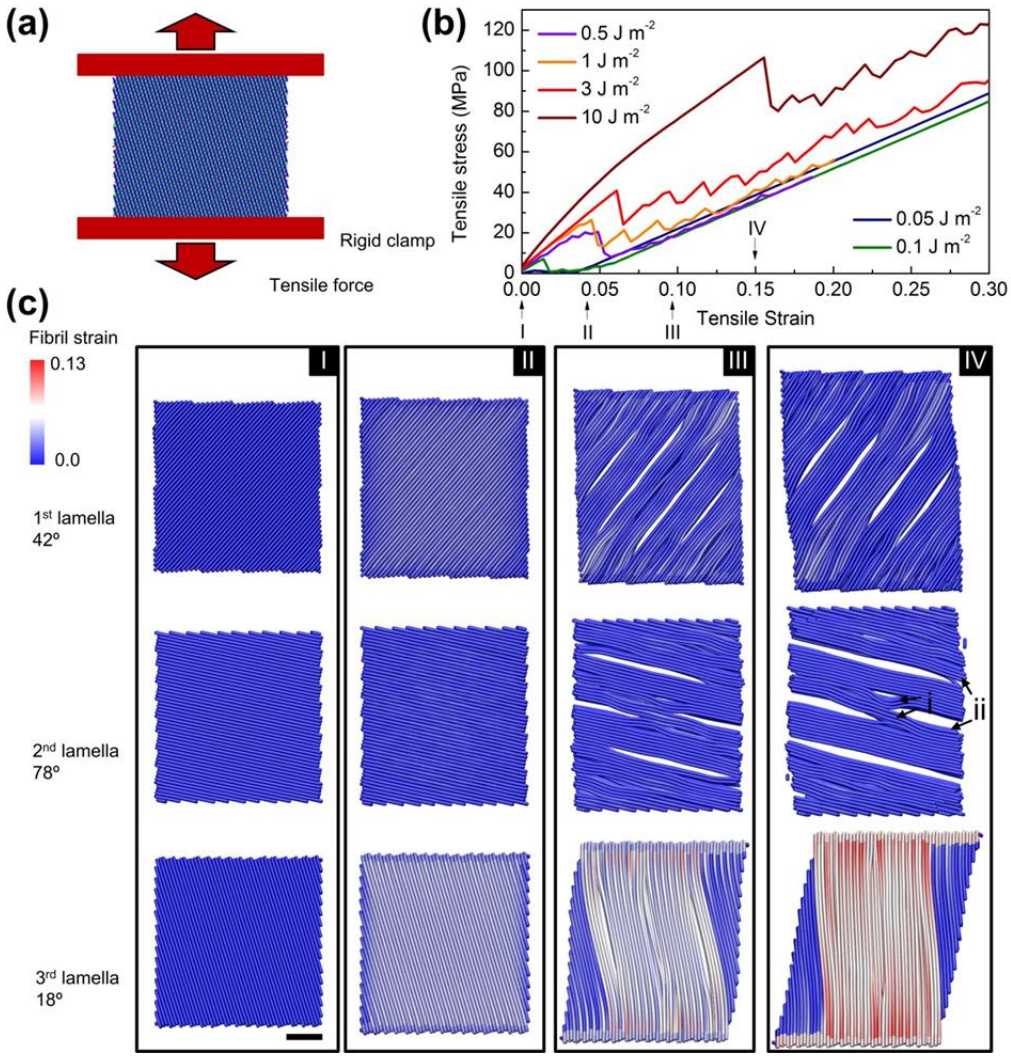

Figure 2.23: Molecular dynamics applied to the arapaima scale. Collagen lamellae are modeled as three layers oriented at different angles to the tensile direction. (a) Schematic of the scale as modeled for MD simulations. (b) Stress-strain curves for different surface energies. 1 J/m^2 gives the best approximation to the experimental stress-strain curve shown in Figure 2.21d. (c) Simulation snapshots of the deformation of each lamella, taken at increasing strains of 1%, 4%, 9% and 15% (I, II, III, and IV marked in b). Molecular dynamics confirms the mechanical test observations: collagen bridging (noted by i), delamination (noted by ii), rotation, and stretching, which is shown for the 18° lamella at a strain of 14 % (red gradient in model). . Scale bar: 10 μm.

2.7.3 Coelacanth (*Latimeria chalumnae*)

The coelacanth is considered a living fossil. It evolved 400 million years ago and was considered extinct until it was rediscovered in 1938 close to Madagascar. It is related to lungfish, reptiles, and mammals, and has vestigial limbs that come from their terrestrial ancestors. It belongs to the Latimerioidei suborder and is one of the few living fish with

cosmoid scales, the other being the Australian lungfish. Thus, its unique structure is of great interest; the only study, to the authors' knowledge, is due to Giraud et al. [115]. The structure of the coelacanth scale, that is being correlated to its mechanical response by Quan et al. [116], is shown in Figure 2.24a. The degree of overlap is quite high, as measured by the covered area/total area ratio of 0.80. The degree of imbrication is correspondingly low (exposed length /total length): 0.32. These values compare with the arapaimas which has a 0.75 degree of overlap and a degree of imbrication of 0.4.

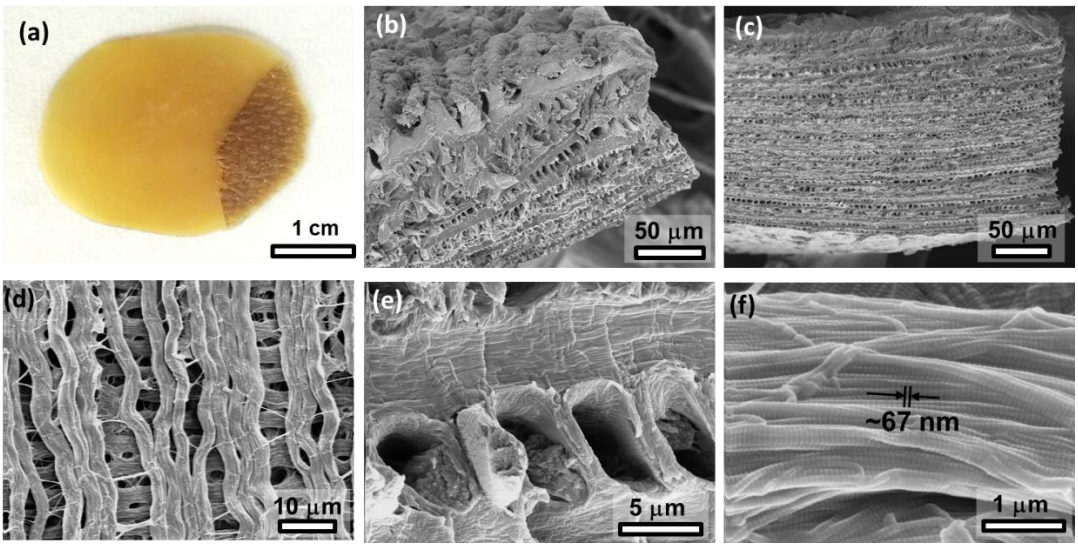

Figure 2.24: Structure of the coelacanth scale. (a) Macroscopic view of coelacanth scale. (b) Perspective view of scale showing external mineralized layer and lamellae. (c) Cross-sectional view of coelacanth scales. (d) Top view of peeled surface showing two adjacent collagen lamellae oriented close to (but not exactly) 90°. (e) Struts between adjacent lamellae forming perpendicular to their plane and connecting them. (f) Collagen fibrils with characteristic d spacing of 67 nm forming the collagen bundle/fiber (from Quan et al. [116]).

The cross-section of the scale, viewed by the inclined view in Figure 2.24b and from the perpendicular direction in Figure 2.24c, reveals the external layer which is highly mineralized and the foundation consisting of parallel lamellae connected by struts. The collagen lamellae are organized into fiber bundles and these are comprised of fibrils. There is also separation between the fibers/bundles in the lamellar planes as shown in Figure 2.24d. The angle between adjacent lamellae is close, but not equal to, 90°. This was

identified by Giraud et al. [115] who also pointed out that this configuration provides in-plane isotropy, which is important for resistance to crack propagation. This type of structure is known as "*Bouligand*-like". In contrast to elasmoid scale of the arapaimas and most teleost fish, the scale of the coelacanth contains struts that connect adjacent lamellae. These are shown in Figure 2.24e. The collagen fibers curve at the extremities of the struts. This configuration provides a greater rigidity to the scale by reducing sliding between the lamellae. The confirmation that the fibers are indeed collagen is provided by Figure 2.24f, which shows the characteristic banding of ~67 nm.

2.8 Collagen in bones, teeth, and other tissues

Another biological material which owes its impressive properties to collagen is bone. In a human body, the bone structure (skeleton) supports the entire weight of the body, yet only represents ~20% of the total weight. Bone must possess exceptional mechanical properties in order to fulfill its role. Figure 2.25a shows a schematic of bone, and Figure 2.25b shows the results of mechanical testing on bone. The mechanical response shown in Figure 2.25b is due to the hierarchical structure shown in Figure 2.25c, which contains blood vessels, osteons, concentric and interstitial lamellae and more. The bone is composed of the mineral and organic matrix, of which 90% is collagen. The collagen and mineral govern the mechanical properties and functional integrity of this tissue [117]. The mineral acts as a reinforcement in the collagen fibril network to provide specialized mechanical properties. Nudelman et al. [118] investigated the mineralization of the collagen fibrils and claimed that by controlling the mineral nucleation, collagen can direct the mineralization actively. With mineral reinforcement, collagen shows a Young's modulus of 5-10 GPa and

yield tensile strain of ~7%, as opposed to non-mineralized collagen with a Young's modulus of ~1 GPa [74].

Gupta et al. [77] investigated the roles of the mineral and collagen in bone, in particular the slip of the mineralized collagen fibrils, by studying the relationship between the tissue strain and local strains of mineral and fibrils. The strain ratio of the tissue, collagen fibril and mineral is 12:5:2, meaning that the mineral only takes up a small amount of strain, while the majority of the strain is absorbed by the collagen fibril, interfibrillar sliding and other mechanisms.

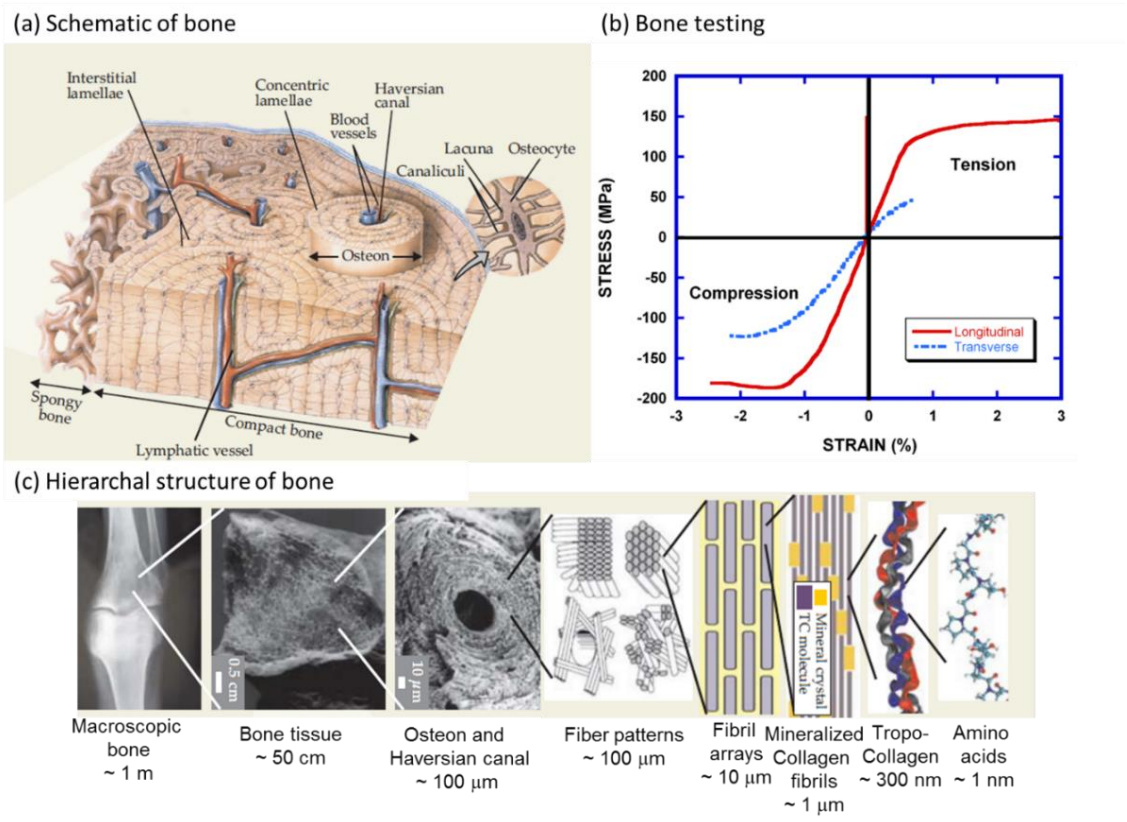

Figure 2.25: The hierarchical structure of bone. (a) A schematic shows both spongy and compact bone, and the arrangement of the osteons, lamella, and Haversian canals within. (b) Tensile and compressive stress-strain curves for cortical bone. [119] (c) The hierarchal structure of bone from the macroscopic level down to the amino acid level [120].

Launey et al. [121] summarized the toughening mechanisms of bone which can be greatly attributed to the mineralized collagen fibrils. These mechanisms were classified into intrinsic and extrinsic, following what had been previously defined in synthetic materials by Ritchie [122]. The intrinsic toughening mechanisms are typically ahead of the crack, while the extrinsic mechanisms operate in the wake region. The schematic drawing in Figure 2.26a illustrates the intrinsic and extrinsic toughening mechanisms of bone. The toughness of the bone is attributed to both extrinsic mechanisms including crack deflection and twist, uncracked-ligment bridging, collagen fibril bridging and some microcracks in the structure, and intrinsic mechanisms which are induced by the plastic deformation in the microstructure, such as molecular uncoiling and intermolecular sliding of molecules, microcracking, fibrillar sliding, and the breaking of sacrificial bonds together with crack bridging by collagen fibrils. Figure 2.26b shows the toughness of human cortical bone as it evolves with crack size. It increase with size demonstrates that the extrinsic mechanisms are operating, rendering propagation more difficult as the crack grows. There are clear differences with orientation, the longitudinal toughness being significantly lower than the transverse one. Long bones cracks preferentially along their axes because of the anisotropy in the organization of the microstructure. The response of elk antler is given in the same plot, for comparison. The extrinsic mechanisms operate as effectively for antler as for bone. The transverse toughness of bone increases from 1 to >10 $MPam^{1/2}$ as the crack grows from ~0.01 to ~0.6 mm. This toughening is extremely important for preventing fractures but unfortunately decrease with age.

As bones age the quality of the collagen decreases, greatly affecting the mechanical properties. This degradation of the mechanical integrity of the collagen network in bone

due to aging was demonstrated by Zioupos et al. [123, 124] and quantified by Nalla et al. [125]. In the case of disease such as osteoporosis, this was demonstrated by Wang et al. [126] and Currey [127]. As aging occurs, the bridges weaken and hence toughness the bone decreases [128].

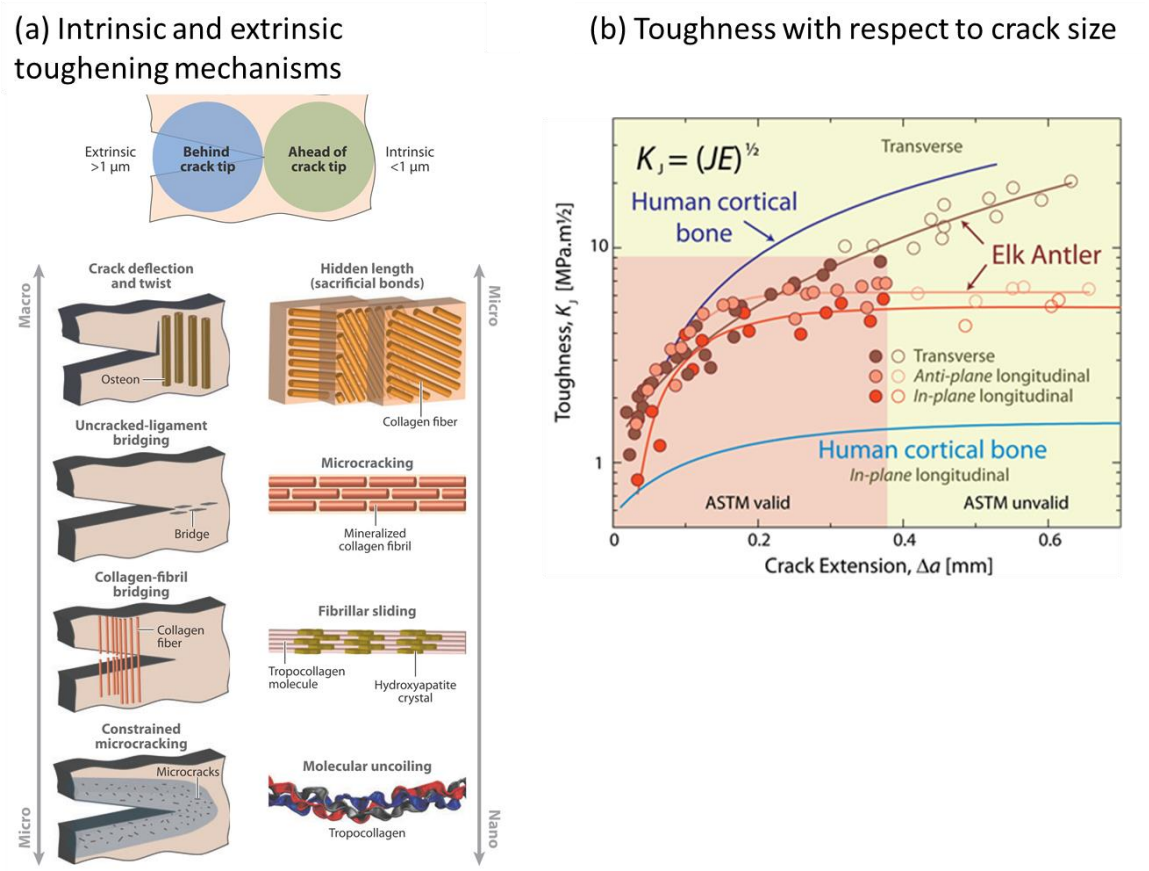

Figure 2.26: Toughening mechanisms of bone. (a) Extrinsic mechanisms occur behind the crack tip, while intrinsic mechanisms occur ahead of the crack tip. [129] (b) Crack-resistance curves showing resistance to fracture in as a function of crack extension, Δa, for hydrated antler and human compact bone in different orientations [130]

2.9 Designer collagen

Thus far, collagen molecules have not been synthesized. However, collagen fibrils have been produced through a process of dissolution of natural collagen, followed by processing and assembly. This process may best be described as guided self-assembly.

Collagen structures may be manufactured in a laboratory environment, and have potential uses for the replacement of ligaments and skin, and building scaffolds. Collagen based constructs with tailored properties have great value for clinical uses. A variety of methods has been developed to design and produce collagen structures. There are methodologies to dissolve collagen and processes to create collagen filaments, strands, ribbons, films, sheets, and pre-shaped implants. More recently, a goal has been to synthesize fibers most like those produced by the fibroblasts in the body.

There are currently nearly 1000 readily searchable patents which mention collagen. Early patents, starting in the 1950s, discuss collagen filaments, sheets, etc. In the 1960s, the focus was placed on methods for solubilizing collagen fibers for usage. Around the 1970s, methods were developed to use collagen as prosthetics and implants. The collagen structures which are produced continue to become more advanced; in 1989, Silver attempted to precisely control the geometry and structure of a collagen matrix, filing a patent on synthetic collagen orthopedic structures [131]. Since the 1950s, research on biodegradable synthetic collagen structures has continued with great success, as methods have been refined. Synthetic fibrils and scaffolds are now produced with properties approaching what is found in the body [55, 132, 133].

Chapter 2, in full, is a reprint of the material as it appears in "The materials science of collagen" Journal of the Mechanical Behavior of Biomedical Materials, vol 52, pp 22-50, 2015. This work was coauthored by W. Yang and M. A. Meyers. The dissertation author is the first and corresponding author of this work.

CHAPTER 3: RESULTS ON FISH SCALES

3.1 Introduction to scales

Nature has produced an extraordinary number of unique and specialized materials over hundreds of millions and even billions of years of evolution. For thousands of years natural designs have provided inspiration for manmade structures, such as ancient armors. However, it is only in recent times that humans have come to realize that studying, understanding, and mimicking these materials may serve as an important route for the design and development of new specialized synthetic materials. Despite being comprised of only a limited palette of constituents with relatively modest mechanical properties, biological materials can exhibit remarkable combinations of strength, toughness and reliability that are crafted through ingenious designs involving hierarchical assemblies and gradients in composition, structure and properties. This has stimulated many studies throughout the world to seek to understand biological materials and the mechanisms that are responsible for their functions, e.g., Sacks and Sun [134], Meyers et al. [135], Ji and Gao [136], and Chen et al. [137]. As the principles underlying the properties of biological materials become clarified, they can be applied to the development of new materials. Two recent examples include a bioinspired glass, produced by Chintapalli et al. [138], which mimics natural designs to display exceptional toughness, and freeze-cast bioinspired anisotropic ceramic scaffolds produced by Porter et al. [139] as a refinement of a synthesis method developed by Deville et al. [140] and Munch et al. [141]. Unfortunately, there are not too many current examples of successful bioinspired *structural* materials and processing them can be extremely complex [142]. However, advancements in

manufacturing are opening new and exciting opportunities, and the development of a bioinspired, synthetic flexible armor is a goal worth pursuing.

With regards to natural dermal armor, fish scales are a common example and have been the subject of much research, particularly over the past decade. They are an intriguing topic because they have provided effective protection to fish for eons; some armored fish have existed prior to the dinosaurs, which came into existence 225 million years ago. The fish scales have been traditionally classified into four groups which are shown in Figure 3.1: placoid, elasmoid, cosmoid and ganoid. Placoid scales are denticles with a flattened rectangular base plate embedded in the fish body, and spines which project from the posterior surface. They have a core with pulp which is surrounded by dentine and an outer vitrodentine layer. Cosmoid scales are similar to placoid scales and likely evolved from the fusion of them; they have dentine, vitrodentine and a tissue complex known as cosmine with interconnected canals and flask-shaped cavities, but lack a pulp core. These rigid rhombic scales are now, unlike the other scale classifications, entirely extinct. Ganoid scales are modified cosmoid scales which are also rhombic, rigid, and jointed articulating scales of two layers. A thin mineral surface layer called ganoine replaces the vitrodentine, and lies atop a bony foundation which replaces the cosmine. Peg and socket joints often join ganoid scales. Elasmoid scales likely evolved from ganoid scales and are the most common among living vertebrates. They are thin and imbricate, resembling shingles on a roof, and consist consist of a bony surface and a fibrous layer beneath of collagen. There are two subcategories, ctenoid and cycloid, the difference between being that ctenoid scales have developed surface spines which are bony and grow from the body of the scale to the surface and the cycloid scales have a smooth surface [143-146].

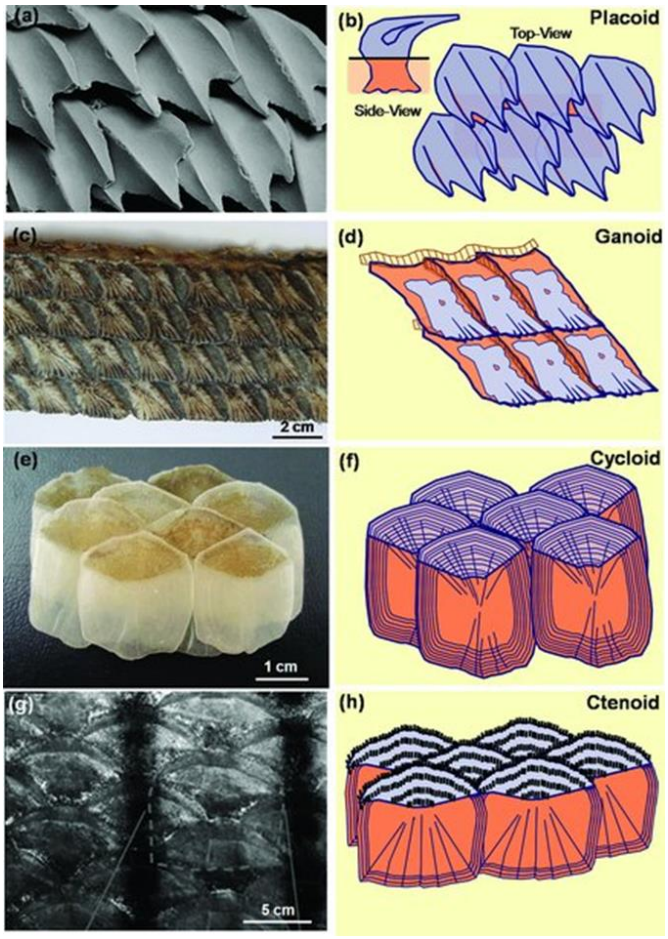

Figure 3.1 Different types of fish scales and their overlaps; from [108] (a-b) placoid, (c-d) ganoid, (e-f) cycloid, and (g-h) ctenoid.

Each of these scales has unique features and provides protection with a modest weight penalty. In order to learn from natural fish scales, modern tools and techniques, such as electron microscopy, nano-indentation, computer x-ray tomography and finite element analysis, provide insight into the features at the nano to macro level and reveal a variety of toughening mechanisms that make fish armors highly effective. Early studies on fish scales of this nature include *Polypterus senegalus* [147, 148], *Morone saxatilis* [149], *Arapaima gigas* [110, 150] and *Atractosteus spatula* [107, 151].

One principal function of fish scales is to resist penetration from predators. In particular, the manner in which they resist pressure by teeth has been addressed by several

researchers. Zhu et al. [109] performed penetration tests on a *Morone saxatilis* (striped bass) fish scale using a steel stylet simulating a sharp tooth. They compared the force-penetration response of whole fish scales and just the collagen layer with that of the synthetic polymers and found marked differences. By analyzing the penetration sequence in the bony surface and collagenous foundation, they classified it into three stages: stage I represents a linear relationship between force and penetration distance due to flexing of the scale and penetrating into the surface bone layer. Stage II begins with a small force drop associated with the crack opening in the bone layer and radiating from the penetration point which finally propagates into the collagen layer. In stage III the force-displacement curve plateaus as the stylet punctures the collagen layer. In similar vein, Vernerey and Barthelat [152] described the load redistribution mechanisms (proportional to scale size) from penetration on the overlapped fish scales (Figure 3.2a). They also described relationships between scale density, ratio of angular attachment stiffness to bending stiffness, and a variety of other properties which are key to the scales' protective function (Figure 3.2b) and vary according to the environment in which the fish lives. If escaping from a predator is critical, the structure of fish scale is "designed" in terms of flexibility (strain stiffening) and lightness; if the protection from a predator is more important, higher resistance to fracture and average bending stiffness are design criteria. Similarly, characterizing the structure, quantifying the mechanical parameters and understanding the salient mechanisms can provide insight to understand the environment in which the fish exist, the types of predators the fish may have faced, and even aids in understanding the evolution of the fish.

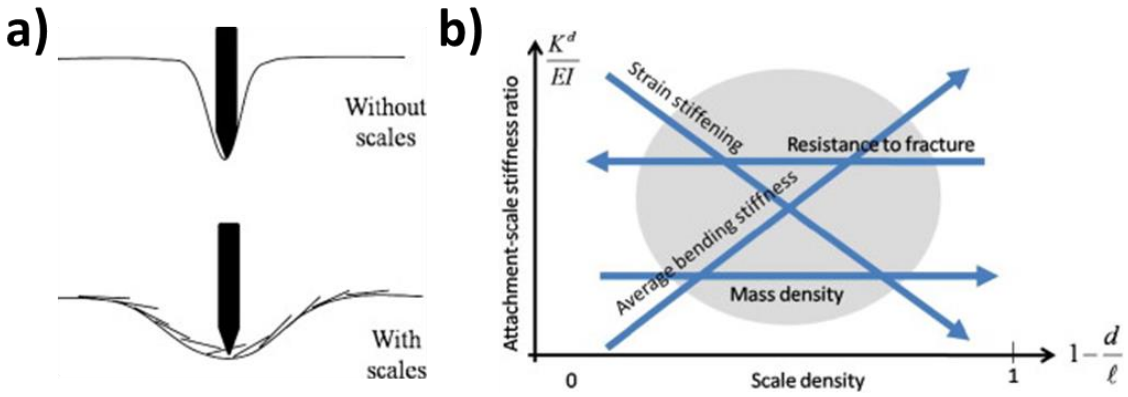

Figure 3.2: Force distribution of scales and relationship between select properties. (a) Scales redistribute an applied load in a region proportional to the scale size. This also leads to a greater penetration resistance. (b) Plot of attachment to scale stiffness ratio as a function of scale density illustrates several relationships between scale properties and features of the response such as average bending stiffness, resistance to fracture, and mass density (from Vernerey and Barthelat [152]).

In this work, we focus on the three resilient fish (Figure 3.3) whose highly effective dermal armors have protected them survive for millions of years, namely *Arapaima gigas* (arapaima) [110, 150, 153], *Latimeria chalumnae* (coelacanth) [154, 155], and *Atractosteus spatula* (alligator gar) [107, 151], with an emphasis on the structure-mechanical property relationships in their respective armored scales. It has been established that the properties of fish scales may vary with the head, body, and tail having unique traits [156, 157], but this case there is no knowledge of what specific part of the animal they are from; this may lead to some experimental variation. The arapaima is a huge fish which lives in the Amazon and grows upwards of 3 m in length and 200 kgf in weight [158]. Its fossil records have remained the same for at least 23 million years, and it evolved in order to peacefully cohabitate with the piranha, a predator with famously sharp tricuspid teeth with a tooth tip radius of 13 μm. Despite its ferocity, the piranha possesses a relatively small bite force, estimated by Meyers et al. [159] as 20 N. The coelacanth is another large fish which lives at up to 700 m deep in the Indian ocean (specimens have been found in the

Madagascar and Indonesian coasts), and grows to 2 m in length and 90 kgf in weight. It has existed for 400 million years, and was thought to have gone extinct with the dinosaurs until rediscovered in 1938 [160]. Shark bite marks found on coelacanths suggest that the shark is one possible predator [161]. Shark teeth are nearly as sharp as the piranha's, with a 16 μm tooth edge radius, but different types of sharks possess biting forces ranging between 1–2400 N [162-164]. The bite force of sharks is surprisingly low, and this is understandable because they do not possess bones and only cartilage. Finally, the alligator gar is a third large fish which lives in the brackish waters around the Gulf of Mexico and grows up to 3 m and 140 kgf [165]. The gar has existed in its current form for roughly 100 million years, and must protect itself from alligators. The alligator has 80 teeth although it may generate 3000 over its life [166], but these teeth which are not particularly sharp, have a tip radius of the order of ~80–130 μm for juveniles and up to 3 mm for adults. This lack of sharpness, however, is compensated by powerful jaws capable of bite forces of 10 N to 10 kN, depending on the size [167, 168].

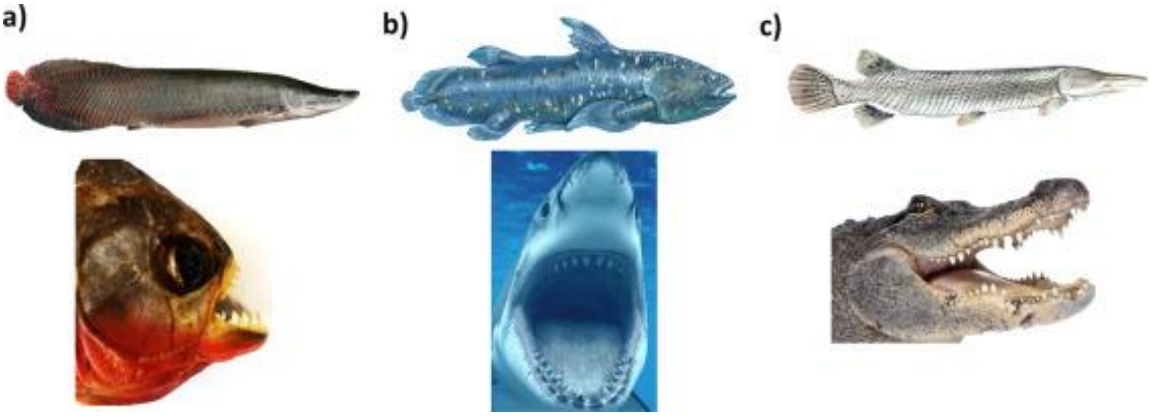

Figure 3.3: Ruthless predators and their prey. (a) The piranha is an infamously ferocious fish which cohabitates with the arapaima in the Amazon; the arapaima grows up to 3 m in length and 180 kgf in weight. (b) The shark is suspected to be the main predator of the coelacanth, which can grow to over 2 m in length and 90 kgf in weight. (c) The alligator, known for its massive jaw strength and powerful attacks, cohabitates the Mississippi basin with the alligator gar, a fish which grows up to 3 m in length and 140 kgf in weight.

3.2 The protective scales of *Atractosteus spatula*

3.2.1 Background

Scales have been a key form of protection for fish for hundreds of millions of years. Although most commonly found in fish and reptiles, scales may also be found in mammals: the pangolin is covered in keratinous scales [169]. Additionally, ancient Romans produced an armor named *lorica squamata*, in which individual iron or bronze scales were sewn to a fabric backing. Although it comes at an additional weight penalty in comparison to other armors, such as *lorica hamata* (chain mail), its effectiveness in battle made it an important defense for Roman legionnaires [170].

As implied by the name, the inspiration for the *lorica squamata* was likely drawn from a biological scale: squama means scales in Latin. Natural scales are becoming the subject of intense investigation [110, 115, 135, 148, 171] because of potential bioinspired applications. The most studied fish scales may be categorized into four types: placoid, cosmoid, ganoid, and elasmoid. Placoid scales, which are commonly found on sharks, are denticles that feature a flattened rectangular base plate. They are embedded in the fish body, and have spines that project from the posterior surface. Similar to teeth, these scales have a pulp core surrounded by a bone-like material (dentine) and an enamel-like outer layer (vitrodentine). Cosmoid scales likely evolved from the fusion of placoid scales, although a tissue complex known as cosmine takes the place of the pulpal core. Ganoid scales are rigid and jointed articulating scales consisting of a thin mineral surface layer made of hydroxyapatite, called ganoine, atop a bony foundation. Elasmoid scales evolved from the thinning of ganoid scales and consist of two subcategories: ctenoid and cycloid. Each consists of a bony mineralized surface layer and a fibrillary plate beneath, which is mostly

collagen. Ctenoid scales have spines, which are bony growths distinct from the body of the scale, while the cycloid scales are smooth [144].

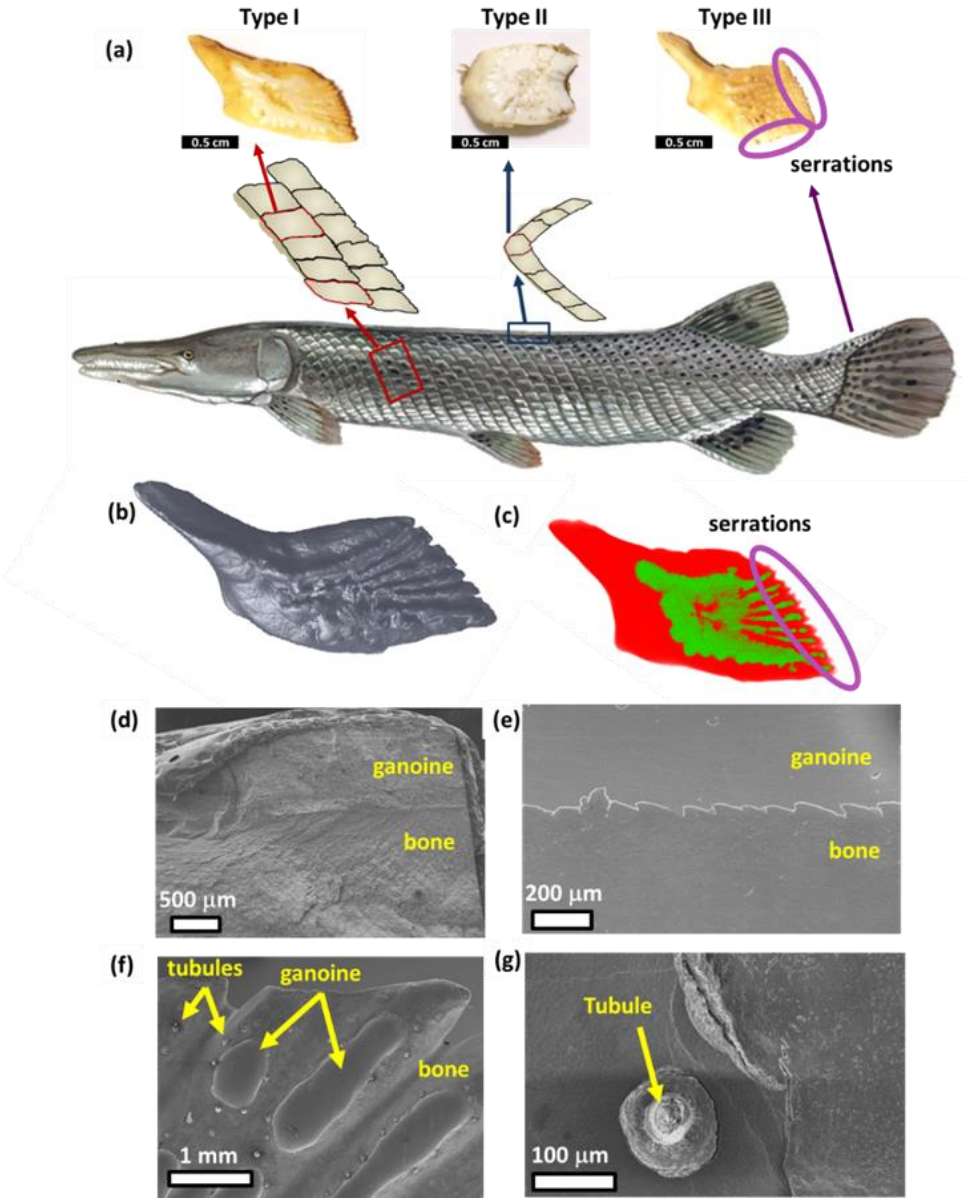

Figure 3.4: Hierarchical arrangement and features of an alligator gar scale. (a) Schematic shows the alligator gar and its three types of scales. Type I are the most common, covering the majority of the fish. Types II and III are found where Type I scales converge and on the edges of the fish. (b) Surface reconstruction from µ-CT of a Type I scale, revealing the morphology of the textured surface. (c) µ-CT where ganoine is shown in green, and bone red. Ganoine does not completely cover the scale surface. (d) SEM of fractured cross-section of scale. The distinction between ganoine and bone is clear. (e) The saw-tooth interface between ganoine and bone observed in a polished scale's cross-section. (f) The outer surface of the scale. Ganoine deposits are clearly visible. Tubules are visible in bone, but not in ganoine. (g) A tubule passes through the ganoine at the edge of the mineral; as additional mineral is deposited these tubules close.

Bruet et al. [147] revealed materials design principles present in the penetration resistance of the ganoid scales of *Polypterus senegalus*, a small fish that reaches only ~200 g in mass and ~20 cm in length. Its scales have multiple layers, each with unique properties, deformation mechanisms, and a specialized manner in which cracking and failure occur in order to absorb energy and protect the fish. Song et al. [148] demonstrated how the structure of the ganoid scale provides toughness, penetration resistance, and non-catastrophic pathways for energy dissipation.

The *Atractosteus spatula*, or alligator gar, is another fish with a ganoid-type scale and is the subject of our research. As one of the largest freshwater fish in North America, large gars may reach 140 kg in mass and 3 m in length. The fish, shown in Figure 3.4, is characterized by a long cylindrical body covered in rigid articulating ganoid scales. Due to attacks by other gars (self-predation) and alligators, the scales of this fish are required to perform exceptionally as an armor. Its scales resist the powerful ambush attack of its predators and interface in a way that allows the fish to maintain flexibility and motion in spite of the scales' individual rigidity.

While most modern fish have overlapping scales which are capable of bending as they swim, this is not the case for the gar or other ganoid fish. The stiff and inflexible design is optimized to protect against prehistoric and modern predators with powerful bite forces (e.g., up to 10 kN for the alligator) [172]. Large overlaps would prevent the stiff scales from being capable of motion, but some overlap is required to distribute forces applied to a single scale and reinforce the vulnerable junctions between them [173]. The impressive protection of the gar is well recognized; Chen et al. [137] revealed the stiffness and hardness of alligator gar scales, similar to those of *Polypterus senegalus* [147], and

Yang et al. [107] identified mechanisms which lead to their fracture resistance. Allison et al. [151] observed circumferential cracks (also observed on *Polypterus senegalus*), which are hypothesized to be beneficial by localizing fracture. However, certain important aspects of the scales have been overlooked. In this work, we describe previously unreported toughening features of the scale microstructure, and show how the scale's shape and arrangement on the fish optimizes a tradeoff between protection and flexibility. These features are key to the effective protection of the alligator gar.

3.2.2 Methods

3.2.2.1 Scale acquisition

Arrays of scales were obtained from fish in Southern Louisiana. They were dried and shipped to UC San Diego for testing.

3.2.2.2 Scanning electron microscopy

Hydrated scales were fractured by bending or by freeze fracturing. Some were polished through the cross-section and etched using 15% phosphoric acid. All samples were coated with iridium prior to observation in a Phillips XL30 environmental scanning electron microscope.

3.2.2.3 Nanoindentation

Scales were mounted in epoxy and polished to produce a flat surface in two orientations: parallel and perpendicular to the scale surface. After hydration, hardness and reduced modulus mapping (5 s load, 2 s hold at ~3 mN load, 5 s unload) was performed in the ganoine region of both orientations. High load indents (5 s load to ~5 N peak load, 5 s unload) were applied to induce fracture.

3.2.2.4 Three-point bending tests

Scales were cut into specimens with ~8 mm width, ~3 mm thickness, and ~20 mm length. They were hydrated and subjected to bending in an Instron 3367 equipped with a 30 kN load cell. A support span of 16 mm and a loading rate of .016 mm/s was applied.

3.2.2.5 Penetration tests

Hydrated scales were polished on the bottom to provide a flat surface. Some scales were polished on the top surface to remove the ganoine layer. Pressure was applied to the scales by a steel indenter with a tip angle of 60^{o} and radius of ~300 μm. Additionally, an alligator tooth with a tip radius of 240 μm was pressed into an array of scales atop a rubber foam foundation. In both cases, the load was applied by an Instron 3367 equipped with a 30 kN load cell.

3.2.2.6 Simulations

Finite element analysis was performed using COMSOL. A representative volume of 1.3 mm by 1.3 mm and 0.3 mm thickness with seven 6.5 μm tubules extending through the thickness was imported from Solidworks. Material properties were extracted from Yang et al. [107], and the dry gar scale was modeled as a linear elastic solid with a modulus of 1 GPa while the hydrated gar scale was modeled as a an isotropic elastoplastic solid with an elastic modulus of 1 GPa followed by a yield stress of 100 MPa and linear hardening with a tangent modulus of 266 MPa. A physics-controlled mesh of 58,342 tetrahedral elements was refined near the tubules in order to ensure an accurate solution. A tensile load of 70 MPa was applied as a step function to the top surface using a stationary solver, while the bottom surface was constrained to its initial plane.

3.2.2.7 X-ray microtomography

X-ray computed microtomography was employed to visualize the three-dimensional morphologies of the gar scale by an Xradia 510 Versa scanner with a voxel size of 0.96 μm. Data was visualized using Amira software.

3.2.3 The hierarchical structure of alligator gar scales

The scales of the alligator gar have two distinct layers, clearly discernable in Figure 3.4a. The white external layer consists of ganoine, which is hard and nearly pure mineral (hydroxyapatite), and covers 40-70% of the surface of the scale; this partial coverage is due to the overlap by surrounding scales as well as irregularities including ridges and gaps throughout. The foundation is a yellow bony composite of hydroxyapatite and collagen. Three types of scales are required to effectively cover the alligator gar surface, characterized by shape. Figure 3.4a shows the three scales in the orientation in which they appear on the fish: Type I scales have an approximately rhombic shape and one serrated edge pointed towards the back of the fish. They overlap in a regular pattern forming inclined rows on most of the fish. It is theorized that the serrated edge may slice the skin of the predator and act as a form of defense as the fish thrashes. The aspect ratio (thickness to length) is 7.8 ± 0.9 and the degree of imbrication (length exposed to total length of scale) is 0.75 ± 0.04. Thus, the scales are thick and have minimal overlap as compared to other fish scales. A μ-CT reconstruction of the morphology of Type I scales is shown in Figure 3.4b-c, with the mineral-dense ganoine shown in green, and the bony foundation in red. Type II scales form the dorsal ridge, where rows of Type I scales from the two sides converge. Type III scales are the least common; they have two serrated edges and occur in the dorsal tail of the fish.

3.2.3.1 Microstructure of scales

Figure 3.4d shows the fracture surface through the thickness of a Type I scale; the interface between the ganoine and bone is clearly distinguishable. Similarly, Figure 3.4e shows a polished cross-section of the Type I scale; the two layers are separated by a saw-tooth shaped interface. Figure 3.4f shows the external surface of the Type III scale near the serrated edge, where bone remains exposed and some tubules are observed at the surface. These tubules are covered by ganoine as it grows, a process which continues throughout the gar's life. Prior to being fully covered, a crater-like pit forms around the tubule; a tubule in the process of being covered by mineral is shown in Figure 3.4g. It is also important to note that ganoine is a true enamel, meaning a layer of skin covers the entire surface of the scales and continuously deposits mineral in the living fish.

The microstructures of all scale types are comparable. The ganoine has a structure which consists of regular and distinguishable layers of hydroxyapatite mineral; each layer is ~30 μm in thickness and consists of sub-layers of 2-3 μm. Layers are made of bundles of twisted cross-plied mineral oriented, on average, approximately normal to the scale surface. These layers are shown in Figure 3.5a, and a close-up of one layer is shown in Figure 3.5b. This is different from some other ganoid scales; in the *Polypterus senegalus*, for example, the ganoine consists of parallel mineral fibers oriented directly towards the scale surface [147]. This may be due to the widely different thicknesses (*Polypterus senegalus*: 10 μm vs. *Atractosteus spatula*: 600 μm) of the ganoine layers. Figure 3.5c shows a fracture surface where mineral crystals protrude from the page, showing that they are oriented normal to the surface of the scale. Figure 3.5d is the external surface of the ganoine, where small protrusions called tubercles [174] are regularly arranged at ~7 μm

across the surface of the scale. This spacing matches the periodicity and corresponds to the heads of the mineral bundles, and tubercles result from the speed of mineral deposition [175].

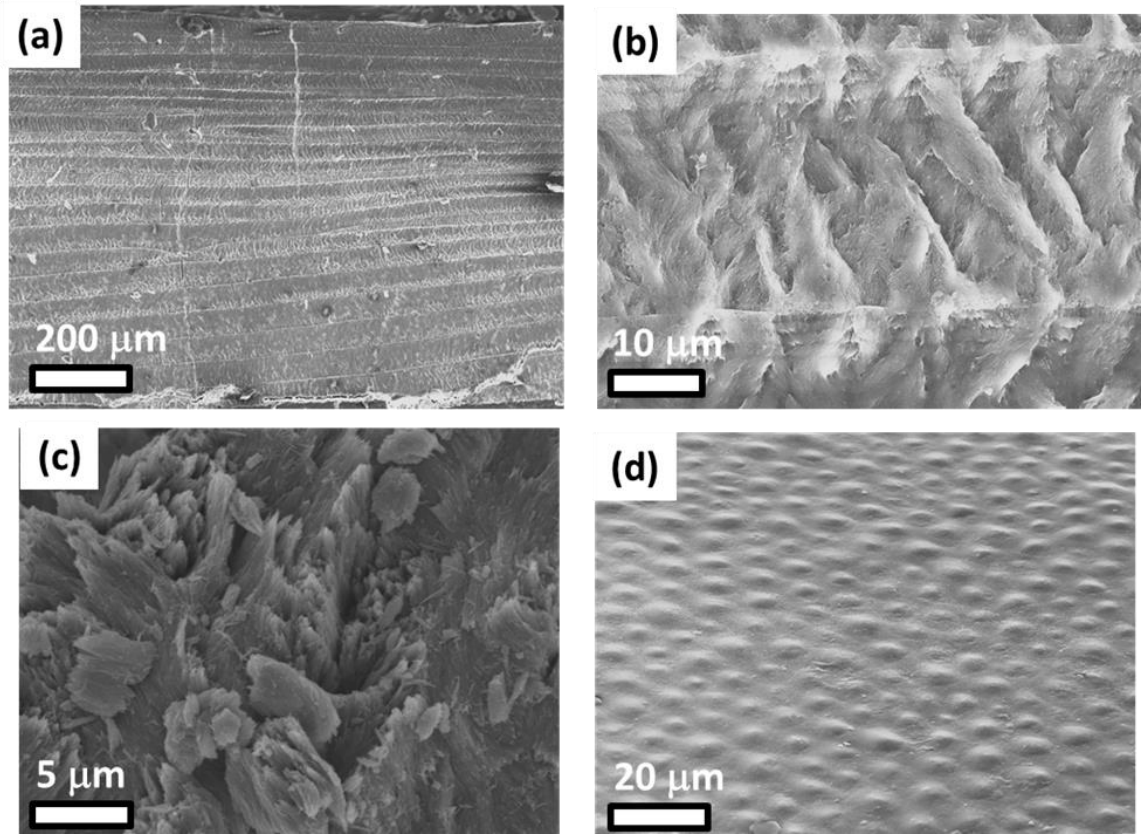

Figure 3.5: Structure of ganoine layer of the scale. (a) Etched ganoine cross-section reveals mineral layers of ~30 μm thickness. (b) High magnification of a ganoine layer shows crossed mineral bundles, and sublayers of 2-3 μm thickness. Bundles are oriented near perpendicular to the surface of the scale. (c) A fracture surface of the ganoine viewed from above the scale shows protruding mineral crystals. (d) The exterior surface of ganoine has tubercles (small rounded reliefs), which correspond to the heads of the mineral bundles.

The bone of the scale consists of mineralized collagen fibrils normal to the scale surface, embedded in a mineral matrix. These fibrils are visible in Figure 3.6a, where mineral crystals fill the space between fibrils (close-up shown in Figure 3.6b). Figure 3.6c is a high-resolution view of a collagen fibril, where the mineral has nucleated in the intrafibrillar region of the collagen fibril. Mineralized fibrils are desirable because their toughness far exceeds that of the hydroxyapatite and collagen constituents, as shown by

Buehler [74]. Hollow tubules run parallel to the fibrils throughout the thickness of the scale. Also shown in Figure 3.3f, these tubules are clearly visible in Figure 3.6d, which is a polished section of the scale as viewed from the normal direction, and visualized using μ-CT in Figure 3.6e. These tubules are vascular channels that deliver nutrients to the skin covering the scales, but have also been attributed to toughening the dry scale [107].

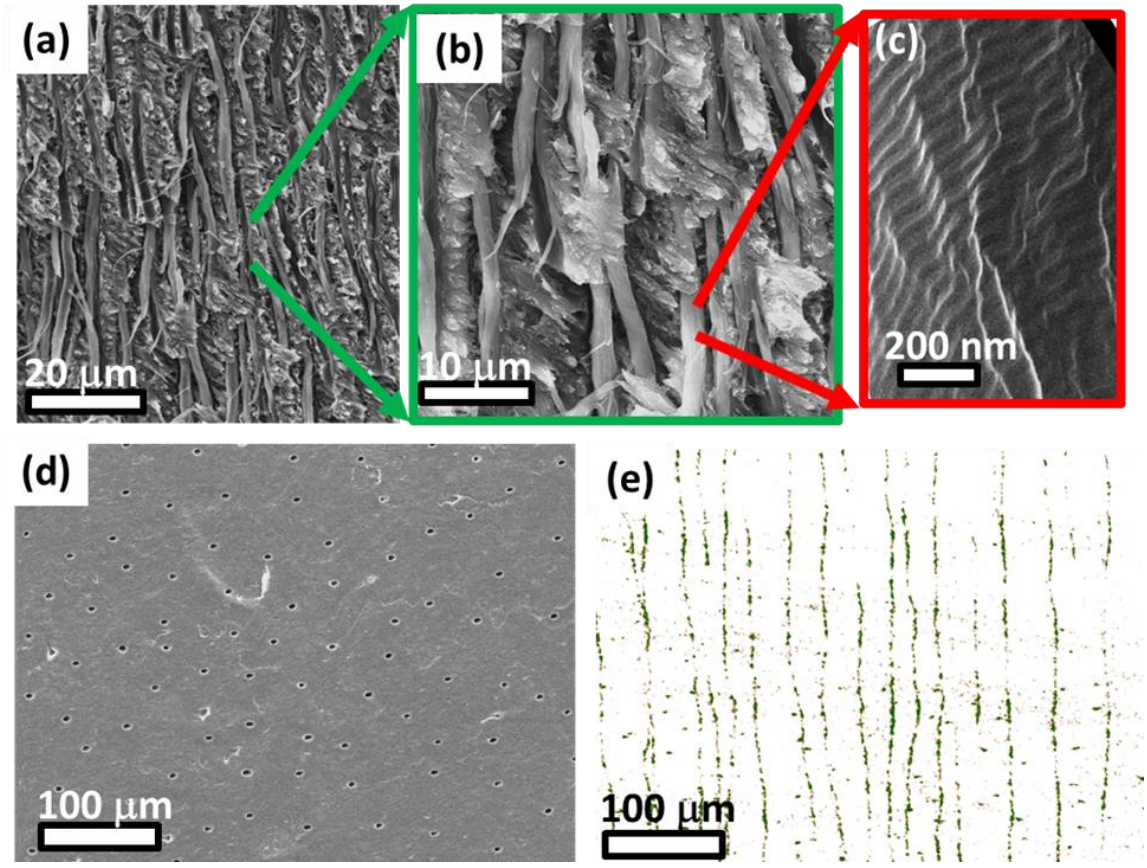

Figure 3.6: Structure of the bony layer of the scale. (a) Fractured surface of bone reveals parallel collagen fibrils. The space between the fibrils is filled with mineral crystals. (b) Increased magnification shows that the mineral crystals are oriented across the collagen fibrils. (c) High resolution image of a mineralized collagen fibril. Mineral nucleates in the gap region of collagen fibrils, and the 67 nm banding is retained as mineral crystals grow. The mineralized surface of the fibril is characterized by flat surfaces and characteristic angles, which reduce the surface energy of the mineral. (d) SEM of polished section of the bony region of scale. Vascular channels called tubules are numerous. (e) μ-CT reconstruction shows that tubules are parallel to each other and nearly perpendicular to the scale surface. They run from the base of the scale towards the outer ganoine surface, where they terminate.

3.2.3.2 Arrangement of scales and flexibility

The macroscopic arrangement of the scales is key to their effectiveness, allowing stiff and strong individual scales, reinforced with the crafted microstructures, to flex and conform to the fish's body as it swims without sacrificing complete protective coverage. It also enables a redistribution of stresses from the point of application due to a tooth over a broader area.

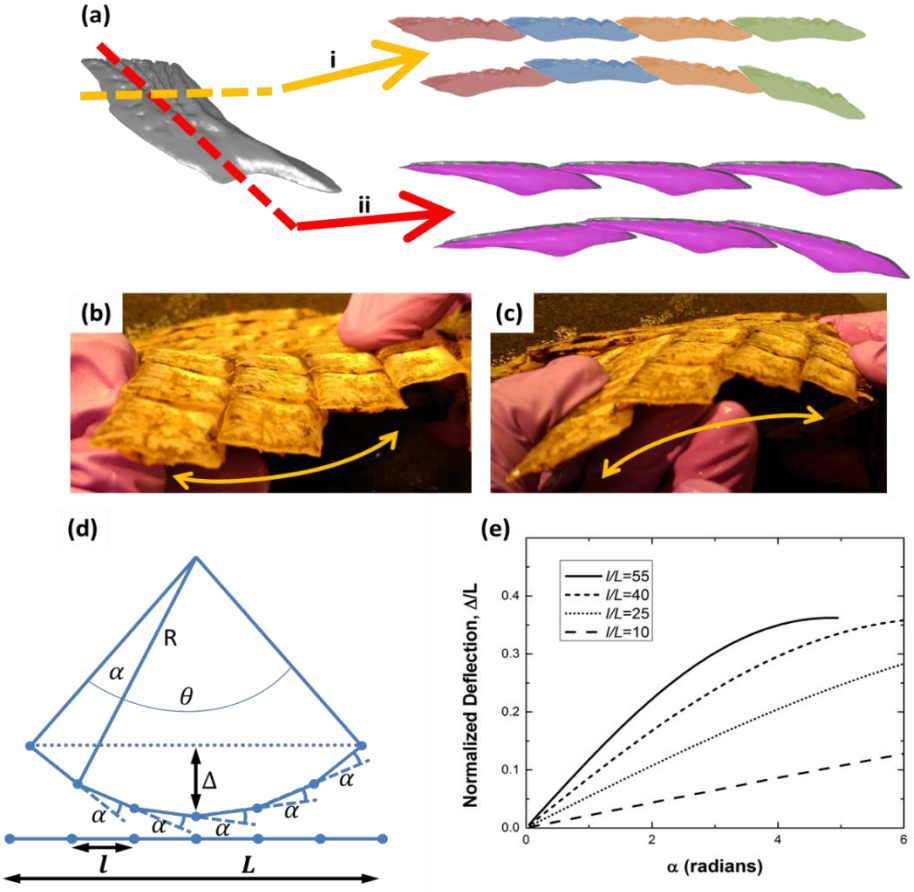

Figure 3.7: Geometric flexibility for a stiff scale. (a) Each scale has two directions of overlap; a cut in each direction is shown by the dashed lines. Overlapping scales hinge on adjacent edges with similar radii of curvature, as shown in the μ-CT cross-sections. Most movement required due to the swimming of the fish is achieved by the motion shown in i. (b) Scale array bending to create a concave surface. (c) Scale array bending to create a convex surface. (d) Manner in which scales on fish accommodate the deflection of the fish body (Δ). (e) Maximum normalized deflection (Δ/L) as a function of α for different ratios of scale length to fish length (l/L); adapted from Chen et al.[176].

In order to compensate for their rigidity, the scales are arranged in such a way that allows geometric flexibility—this is what enables the fish to move as it swims. This is illustrated in Figure 3.7a: adjacent scales have matching radii of curvature at their interfaces, which allows for a hinge-like motion on one another as they slide. An array of scales can be bent both towards and away from the surface, forming convex and concave surfaces, respectively, while maintaining full coverage, as is shown in Figure 3.7b-c. Figure 3.7 shows scales at the maximum deflections; in their natural configuration, each scale may form an angle of ~6° with the adjacent scales. This limit is due to the extensibility in the soft tissues, which connect adjacent scales. The amount of curvature possible is dictated by the misorientation between adjacent scales and the total number of scales. Therefore, scales must be sufficiently small to achieve high amounts of curvature on the fish body. Figure 3.7d shows how deflection (measured by Δ) is a function of the ratio of scale length (l) to total fish length (L) and misorientation between scales (α). Figure 3.7e plots Δ as a function of α, l and L, based on the relationship [176]:

$$\frac{\Delta}{L} = \frac{1}{\alpha}\left[1 - \cos\left(\frac{\alpha L}{2l}\right)\right] \tag{25}$$

During this rotational deflection, the matching curvature of adjacent scales maintains full protective coverage without the formation of gaps. It is also important that the scales do not separate from their foundation during curvature. This effect is shown in Figure 3.8a, and δ, the gap between scales, may be calculated as a function of scale length (l) and bending radius (R) through the relationship:

$$\frac{\delta}{l} = \frac{1}{\sin\left(\arctan\left(\frac{l}{R}\right)\right)} - \frac{R}{l} \tag{26}$$

As the normalized ratio of *R/l* decreases, the size of gaps (*δ/l*) increases. The relationship between these parameters is plotted in Figure 3.8b.

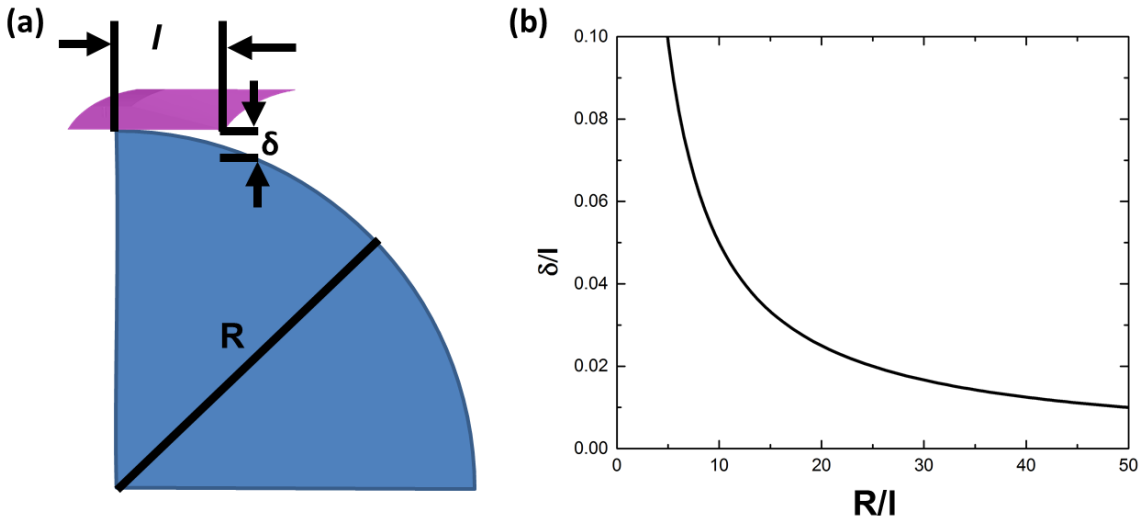

Figure 3.8: Relationship between scale size, deflection, and radius of bending curvature. (a) Schematic shows the unavoidable separation (δ) between flat scales of length (*l*) on a curved surface with radius of curvature (R); (b) relationship between R, *l*, and δ.

Simple flexing of scale arrays is not sufficient. An additional requirement is the ability to conform to a change in length of ~25%, which is both positive in the outside surface and negative on the inside, as calculated through measurements of a highly flexed fish. This dimensionless value is determined from photographs of gars using a simplified representation, shown in Figure 3.9a. The body of the fish is modeled as a cylinder, and the maximum strain based on thickness (*2r*), bending radius (*R*), and degree of flexing (θ) is:

$$\varepsilon_{\max} = \frac{final \quad length}{initial \quad length} - 1 = \frac{(R+r)\theta}{R\theta} - 1 = \frac{r}{R} \tag{27}$$

Linear sliding between scales cannot accommodate this large strain due to the small percentage of overlap between them. Thus, the scales must both slide and reorient in a

specialized and biomechanically optimal manner that can be decomposed into the three stages shown in Figure 3.9b-c: increase in length shown by *d*, which produces tensile extension but leads to separation between scales; sliding shown by *s*, which is a vertical shift and closes the gaps; and lastly a rotation of the scale array of β. These three components are permitted by the compliance of the connective tissue between the gar scales and enable the scale arrays to accommodate the significant dimensional changes required by the movement of the fish. The minor angle of the scales (γ) has a significant effect on the requirements of the scales to rearrange and provide protection. There is a tradeoff between protection and physiological requirements: a minimal amount of weak interfaces is optimized as γ approaches 90°, but the physiological requirement of maintaining coverage causes a large amount of sliding (*s*) to close the separation (*d*) as γ approaches 90°, while reorientation of the scale array becomes excessively large. With respect to *s* and *d*, γ must be sufficiently small in order to be mechanically feasible. This relationship is:

$$\frac{s}{d} = \tan\gamma \tag{28}$$

It is also desirable to maximize the individual scale coverage, hence minimizing the length of perimeters that create interfaces, which are weaker regions. The reduction in coverage for a scale of a certain perimeter based on γ is:

$$\frac{A_{\max}}{A} = \frac{l^2}{l^2 \sin\gamma} = \frac{1}{\sin\gamma} \tag{29}$$

where *A* is the area of a scale, and *l* is the length of one side of the scale. Equations 4 and 5 are plotted in Figure 3.9d. As γ approaches 0 (elongated scales), minimal *s/d* ratios result,

but there is a large reduction in scale area compared to a square scale of the same perimeter. As γ approaches 90°, a nearly square scale optimizes the coverage but leads to infeasible ratios of s/d and excessive reorientation required of the scale arrays. The rotation of the scales, β, is equal to:

$$\beta = \tan^{-1}\left(\frac{s}{d+l}\right) = \tan^{-1}\left(\frac{d\tan\gamma}{d+l}\right) \tag{30}$$

The optimal value of γ lies somewhere in-between; a physiological value is found by measuring scales, equal to 55°. This value is marked on the plot. A well designed scale captures effectiveness in coverage and allows for the flexibility of the natural armor. Both size (l) and shape (γ) are important.

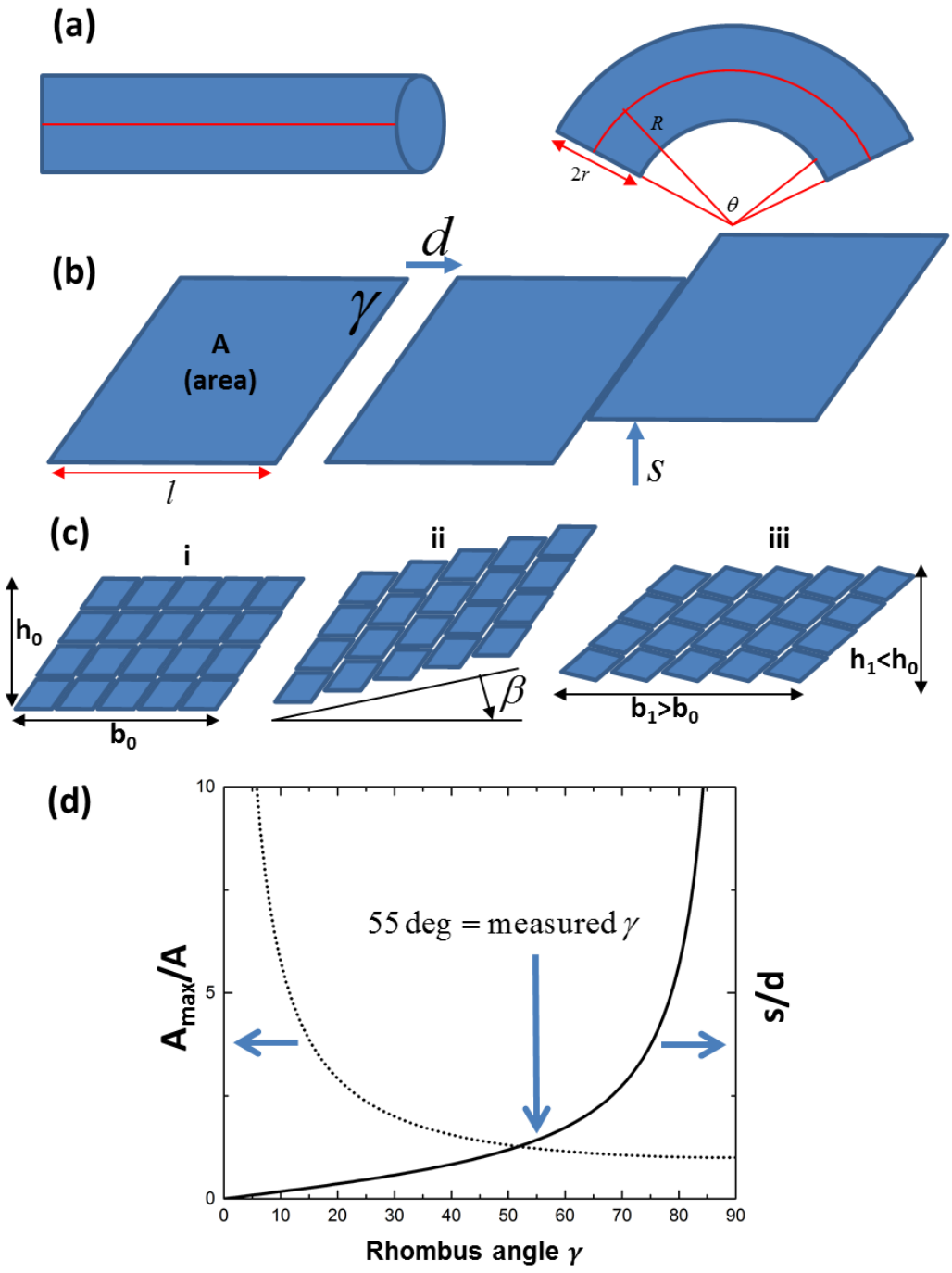

Figure 3.9: The mechanics of gar scales flexing. (a) A simple model of the gar's flexing, which is used to calculate the maximum strain that must be accommodated by the gar scales. (b) Translation by the scale to accommodate strain: *d* is extension, which lengthens the array but leaves gaps. *s* is shift, which closes the gaps formed by *d*. (c) i: The original array of scales. ii: Translation by *d*, *s*. iii: Rotation of *β*, which results in the accommodation of strain ($b_1 > b_0$) (d) Ratios that effect the scale coverage area (A_{max}/A) and amount of sliding required (*s*/*d*) as a function of γ; it is desired that both are minimized. 55° is measured from fish as the value of γ.

3.2.4 Mechanical performance of the gar scale

The mechanical performance of gar scales is summarized in Figure 3.10a [107, 108, 137, 151]; the solid lines show the compression results of ~2 mm hydrated cubes cut from the bony region of gar scales [107]; characteristic responses are shown in black (compressed normal to the scale surface) and green (compressed in orthogonal directions parallel to the scale surface). The compressive strength and failure strain of hydrated samples vary widely: perpendicular to the surface respective values are 310 ± 30 MPa and ~0.3, and in the two in-plane directions strengths are 200 ± 30 MPa and 240 ± 30 MPa with strains of ~0.17 and ~0.25. In contrast, the moduli reported by nanoindentation vary by less than 1% when wet (9.98-10.04 GPa) and roughly 25% (10.9-13.8 GPa) when dry [107]. There are two key findings in these results. Firstly, in-plane mechanical properties of the scale do not have significant anisotropy due to the reported uncertainties. This is reasonable as there are no apparent structural features that would lead to in-plane anisotropy. Secondly, the ultimate strength and failure strain normal to the scale surface under compression are significantly improved from the two in-plane directions. This is due to microstructural features including the presence of collagen fibrils and tubules, which enhance the failure properties, and are discussed thoroughly in Section 3.2.5. However, these differences are not manifested during nanoindentation, which evaluates small material regions without tubules and does not induce failure.

Figure 3.10a also shows band plots of tensile curves from tests performed in-plane with the surface of the scale and highlight differences between the wet and dry responses [107]. Both exhibit similar stiffness and strength, but there is a notable and important difference: wet scales experience plasticity in tension, which is due to the breaking and

reforming of hydrogen bonds between water molecules and collagen fibrils. This occurs when a critical stress is reached and hydrogen bonds within the scale no longer support the load. Upon unloading, the plastic strain, which is the strain after the transition, is not recovered. We find that this bilinear response plays a crucial role in the failure aversion of the gar scale and discuss this in Section 3.2.5. Dry scales, on the other hand, fail with less non-linear deformation. Figure 3.10b shows the variation in microindentation and nanoindentation hardness throughout the (normalized) thickness of the scale [159]. Due to distinct differences in the structure and composition of the ganoine and bony regions, an abrupt change (characteristic of ganoid scales [172]) occurs at the interface between the two. The higher microindentation hardness is in ganoine (2500 MPa) and the lower in the bony region (around 350 MPa) [137].

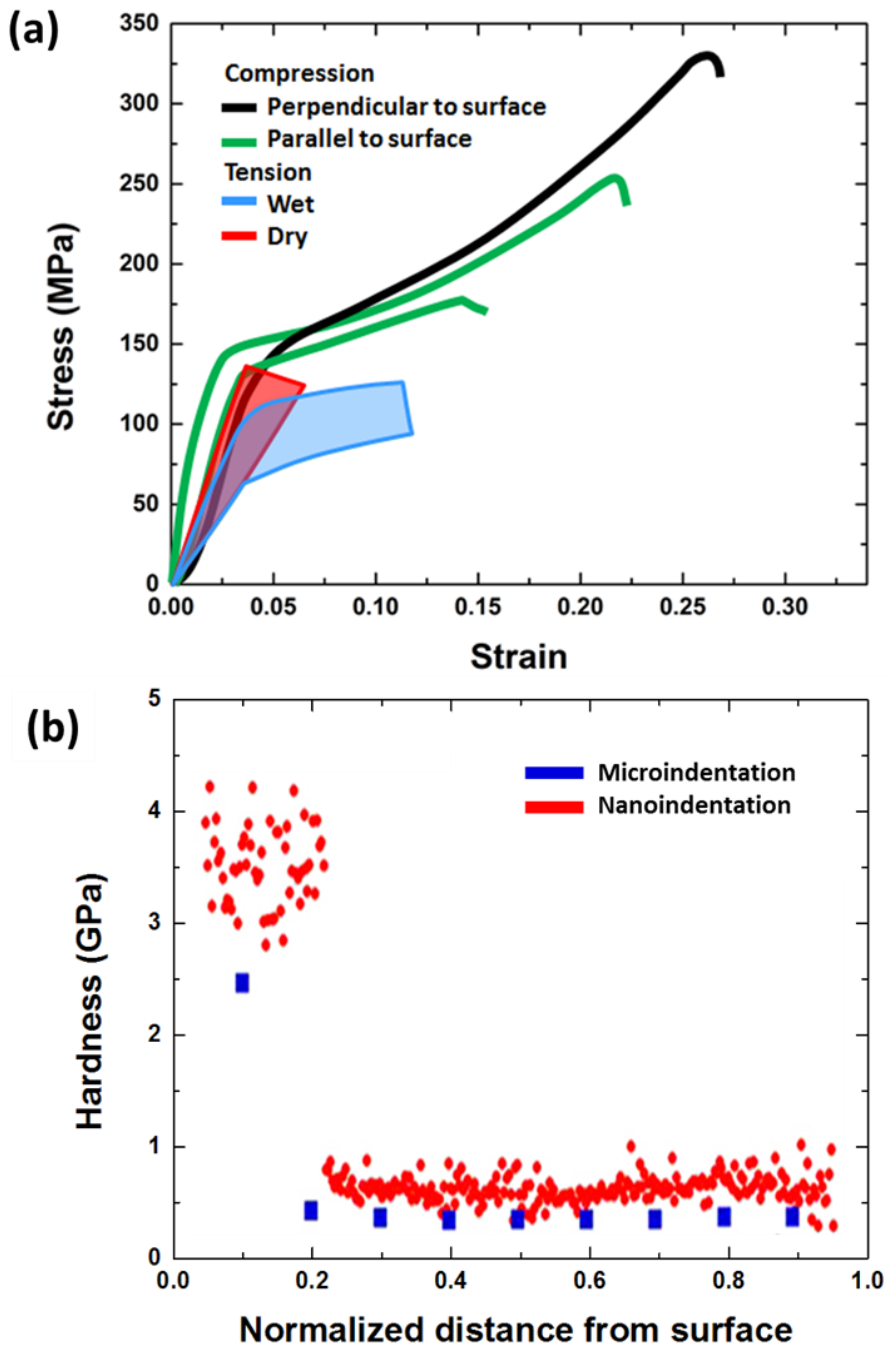

Figure 3.10: Previously reported mechanical properties of the scale. (a) Compressive tests of ~2 mm cubes in multiple orientations and range of tensile stress–strain curves of wet and dry alligator gar scales tested along the length of the scale. Note the bilinear response of the wet gar scale. Adapted from Yang et al. [107]. (b) Hardness of the scale. The ganoine outer surface is roughly 6 times harder than the bony part of the scale. There is little variation within each individual region. Adapted from Chen et al. [137].

The ganoine exhibits structural anisotropy, shown in Figure 3.6, where twisted cross-plied bundles of mineral extend towards the surface of the scale. Nanoindentation was performed and loading was applied in two orientations: inclined to the scale surface (nearly perpendicular to it), and parallel to the scale surface. The slightly inclined orientation was chosen so that mappings would span the ~30 μm thick cross-plied mineral layers, and show corresponding variation in properties. Results indicate that the ganoine is indeed anisotropic: when loaded in the direction aligned with the plane of the scale, the reduced modulus (E_r) is 59 ± 6 GPa. In the direction nearly perpendicular to the scale surface, the stiffness is increased (E_r = 67 ± 5 GPa). These indentations are shown in Figure 3.11a, with the interface between layers marked. Figure 3.11b shows the gradient in stiffness across the mineral layer, which is observable in both orientations; these gradients also result in increased uncertainties. The differences within layers correspond to the structure and organization of the mineral bundles in each layer, which also contribute to the toughening of the mineral. High load indents (Figure 3.11c-d) show areas where failure was induced. The fracture toughness of the two orientations may be estimated [177, 178]:

$$K_c = A\left(\frac{E}{H}\right)^{0.5}\frac{P}{c^{3/2}} \tag{31}$$

where E is the Young's modulus, H is the hardness, P is the load, c is the half-crack length (measured from the center of the indent to the crack tip), and A is a fitting parameter, equal to 0.04 [179]. Although this technique is designed for isotropic and homogeneous materials, it has been applied for anisotropic and inhomogeneous materials such as enamel or ceramic coatings where conventional toughness tests are not feasible [180]. The maximum crack size from 5 N indents perpendicular to the scale surface is ~60 μm, while

the maximum crack size from 5 N indents parallel to the surface is ~140 μm; the corresponding fracture toughness estimates are 2.8 and 0.8 MPa $m^{1/2}$, which compare well with tooth enamel (K_c=0.7-1.27 MPa $m^{1/2}$). This fracture toughness is superior to that of single crystal hydroxyapatite, and indicates that the ganoine is toughened by the cross-plied mineral bundles, which are observable throughout. Additionally, the ganoine is 3.5 times tougher when subjected to indentation from the outer surface, coincident with the loading which would be applied by a predator tooth, as the microstructure restricts cracking. Previous fracture toughness measurements performed on the bone region of the scale by Yang et al. [107] used notched beams to yield fracture toughness crack-resistance curves in three orientations. The toughness rises to K_j=6 MPa $m^{1/2}$ as the crack grows, depending on orientation. Our toughness values of 0.8 to 2.8 MPa $m^{1/2}$ represent the early stages of crack growth where extrinsic toughening mechanisms start to become operational, and are consistent with the first part of the fracture toughness crack-resistance curves by Yang et al. [107].

Three-point bending tests were performed on specimens of the scale that include both ganoine and bone regions. Two loading directions were used, and results are shown in Figure 3.12. Significant differences in response between the two directions exist: when the scale is bent with the ganoine in tension, the maximum flexural stress is 73 ± 6 MPa. The brittle mineral is not effective at supporting substantial tensile loads and failure originates in the ganoine. In contrast, the ganoine has a high compressive strength and, when loaded in compression, the maximum flexural stress increases to 160 ± 20 MPa. This coincides with the functional requirements of the gar scale and many other armors, where attack and pressures occur from the exterior and a hard outer surface exists to prevent

penetration, but a more compliant foundation capable of supporting tensile loads is required. In the gar scales, the ganoine is in compression and the bone provides the required tensile strength.

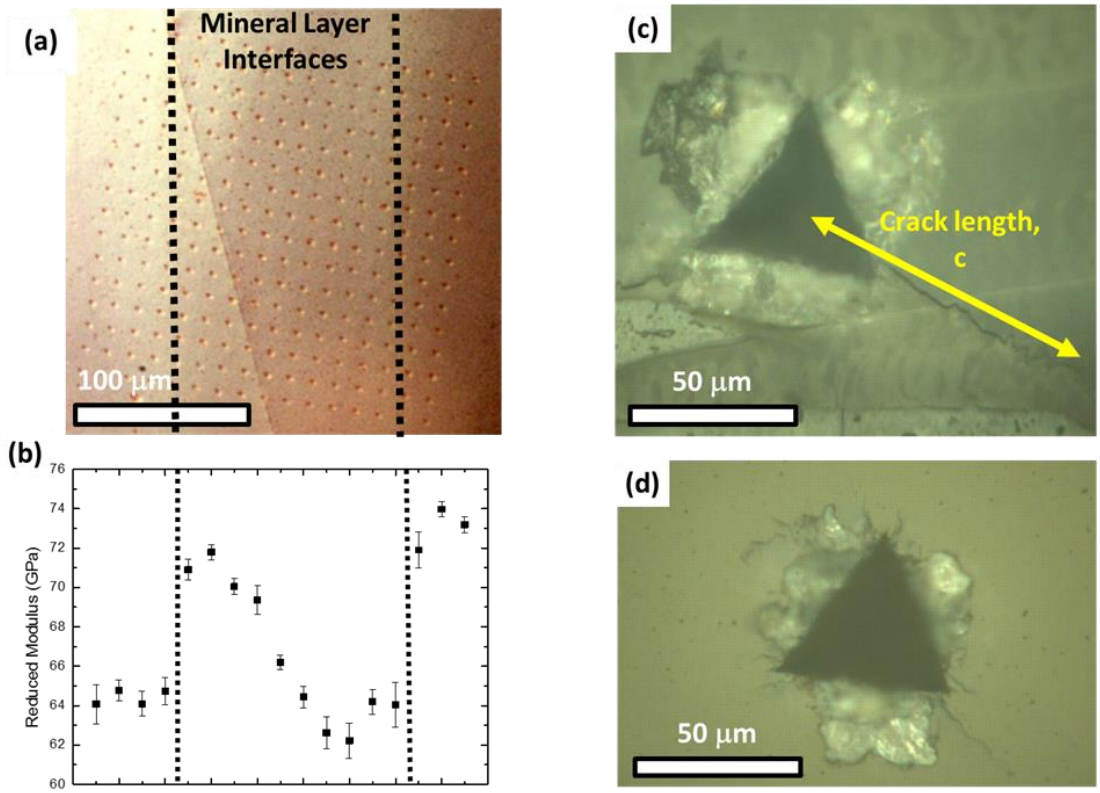

Figure 3.11 Nano indentation of ganoine normal to and parallel to the scale surface. (a-b) The variation of modulus corresponds to the layers of ganoine. (c) In the transverse direction of the scale, a high load indent causes cracks to grow; crack semi-length, *c*, is marked. (d) In the normal direction to the scale, smaller cracks caused by a high load indent correspond to an increased toughness.

Penetration tests were performed using a steel indenter with a 300 μm tip radius on individual scales with and without the ganoine layer, in order to determine its contribution. The ganoine layer was removed just beyond the interface of the two layers by careful polishing to prevent the introduction of damage. The results, shown in Figure 3.13a, are surprising. The presence of ganoine against a steel indenter produces a slight decrease in the maximum force. In each case, the force to failure still remains sufficiently high to defeat predators as over 1,500 N is required to cause failure. For comparison, large alligators may

have a bite force of up to 10 kN, which is distributed among the ~80 teeth in the alligator's mouth [172]. It is difficult to evaluate the force per tooth because this depends on the relative size of fish and alligator mouth. We assume, to a first approximation, that one third of the teeth are in contact. This gives an average force per tooth of up to 375 N. One possible explanation for this behavior is that the localized penetration resistance decreases slightly with the ganoine layer but the flexure strength increases.

An additional penetration test performed with an alligator tooth is shown in Figure 3.13b, which results in the failure of the tooth at 500 N. The cracking of the alligator tooth is induced by the hardness of the ganoine layer, which prevents deformation and a distribution of the load across the alligator tooth. This shows that, with the ganoine layer, the gar scale is sufficiently strong to withstand local loads due to alligator bite force. Additionally, the hardness of ganoine may play a role in inducing the failure of teeth.

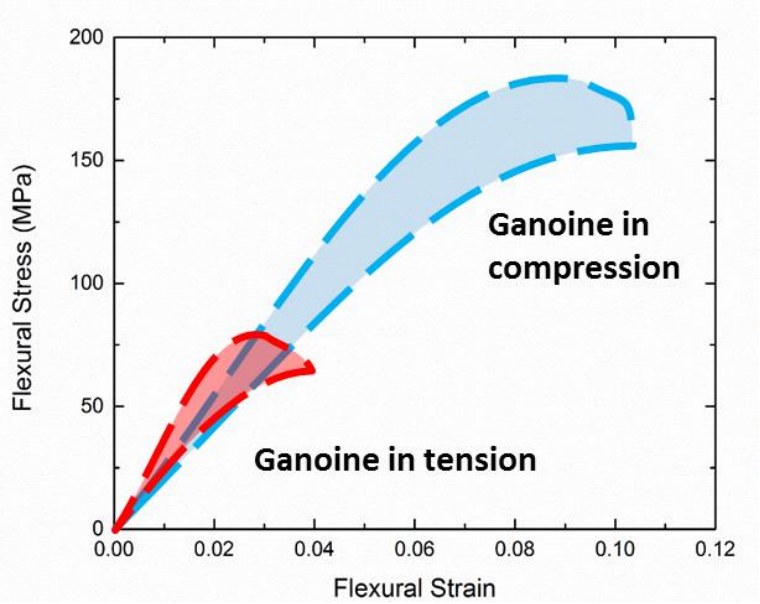

Figure 3.12: Three-point bending of scale with ganoine and bony layers along two opposite directions. Bending tests produce tension on the convex face, and compression on the concave face. When the ganoine side is subjected to compression, higher flexural stresses and strains are achievable. This is due to the ganoine's compressive strength, and the bone's ability to resist high strains. The ganoine's weakness in tension decreases the flexural strength.

The sequence of images shown in Figure 3.13c shows an array of scales deformed to accommodate the movement caused by the pressure on a central scale. A compliant foundation mimicking the flesh of the animal was used. The alligator tooth is embedded in the tip of a threaded rod, and pressure is initiated at (i). When the force reaches 500 N, the alligator tooth fractures (ii). Upon removal of the force (iii), the array of scales returns to the flat and undeformed state. Through linkage with adjacent scales, the load is distributed from the point of application, reducing pressure and damage to the underlying soft tissues. Figure 3.13d indicates how the pressure from indentation leads to flexural loadings, and shows how the ganoine may be beneficial in this regard.

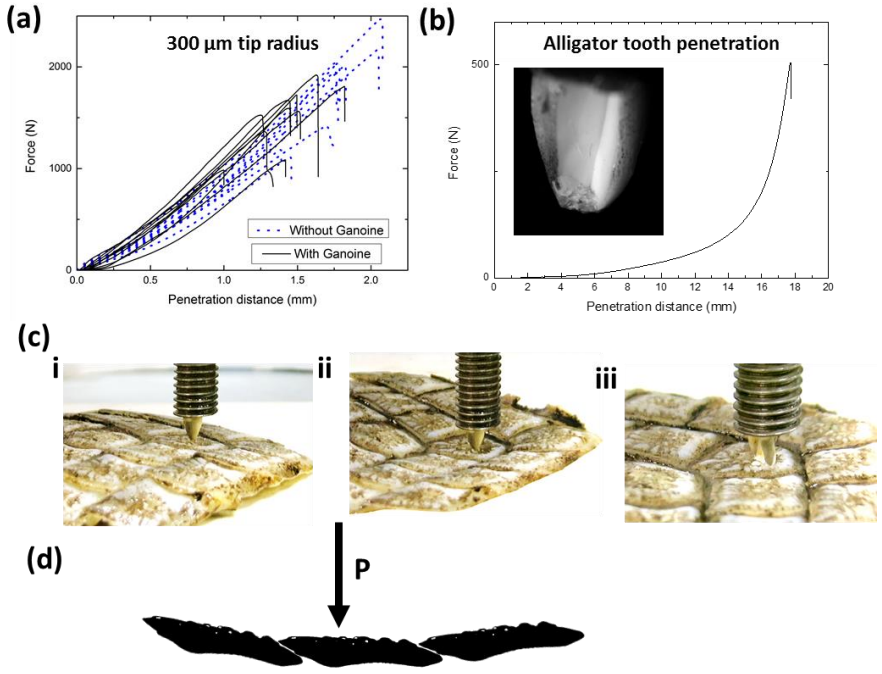

Figure 3.13: Penetration of individual scale by steel and alligator tooth. (a) Sections of scale both with and without the ganoine layer are indented by a steel tip. Scales without ganoine frequently experienced additional penetration, compaction, and higher failure forces. In contrast, scales with the ganoine layer showed a reduced penetration at any force, but also slightly reduced failure loads. (b) Load vs. penetration of gar scale array by a young alligator tooth with a tip radius of 240 µm. Foam beneath the array simulates flesh. Tooth failure occurs at 500N, which is significantly less than what the scale is capable of withstanding, as illustrated in (a). (c) Sequence of scale penetration. i: undeformed scales. ii: scales conforming to the pressure of the tooth. iii: tooth fails. (d) Schematic representation of cooperative motion of scales linked by connective tissue in response to load P.

3.2.5 Failure aversion strategies in the gar scale

There are three regions in the single gar scale where key failure aversion features occur: 1) in the ganoine, where cracks initiate during predatory attack; 2) at the interface between the ganoine and bone; 3) in the bone region, which is the last stage of crack propagation, the fracture of which leads to complete failure of the scale.

Penetration tests into the ganoine reveal robust toughening features. Figure 3.14a is an indent caused by penetration of a steel indenter into the ganoine surface of the scale. After loading to 1000 N, damage to the ganoine is apparent as some crushing takes place, but the cracks do not propagate through the thickness of the scale. Cracking occurs directly beneath the indenter, and some cracks radiate out from the indenter but are contained within the ganoine layer. This is directly related to the fracture toughness, which is enhanced by the twisted cross-plied mineral, and a likelihood of multiple cracking within the ganoine, as observed in the conch shell [181]. Similarly, in a compression test of a portion of the scale with the ganoine layer intact (Figure 3.14b), failure occurs in the ganoine layer but does not propagate to the interface with the bone layer. Close observation of the failure surface of ganoine (Figure 3.14c) shows that, as cracks progress, they must twist and deflect since they follow the interfaces of cross-plied mineral bundles. This deflection toughens the mineral and inhibits the propagation of cracks, which are often arrested prior to penetrating the mineral layer. Figure 3.14d shows the containment of a crack in the ganoine layer.

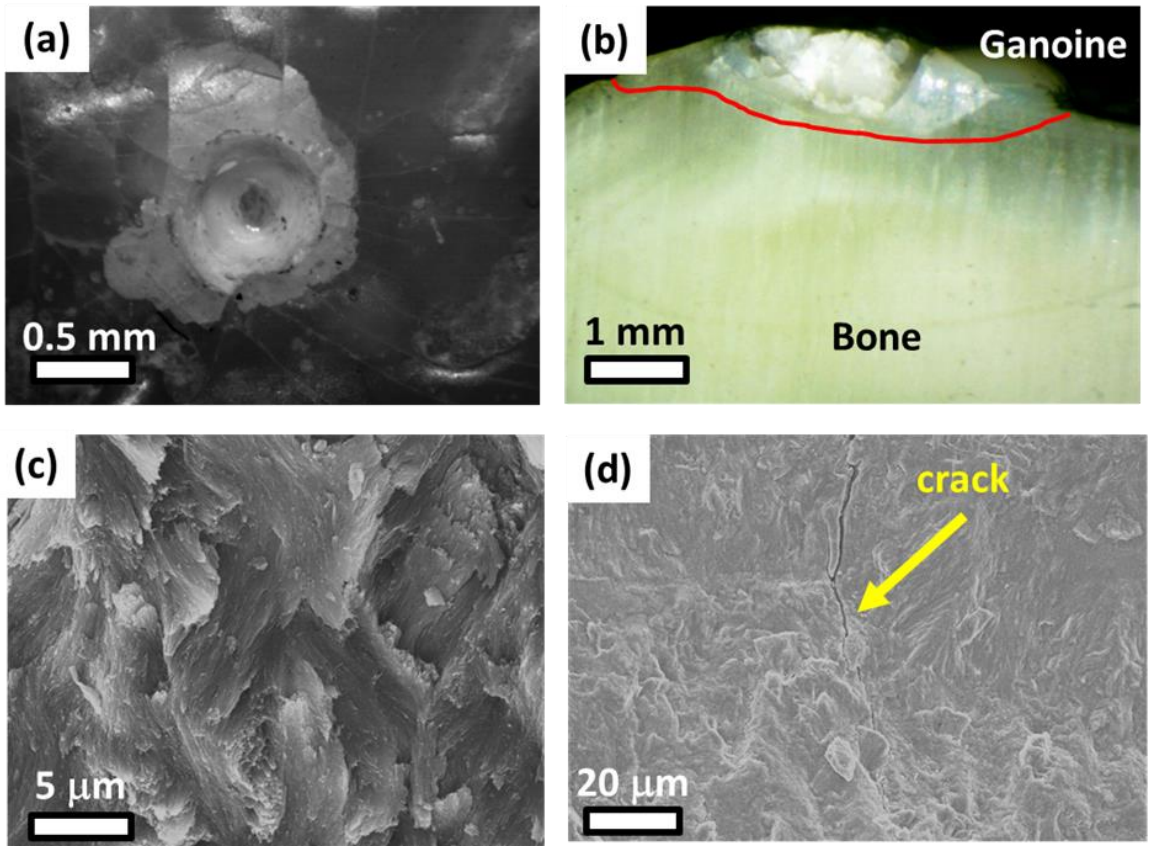

Figure 3.14: Toughening of the ganoine region. (a) Cracking of ganoine from penetration test loaded to 1000 N shows partial mineral failure, while bone remains intact. (b) Failure of ganoine during a compression test: failure is contained within the ganoine and does not propagate to bone. (c) Fracture surface of ganoine shows cross-plied mineral bundles that provide toughening. (d) A crack is arrested in the ganoine.

The ganoine in the gar scale has the robust ability to arrest cracks, but this is not always sufficient. Figure 3.15a shows a crack, which originated during a three-point bending test and progressed through the ganoine into the bone. Material mismatch between two regions may cause crack deflection at the interface, based on Dundurs' parameters [182]. Imbeni et al. [183] present a solution for linear elastic materials based on the first Dundurs' parameter, $\alpha = \frac{E_1 - E_2}{E_1 + E_2}$, and the magnitude of material toughness on each side of the interface, $\frac{G_1}{G_2}$. For the case of a crack penetrating from ganoine towards bone, α=0.71 and G_1/G_2=0.17, indicating that cracks originating in the ganoine and arriving at

the interface are well within the regime in which deflection is expected. Figure 3.15b shows a crack that arrives at the interface and is deflected along the border. The interface has a saw-tooth shape that directs cracks towards the mineral layer where it is either arrested by the robust toughening mechanisms within the ganoine or returns to the interface; this process may repeat and is shown in Figure 3.15c.

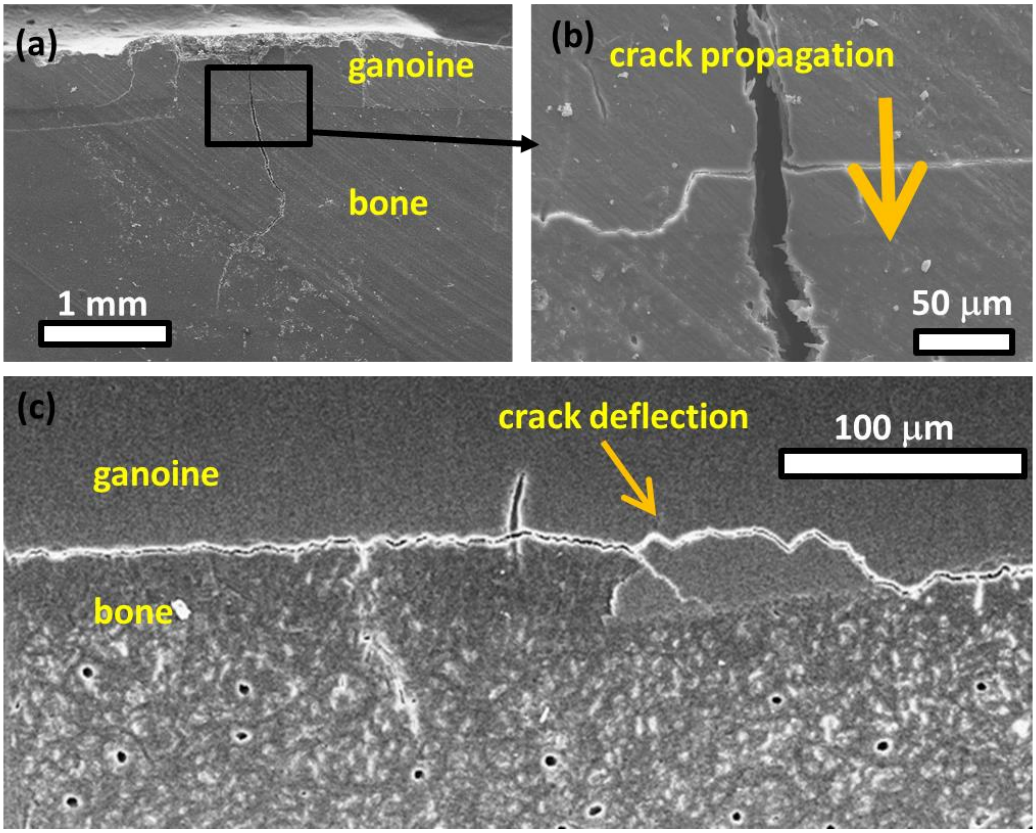

Figure 3.15: Interfacial toughening via crack deflection. (a) Large cracks penetrate through the ganoine and bone. (b) Magnified view of the interface in (a). Upon arrival at the ganoine-bone interface, cracks are deflected along the interface and, dependent on loading, may also continue into the bone. (c) Upon encountering the saw-tooth ridges in the interface, cracks are deflected into the ganoine where the toughening features within attempt to arrest the crack.

With sufficient load, the bone will also crack. Energetically, it is expected that cracks propagate straight through the scale, along tubules (shown in Figure 3.6), which create stress concentrations. Figure 3.16a-b shows an actual cracking path and overall jagged fracture surface, which results in a significant increase in the energy required to

progress the crack. This meandering, possibly caused by the orientation of mineral crystals in the bone (shown in Figure 3.16c), forces cracks to traverse highly mineralized fibrils with exceptional toughness, strength, and elasticity. This closely aligns with the results by Yang et al. [107], which indicated that fracture toughness is enhanced for orientations where fibrils span the crack wake. Figure 3.16d shows one instance where collagen fibrils bridge a crack and aid in stopping propagation.

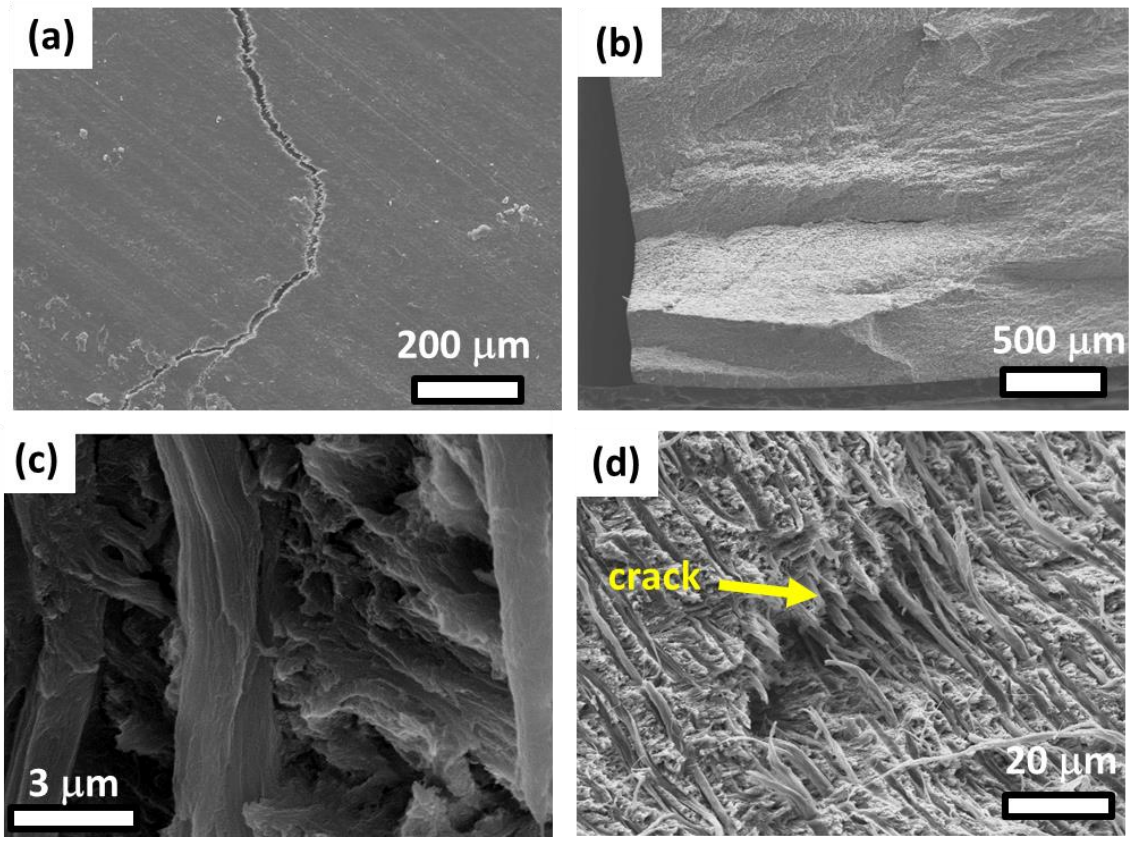

Figure 3.16: Toughening features of bony region: mineralized collagen fibrils. (a) The crack path as it penetrates through the bone layer is jagged. (b) The fracture surface of a hydrated scale. (c) A collagen fibril is shown with mineral crystals oriented across the fibril. This orientation is found throughout the scale. (d) Collagen fibrils stretch across a crack and prevent its propagation.

The role played by the tubules in the dry scales is well documented by Yang et al. [107] who notes that in dry scales cracks are deflected between tubules, leading to an enhanced fracture resistance through crack meandering. This causes the dry brittle material

to have similar and sometimes superior properties to the wet material, where these toughening effects do not occur. These results are shown in Figure 3.17a-b. Due to the typically hydrated state of the gar scales, finite element simulations were performed, in order to observe the effects of the tubule in wet and dry scales. The results, shown in Figure 3.17c-d, confirm the high stress concentrations in the vicinity of tubules in the dry state. Elastoplastic (simulating the wet scale) and linear elastic (simulating the dry scale) responses applied to the material are shown in Figure 3.17e. Due to the linear elasticity of the dry material, the stress concentration around tubules closely corresponds with the relationship $\sigma_{\max} = 3\sigma_{applied}$: $\sigma_{\max} = 201$ MPa for $\sigma_{applied} = 70$ MPa. The stress distribution is inhomogeneous and high stresses at the edges of tubules induce failure. Crack tips tend to orient towards the direction perpendicular to the maximum normal stress, although in this case attraction to the intense stress around tubules leads to meandering. "Wet" simulations incorporate the elastoplastic response of the material; this leads to a situation where $\sigma_{\max} < 3\sigma_{applied}$: $\sigma_{\max} = 124$ MPa for $\sigma_{applied} = 70$ MPa. The elastoplastic response reduces the stress intensity by 38%, while regions of high strain form around tubules (15% vs. 11%), absorbing strain energy. These calculations explain the previous results by Yang et al. [107], confirming that the stress concentrations at the tubules direct the crack tip towards them and thus is a toughening mechanism. This does not occur in the wet scales, where simulations indicate that intrinsic toughening due to the plasticity of the bone operates in the vicinity of tubules. The reduction of stress intensity around tubules results in a more homogenous distribution of stress. Therefore, an overall high value of strain is

achieved prior to the material reaching failure, and an exceptional toughness as measured by the area beneath the tensile stress-strain curve in Figure 3.10a.

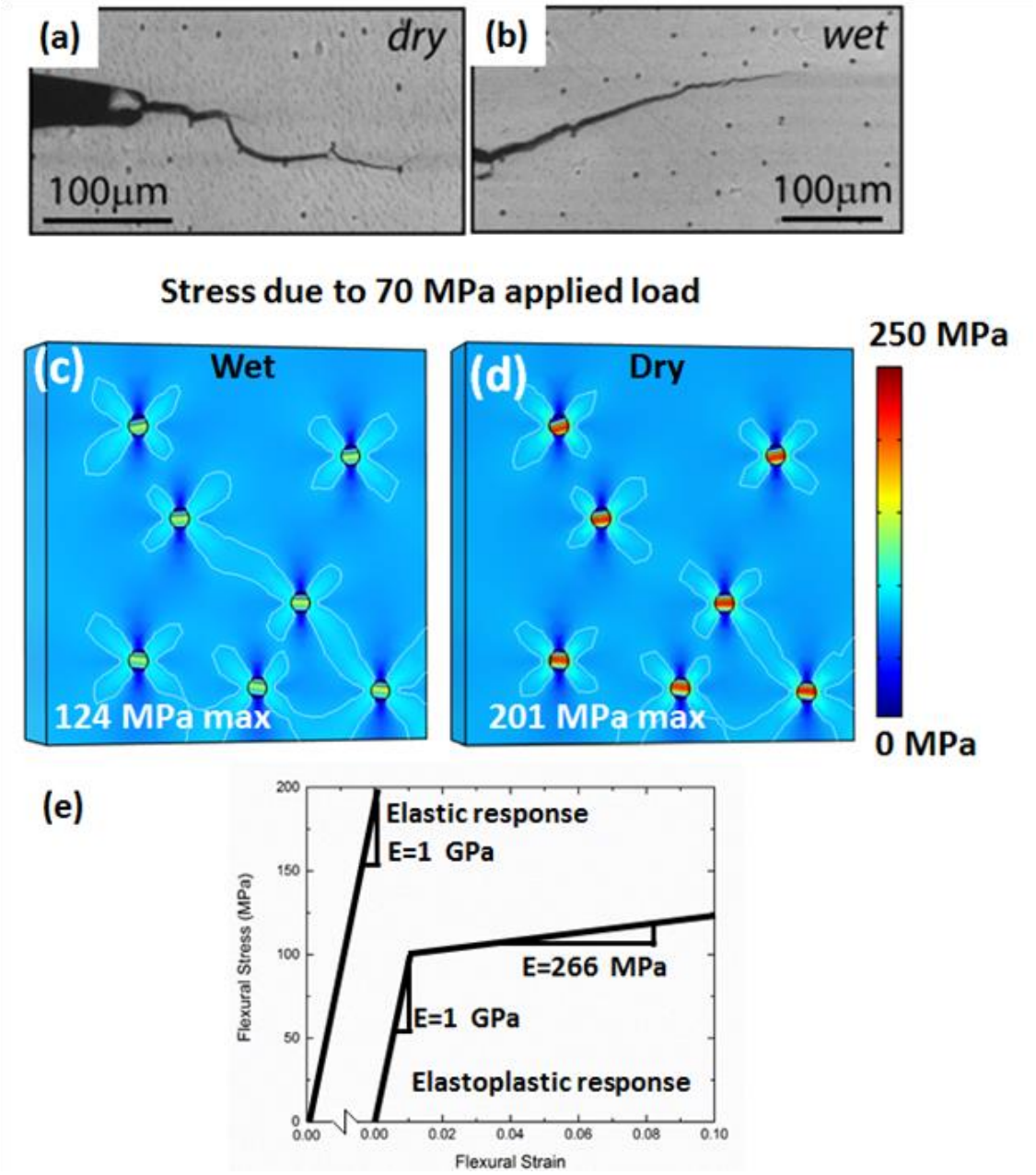

Figure 3.17: Toughening features of bony region: tubule effects. (a) A crack in a dry scale progresses by jumping from one tubule to the next. (b) A crack in a wet scale progresses without strong influence of the tubules. Adapted from Yang et al. [107]. (c-d) Simulations calculate stress in the presence of tubules when wet and dry. Stress concentrations around dry tubules correspond closely with 3 times the applied load, while stress concentrations around wet tubules are reduced by 38%. (e) The material responses applied for the elastic and elastoplastic responses.

3.2.6 Summary

The goal of studying natural armor is to understand key features for potential incorporation into superior protection for personnel and equipment. Being in a hostile environment demands an effective armor capable of withstanding projectiles and impacts without inhibiting mobility. Tactical advantages are provided by advanced robotics, and armor which allows for flexibility is key to the protection of both human and machine.

This work extends the earlier contributions of our own group [107, 137], which focused solely on microstructural features, and reveals design principles on the micro and macroscales. These features are currently in the process of being incorporated into synthetic scale-inspired flexible designs: at the microscale, key features lead to the required material properties such as toughness and strength. At the macroscale, geometry provides the required coverage and flexibility while minimizing weaknesses. The following are the principal findings:

- The arrangement of scales in the quasi-cylindrical body of the gar makes an angle of γ=55° with the longitudinal axis. Upon flexing, one side of the gar is stretched while the other is compressed. Both sliding and rotation, necessary to permit the length changes, are quantitatively expressed as a function of the flexing radius of the fish. Calculations show that the angle γ=55° is a compromise between coverage area per tile and sliding/rotation on stretching.
- The scale, placed on a muscle simulant, was subjected to the increasing force of an alligator tooth. The scale resisted a bite force of 500 N, and the tooth broke. The radius of the tooth and maximum bite force depend on the mass and nature of the predator, but it is clear that the hard ganoine layer is effective in producing fracture

of the tooth. Bending tests show that the flexural strength shows a considerable asymmetry; the orientation corresponding to attack (compressive force by an external load) is significantly enhanced.

- Toughening features exist in each layer of the scale. In the outer ganoine, twisted cross-plied mineral enhances fracture toughness and arrests cracks. The microstructural arrangement of the composite bone lengthens crack paths and utilizes the tough collagen fibrils. The saw-tooth interface between the two layers is designed to deflect and arrest cracks.

3.3 The protective scales of *Arapaima gigas*

3.3.1 Background

Natural protective layers, exhibited by seashells, fish scales, turtle carapaces, armadillo and alligator osteoderms, have developed and refined over hundreds of millions of years through a process of convergent evolution [108]. These biological materials have hierarchical architectures and exhibit excellent properties with complex mechanisms of failure avoidance. They are inspiring man-made structural materials that are lightweight and demonstrate outstanding toughness; good examples are nacre-inspired, freeze-cast structures [139, 141, 184].

Dermal protection of animals ranges from rigid to flexible. Flexibility enables mobility while rigid components maximize protection. Fish scales uniquely combine these two traits, and can be classified into four groups: placoid [143, 185], ganoid [107, 147], cosmoid [154, 186, 187] and elasmoid (cycloid and ctenoid) [109, 171, 188, 189]. Yang et al. [108] reviewed the four types and provided a schematic drawing of their morphologies as well as their connection mechanisms. Placoid scales are denticles, or small modified

teeth, which cover the cartilaginous fish's skin. They give the skin a rough feel, and may contribute to favorable water flow while swimming. Ganoid scales are recognized by a thick surface layer of enamel or ganoine, on top of a dentin or bony base. Cosmoid scales consist of a double bone layer, comprising lamellar and vascular bone; the outer layer is considered as a dentin-like cosmine. Elasmoid scales are thin, lamellar collagenous plates. Cycloid scales are composed of concentric rings and ctenoid scales are composed of fringed projections along the posterior edge. In fish, scales are lightweight and enable flexibility to swim, yet are sufficiently rigid to provide protection from predators.

Most fish scales have similar constituent materials: calcium-deficient hydroxyapatite (HAP) and type I collagen fibrils [137, 190, 191]. The mineralized collagen fibrils form different architectures, such as the plywood (*Bouligand*-type) structure [110, 192, 193] or, in the case of ganoid scales, a bony structure with a complex structure interlaced with HAP crystals [107, 147]. Additionally, scales commonly exhibit a composite or graded structure with hardness decreasing from the outer to the inner layers.

Studies on the penetration of scales using either real teeth or simulated indenters to mimic fish bites provide a good estimate of the effectiveness of the scale's complex structure. Zhu et al. [109] penetrated single scales of striped bass (*Morone saxatilis*) with a sharp indenter, and analyzed the sequence of events, dividing it into three stages: elastic deflection of the scale, fracture of the mineralized layer and penetration of the collagen lamellae. Meyers et al. [159] penetrated the arapaima scale with a real piranha tooth since piranha is the major predator to arapaima in the Amazon River; despite being twice the hardness of the scales, the tooth failed to penetrate them. Zhu et al. [149] found that overlapping three scales essentially multiplies the puncture resistance by three. Friction

between the scales is negligible, and therefore does not generate additional resistance to deformation or puncture, regardless of the arrangement of the scales. The force dispersal from scales prevents unstable localized deformation of the skin and damage to underlying tissues. Finite element modeling of the penetration into ganoid [148] and elasmoid [173] scales was conducted to establish the interactions between tooth sharpness, scale flexibility and other parameters.

It was established by Lin et al. [110], Meyers et al. [159] and Zimmermann et al. [153] that the structure of the arapaima scale consists of an external layer with a highly mineralized, rough surface and inner foundation of collagen layers organized in a *Bouligand*-type structure with lamellae (~50-60 μm thick for each) of parallel collagen fibrils in different orientations. However, the understanding of the fundamental mechanisms of deformation and damage avoidance in elasmoid scales is still incomplete. The objective of this work is to present a comprehensive evaluation of the mechanisms governing the strength, ductility and toughness of the scales of the arapaima fish (Figure 3.18a) through three complementary methods: experimental, analytical and computational. The damage mechanisms of the penetration by teeth are identified and quantified through controlled experiments. The principal experimental method is the in situ observation of the deformation of a scale. This is supplemented by an analysis based on the interaction between the different lamellae and by molecular dynamics (MD) calculations.

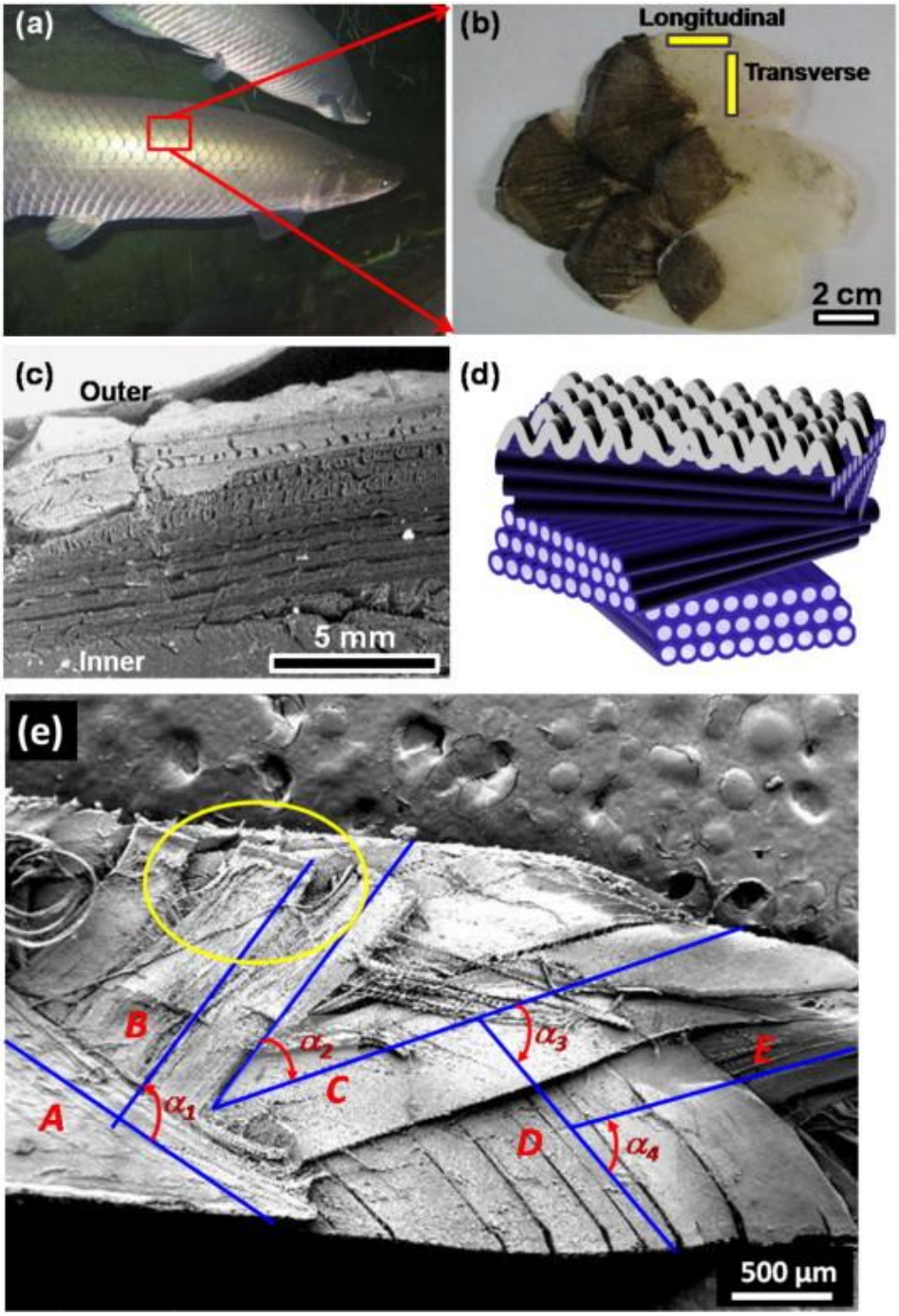

Figure 3.18: Arapaima fish and its scales. (a) Arapaima fish with overlapped scales on its body; (b) close-up of the overlapped scales (darker regions were exposed, lighter regions were covered by other scales) showing longitudinal and transverse directions of specimens for tensile tests; (c) scanning electron micrograph of the cross-section of a scale (note that the small cracks in the collagen layer are artifacts, formed when the scales dried out in vacuo; (d) schematic drawing of the structure of the arapaima's scale: the outer layer is highly mineralized, whereas the inner layer has different orientations of collagen fibrils arranged in lamellae; (e) tensile failure region of the lamellae: $\alpha_1 = 87°$, $\alpha_2 = -34°$, $\alpha_3 = -69°$, $\alpha_4 = 67°$. The yellow ellipse in (e) shows two events where lamellae separate leading to changes in the angle.

3.3.2 Methods

The arapaima scales (Figure 3.18b), which typically are 50–120 mm in size, were characterized using a range of experimental procedures to determine their structure and mechanical performance. In particular, indentation and tensile tests were performed on whole scales and on the collagen layer alone (after removing the outer mineral layer) to establish the individual function as well as deformation and fracture mechanisms in each layer. Additionally, the local behavior of the collagen was investigated using *in situ* small-angle X-ray scattering (SAXS) studies during uniaxial tensile testing; this behavior was also analyzed using MD techniques to quantitatively predict the controlling damage mechanisms in the inner layer.

3.3.2.1 Characterization of scales

The structure of the scales, as well as failure mechanisms and distribution of damage after mechanical testing, were investigated in an FEI SFEG ultrahigh-resolution scanning electron microscope (SEM; FEI, Hillsboro, OR), Veeco scanning probe microscope (Veeco, Plainview, NY) and an FEI Tecnai 12 transmission electron microscope (TEM) operating at 120 kV. All samples for SEM characterization were sputtered with iridium prior to observation.

3.3.2.2 Penetration and indentation

The penetration resistance of the entire scale including the external layer was examined using an Instron 3367 mechanical testing machine (Instron Corp., Norwich, MA) with a load cell of 30 kN. The scales in fish are in general designed to resist penetration by teeth. In the case of the arapaima scales, this necessity is extreme due to the sharp teeth of their principal predator, the piranha. It was demonstrated by Meyers et al. [159] that the

piranha tooth is unable to penetrate through the scales without being arrested or broken by the highly mineralized external layer of the scale. A piranha tooth was removed from the fish's head and attached to the upper punch in order to indent the entire arapaima scale (through the external layer), which was glued on a synthetic rubber layer with a compressive elastic modulus of ∼10 MPa attached to the lower punch. The low modulus of the rubber simulates the flesh under the scale, which was established by Meyers et al. [159]. The penetration tests were performed at a displacement rate of 10 mm min^{-1}. Indentation of the inner layer (lamellar structure without mineralized surface) was carried out using an indentation load of 1 kgf and a holding time of 10 s using a LECO M-400-H1 (LECO, Joseph, MI) hardness testing machine. Both types of penetration/indentation tests were performed on wet scales (kept in water at 25 °C for 12 h).

3.3.2.3 Tensile behavior

Using a surgical blade, 15 × 2.3 mm tensile samples were cut in two orientations (Figure 3.18) from the scales with thickness of 0.6–1.2 mm. The outer layers of some samples were removed using silicon carbide polishing paper of 180#–2500#, leading to final thickness between 0.6 and 0.8 mm (Figure 3.18b). In order to prevent slippage, the ends of the samples were glued between sand paper sheets using cyanoacrylate glue, resulting in a gauge length of ∼8 mm. Uniaxial tensile tests were carried out on an Instron 3342 mechanical testing machine (Instron Corp., Norwich, MA) with a load cell of 500 N at a strain rate of 10^{-2} s^{-1} immediately following the removal of samples from fresh water, where they were kept prior to testing. The tensile results were expressed in terms of engineering stress–strain curves. The ultimate tensile stress, uniform elongation (strain at

maximum stress) and the toughness, as measured by the area beneath the stress–strain curves, were established.

3.3.2.4 In situ observation under tensile loading

To discern the salient energy absorbing mechanisms during penetration and to visualize the distribution of damage and corresponding resistance to cracking, both rectangular tensile samples and single-edge notched tension (SE(T)) samples, with and without the mineral layer, were prepared in the longitudinal direction with an 8 mm gauge length using the same dimension and procedure as in the prior section. The notch in the SE(T) samples was first cut using a diamond blade and sharpened by polishing with a razor blade irrigated in 1 μm water-based diamond suspension; the resulting micro-notch had a depth of approximately half the specimen width with a consistently sharp root radius of ~5 μm.

Uniaxial tension tests were performed at 25 °C in an environmental Hitachi S-4300SE/N (Hitachi America, Pleasanton, CA) SEM under wet conditions. To minimize any dehydration, the samples were soaked in water for at least 12 h prior to testing. Testing was performed at a displacement rate of 0.5 mm min^{-1} using a Gatan Microtest 2 kN bending stage (Gatan, Abington, UK) inside the SEM; the samples were imaged in electron back-scatter mode under variable low pressure conditions at a vacuum of 35 Pa. Such low pressure is often used for biological materials to limit the effect of dehydration and keep the properties of the material relatively unaltered; however, while the outer surface of the scale generally slightly dehydrates, the interior remains wet until exposed. Due to the excessive deformation during testing, as well as constant and significant relaxation during imaging, a reliable measurement of load and displacement could not be obtained;

consequently, the stress–strain curves, fracture toughness and crack-resistance curves (*R*-curves) could not be measured.

3.3.2.5 Small-angle X-ray scattering

Rectangular samples, 15 × 1 mm in size with ~0.6 mm thickness and gauge length of 10 mm, were sectioned with a razor blade using the same polishing procedure described above. The scales were hydrated in water for 12 h prior to mechanical testing.

The hydrated samples were loaded in uniaxial tension and exposed to X-rays at beamline 7.3.3 at the Advanced Light Source (ALS) synchrotron at the Lawrence Berkeley National Laboratory (Berkeley, CA). The mechanical tests were performed with a custom-made rig using a 10 mm displacement stage and an Omega LC703-10 load cell, calibrated to 45 N, to measure the force; this set-up permits SAXS data collection to be recorded in real time with the simultaneous measurement of the load–displacement curve. The mechanical tests were performed at 25 °C at a displacement rate of 1 μm s^{-1}, on hydrated samples maintained through the use of a hydration cell comprising a strip of cellophane held to the sample through capillary action of a few drops of water.

A Pilatus 1 M detector (Dectris Ltd, Baden, Switzerland), used to collect the SAXS data, was located at the largest allowable distance from the sample (~4 m) to permit detection of the fine changes in the collagen peak positions. The sample was exposed to X-rays for 0.5 s at ~5 s intervals during mechanical testing; exposures were in the less than 20 kGy range, below a level that would adversely degrade the tissue [194]. Further details concerning the data collection and analysis are given in Zimmermann et al. [153].

3.3.2.6 Preparation of TEM specimens

The preparation procedures used for biological specimens involved a number of stages. The arapaima scales were first immersion-fixed in 3% glutaraldehyde in 0.15 M sodium cacodylate buffer (pH 7.4) for 4 h, and then post-fixed using 1% OsO_4 solution with 8% potassium ferrocyanide in 0.15 M sodium cacodylate buffer for 12 h at 4 °C. The scales were subsequently stained with 2% aqueous uranyl acetate for 12 h and dehydrated with an ascending ethanol series (50, 70, 90 and 100%), followed by a 1/1 ratio of 100% ethanol and 100% acetone and finally 100% acetone. Samples were then embedded in Spurr's low viscosity resin and polymerized at 60 °C for 48 h. Samples were subsequently sectioned perpendicular to the scale surface to generate slices 80–200 nm thick using a Leica Ultracut UCT ultramicrotome (Leica, Wetzlar, Germany) and a Diatome diamond knife (Diatome, Hatfield, PA). The sections were post-stained with 1% uranyl acetate for 10 min and Sato lead for 1 min. At this stage they were ready for examination in an FEI Tecnai 12 TEM at 120 kV.

3.3.2.7 Preparation of atomic force microscope specimens

The lamellae with a thickness of ~200 μm were peeled off from the inner layer of arapaima fish scale. The inside peeled surfaces of the lamellae samples were probed in water with a Veeco scanning probe microscope using the SNL-10 Bruker tips (Bruker, Billerica, MA).

3.3.2.8 MD analysis

A MD model, based on a simple elastic network model [113, 114], was used to theoretically investigate the mechanisms of the deformation and delamination in the arapaima scales under uniaxial tension. This model does not take the fibrils as elements but

rather considers the larger collagen fibers to better simulate the response of the lamellae. Based on Lin et al. [110], the initial inter-bead distance is r_0 = 1 μm, which is the same as the average diameter of the collagen fiber d_c. Each collagen fiber is modeled as a series of beads connected by harmonic springs. Since the density of the collagen is 1.34×10^3 kg m^{-3}, the mass of each bead is equal to 1.05×10^{-15} kg. The total deformation energy of the simulation system is given by:

$$U_{total} = U_T + U_B + U_{weak}. \tag{32}$$

As the total energy (U_{total}) is given by the sum over all pair wise (U_T), three-body (U_B) and weak inter-fiber interactions (U_{weak}) where $U_T = \sum_{\text{pair}} \varphi_T(r), U_B = \sum_{\text{triplets}} \varphi_B(\theta)$ and $U_{weak} = \sum_{r<r_{\text{cutoff}}} \varphi_{weak}(r)$ with $\varphi_T(r)$ as the energy of inter-bead spring in tension, $\varphi_B(\theta)$ as the energy of angular spring in bending and interaction energy of inter-fiber beads. Here $\varphi_T(r) = K(r - r_0)^2$ is the energy of each inter-bead spring in tension, where K is the stiffness of the springs is assigned according to $K = EA/2r_0$ (estimated value of the Young's modulus of collagen fiber, E = 2 GPa) and $A = \pi d^2/4$ is the cross-section area of the collagen fiber. An angular spring between two neighboring springs is used to define the bending stiffness of the collagen fiber, and its energy is given by $\varphi_B(\theta) = K_B(\theta - \pi)^2$, where the bending stiffness of the thread is given by:

$$K_B = EI_t / (2r_0) = E\pi d_c^4 / (128 r_0), \tag{33}$$

where I_t is the area moment of inertia of the cross-section. The inter-fiber interaction is denoted by:

$$\varphi_{weak}(r) = 4U\left[(\sigma / r)^{12} - (\sigma / r)^6\right], \tag{34}$$

where U is the interaction energy between two inter-fiber beads that is given by $U = d_c r_0 \gamma$ as γ is the surface energy of the collagen fibers, and $\sigma = d_c / \sqrt[6]{2}$ decides the equilibrium distance between two neighboring collagen fibers, which equals d for this selection. To ensure that the collagen fibers only interact with their nearest neighbors, the cutoff of the interaction is set as $r_{cutoff} = 1.5 d_c$.

The model of the arapaima scale is composed of multiple layers of parallel collagen fibers [110] making specific angles which were found to vary from 35° to 85°. Considering that the mean angle between two neighboring lamellae is ~60°, it suffices to model three lamellae with 60° (one centrally sandwiched between two lamellae) to capture the most important events. For simplicity, each lamella is modeled by three layers of collagen fibers that initially align in the same direction; the thickness of each lamella is ~3 μm. This is much lower than the actual lamellar thickness, ~50 μm, but sufficient to capture the essential phenomena since we also include the periodic boundary conditions in the direction perpendicular to the lamellae.

We applied a uniaxial tensile strain to deform the entire multi-lamellar film in a quasi-static way. For every deformation increment, we applied a uniaxial strain of 0.004 to the model, fixed the single layer of beads at the two ends of the lamellae along the pulling direction and carried out energy minimization and equilibrium for 20,000 integration steps. We recorded the total force applied to the beads at the boundaries and obtained the stress–strain curve of the material during deformation. We also monitored the deformation of all the collagen fibers during the entire loading process. This model enabled a systematic investigation of how different mechanical and geometric characteristics of the arapaima

scale influence its response to loading, e.g. the angle between two lamellae, the inter-fiber interaction strength and the stiffness of a single collagen fiber.

3.3.3 Results

3.3.3.1 Structural Characterization

The cross-sectional structure of the entire arapaima scale is shown in Figure 3.18c. Three parameters can be used to describe the geometrical characteristics of scales [195]: aspect ratio (= total length/thickness), degree of imbrication (=exposed length/total length) and the angle of scales with the surface plane. The (elasmoid) scales of this fish have an aspect ratio of ∼50 and a degree of imbrication of 0.4 (Figure 3.18a-b). They consist of hydroxyapatite and type I collagen arranged in two distinct layers: a rough, highly mineralized, outer layer and a poorly mineralized collagen inner layer (Figure 3.18c). Our group [110] performed Fourier transform infrared spectroscopy, which showed several strong absorption peaks, similar to previous studies [150, 189]. The absorption peaks at 1637, 1546 and 1239 cm^{-1} are the three characteristic peaks which correspond to amide I, amide II and amide III of type I collagen, respectively. Lin et al. [110] present a table comparing the peaks. There are also peaks at around 1000 cm^{-1}, which represent the phosphate groups at 872 cm^{-1}, peaks at 1401 and 1450 cm^{-1} correspond to carbonate anions. Within the inner layer, the fibrils align parallel within layers called lamellae that have a characteristic thickness of 50–60 μm [110, 150]. Neighboring lamellae are rotated to form a twisted plywood structure similar to that proposed by *Bouligand* [196]; we refer to this as the *Bouligand*-type structure (Figure 3.18d). Figure 3.18e shows the extremity of a specimen that was stretched until complete failure (strain ∼0.3); the arrangement of the different orientations of collagen fibrils in the *Bouligand*-type structure is clear. Collagen

lamellae are labeled from the outside to the inside as A to E. It is apparent that the angles between the fibrils of adjacent lamellae are not equal, as would be the case for the classical *Bouligand* structure. Using the nomenclature defined in Figure 3.18e, these angles are: $\alpha_1 = 87°$, $\alpha_2 = -35°$, $\alpha_3 = -70°$, $\alpha_4 = 67°$, i.e. displaying an irregular orientation which varies from lamella to lamella.

The properties of the scales are highly dependent on the level of hydration [110], due to the effect of water molecules on the bonding between fibrils, as computed by Gautieri et al. [34]. The calculated density of collagen decreases from 1.34 to 1.19 g cm^{-3} with hydration and is accompanied by a decrease in the Young's modulus from 3.26 to 0.6 GPa.

Figure 3.19 shows the individual collagen fibrils imaged by TEM and atomic force microscopy (AFM). The fibrils imaged in Figure 3.19a are not equiaxed because the foil plane is not exactly perpendicular to the fibril axis. The fibrils, initially cylindrical, become faceted because of the necessity of tight stacking and the lamellar orientation. In Figure 3.19b two fibril orientations from two adjacent lamellae are imaged. The fibrils in the left image are close to perpendicular to the foil plane; the ones in the right image are close to parallel. The interface between lamellae with different orientations is abrupt, i.e. there is no gradual transition stage. The fibrils are cylindrical and arranged in the most compact fashion. The surfaces at which adjacent fibrils touch are somewhat flattened, enabling a tighter stacking. The apparent period in the collagen fibrils measured in the TEM micrograph of Figure 3.19b is ~50 nm. The banding consists of three white radial lines, due to the fact that the foil thickness (60–200 nm) can exceed the fibril diameter. Thus, two or three fibrils may simultaneously be imaged, creating the unusual pattern. The *d* period

of the collagen in the right side of Figure 3.19b is less than the expected value of 67 nm. This indicates that this lamella is not parallel to the foil plane but at an angle. Assuming a *d* period of 67 nm, one obtains an angle between the fibril and the foil of 42°. Assuming that the fibrils on the left are perpendicular to the foil axis, the angle between the two lamellae is (90–42) = 48°, confirming that the angles between adjacent lamellae vary.

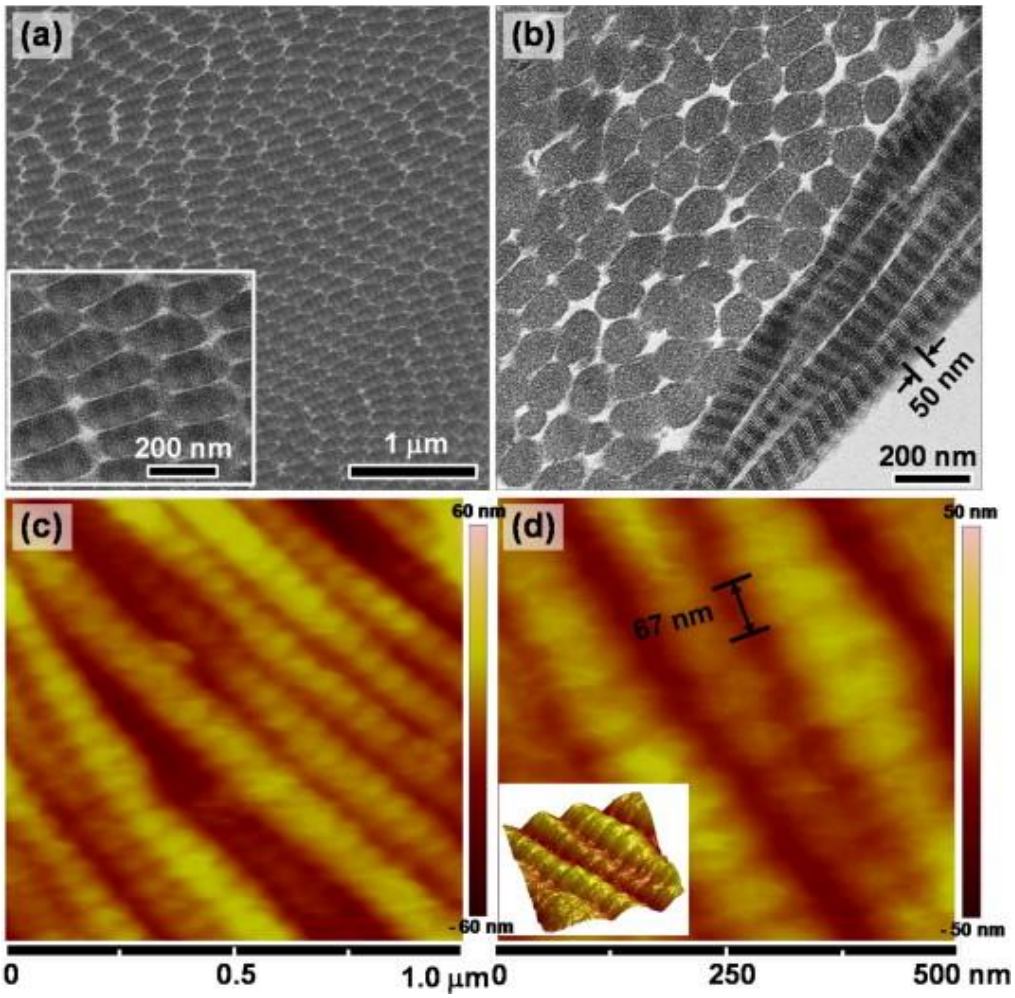

Figure 3.19: Characterization of collagen by (a-b) TEM and (c-d) AFM. (a) TEM image of the foil plane inclined to fibril axis; the smallest dimension of the fibrils is ~100 nm. (b) Two orientations of fibrils are shown: on the right-hand side the fibrils are inclined to the foil plane showing *d* bands of 50 nm (projected value of 67 nm), on the left-hand side the fibrils are close to being perpendicular to the foil. Note the regular fibril diameter, ~100 nm. (c) AFM of parallel fibrils. (d) Higher magnification AFM showing 67 nm *d* bands and tridimensional rendition of fibrils in the insert.

AFM corroborates the TEM characterization and provides additional detail (Figure 3.19c-d). Since the fibrils were peeled from the scale and the AFM tip provides an accurate representation of the surface, the *d* banding observed is the actual value of 67 nm. This is shown clearly in Figure 3.19d. The three-dimensional rendition in the lower left hand corner of Figure 3.19d shows that the fibrils are indeed cylindrical.

3.3.3.2 Protective function of the entire scale against penetration

The penetration of the scale by a piranha tooth (Figure 3.20a-b) is severely hampered by the mineral layer, amounting to a ~1 mm deep indentation into the scale under a 1 kgf load applied for 10 min, with relatively minimal damage around the indent (shown in Figure 3.20a). The surroundings of the indent were damaged more seriously due to the severity of load concentration and serrations on the edge of the teeth (shown by the detail in Figure 3.20a). Two orientations of collagen fibrils were exposed at the wall of the indent (circular line in Figure 3.20a) as the external layer became damaged (Figure 3.20b); the fibrils are delaminated, fractured and change orientation (Figure 3.20b); these processes permit the internal collagen layer to dissipate energy during penetration.

Figure 3.20c-d shows the damage from penetration of a microindenter in the collagen layer (without the mineral layer). In the vacuum of the SEM, the collagen layer dries and shrinks, and separation between collagen fibers becomes evident, which is not characteristic of the intact, water-saturated scale. Nevertheless, the damage mechanisms around the indentation can still be clearly seen. Different orientations of collagen fibers are observed at different levels. The potential indentation region is marked by the dashed square in Figure 3.20c. Collagen fibers are bent and fractured through the action of the indenter, but the overall effect of the different lamellar layers is to localize damage to the

immediate vicinity of the indenter, without propagation throughout the scale. The failure of the collagen fibers is preceded by deflection, stretching and necking, characteristic of significant inelastic deformation prior to failure (Figure 3.20d). As a result, crack initiation and propagation are avoided.

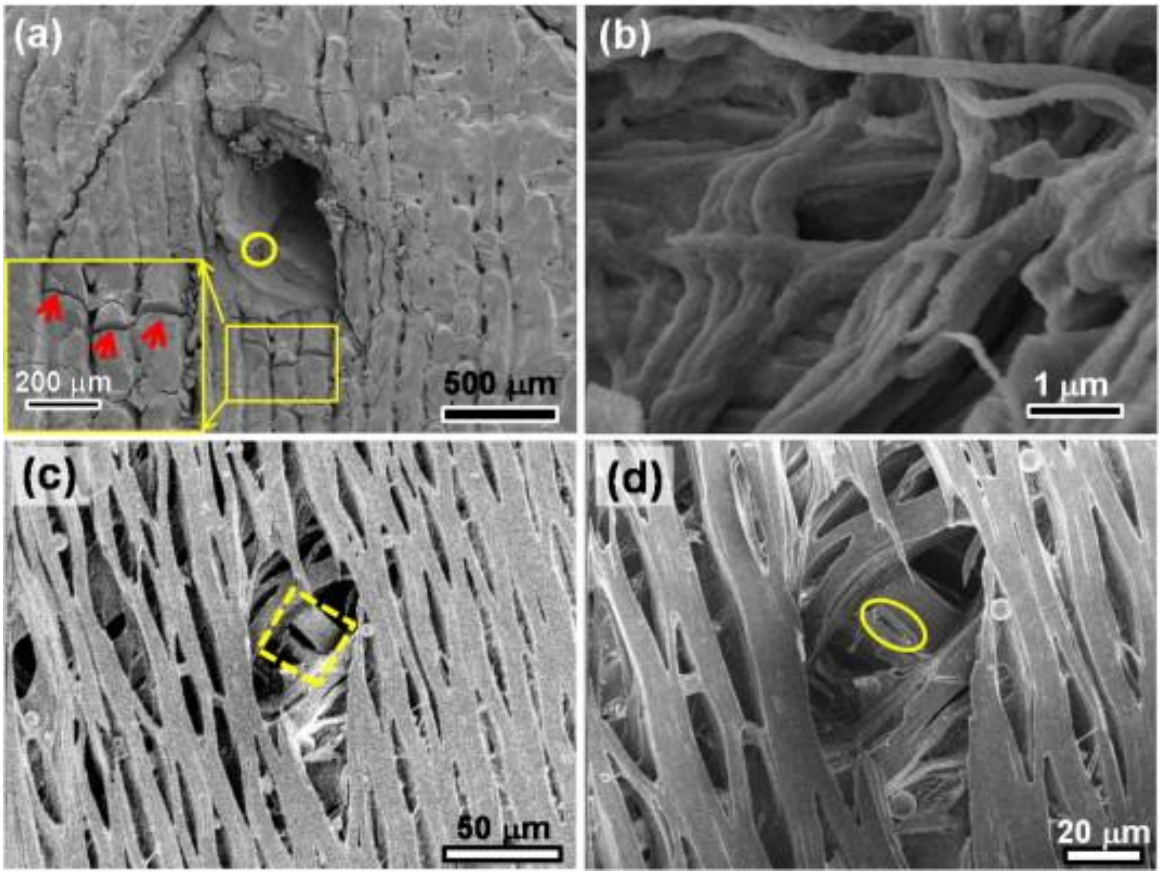

Figure 3.20: Penetration of the arapaima scale by a piranha tooth and microhardness indenter. (a-b) Penetration of the scale by a piranha tooth from the outer layer towards the inner layer. (a) Entire penetration indent of the scale; cracks were deflected and arrested at orthogonal cracks caused by fracture of the mineral (red arrows), with more serious damage at the corner of the penetration. (b) Collagen fibrils exposed from the damage of the mineral observed from the circled region in (a). (c-d) Penetration of collagen layers by a microhardness indenter; the original indentation is shown by the dashed square; the fibers are displaced but the gaps on the samples are due to dehydration in the vacuum of the SEM, the ellipse in (d) is the region that was produced by the indenter tip.

3.3.3.3 Tensile mechanical behavior of scales

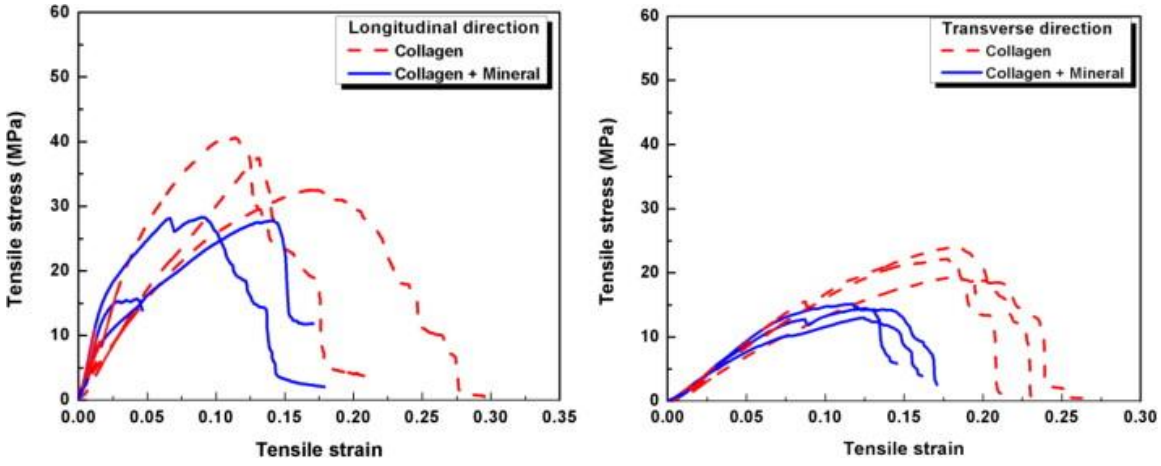

Figure 3.21: Uniaxial tensile stress–strain curves of the scales (solid lines) and of the collagen layers with mineral removed (dashed lines). Tests were performed at a strain rate of 10^{-2} s^{-1} in the (a) longitudinal and (b) transverse directions, as defined in Figure 3.18.

Figure 3.21 shows the uniaxial tensile response of the entire scales and the collagenous lamellar layer (after removal of the external mineralized layer) in the longitudinal and transverse orientations defined in Figure 3.18b. Three specimens were tested in each condition. Additionally, the tensile response of the collagenous lamellar layer, including the load–time curve and the behavior of collagen fibrils in different lamellae, was also determined in the SAXS tests, as discussed in the results section. Based on these tests, the following results can be deduced (deformation mechanisms are discussed in the results section):

a. The strength of the scales is ~50% higher in the longitudinal than in the transverse orientation, indicating that the lamellae are not distributed to produce in-plane isotropy. Contrary to our results, Zhu et al.'s [149] measurements on striped bass show that specimens with an orientation of 45° or 90° to the longitudinal axis of the fish have higher strengths (~60 MPa) than the 0° orientation (~40 MPa). This shows that in-plane anisotropy exists in both the cycloid and ctenoid scales. The

strength of the scales including the mineralized layer in the longitudinal direction (23.6 MPa) is considerably higher than in the transverse direction (14.2 MPa) shown by Table 3.1.

Table 3.1: Uniaxial tensile testing results for the entire scale and for the collagen layer, loaded in the longitudinal and transverse orientations.

	Longitudinal orientation		Transverse orientation	
Tested part of scale	Collagen layer	Entire scale	Collagen layer	Entire scale
Young's modulus (GPa)	0.86 ± 0.32	0.47 ± 0.25	0.21 ± 0.02	0.21 ± 0.03
Ultimate tensile stress (MPa)	23.6 ± 7.2	36.9 ± 7.4	14.2 ± 1.1	21.8 ± 2.4
Engineering strain at maximum stress	0.08 ± 0.07	0.14 ± 0.06	0.12 ± 0.01	0.18 ± 0.01
Energy dissipation (MPa)	1.47 ± 1.08	3.12 ± 0.98	1.07 ± 0.08	2.53 ± 0.40

b. Removal of the external and highly mineralized outer layer increases the tensile strength of the scale. Although this appears to be counterintuitive, it results from several factors. Most importantly, the external layer is designed for compressive strength; being highly mineralized it is brittle and weak in tension. This is consistent with the SEM images in Figure 3.22a-b, which show the tension samples in the transverse orientation after failure; the external layer fractures in a brittle manner either through the attack of a piranha or other circumstances, leading to tensile stresses in that layer (Figure 3.22a: mineralized layer is labeled 1 and has a thickness of ~280 μm). Such a fractured layer cannot carry any load, which leads to a decreased strength of the entire scale resulting from the increased cross-section compared to the collagen-only samples. Additionally, due to failure of the outer mineral layer, there is very likely significant damage evolution in the form of delamination and separation of fibers in adjacent lamellae prior to failure of the entire scale (Figure 3.22c). Figure 3.22a shows five lamellae, marked by the

numbers 1–5 (thickness 50–60 μm), throughout the thickness of the scale; the lamellae close to the mineral layer might be hindered in their ability to rotate upon tensile loading, which could reduce the strength of the collagen layer. The function of the mineralized layer can be rationalized through a comparison with modern armor, which consists of a hard face supported by a tougher foundation. The hard layer operates under compression and therefore resists projectile penetration, whereas the backing, being tougher and more flexible, ensures the integrity of the structure.

c. The tensile behavior of the collagen layers was examined in the wet condition; the solid plots in Figure 3.21 represent the tensile stress–strain curves of these collagen layers. It is interesting to note that the collagen layers in the transverse orientation have the same modulus as the scale, but a larger strain at failure, suggesting that when the scale is dried and bent in this orientation, cracks are not easily generated. Figure 3.21 shows the tensile properties of the scale in the two orientations (longitudinal and transverse). As noted above, the collagen-only samples have a higher strength and display higher uniform strain and energy dissipation (as measured by the area under the stress–strain curves) than the complete scale samples.

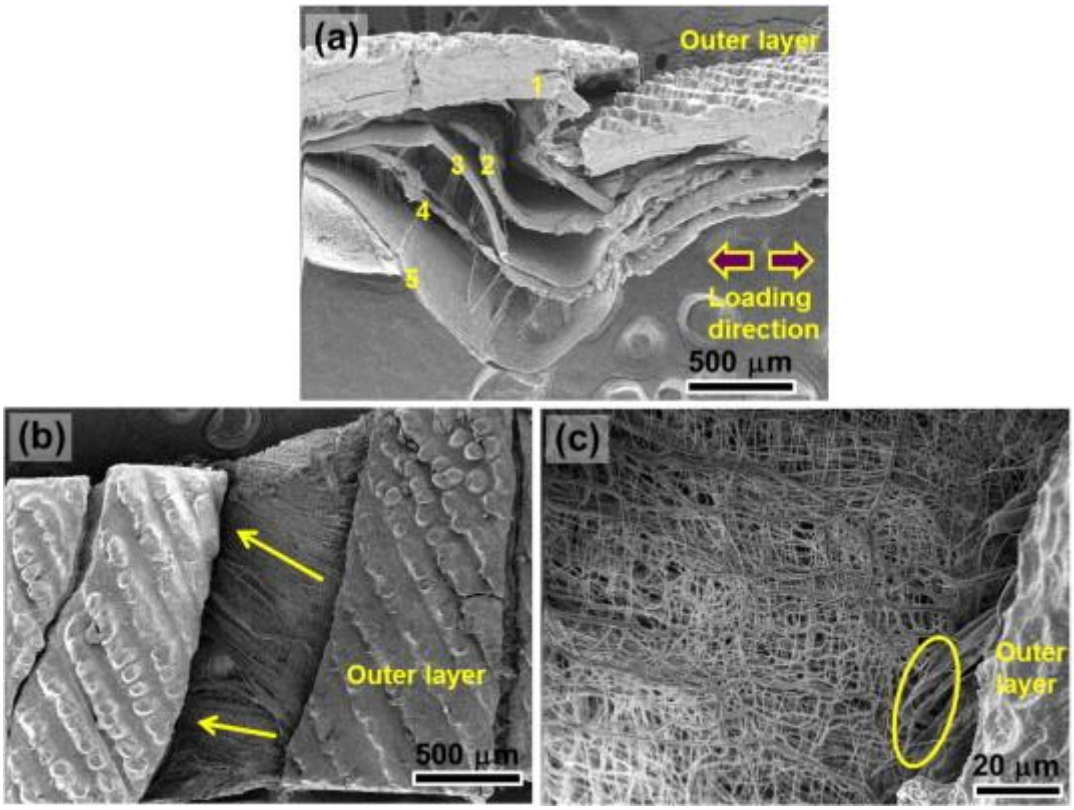

Figure 3.22: SEM images of tested tensile samples. (a) Side of a tensile sample of the scale after mineral failure, five lamellae were delaminated from each other labeled from 1 to 5; (b) the top view of the tensile sample shows the mineral domains separated and the collagen exposed (the arrows show two orientations); (c) fractured collagen fibrils, some of which are close to the mineral layer (shown by the ellipse); the collagen fibrils beneath are delaminated and separated.

3.3.3.4 Tensile behavior of the scale in notched and unnotched specimens

Figure 3.23 shows crack propagation in a specimen in which the highly mineralized external layer was removed, i.e. exclusively in the lamellar structure of the collagen. A crack starting from the root of the notch is forced to grow under the action of tensile forces with a direction marked in Figure 3.23a. At the onset of crack propagation, collagen fibers in different orientations are exposed and show different damage mechanisms (Figure 3.23b-c). The top lamella (labeled 1), with an orientation of the collagen fibrils perpendicular to the loading direction, undergoes separation by splitting. The fibers in the other underlying orientations (labeled 2, 3 and 4) are more closely aligned to the loading

direction and are stretched and rotated. The fibrils (labeled 2) close to the split lamella (labeled 1) fracture; however, some lamellae (labeled 3 and 4) are only stretched and rotated (Figure 3.23c-d). Some collagen fibrils are bent (arrow in Figure 3.23d) by the loading and then relaxed and curved back after unloading or fracture (dashed square). The full range of failure mechanisms, specifically delamination, tensile failure, rotation and bending of fibrils, is shown in Figure 3.23e. Due to the high flexibility of the collagen lamellae and excessive failure distribution upon tensile loading tests, samples showed large crack-tip openings but negligible crack propagation. Failure mechanisms of samples with a highly mineralized external layer occurred in a comparable manner to samples without an outer layer and are hence not shown individually. Figure 3.23e-f shows the progression of damage without any appreciable increase in the crack length.

The individual deformation process and mechanism occurring in a tensile test from an unnotched sample are additionally shown in Figure 3.23g and Figure 3.24 using the SAXS method. The splitting of the individual layers, their rotation and separation as well as curling of fractured fibrils can be also seen. This demonstrates that the processes of fibrillar rotation, stretching, delamination and reorientation occur in the entire specimen being subjected to deformation.

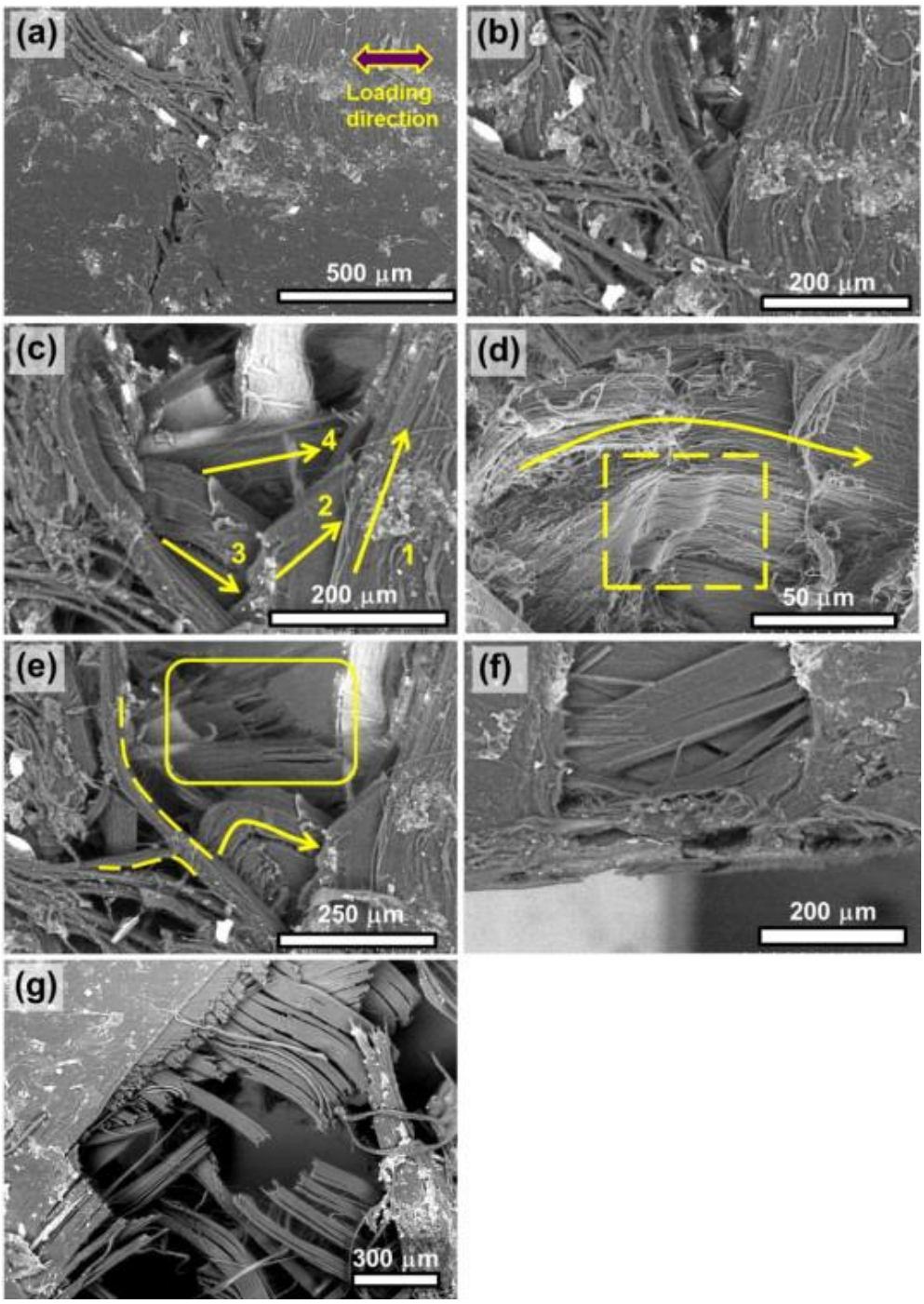

Figure 3.23: Damage propagation in the collagen layers containing a notch. (a) Initial configuration at the onset of loading (the notch is in the center of the image with the notch root pointing towards the bottom); (b) the collagen fibrils separate when the samples are being loaded; (c) four orientations of lamellae are being exposed (shown by the individual arrows); (d) the collagen fibrils bend and stretch as shown by the arrow, some of the collagen fibrils were relaxed when the test stopped; (e) the lamellae and collagen fibrils bend (arrow), delaminate (dashed lines) and fracture (square); (f) continued loading characterized by sliding of the lamellae indicating the absence of significant crack propagation; (g) damage in unnotched specimen tested under the same configuration up to failure.

3.3.3.5 SAXS, diffraction and mechanisms of collagen reorientation

Synchrotron radiation has been used previously to measure the reorientation and elastic stretching of collagen in bone and human aorta [197-199]. The current results for *Arapaima gigas* confirm the previous analyses but importantly introduce another element: the organized reorientation of the lamellae of parallel collagen fibrils, a process that is significantly different from that in other biological systems and which results from the *Bouligand*-like structure.

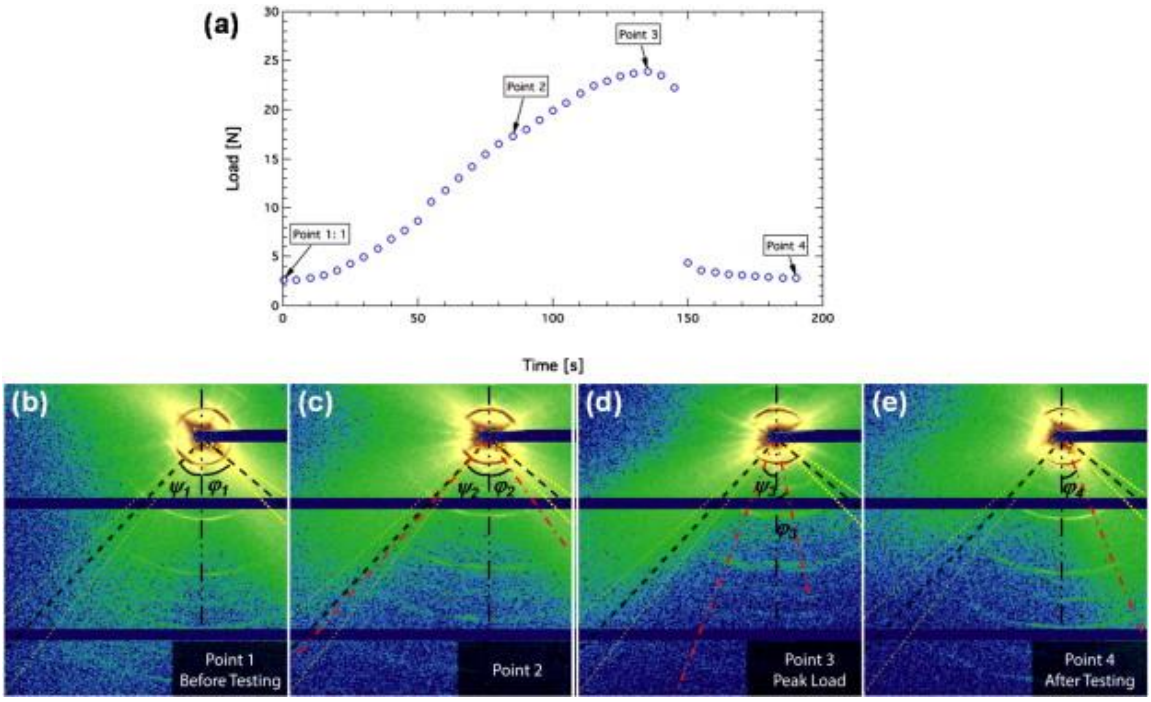

Figure 3.24: SAXS results of arapaima collagen layer under tensile load. (a) Tensile load–time plot, SAXS images were taken at four points: (b) before testing, (c) during testing, (d) at the peak load, (e) after testing. Note that the black dashed line shows the average angle (orientation) of the lamellae in scale before tests, the red short dash–dot line shows the average angle (orientation) of the lamellae during the *in situ* tension tests, orientation change of the lamellae can be observed easily from the difference between black dashed line and red short dash–dot lines in the individual (c–e).

SAXS tests were performed on the inner collagen layer to reveal and quantify the mechanisms of collagen lamellae deformation and reorientation during tensile straining, which are essential to the understanding of the resistance of the scale to external loading.

The procedures and detailed results are described by Zimmermann et al. [153]; only the principal mechanisms are introduced here to highlight the modes of deformation. The uniaxial load–extension curves on the collagen layer, taken during the SAXS experiment, show an approximately linear response, in agreement with the tensile results of Figure 3.21. As the lamellae within the scale's inner collagen layer have a *Bouligand*-type structure, each lamella will have a distinct orientation that is visible in the two-dimensional X-ray diffraction pattern. Thus, the strain and orientation of the collagen fibers in each lamella can be measured during tensile deformation; the reorientation is clearly visible through the change in the orientation of the arcs with respect to the tensile axis and the strain can be measured by the change in the arc's radial position with respect to the beam center. Four points are marked in the tensile load-time plot (Figure 3.24a) measured where SAXS observations were recorded (Figure 3.24b and e, respectively), corresponding to points 1–4: before testing (point 1), during testing (point 2), at the peak load (point 3) and after testing (point 4). In the SAXS images, as the collagen fibrils rotate, the angle of the arcs on the SAXS spectra changes; the dash–two dots lines show the tensile loading direction, the dashed lines show the original orientations of collagen fibrils before testing and the dash–dot lines show the changed orientations of collagen fibrils after the testing starts.

Before testing, two main orientations of collagen make angles of $\psi_1 = 43°$ and $\varphi_1 = 49°$ to the tensile loading direction (Figure 3.24b). During tensile testing, the collagen fibrils rotate towards the tensile direction (Figure 3.24c) such that $\psi_2 = 41°$ and $\varphi_2 = 35°$. At the peak load, the two fibril orientations rotate closer to the tensile direction: $\psi_3 = 21°$ and $\varphi_3 = 12°$. At this point, the SAXS patterns (arcs) of collagen fibrils in two orientations almost meet each other (Figure 3.24d). After sample failure (Figure 3.24e), one orientation

of collagen fibrils releases back to a larger angle (φ_4 = 22°), whereas the other fibril orientation can no longer be seen, which implies possible fracture.

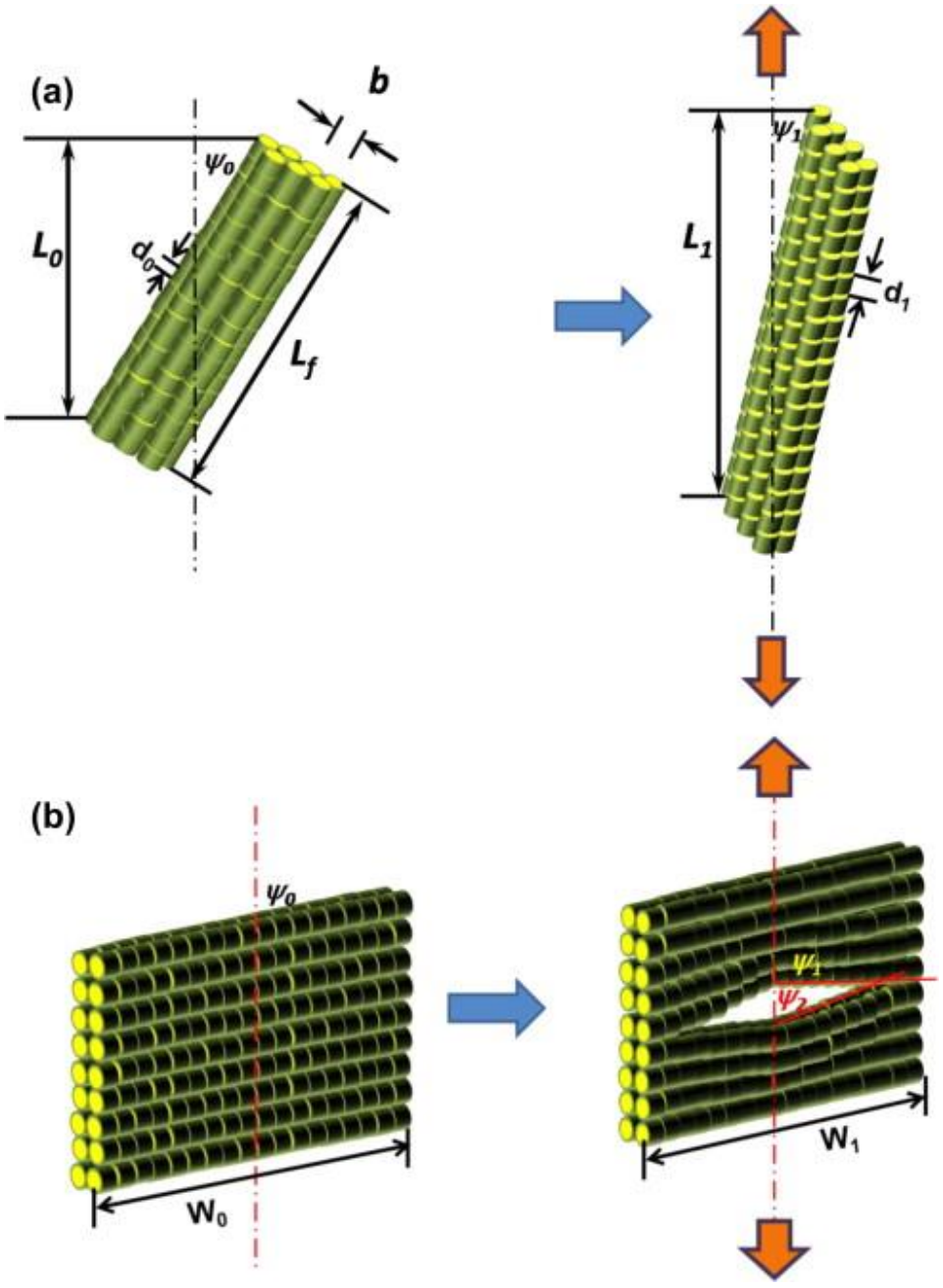

Figure 3.25: Mechanisms of collagen fibril deformation under tensile load. (a) Rotation through interfibrillar shear and elastic stretching of collagen fibrils. Fibril stretching and interfibrillar sliding decrease the angle between the fibrils and the loading direction from ψ_0 to ψ_1. The initial d period along the fibrils is equal to d_0; after extension, this d period increases to d_1 as the overall length increases from L_0 to L_1. (b) The tensile opening of interfibrillar gaps acts to change the angle, at the extremities of the fibrils, fromψ_0 to ψ_1 and ψ_2; note the change in width from W_0 to W_1 that can cause Poisson contraction (adapted from [153]).

Such rotations of collagen fibrils both towards and away from the loading direction observed in the *in situ* SAXS experiments can be attributed to two principal mechanisms, as follows.

a. Collagen fibril rotation towards tensile loading through interfibrillar shear and elastic stretching (Figure 3.25a): when a bundle of collagen fibrils aligned in the same orientation rotate towards the tensile direction, the interfibrillar hydrogen bonds break so that the collagen fibrils can experience shear strain. Figure 3.25a shows the collagen fibrils rotating toward the tensile direction ($\psi_1 \leqslant \psi_0$), as well as their elastic stretching, leading to a tensile strain $\varepsilon = (L_1 - L_0)/L_0$, where L_0 is the initial projected fibril length, L_1 is its stretched length projected in the tensile direction and d_0 and d_1 are the spacing characteristics of collagen fibrils (*d* period) before and after stretching, respectively.

b. Orientation of collagen fibrils change due to formation of an interfibrillar gap (Figure 3.25b): when a lamella with collagen fibrils makes a large angle with the loading direction, the fibrils can separate, allowing a gap to open up; thus, regions with two new orientations of collagen fibrils are generated with one at a larger angle ($\psi_1 > \psi_0$) and another at a smaller angle to the loading direction ($\psi_2 < \psi_0$). In addition to the above mechanisms, Zimmermann et al. [153] consider "sympathetic" fibril rotation, which can rotate the fibrils toward the tensile axis.

In summary, for collagen fibrils aligning at a small angle to the tensile direction, fibril rotation can easily occur towards the loading direction, whereas for fibrils at a larger angle this rotation is far more difficult. Both rotation toward and away from the tensile axis can be induced.

The rotation of the lamellae toward the tensile axis can be calculated as a function of the total applied tensile strain when the initial angle ψ_0 is small. Two components of strain are considered. The total strain is obtained from the elastic stretching of fibrils (ε_{el}) associated with the increase in *d*-period of collagen and from the fibril rotation (ε_r) that is the result of interfibrillar shear:

$$\varepsilon_t = \varepsilon_r + \varepsilon_{el}. \tag{35}$$

The strain due to the rotation of the fibrils (involving interfibrillar shear and ignoring the fibrillar stretching) is directly obtained from Figure 3.25a; it is equal to:

$$\varepsilon_r = \frac{L_1 - L_0}{L_0} = \frac{\cos\psi_1}{\cos\psi_0} - 1 \tag{36}$$

The elastic strain, shown by the increase in the *d* period from d_0 to d_1 ($d_1 > d_0$), also has to be expressed in the tensile direction, considering the fibril length L_f and its initial and deformed values, L_{f0} and L_{f1}:

$$\varepsilon_{el} = \frac{L_{f1}\cos\psi_1 - L_{f0}\cos\psi_0}{L_{f0}\cos\psi_0} = \frac{L_{f1}\cos\psi_1}{L_{f0}\cos\psi_0} - 1 \tag{37}$$

The elastic stretching of the collagen fibers follows the linear equation, where E_f is the elastic modulus of the fibrils, estimated to be 2 GPa by Gautieri et al. [34]. Thus:

$$\frac{L_{f1} - L_{f0}}{L_{f0}} = \frac{\sigma}{E_f}. \tag{38}$$

Substituting Equation 38 into Equation 37 and this result with Equation 36 into Equation 41 gives the strain in the collagen fibrils:

$$\varepsilon_t = \frac{\cos\psi_1}{\cos\psi_0}\left(2 + \frac{\sigma}{E_f}\right) - 2. \tag{39}$$

The constitutive behavior for an assembly of collagen lamellae has been expressed, as a function of strain rate, though a viscoelastic relationship [110]. The one commonly used for biological materials is called the Ramberg–Osgood equation [200]; it was originally developed for metals but its use in the viscoelastic response of bone is well recognized [201]. It describes the strain-rate sensitivity *m* of the elastic modulus *E* (which is expressed as σ/ε):

$$\frac{\sigma}{\varepsilon_f} = C\left(\frac{\dot{\varepsilon}}{\dot{\varepsilon}_0}\right)^m, \tag{40}$$

where *C* is an experimentally measured parameter, $\dot{\varepsilon}$ is the strain rate and $\dot{\varepsilon}_0$ is a normalization parameter, which we can assume to be equal to 1 s^{-1}. Indeed, Lin et al. [110] demonstrated that the arapaima's collagen exhibits a high value of $m \sim 0.26$, with the constant $C = 1.5$ GPa. Substituting Equation 40 into Equation 39, we obtain:

$$\varepsilon_t = \frac{\cos\psi_1}{\cos\psi_0}\left[2 + C\left(\frac{\dot{\varepsilon}}{\dot{\varepsilon}_0}\right)^m \frac{\varepsilon_t}{E_f}\right] - 2, \tag{41}$$

which is expressed in a format of the changing orientation of the collagen fibrils similar to that used by Zimmermann et al. [153], gives:

$$\psi_1 - \psi_0 = \arccos\left[\frac{\cos\psi_0(\varepsilon+2)}{2 + C\left(\frac{\dot{\varepsilon}}{\dot{\varepsilon}_0}\right)^m \frac{\varepsilon_t}{E_f}}\right] - \psi_0. \tag{42}$$

Figure 3.26a shows the change in collagen orientation given by Equation 42 vs. the total strain in the range $\varepsilon \sim 0$–0.12. The strain rate used in Equation 42 was 10^{-4} s^{-1} to

match the experimental SAXS results. These values are plotted for different initial values of ψ_0: 5°, 10°, 20°, 45° and 70°. It can be seen that the fibrils rotate toward the tensile axis for all cases and that rotation stops once the rotation angle reaches the original misorientation angle. When all the collagen fibrils align towards the loading direction (ψ_0 = 0°), there is no strain contributed by the rotation of collagen fibrils. For small angles ψ_0, the rotation is more pronounced. The fibrils originally at an angle between 31° and 90° have no chance to rotate towards the tensile axis and either do not change orientation or rotate away.

The results of the SAXS experiments are given in angular ranges: 0–14°, 15–30°, 31–60° and 61–90°. During tensile testing, we can observe collagen fibrils rotating both towards (positive $\Delta\psi$) and away from (negative $\Delta\psi$) the tensile direction (Figure 3.26b). The positive values and the rates of rotation are well described by the above analysis.

Negative values of $\Delta\psi$ (rotation away from tensile direction) require mechanisms not incorporated into the analysis. Three principal mechanisms can be considered: the splitting of lamellae creates regions of separation, causing changes in the angle ψ of the lamellae to the tensile direction, as shown schematically in Figure 3.25b (the changes in the angle can be both positive and negative); sympathetic rotation through which a layer is sandwiched between two layers which "drag" it and force it to rotate away from the tensile direction; and contraction by Poisson's ratio effects, leading to rotation. In summary, the analysis predicts the positive $\Delta\psi$ rotations (rotation towards the tensile direction) fairly well. It should be noticed that the analysis uses independent values; no parameters extracted from the SAXS experiments were employed.

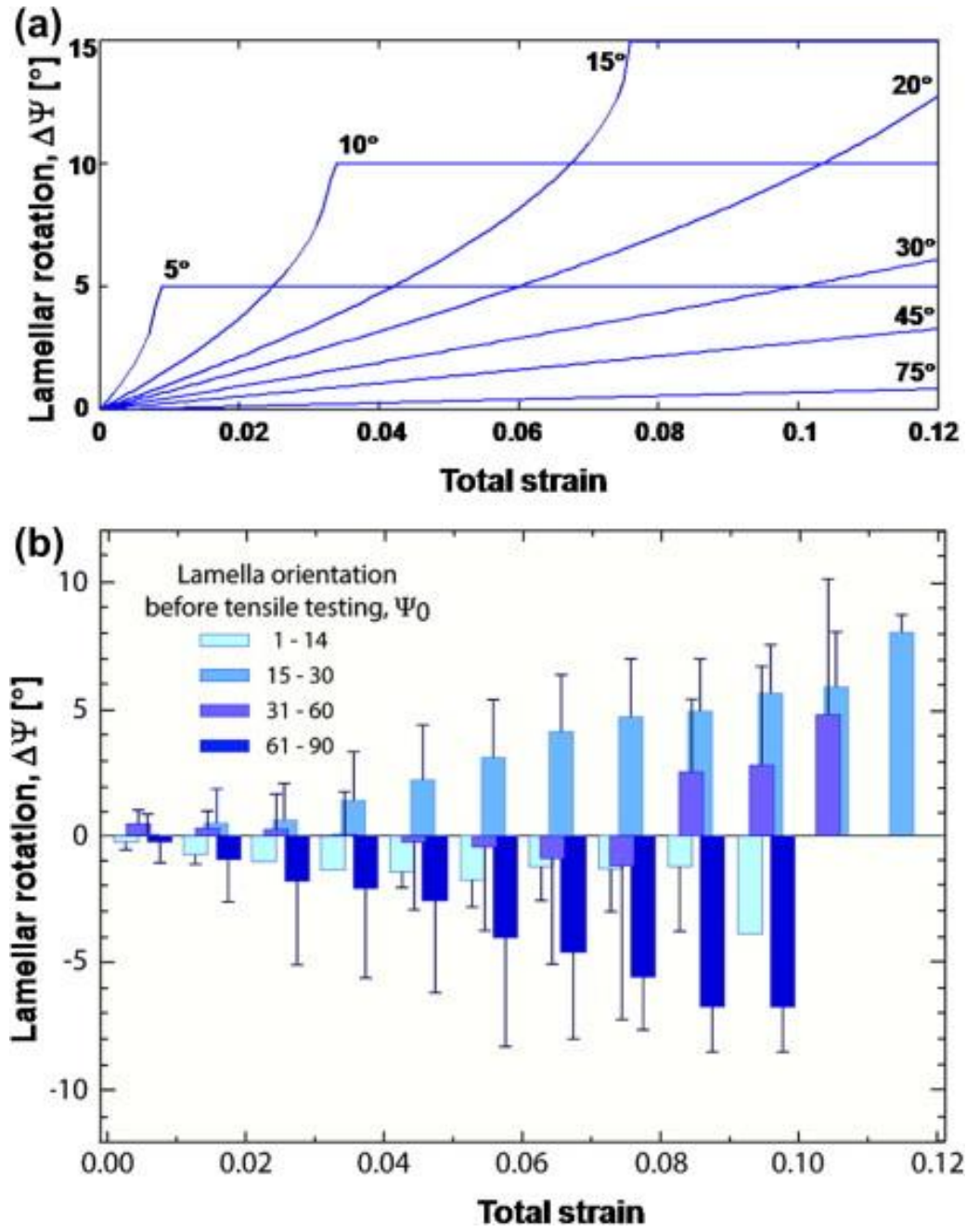

Figure 3.26: Nature of the rotation and deformation of the lamellae during tensile loading of the scales. Positive values of the angle $\Delta\psi$ represent rotation of fibrils toward tensile axis and negative values rotation away from tensile axis. (a) Changes in the angles of collagen fibrils with the tensile axis are shown from analytical calculations. Note that when $\Delta\psi$ reaches the value of the initial angle ψ_0, the rotation stops because the alignment with the tensile axis is reached (at strains ~0.01 for 5° and 0.035 for 10°). (b) Changes in the angles of collagen fibrils with respect to the tensile axis measured from small-angle X-ray diffraction patterns; the latter were taken from Ref. [153].

3.3.3.6 MD calculations on collagen layers in tension

In order to confirm the rotation of the lamellae and individual fibrils observed by SAXS and *in situ* SEM tensile experiments, the process was modeled at the fiber level. MD calculations of the tensile deformation of the collagen layer with three orientations of collagen lamellae (42°, 78° and 18°) were performed to model the mechanisms of deformation. Periodic conditions are applied to the out-of-plane direction and thus each collagen lamella is sandwiched between two other lamellae with a 60° angle with each of them. This configuration is built according to the experimental observations as the angle between two neighboring lamellas is measured to vary between 35° and 85°[110]. An earlier study had reported ~60° but this was an oversimplification [159]. We use this model and apply uniaxial tensile force by fixing a single layer of coarse-grained beads at each edge of the pulling direction and controlling their displacement quasi-statically, as detailed in the methods section (Figure 3.27a). The Young's modulus used to model the collagen fiber is 2 GPa, which is an average estimate from collagen microfibrils from both computational and experimental approaches [34]. It is noted that the inter-fiber interaction energy depends on surface chemistry (in terms of protein sequence and mineral composition), degree of hydration and roughness, and it is difficult to directly measure this experimentally. However, we are able to model this interaction by referring to the results of full atomistic simulations. We model the inter-fiber interaction by using the surface energy of tropocollagen molecules, which is measured to have a range from 0.05 to 3 J m^{-2} in simulations with different constraints [202].

Using the present model, we obtain multiple stress–strain curves by using different surface energies, as shown in Figure 3.27b. These calculated curves have a typical saw

tooth shape, with the stress first increasing linearly with the increasing strain at small deformation followed by significant stress drops before increasing again. The peak stress before the drop region depends on the surface energy; as the surface energy increases, the stress increases, because the bonding between adjacent collagen microfibrils increases. In Figure 3.27b, it can be seen that the peak stress increases to over 100 MPa when surface energies are increased to 10 J m^{-2}. For 1 J m^{-2}, the peak stress is equal to 26.4 MPa, which is close to the magnitude of the experimental peak stress of fish scales, as shown in Figure 3.21. We therefore use this surface energy to model the inter-fiber interaction. By comparing the simulation snapshots shown in Figure 3.27c, we find that during the linear and yielding region, all the collagen fibers in the model retain the orientation of the initial configuration and the deformation strain is homogenously distributed in the fibers. The first stress drop corresponds to the appearance of collagen delamination within the material; this is an important mechanism for releasing the deformation energy stored in fibers, since it creates microcracks along the fibers. For smaller surface energies (e.g. 0.1 and 0.05 J m^{-2}), the simulations show neither a significant stress drop nor collagen delamination. The last region of the bumpy but upward trend is principally caused by the alignment of the fibers in the third lamella; stretching of those aligned fibers requires larger stress. It is noted that the stress can increase significantly in this region because we assume that the collagen fibers are purely elastic and non-breakable, which simplifies the mechanics but quickly enables us to see the strain distribution and mechanisms of the collagen delamination and bridging. An improved model needs to incorporate the entire force–extension curve of the collagen fiber; this can be obtained in future from either micro tensile test experiments or large-scale modeling of collagen fibers using molecular

simulations [203]. Figure 3.27c shows the change in orientation and delamination of the lamellae as a function of applied tensile strain. Four values were used for comparison: 0, 0.04, 0.09 and 0.15. They are labeled I, II, III and IV, respectively. The delamination is more prominent for the first and second lamellae, which have initial angles of 42° and 78°. In the regions at the ends of the delaminations, the angles change significantly. This is indicated by arrows for the second lamella at strain IV. This rotation at the end of the delamination supports the mechanism derived from experiments, as shown in Figure 3.25. For the third lamella, which makes an initial angle of 18° to the tensile axis, the rotation towards the tensile direction reduces the angle.

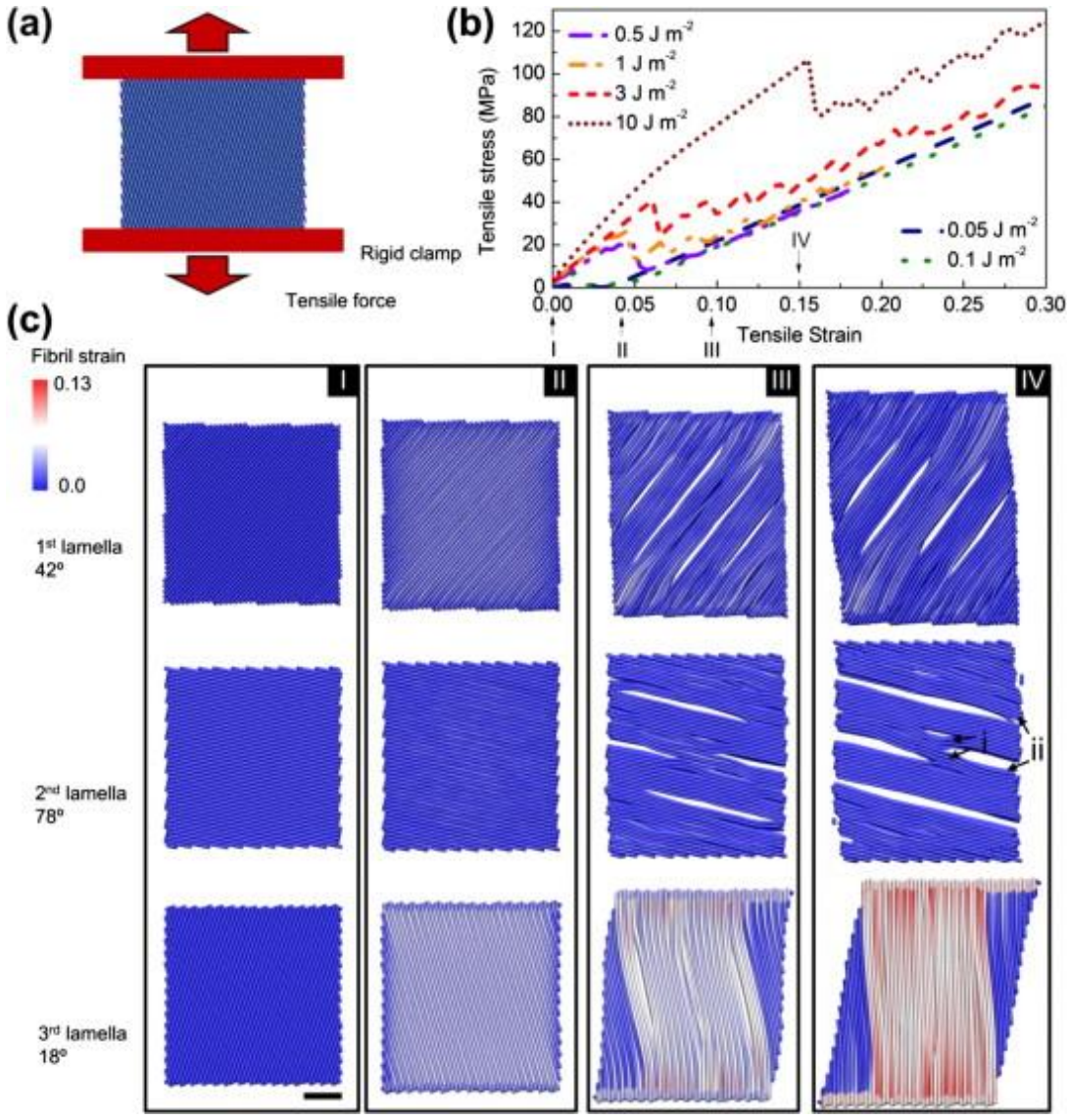

Figure 3.27: MD of collagen fibrils in three different directions with initial lamellar angles of 42°, 78° and 18° to the tensile direction. (a) Schematic of the scale model and the loading condition used to investigate the response under uniaxial tension. (b) The stress–strain curves obtained for different surface energies used in model. It is noted that for 1 J m^{-2} the first stress drop is 26.4 MPa, which gives the best approximation to the stress–strain curve of collagen layer and scales as shown in Figure 3.21. (c) Simulation snapshots of the deformation of each lamella in the scale model, taken at different strains as noted in panel (b) at increasing strains: (I) strain = 0, (II) strain = 0.04, (III) strain = 0.09 and (IV) strain = 0.15. Collagen delamination (noted by ii) and bridging (noted by i) are marked for lamella 2 at strain = 0.15 (IV), as illustrated (scale bar: 10 μm).

The average value and standard deviation of the angles between the fibers and the tensile direction in each collagen lamella was computed; results are summarized in Figure 3.28. It is shown that for the lamella with the largest initial angle (78°, second lamella), the

average value stays at a constant level, which agrees with the analytical calculations (Figure 3.26a). The standard deviation of the angle in this lamella increases significantly for large deformation, which can be understood by collagen bridging, explaining how a part of the collagen fibers rotates away from the tensile direction (Figure 3.27c). The calculations also show that the lamella with a smaller angle with the tensile direction (third lamella, making an initial angle of 18°) rotates faster than the other lamella (first lamella, with angle of 42°) toward the tensile direction, which also agrees with the analytical calculations (Figure 3.26a).

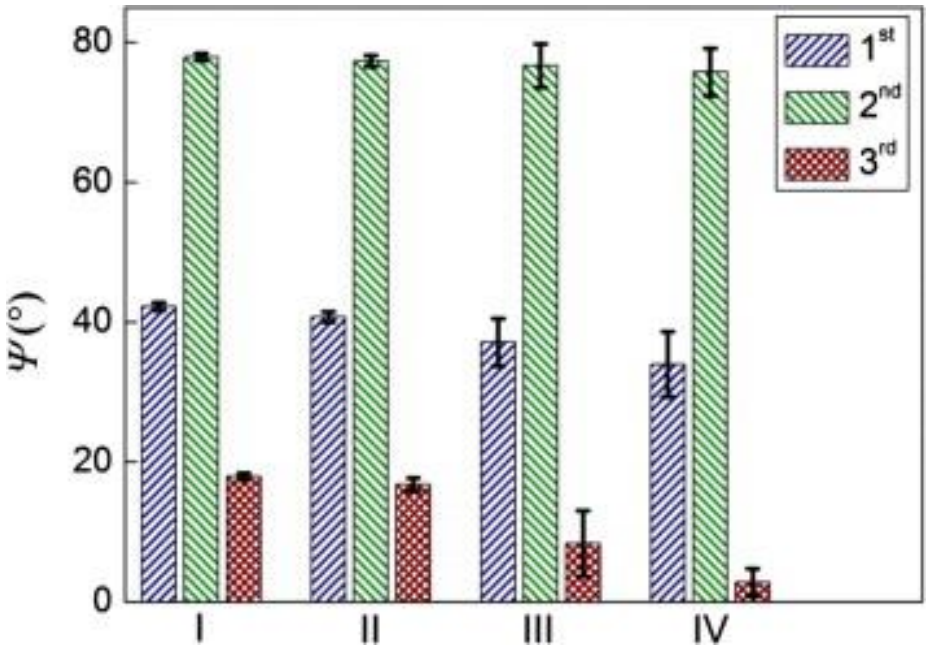

Figure 3.28: Simulation results showing evolution of angles ψ of the collagen fibers in each lamella for increasing strains (I < II < III < IV). The three layers have configurations shown in Figure 3.27c. The four strains used here to scan the angle are 0, 0.04, 0.09 and 0.15 for strains I–IV (same as that used in Figure 3.27c), respectively. The variation in the angles increases with strain (marked by bars on top of each bar plot). Lamella 3 shows a significant decrease in angle with increasing strain due to rotation of fibers toward the tensile axis.

3.3.4 Discussion

The arapaima scale has two important functions: (i) it resists penetration and (ii) it redistributes the force from the location of the bite over a much larger area. According to

Zhu et al. [109], the whole penetration process can be divided into three stages with progressively increasing penetration depth: stage I is essentially elastic loading, which terminates with cracking of the external mineral layer; stage II involves the penetration of collagen; while in stage III the tip of the indenter completely traverses the scale. This is indeed what happens in the scale of the arapaimas. Song et al. [148] conducted a finite element analysis of the ganoid scales where they varied tooth and scale parameters and established what effects this had on the mechanical response. One important conclusion is that the radius of curvature of the tip of the tooth had a profound effect on the force necessary to penetrate the scale. This was extended to elasmoid scales by Browning et al. [173] and Varshney et al. [204]. Their conclusion was that the redistribution of loads around the penetration point is critically dependent on the following scale parameters: angle of the scales, degree of scale overlap, composition (volume fraction of the scales), aspect ratio of the scales and material properties (tissue modulus and scale modulus).

Figure 3.29a shows schematically how the stresses are redistributed over a large area by the collective action of the scales. This enables the flesh to resist the compression by the application of the bite force. The flexibility of individual scales and their overlap are designed to increase the area of redistribution, as was pointed out by Vernerey and Barthelat [152]. Specifically, the scales are designed to function with the external layer under compressive stresses (Figure 3.29b). Indeed, Meyers et al. [159] proposed that the design of scales could lead to a bioinspired flexible ceramic composite and suggested that, in the case of the arapaima scales, the surface ridges minimize the stresses in the ceramic and enable flexing without fracture.

The foregoing results of experiments, characterization and analysis provide an improved understanding of the mechanisms of deformation and damage in the scales. The external mineral layer is designed to operate under compression; the tensile strength of the scales is actually increased by its removal. This is paradoxical but can be explained by the fact that the mineral does not contribute significantly to the tensile strength. Thus, its effect is strictly to increase the cross-sectional area, thereby decreasing the stresses. A second effect is that the lamellae adjacent to the mineral layer do not benefit from the rotational mechanisms discovered by Zimmermann et al. [153]. Indeed, the mineral layer is designed to operate in compression, as shown in Figure 3.29b. The application of a force by a tooth bends the scale in such a manner that the external mineralized layer is put under compression whereas the internal layers are subjected to tension (Figure 3.29c). In fact, penetration by a tooth is hampered significantly by this layer, leading often to the fracture of the tooth.

The lamellar structure of the collagenous foundation comprises many layers in a *Bouligand*-like arrangement. As a tooth penetrates, the layers separation and scale fracture are avoided through interlamellar and interfibrillar sliding mechanisms. The reorientation of the lamellae was observed through *in situ* experiments conducted on pre-notched specimens. These experiments show the sliding and reorientation of the lamellae and the absence of crack propagation. SAXS experiments confirm the change of orientation of the collagen fibrils. These phenomena were modeled by MD; this confirms that at small angles ($\psi < 45°$) the lamellae rotate towards the tensile axis, while for larger values, interlamellar splitting causes local increases in ψ.

The combination of a highly mineralized surface region designed to operate in compression with a flexible foundation, which can undergo significant tensile stresses, provides mechanical properties that minimize the penetration ability of teeth and can distribute the compressive traction effectively while ensuring significant mobility to the fish. This is accomplished at a modest weight penalty: the scale weight/fish weight ratio is only ~0.1.

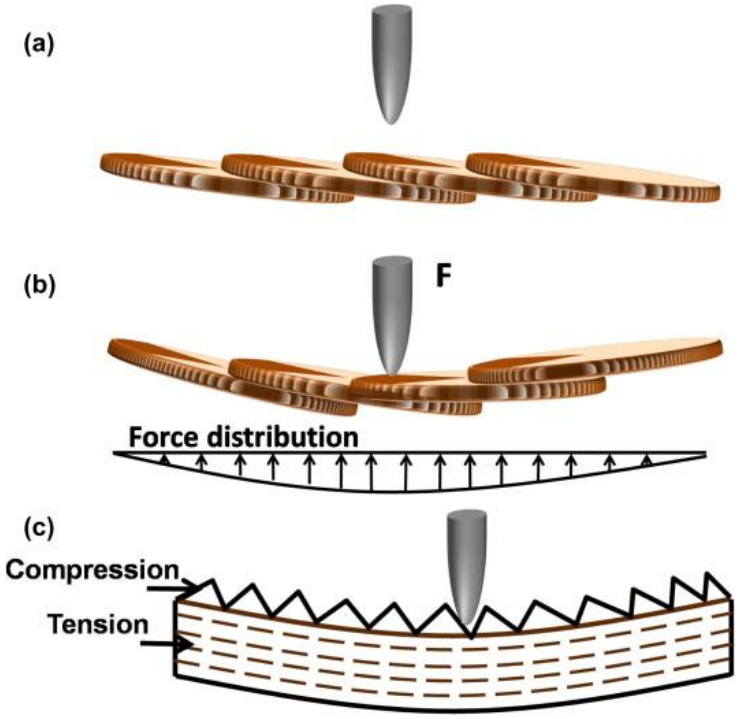

Figure 3.29: Protection mechanisms of the arapaima's scales against the penetration of a tooth: (a) schematic configuration of the scale overlap (imbrication); (b) flexing and redistribution of compressive stresses on the tissue; (c) flexure of scale leading to compressive stresses in the mineralized surface layer and tensile stresses in the flexible collagen lamellae.

3.3.5 Summary

Arapaima gigas is one of the largest freshwater fish; it is covered with elasmoid scales that act as flexible dermal armor and provide protection, primarily from attacks by piranhas, the principal predators in the Amazon basin. In this study, the penetration response and tensile behavior of the scales were investigated, with particular attention to

the mechanisms of damage in the individual collagen layers. This was achieved experimentally through the use of tensile tests on hydrated scales and indentation experiments, analytically by predicting the various mechanisms that retard damage in the scales, and computationally with MD calculations performed to understand the response of collagen fibrils to tensile loading. Based on these studies, the following specific conclusions can be made:

TEM and AFM confirm that the collagen fibrils have diameters of ~100 nm and are parallel in one lamella. The *d* band spacing of the collagen is clearly revealed by AFM and is equal to 67 nm, characteristic of type I collagen.

The scales act to efficiently resist bites from other fish. As a tooth attempts to penetrate the scale, first the brittle external layer is placed under compression and would eventually crack due to the stress concentration and gradients, exposing the collagen layers beneath. As the penetrator enters more deeply into the scale, the collagen fibrils are pushed apart and separated. Since it has to traverse several lamellae with different orientations, no macroscopic cracks are formed. In an extreme case, eventually, individual collagen fibers fail in tension, exhibiting necking which is characteristic of considerable permanent deformation.

We confirm and quantify earlier conclusions by Zimmermann et al. [153], namely that the stretching, rotation, delamination and fracture of collagen fibrils are the principal mechanisms of energy dissipation in the flexible foundation. Under tensile loading, most of the collagen fibrils are stretched and rotate toward the tension direction; the collagen fibrils with a large angle to the loading (closer to 90°) delaminate as portions can rotate away or towards the tensile direction. An analytical model predicts the rotation of the

collagen fibers toward the tensile axis; the model is in good agreement with measurements by SAXS.

MD calculations of interfibril separations yield results that match quantitatively the experimental measurements, with interaction energy between microfibrils of 1 J m^{-2}being assumed. The calculations correctly predict the separation of fibrils and angular rotation toward and away from the tensile axis for large angles, and rotation of fibrils toward the tensile axis for small angles. Since only three lamellae are used in the computation, their splitting is accompanied by significant load drops; the drop at a stress of 26.4 MPa corresponds closely to the maximum stress of 30–40 MPa experimentally observed.

3.4 The protective scales of *Latimeria chalumnae*

3.4.1 Structure

The coelacanth has an ancient type of elasmoid scales, which occured several times throughout evolution (Figure 3.30). Similar to cycloid scales, these scales have a dark region with a rough and more mineralized exposed surface, and an overlapped (embedded) region of which the surface is light and smoother. The individual scales have an elliptical shape with various sizes corresponding to the size of the fish and they are typically ~10–35 mm in size for a 1 m fish. The degree of imbrication is ~0.34 and the aspect ratio is ~55, similar to the arapaima. These scales provide protection by means of a highly mineralized outer layer with unique “double-twisted” *Bouligand* foundation [115]. The surface of embedded region is shown in Figure 3.30b. From the center of the scale circular annular ridges with various spacings can be observed. Additional ridges radiating from the center are initially perpendicular to the annuli and then orient towards the dorsal-lateral direction. These ridges, shown in Figure 3.30c, have a spacing of approximately 30 μm. On the

surface of the exposed region, denticles protrude from the scale towards the direction of the fish tail (Figure 3.30d). The mineral layer is needed for protection, although Sudo et al. [205] studied the scales of the *Sebastes inermis* (rockfish), which also has ctenoid scales, and showed the surface roughness aligns with the direction of the water current and serves to channel flow for a hydrodynamic advantage.

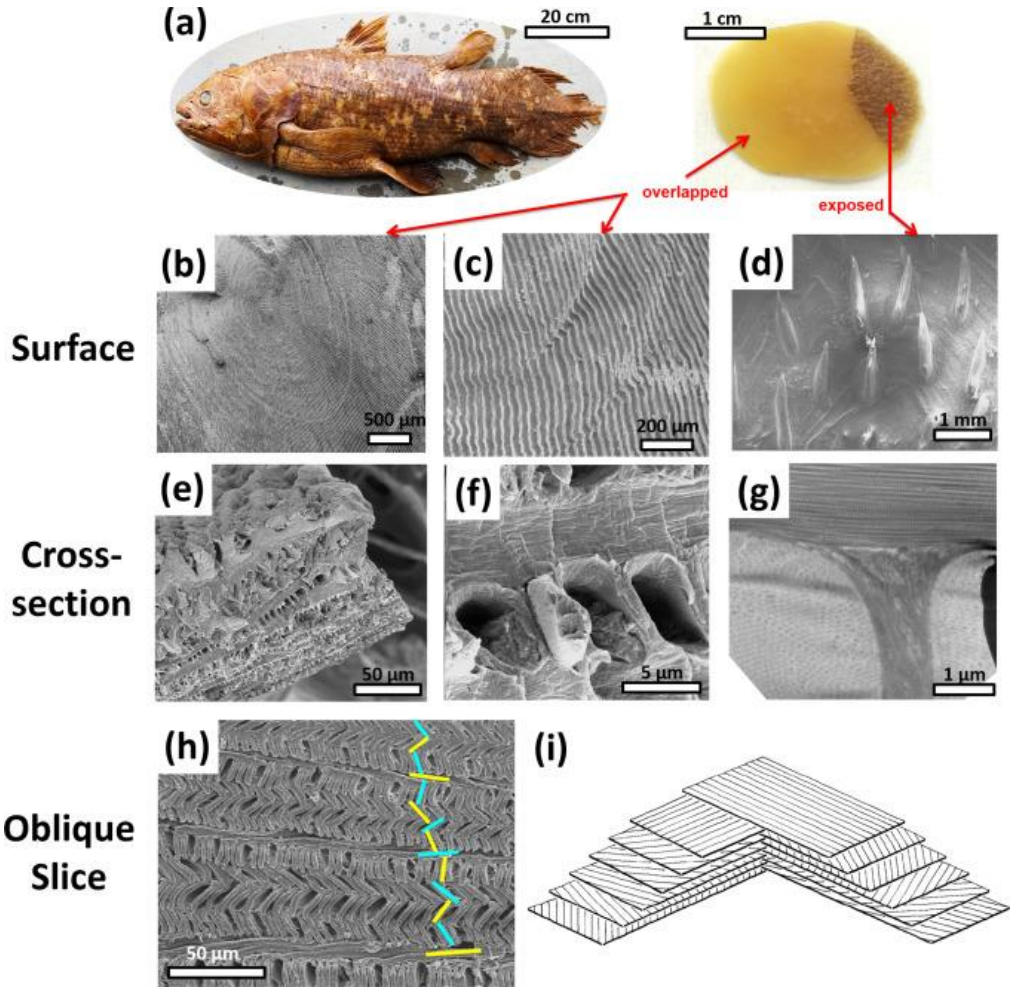

Figure 3.30: Overview of the scale of coelacanth. (a) The entire body of coelacanth is covered by elasmoid scales. (b) The scales are oblong and the complete surface of the scale is comprised of stacked layers, which originate at the intersection of the exposed and covered portions of the scale. A ridge at the edge of each oval layer transitions to the layer beneath. (c) Each layer has comb-like ridges which radiate from the center of the scale. (d) The exposed portion of the scale has denticles which angle towards the tail of the fish. (e) Cross-sectional view of the scale shows the internal collagenous lamellae. (f) SEM and (g) TEM of adjacent lamellae the collagenous struts connecting them. (h) An oblique cross-section shows the change in orientation of adjacent layers. (i) The progression of layers and orientations shown schematically (from Giraud et al. [115]).

Beneath the rough and hard exposed surface, the majority of the scale thickness is composed of collagenous lamellae, identified as isopedine [115, 155, 185, 186]. Isopedine is also present in the ganoid scales of Senegal bichir [147]. The laminated structure of the coelacanth scale is shown in Figure 3.30e. The lamellae in the isopedine have two superimposed and interpenetrating *Bouligand* structures with a remarkably regular arrangement in which the parallel fibers in any one lamella lie at a roughly 90° angle to the fibers in adjacent lamellae (Figure 3.30i) [115, 155]. The architecture of the coelacanth scale differs from the arapaima scales, as they have struts with less ordered collagen fibrils connecting the lamellae and filling the gaps between collagen bundles. Figure 3.30f shows holes in the scale cross-section which indicate that the collagenous bundles "pull-out" when the sample is fractured. Transmission electron microscopy of these scales (Figure 3.30g) shows aligned collagen fibrils along the lamellae and less organized fibrils in the struts, forming a continuous network. The orientation of lamellae can be readily identified from the oblique slice shown in Figure 3.30h. The fibril directions are marked and show that the orientations of the collagen lamellae in adjacent layers are nearly orthogonal, while successive bilayers are characterized by a clockwise rotation of ~30° (when observing from the top of the figure down). This arrangement, first described by Giraud et al. [115] and subsequently termed "double twisted", is illustrated schematically in Figure 3.30i, which shows the collagen orientation in each odd layer and each even layer (including the rotation between the layers), and how the combination of the two *Bouligand* structures forms the double twisted structure.

3.4.2 Mechanical response

The pseudo-orthogonal ‘plywood’ structure of the isopedine of the coelacanth scales leads to in-plane isotropy, with no significant difference between the mechanical responses along longitudinal and transverse directions. Tensile stress-strain curves, shown in Figure 3.31a-b, reveal a Young's modulus in the longitudinal direction of ~210 MPa with a tensile strength of ~50 MPa, as compared to respective values of ~250 MPa and ~50 MPa along transverse direction. This in-plane ‘isotropic’ mechanical response is substantially different from the mechanical response of arapaima scales, which have higher strength and stiffness in the longitudinal direction. The work-of-fracture in coelacanth scales (area under the stress-strain curve) before complete fracture is about 10 MJ m^{-3} in both longitudinal and transverse directions. This is much higher than the work-of-fracture in arapaima scales, which is 1–2 MJ m^{-3}. This indicates that the role of collagen struts between the lamellae is important and provides additional deformation ability to the structure, contributing significantly to the toughness of these scales.

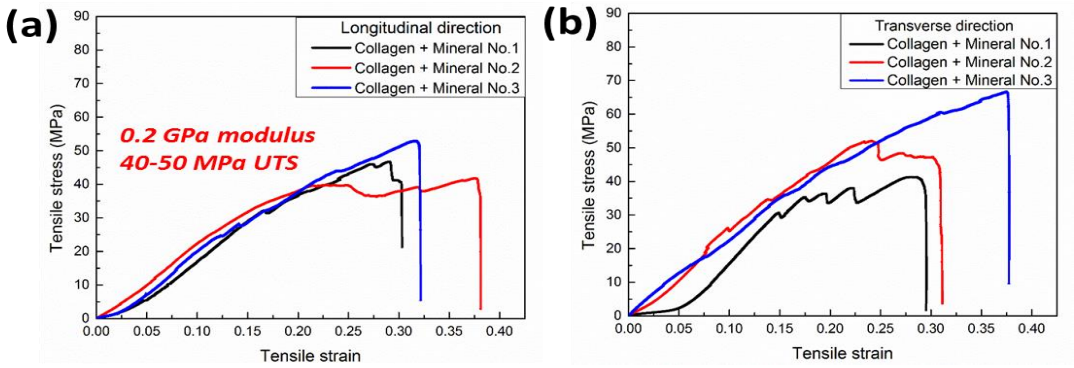

Figure 3.31: Mechanical response of the coelacanth scale. Comparison of the tensile stress as a function of strain for the coelacanth scales in (a) the longitudinal and (b) the transverse direction. The in-plane isotropy results from the periodic relationship between lamellae; the lamellae are oriented as two interpenetrating *Bouligand* structures (ABAB) where the A and B orientations are perpendicular to one another and subsequent AB pairs are twisted by ~30° with respect to the previous pair. This structure promotes strength as well as isotropy; the relatively strong scales have an ultimate tensile strength between 40 and 50 MPa.

3.4.3 Failure prevention strategies

Figure 3.32a-b shows the extension of a crack in a pre-notched coelacanth scale. As the crack propagates, the collagen fibers form bridges in front of the main crack front and delocalize failure. Thus, the crack tip becomes blunted by collagen fibrillary bridging, similar to that shown in striped bass scales [206]. Figure 3.32c shows the highly mineralized surface layer (top); element mapping of calcium in Figure 3.32d indicates that this outer layer of the scale has much higher mineralization than the inner layer.

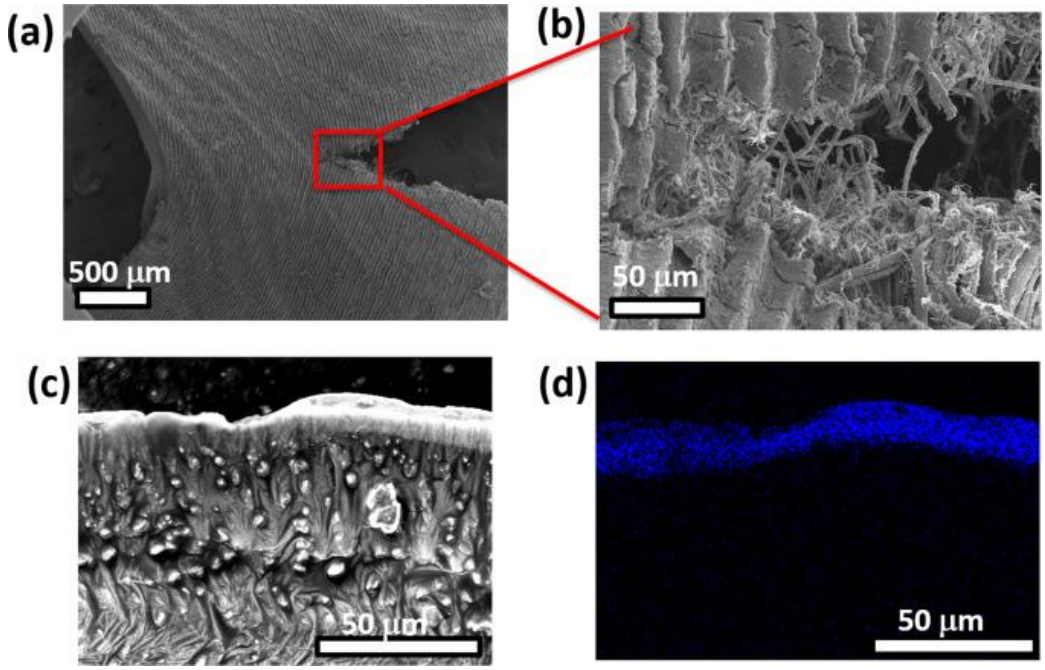

Figure 3.32: Crack arrested by the collagen fibrils and EDX image of outer layer of coelacanth scale. (a) A notched tensile test is paused to illustrate the opening of the scale during tensile crack propagation. (b) Expanded view of crack tip demonstrating extensive bridging of the crack by collagen fibers and blunting of the crack tip. Individual lamellae are not visible, but a large amount of collagen fiber pullout and complete lamellar delamination are the key energy absorbing features. (c) SEM of the cross-section of the scale used for energy dispersive x-ray analysis (EDX). (d) EDX shows high mineral content of outer surface as well as a small amount of mineral distributed in the scale indicated by the blue features. The black area corresponds to low mineral content.

To examine how these scales defend against an attack by the coelacanth's predator, the shark, a shark's tooth is attached to a load frame and penetrated through two scales, with fish flesh placed underneath to mimic the coelacanth body. The force vs. displacement

curve in Figure 3.33 shows two drops as the tooth penetrates through the two scales. The penetration of one coelacanth scale occurs at approximately 15 N (the first drop in the curve) and 25 N for the subsequent scale, which is inferior to the arapaima scale that can withstand loads in excess of 100 N. As potential predators of the coelacanth, sharks with ~ 70 teeth (depending on the species) may have a bite force of up to 2400 N (blacktip shark: 420 N; horn shark: 200 N; hammerhead shark: 2400 N; bullshark: 1000 N as summarized by Mara et al. [163]). The bite force is distributed across a number of teeth, although in some cases, especially with larger sharks, the scales would be expected to suffer penetration. The coelacanth scales would successfully defend from many smaller sharks, but inevitably the fish would fall victim to the more powerful sharks in the ocean. For this reason, the fish's ability to remain hidden [161] is crucial to its survival.

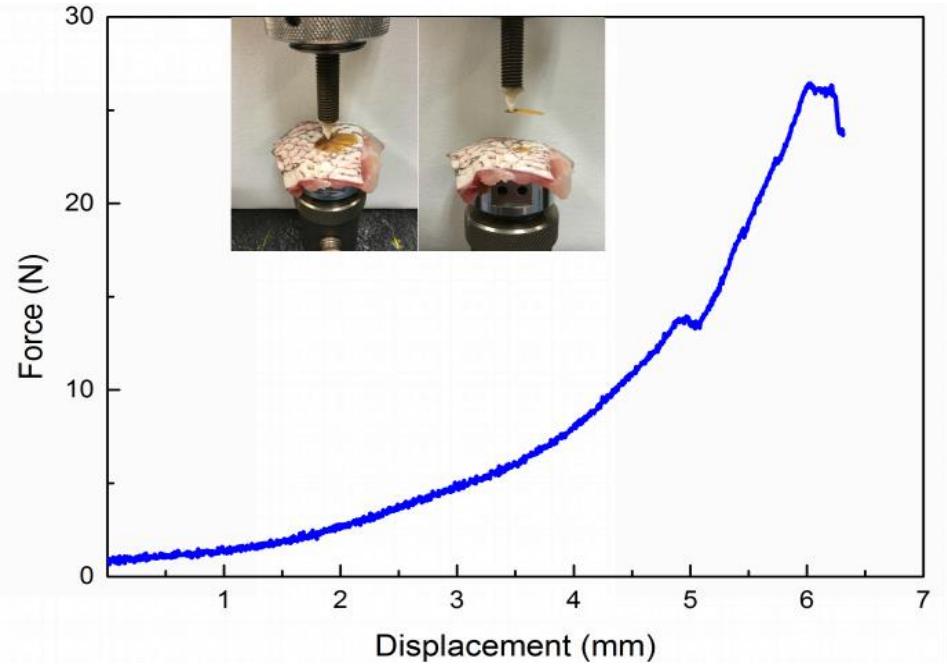

Figure 3.33: Penetration of a coelacanth scale by a shark tooth. Two overlapped scales are penetrated in the exposed area by a shark tooth. The arrangements of the coelacanth scales are such that the covered portion of a second scale exists immediately below exposed surfaces. The force displacement diagram indicates that penetration and damage of the scale is possible due to the shark's bite force; the two drops in load correspond to visible penetration of the shark tooth through two scales.

3.4.4 Summary

The coelacanth has a unique ctenoid scales with a double-twisted *Bouligand*-like collagen structure, where adjacent layers are connected by struts. This structure results in strong scales which excel at energy dissipation, in order to provide protection from the many predators which exist throughout the ocean. The scales are specifically designed to protect from sharks, the fish's main predator, although in some cases (such as with the great white shark) the scales may be insufficient to thwart attack. Therefore, camouflage and hiding are used in conjunction with the scales in order to defend the coelacanth.

3.5 Comparison of the three fish scales

The arapaima, coelacanth and alligator gar scale have different predators, and comparing the mechanical properties with the structural characterization as well as the toughening mechanisms which were described in the previous sections provides insights on the armor suited for different applications. Key features of the three types of scales being compared are presented in Table 3.2. The relative hardness and stiffness of the three fish scales, calculated using micro- and nano-indentation measurements, are plotted in Figure 3.34. Although the hardness and stiffness of these scales are different for each fish because of their specific protective requirements, they are all designed with the concept of a hard and stiff outer surface with a relatively soft and tough foundation to accommodate excessive damage. Beyond this common design principle, each scale has a specialized structure which corresponds to the specific mechanisms providing a competitive advantage over their predators, which have been discussed above. These mechanisms of protection against predators have clearly been successful as they have enabled these fish to survive for millions of years.

Table 3.2: Comparison of the properties of arapaima, coelacanth, and alligator gar scales.

Fish	Aspect ratio	Imbrication degree	Mineral content	Structure	Ultimate tensile strength	Tensile modulus	Nanoindentation hardness
Arapaima	50	0.4	43%	*Bouligand*	15 MPa-40 MPa	200 MPa-500 MPa	1.3 GPa to 0.5 GPa
Coelacanth	55	0.34	53%	Double-twisted *Bouligand*	50 MPa	200 MPa	0.5 GPa to 0.2 GPa
Alligator gar	8.6	0.78	65%	Bone and enamel	90 MPa-115 MPa	2 GPa	3.7 GPa and 0.75 GPa

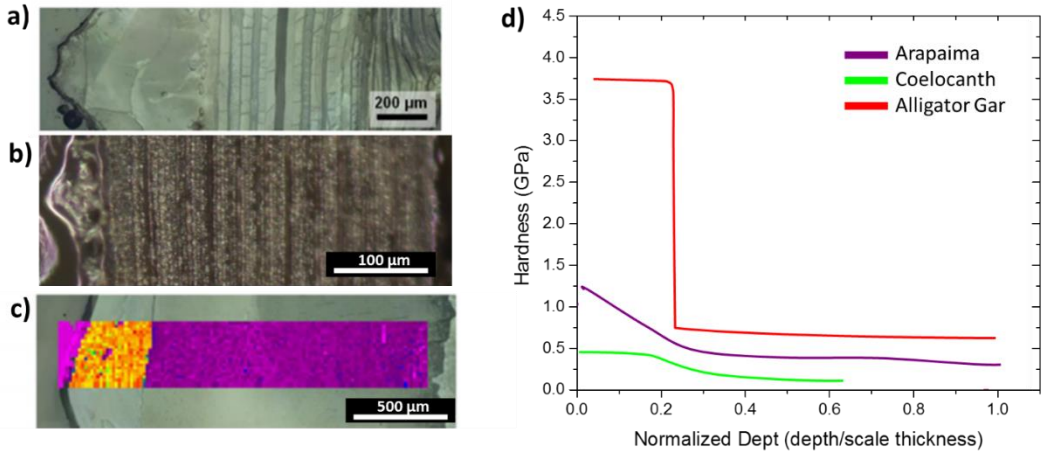

Figure 3.34: Nanoindentation and microindentation of the cross-sections of scales. (a) Nanoindentation of the arapaima scale shows that the surface mineral has a hardness of ~1.3 GPa; the hardness decays with decreasing mineral to a value of ~0.5 GPa in the *Bouligand*-type foundation. (b) The coelacanth scale has a nanoindentation hardness of ~0.5 GPa in the mineral layer which, similar to the arapaima, continuously decreases to ~0.2 GPa as mineral content decreases. (c) The alligator gar scale has a nanoindentation hardness of ~3.7 GPa in the mineralized ganoine outer surface; a sharp transition between the outer surface and the boney base causes an immediate hardness decrease to ~0.75 GPa. (d) Hardness vs. normalized depth plots of across each of the three scales reveal harder outer surfaces and softer foundations.

To compare the three fish scales and their defense capability, predator tooth sharpness, predator bite force as well as the modulus of the fish scales are summarized in Figure 3.35. To give a clear comparison, values are normalized by maximum values. It is clear that minimal overlap (and corresponding large degree of imbrication) of systems with stiff scales, such as alligator gar, can defend against a predator with a large bite force but a

large radius of the teeth tips. However, facing predators with sharp teeth (small tip radius) requires more flexible scales with large overlap regions (consistent to a low degree of imbrication).

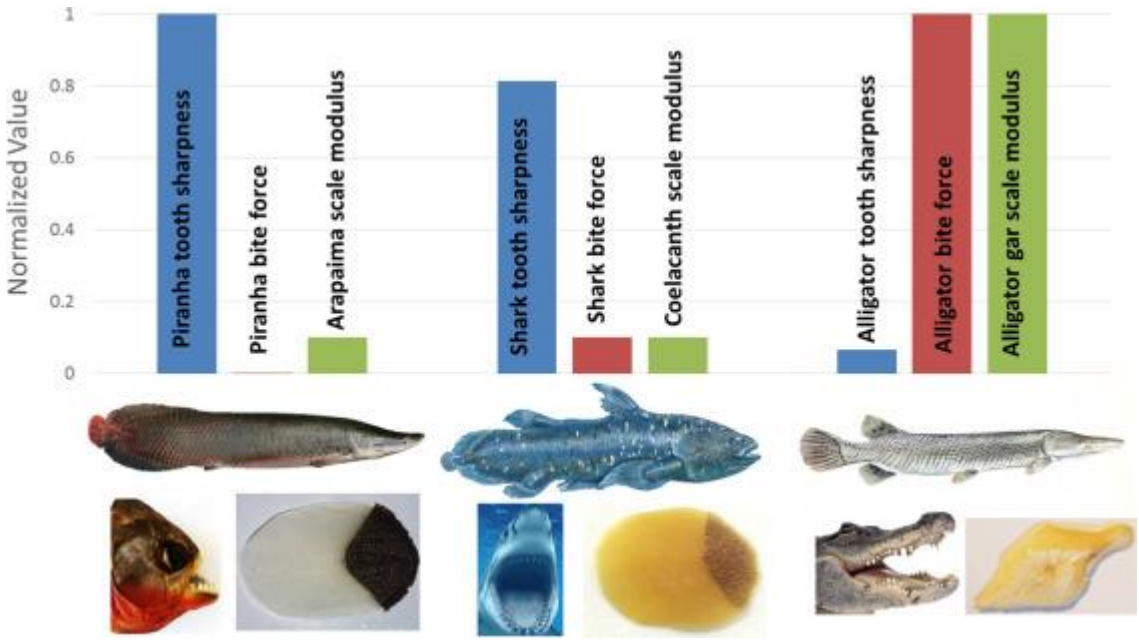

Figure 3.35: Comparison of normalized predator tooth sharpness, predator bite force, and prey scale modulus. The high imbrication of stiff alligator gar scales can defend against predators with large bite forces and dull teeth (large tooth tip radius), while the more flexible scales of the coelacanth and arapaima can defend against sharp teeth (small tooth tip radius).

3.6 Bioinspired flexible armor

The goal of studying natural armor is to understand key features for potential future incorporation into superior synthetic structures that provide protection for personnel and equipment. In particular, the increasingly versatile robots being developed and produced offer promising alternatives to the use of soldiers in war zones. Being in a hostile environment demands an effective armor which can withstand projectiles and impacts without inhibiting mobility and tactical advantages provided by advanced robotics. In

particular, armor which allows for flexibility of joints is key to the protection of both human and machine.

Inspiration from nature in the design of armor has existed since the days of the Roman Empire. The *lorica squamata* mimicked lizard skin and provided protection to the soldiers while ensuring mobility. Indeed, the name squama signifies "scales" in Latin. The plates of *Lorica squamata* were 0.5–1 mm thick and had dimensions of 15–25 mm across, similar to the arapaima and coelacanth. These scales provided the best protection, superior to *Lorica segmentatata* (metal lamellar hoops associated with Roman legionnaires in movies), and *Lorica hamata* (chain mail). *Lorica squamata* was superior because the majority of the body was covered by two plates in which the kinetic energy of projectiles was transferred laterally.

Researchers are currently using new techniques to mimic the overlap system of the fish scales as well as specification of the aspect ratio and imbrication in order to tune the flexibility and protection function of future bioinspired armor. Rudykh et al. [207] investigated the resistance to penetration of a microstructured elasmoid scale-inspired armor. Indentation and bending tests on bioinspired 3-D printed structures, shown in Figure 3.36a-b, optimized protection against penetration and flexibility, amplifying penetration resistance by a factor of 50 while reducing flexibility by less than a factor of 5. This was achieved by identifying and separately analyzing the mechanisms which govern flexibility and penetration resistance. Similar efforts by Funk et al. [208] have led to the creation of a synthetic "fish skin" for the production of soft materials through a combination of a mesh or dermis-like layer and rigid scales. The assembled product is not specific to any particular classification of fish scale, but incorporates components that are key to the armors

mechanical response. The resulting assembly, shown in Figure 3.36c-d, is flexible, lightweight, transparent, and robust under mechanical load. It is claimed to have a potential application as a thin protective coating for soft materials. It is also important to understand how a stiff plate performs on a soft substrate; Martini and Barthelat [209] showed that small plates may fail by tilting due to a localized force, and emphasized the importance of avoiding this dangerous failure mode which drastically reduces the effectiveness of stiff armor plates. Additionally, Martini and Barthelat [210] produce a bioinspired armor shown in Figure 3.36e,f, made of ceramic tiles and a soft substrate and capable of a large degree of flexibility and also resistant to penetration.

Another unique biological feature learned from the arapaima scale is that of the concept of "flexible ceramics". This refers to the ability of the collagenous foundation of the scales to flex without damaging the mineralized surface [159], as shown in Figure 3.36g-h, which allows arrangements of larger scales to retain flexibility. The tensile strains at the bottom of the mineralized ridges are considerably lower than those encountered if the mineralized layer had a homogeneous thickness. Correspondingly, localized cracking occurs at the bottom of the ridges but is much less damaging. Rudykh and Boyce [211] similarly demonstrated that super flexible composites may be produced with an elasmoid scale type arrangement, using a large volume fraction of the stiff phase in order to promote protection with little compromise in flexibility.

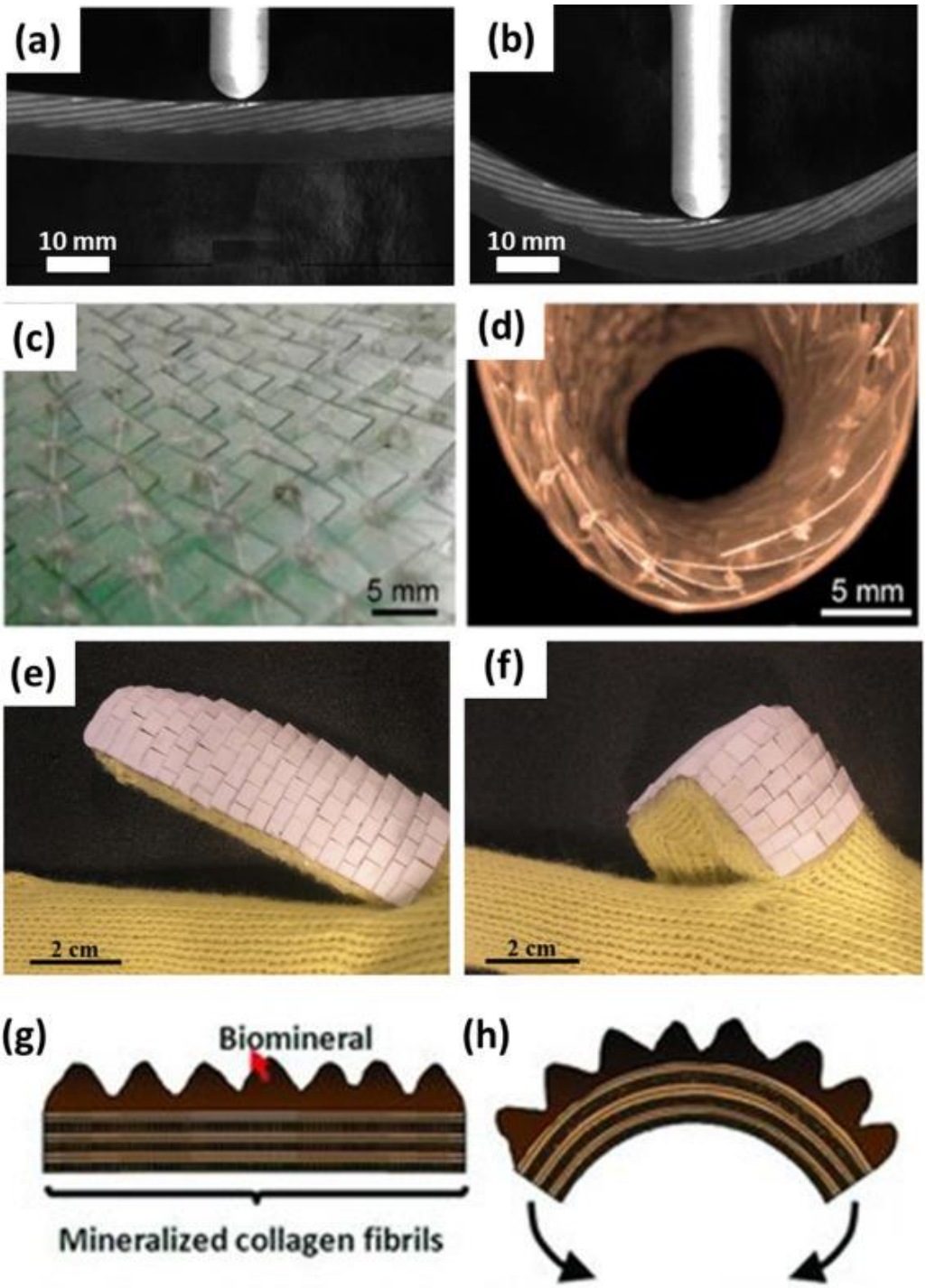

Figure 3.36: Bioinspired armor designs. (a-b) Microstructured elasmoid scale armor produced by Rudykh et al. [207] amplifies penetration resistance by a factor of 50 while reducing flexibility by less than a factor of 5. (c-d) A synthetic "fish skin" developed by Funk et al. [208] combines a mesh or dermis-like layer and rigid protective scales. (e-f) Martini and Barthelat [210] produced the this armor by stretching a soft substrate and affixing ceramic tiles, which leads to imbrication upon release. (g-h) Schematic of the flexing of the arapaima scale, which illustrates the concept of a "flexible ceramic". Ridges minimize the tensile strains in the mineralized layer, preventing large cracks from forming during flexing. From Meyers et al. [159].

Our studies have targeted the design of armor plates inspired from the architecture of the alligator gar scale. There are two length scales at which the gar scales may serve as bioinspiration. The first is at the macro level where both the specialized geometry and material properties provide the required coverage and flexibility through assemblages of scales. The second is at the microscale, where features lead to the required material properties such as stiffness and toughness. On the macroscopic level, a gar-inspired geometry shown in Figure 3.37a was designed with essential features. The geometry is simplified and symmetric about the major axis when viewed from above, (Figure 3.37b). By simplifying the geometry, the complexities due to different scale shapes which exist on gars are decreased. A cross-section of the scale (Figure 3.37c) shows that the scales have identical radii of curvature on all sides, allowing them to hinge on one another. A degree of overlapping enables full coverage during flexibility, and a single row of scales is shown in Figure 3.37d. In the design of a ganoid-scale-inspired armor, the curvature is limited by the size of the scale. As illustrated in Figure 3.7 and Figure 3.8; smaller scales enable increased flexibility, although there is a corresponding reduction in protection.

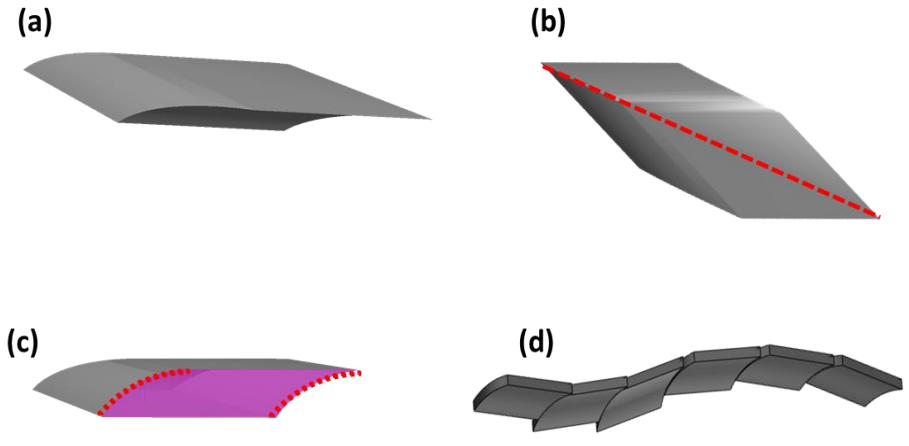

Figure 3.37: Geometric design inspired from the gar scale. (a) Overall view of gar inspired geometry. (b) Line of symmetry down middle of scale. (c) Matching radii of curvature on all edges of scale. (d) Array of scales conforming to curves.

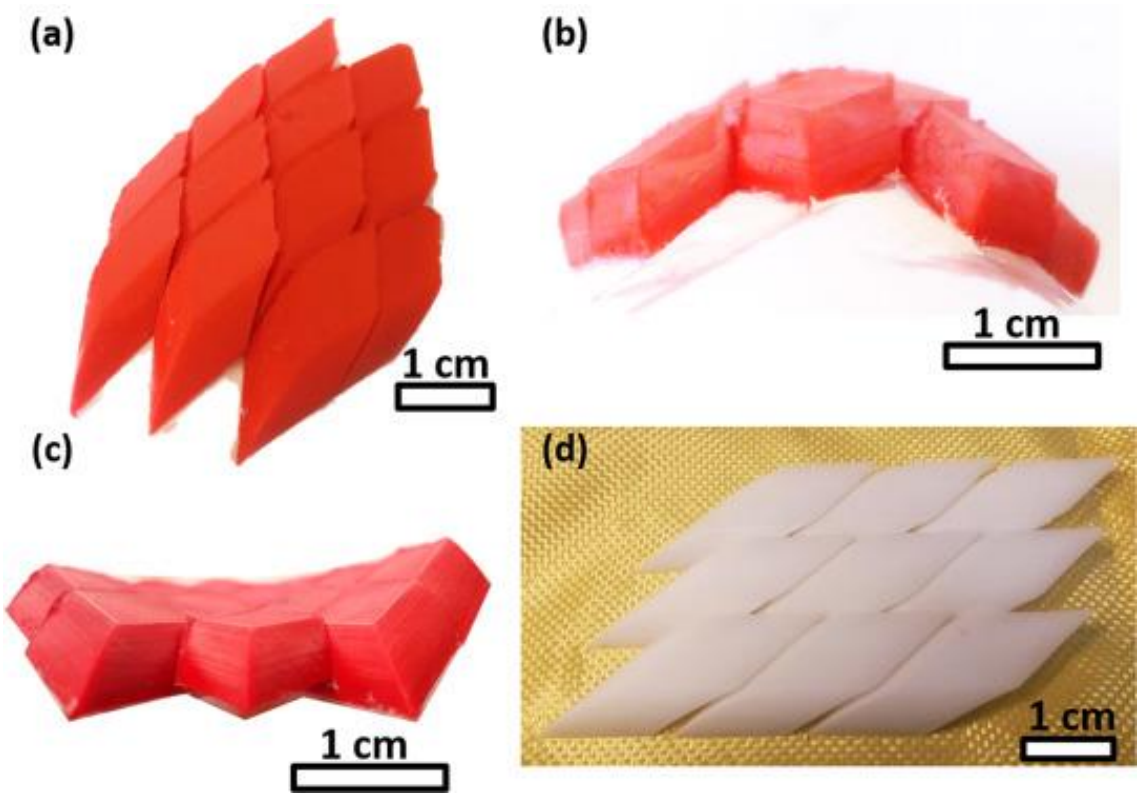

Figure 3.38: A bioinspired prototype. (a-c) 3d printed ABS samples. (d) Samples made from zirconia and glued on Kevlar. The shape of the scale is simplified in order to capture the key features which make the scale flexible, while creating a simplified and more manufacturable scale. These model scales are capable of hinging with respect to adjacent scales; a pattern of these scales should bend and absorb strain in all directions while maintaining the protective function. In order to effectively glue zirconia scales, they were etched in 9.5% hydrofluoric acid at 25 °C for 2 h to create surface roughness.

The design of the scales was mimicked in order to demonstrate the coverage and flexibility of an array of scales using two methods: 3D printed using ABS (Figure 3.38a-c) and machined from zirconia (Figure 3.38d). Zirconia scales were cut from discs using a CNC mill, and subsequently sintered at 1520 °C for 2 h. The shrinkage associated with sintering was incorporated into the design. For future improvement on the zirconia, several key structural features may be incorporated. The first is the bi-layered configuration of the scales; the outer of the two layers should be a region which is particularly hard and penetration resistant, like ganoine. This layer may be replicated with a pure ceramic layer, incorporating extrinsic toughening through decussation, which is readily observed in both

the scale ganoine and in tooth enamel [212]. The inner of the two layers should be tough and energy absorbent, like the bony region of the scale. In order to mimic this layer, a ceramic-based composite with fibers resembling mineralized collagen, and a stiff ceramic phase between the fibers needs to be synthesized and processed. The presence of tubules would be desirable in order to promote toughening through crack deflection.

3.7 Summary of fish scales

In our work, we have investigated the armored scales of three large fish: the *Arapaima gigas* (arapaima), *Latimeria chalumnae* (coelacanth) and *Atractosteus spatula* (alligator gar). Each of these fish utilize a different class of scales for protection, respectively cycloid, ctenoid, and ganoid. These finely tuned dermal armors have protected these fish for millions of years, and barring direct or indirect human intervention, will likely continue to do so. Like most armors, these scales are designed with a hard outer surface to resist penetration and a tough inner foundation to accommodate excessive strains. However, each type of scale owes its effectiveness to specific features which are related to the fish's main predators:

- The elasmoid (cycloid) scale of the arapaima enables flexibility in spite of a highly mineralized exposed surface and substantial overlap to effectively resist the penetration of piranha teeth. The ridges on the surface enable the mineral to effectively flex, minimizing the tensile stresses acting on it.
- The elasmoid (ctenoid) scale of the coelacanth has a much lower stiffness but higher ultimate strength (40–60 MPa) than that of the arapaima (30 MPa), with a considerably higher work-of-fracture (9–10 MJ m^{-3} vs. 1–1.5 MJ m^{-3}). Although the coelacanth scale uses similar mechanisms to the arapaima, the interfibrillar

collagen struts between the collagen bundles in the structure contribute significantly to the energy dissipation.

- The ganoid scale of the alligator gar resists the extreme bite forces of its predators by having a highly mineralized, tough and strong foundation beneath a hard and stiff ganoine outer layer. The wet gar scales dissipate energy as the water molecules act as a plasticizer to promote ductility while in the dry scales the tubules provide toughening through crack deflection and meandering.

Each type of scale has unique and fascinating features in its nano-, micro-, and meso-structure which lead to its capacity to prevent failure when under attack by either sharp teeth or crushing force of predators. If placed in alternative environments, each fish would be likely to suffer as the minimally overlapped gar scales may provide regions where a piranha's sharp teeth can penetrate into the fish's connective tissue and flesh, while the cycloid scales of the arapaima may not resist the powerful bite of the alligator. The understanding of these dermal armors and their effectiveness in protecting these three fish may inspire the production of novel designs for flexible body armor which provides superior safety and protection from physical threats.

Chapter 3, in part, is published as “Microstructural and geometric influences in the protective scales of Atractosteus spatula” Journal of The Royal Society Interface, in press, 2016. This work was coauthored by N. A. Yaraghi, D. Kisailus and M. A. Meyers. The dissertation author is the first author of this work.

Chapter 3, in part, is published as “Protective role of Arapaima gigas fish scales: Structure and mechanical behavior” Acta Biomaterialia, vol 10, pp 3599-3614, 2014. This work was coauthored by W. Yang, B. Gludovatz, M. Mackey, E. Zimmermann, E. Chang,

E. Schaible, Z. Qin, M. Buehler, R. Ritchie and M. Meyers. The dissertation author is the second author of this work.

Chapter 3, in part, is published as "A comparative study of piscine defense: The scales of *Arapaima gigas*, *Latimeria chalumnae* and *Atractosteus spatula*" Journal of the Mechanical Behavior of Biomedical Materials, in press, 2016. This work was coauthored by H. Quan, W. Yang, R. Ritchie and M. Meyers. The dissertation author is the first author of this work.

CHAPTER 4: RESULTS ON SKIN

4.1 Introduction

Vertebrates are covered with organ skin, which provides protection from the environment, temperature regulation, camouflage, thermal energy collection and a host for embedded sensors [213]. Skin consists of three layers, epidermis, dermis and endodermis, with mechanical properties dictated primarily by the dermis, the thickest layer. Its major constituents are type-1 collagen and elastin: collagen provides mechanical resistance to extension, whereas elastin accommodates the deformation [214]. To fulfill its multifunctional role, skin must possess a tailored mechanical response to accommodate the body's flexibility and movement coupled with damage minimization strategies to prevent tearing.

Research into skin's mechanical properties began in 1831 when Guillaume Dupuytren [215] observed a patient who had stabbed himself over the heart three times with a stiletto having a circular cross-section. Doubting the patient's truthfulness due to the elliptical shape of the wounds, Dupuytren found that perforations made from an awl may either narrow or broaden depending on the tension of the skin across the wound. This led to Langer's proposal of lines representing the anisotropic nature of the skin that follow directions where the skin is under most tension [216]. The existence of Langer's lines is well recognized; indeed, surgeons find that incisions made along the lines close easily and heal rapidly, whereas incisions perpendicular to the lines tend to pull open, with prolonged healing and scarring [217]. By using an awl to make multiple wounds in cadavers, maps of Langer lines as shown in Figure 4.1 are created.

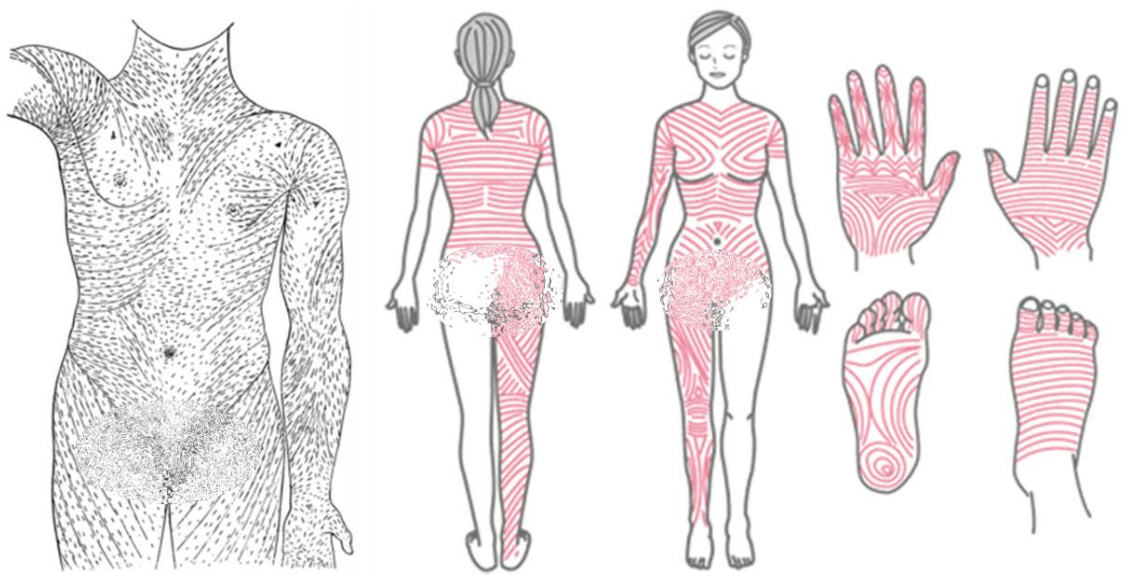

Figure 4.1: Depiction of Langer lines. (a) Original depiction of Langer lines by Karl Langer [218] (b) Schematics of Langer lines by Sophis inc. who offers "The Langer lines massage" [219].

Skin is often considered as a nonlinear-elastic material with low strain-rate sensitivity [80, 106]. Most work on its mechanical deformation has focused on the collagen, the main structural component of the dermis [198]. Deformation in collagen involves several distinct stages [220]. In arterial walls, for example, collagen fibril straightening, reorientation and elastic stretching have all been identified [197, 199, 221], akin to their alignment on stretching in tendons [51, 222]. Constitutive models are based on phenomenological curve-fitting [223], energy-based formulations [87] and physically based relationships [61, 94, 224].

We have performed a variety of experiments on chicken and rabbit skin. These two skins were chosen due to accessibility of material, and differences in functional requirements. In rabbits, the skin provides protection from physical assault by its surroundings such as sticks, brush and predatory attack. Additionally, the rabbit is an athletic animal whose motion requires a large amount of stretch by the skin. Avian skin has other unique characteristics and functional requirements; it is adapted to provide support

for the feathers, and does not have sweat glands. The differences in function between the skins lead to specialized structures and varying mechanical properties. These differences are clearly conveyed in the characterization and experimental results which follow.

Figure 4.2: A cottontail rabbit running through snow. (a) As the rabbit runs, the skin must accommodate large strains. (b) The skin in the non-stretched state while the rabbit runs.

4.1.1 Rabbit (*Oryctolagus cuniculus*)

Rabbit skin is a highly extensible, anisotropic and strain rate sensitive material. Rabbits live in brush environments [225], and their skin must be capable of withstanding the possibility of pulling, poking and rubbing from sticks and branches. In addition, rabbits are prey of many animals, and natural selection favors animals with the best survival characteristics-such as an effective and protective skin. Further functional requirements of skin are due to the athleticism of rabbits [226]; as they run, their skin must be capable of accommodating large deformations. Due to the ability to retrieve fresh rabbit skin specimens, they were chosen as the subject for our studies which resulted in Section 4.2 and 4.3. However, some initial characterization was performed on the skin of the brown chicken, and these results follow.

4.1.2 Brown Chicken (*Gallus gallus*)

Avian skin has evolved and specialized for different purposes than mammalian skin. Birds avoid attack through flight, and their skin has a main purpose to support the

feathers. Structural coloration is another common feature of avian skin which is, where highly refined structures in the dermis create vivid colors in order to attract mates [227]. It is interesting that structural coloration is an important feature for many birds and a prime example of convergent evolution; this mechanism of color production has evolved more than 50 independent times within extant birds [228].

Preliminary tests and observations on chicken neck skin revealed large differences in strength and extensibility compared to rabbit skin. These tests are shown in Figure 4.3. The neck skin of the chicken was chosen as an ideal location from which to harvest skin, in order to be able to effectively establish the direction of Langer lines. The two principal directions chosen are transverse, or across the neck, and longitudinal, or in the axial direction of the neck. Figure 4.3 shows that the total amount of strain before failure is comparable in both directions: $\lambda \approx 0.7\text{-}0.9$. However, the stiffness and failure stresses are different; the transverse direction has a stiffer linear region and fails at ~1.0 MPa. In contrast, the longitudinal direction fails at only ~0.4 MPa. These results show clearly that strength is not vital to the chicken skin, as it is for the rabbit.

In order to understand the lack of strength of chicken skin, it was observed using a SEM. The behavior of the chicken skin in the tensile tests is clearly related to the microstructure of the skin, shown in Figure 4.4. Observation shows that (a) chicken skin which is made up of a dermis consisting of two parts: a thick spongy layer (labeled 1) with a thinner compact zone of two layers (labeled 2 and 3) beneath. The porous spongey structure is not dense with collagen fibers, and therefore makes minimal contributions to the strength of the skin. The two layers in the compact zone of the dermis are clearly visible in (a) and show two distinct and different orientations. Each layer is made of large fascicles

(which are made of fibers and fibrils), and the layers are independent of each other so that minimal interaction between layers is expected. This leads to the large differences in maximum stress between the transverse and longitudinal orientations; in the transverse orientation, the load is carried mainly by the lower (thicker) layer in the dermis while in the longitudinal orientation, the load is carried mainly by the upper (thinner) layer in the dermis. Therefore, the failure stresses are higher in the transverse direction. (c) and (d) show a close up of the fascicles, and the clear distinction between layers. While fibers are not immediately clear in these fascicles, by freezing and breaking the skin (e) we can see that the fascicles are made of bundles of fibers. Upon closer inspection (f), each fiber is made up of bundles of collagen fibrils. This structure is what leads to the anisotropic response of the chicken skin.

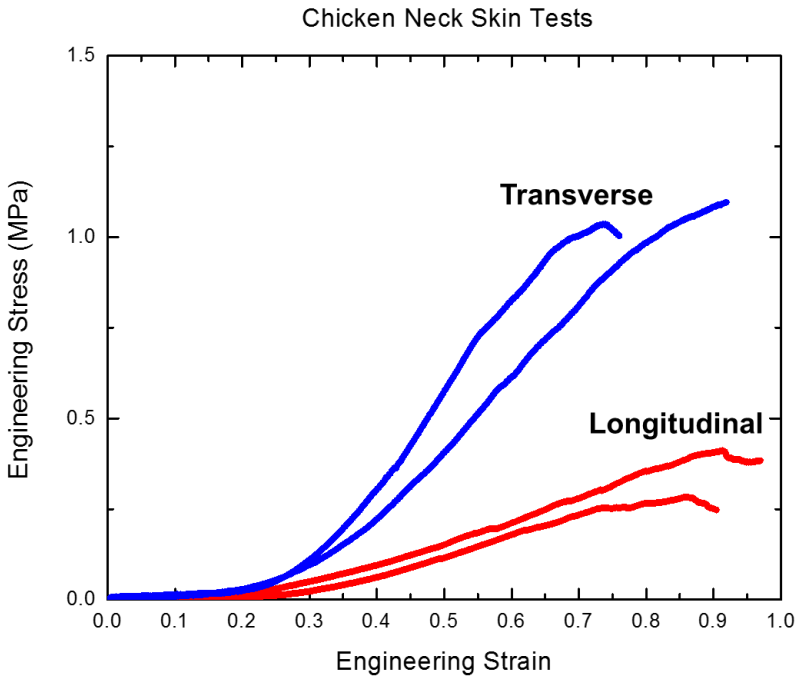

Figure 4.3: Tests on chicken neck skin at $\dot{\varepsilon}$=0.01. Longitudinal and transverse directions achieve similar maximum strains ($\lambda \approx 0.7$-0.9), but the transverse direction has a failure stress more than double that of the longitudinal direction.

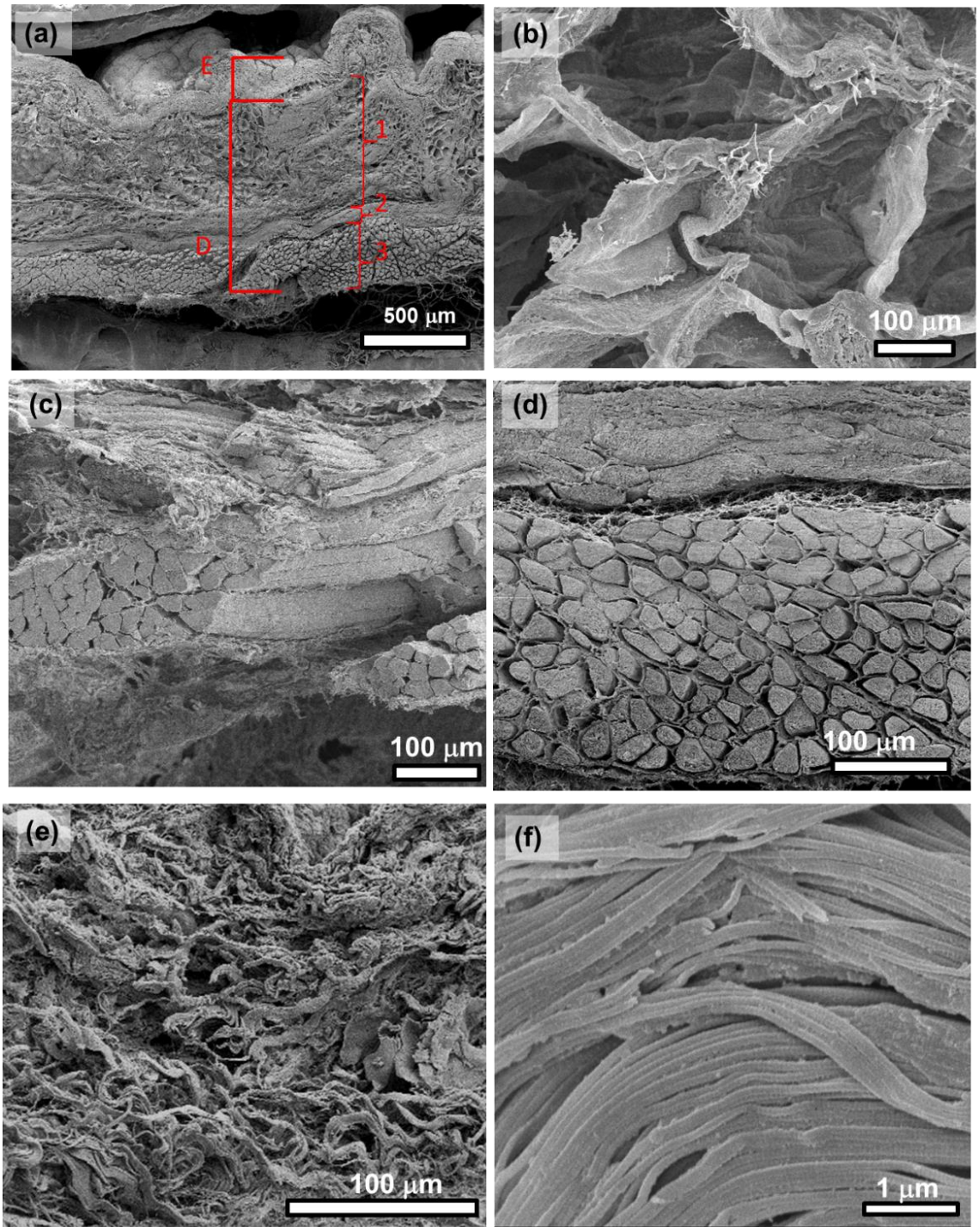

Figure 4.4: SEM of chicken skin. (a): chicken skin cut cross section. On the bottom (labeled D), there is a dense section of the dermis with two distinct layers. Above the thick section is a spongy region, which makes up the majority of the thickness of the skin, and the epidermis. The spongy pores are detailed in (b). (c) and (d) show the dense part of the skin. Both show large fascicles, and fibers are not distinguishable in these fascicles. (d) highlights the two layers, composed of fascicles in different orientations. (e) is a resection of the fracture surface of the skin. When fractured, the fascicles separate into fibers, and the fascicles are no longer distinguishable. (d) Upon closer observation of the fibers, collagen fibrils are observed.

4.2 Structure and mechanical response of rabbit skin

4.2.1 Background

Skin is an organ of utmost importance, and therefore has been the subject of in-depth research for many years. In 1831, anatomist and surgeon Guillaume Dupuytren observed a patient who claimed to have suffered elliptical stab wounds from a blade with a circular cross-section (a stylet). Due to his disbelief that a circular blade could cause these wounds, Dupuytren experimented on a cadaver and discovered that holes made with a circular knife stretched or closed into ellipses [215]. Karl Langer expanded on this observation and used an ice pick to perforate the skin of cadavers. From these results he proposed lines which exist throughout our body, representing the direction of maximum tension in skin and describing its anisotropy; these are known as Langer lines [216]. Maps of these lines are currently used by surgeons to ensure that incisions heal quickly and with minimal scarring. Multiple investigations have studied the skin of cat [82], frog [229], rhinoceros [105], and rabbit [58]. Skin is also inspiring modern technology. Replication of certain properties of the skin is highly desirable in many applications such as flexible electronics, soft robotics and prosthetics. The physicochemical and mechanical design principles of an artificial skin are described by Yannas and Burke [230]; Burke et al. [231] made successful use of a physiologically acceptable artificial skin to treat burn injuries. Today there are a variety of commercial skin substitutes which may be used for therapeutic and testing purposes [232]. Non-biological skins intended for other uses have also been produced; Tee et al. [233] created the first electrically and mechanically self-healing, highly extensible skin for electronics applications by using a composite inorganic nanostructured metal particles in an organic supramolecular polymer host. One interesting constitutive model for the

epimysium of muscle, somewhat resembling skin because of the collagen is in a wavy configuration, is the one by Gao et al. [234] which assumes a sine shaped collagen fiber integrated with the ground substance.

The objective of the investigation whose results are presented herein is to provide a mechanistic understanding of the deformation of skin under uniaxial loading. In order to accomplish this, experiments on rabbit skin are compared with a constitutive model based on the straightening of fibers. This model is validated by experiments on idealized circular segments, to which a viscoelastic component is added. This research extends recent work that focused on the tear resistance of skin [58].

4.2.2 Experimental and computational methods

4.2.2.1 Natural skin and testing

Butchered and cleaned sexually mature female rabbits were obtained immediately after slaughter from Da Le Ranch in Lake Elsinore, CA. The rabbits were then shaved and skinned. Rabbits were chosen due to a lack of an estrous cycle, which affects the mechanical properties of skin. The use of females reduced variation due to gender differences, so that the effects of varying strain rates may be effectively quantified. Specimens for characterization were frozen in water for preservation. Using surgical blades, skin samples with dimensions of $20 \times 5 \times 0.6$ mm were cut along directions parallel and perpendicular to the backbone of the rabbit. Uniaxial tensile tests were carried out on an Instron 3342 mechanical testing machine with a load cell of 500 N. The strips were gripped by the load cell and allowed to hang, at which point the load was tared. Samples were tested without preconditioning with a span of 12 mm at strain rates of 10^{-1} and $10^{-3}\ s^{-1}$, and deformation was measured grip-to-grip. These strain rates were chosen so that

they would span two orders of magnitude and provide insight into the viscoelastic effects of skin, while remaining within the limitations of our equipment. To retain hydration during tests, phosphate-buffered saline solution was sprayed on the samples periodically.

4.2.2.2 Scanning and transmission electron microscopy

For SEM observation, undeformed rabbit skin was immersed in 2.5% glutaraldehyde for 3 h to fix the structure, and subsequently dehydrated with an ascending ethanol series. Strips of skin were cut using a surgical blade. Some samples were fractured by freezing in liquid nitrogen. The samples were then dried in a critical point dryer (Tousimis Auto Samdri 815A). The surfaces were sputter coated with iridium using an Emitech K575X and examined using a FEI SFEG ultra-high resolution SEM. For TEM observation, the skin was cut using a scalpel into 5 mm strips. A primary fixation was performed by immersing the tissue sections in 2.5% paraformaldehyde, 2.5% glutaraldehyde in 0.1 M cacodylate buffer for 2 hours. Post-fixation was done for 12 hours in 1% osmium tetroxide in 0.15 M cacodylate buffer. The specimens were then stained in 1% uranyl acetate for 12 hours and dehydrated with an ascending ethanol series, followed by a 1:1 ratio of 100% ethanol and 100% acetone, and finally 100% acetone. Samples were subsequently embedded in Spurr's low-viscosity resin, polymerized at 48 °C for 48 hours, and sectioned parallel and normal to the skin surface using a Leica Ultracut UCT ultramicrotome and a Diatome diamond knife. Sections 70-100 nm thick were placed on copper grids for TEM observation, and post stained with Sato lead for 1 minute.

4.2.2.3 Synchrotron X-ray characterization

Uniaxial tensile samples were prepared using a surgical blade and sprayed lightly with phosphate-buffered saline to preserve hydration during testing. These samples were

loaded in uniaxial tension at 25 °C, and data was collected throughout the experiment. Biaxial tensile samples were stretched by hand using an embroidery hoop to ~50% biaxial strain, measured optically using a grid drawn on the skin. This is consistent with studies by Lanir and Fung [106], which showed that the heel region of a biaxially stretched sample occurs at stretch ratio of ~1.5. The samples were then fixed in 2.5% glutaraldehyde in order to preserve the stretched structure, followed by dehydration using a graded ethanol series. A surgical blade was used to cut samples for observation from the stretched and fixed skin. All samples were exposed to X-rays at beamline 7.3.3 at the Advanced Light Source synchrotron at the Lawrence Berkeley National Laboratory. A Pilatus 2M detector was used to collect data at a distance of ~ 4 meters from the sample.

4.2.2.4 Simulated tests

A beam of connected circular segments with a circular cross-section was used to model the tensile behavior of a single collagen fibril. The response was verified using a steel beam shaped into circular segments with radius, r, of 30, 60 and 120 mm and angle, ω, of 30°, 50°, 70°, 90°, 110° and 130°. The beams were tested in quasistatic tension to verify the model. The geometry is observable in Figure 4.9.

4.2.2.5 Calculational techniques

Model geometry was drawn using Solidworks, and imported into COMSOL Multiphysics. One face on the end of the wire was constrained to its initial location, but rotation was allowed. A force was applied to the face on the other end of the wire and pulled along the x axis, while allowing rotation of the face. These conditions avoided errors due to singularities, and resulted in displacements which were converted to strains.

Castigliano's theorem was used in the derivation for the straightening of an initially circular segment of a steel wire under tension. Results were plotted in MATLAB.

4.2.3 The hierarchy of the dermis

The dermis is the structural component of skin. It gives it the mechanical response required for protection. Collagen (80-90% of dermis) and elastin (3-6%) are the principal proteins responsible for the mechanical properties of the skin [235]. The dermis has been described as an arrangement of wavy fibers, of 2-10 μm in cross-section, which are made of randomly oriented fibrils of ~100 nm in diameter, as shown in Figure 4.5a. However, Figure 4.5b, which shows intact skin, reveals a well organized structure where the top surface is what appears to be a single layer collagen fibers, aligned in a distinguishable direction. Figure 4.5c shows one single layer being peeled from the dermis beneath, illustrating that individual layers have some independence from the layers around them. Figure 4.5d shows a skin cross-section, where the layers are observable, and Figure 4.5e shows the ends of cut collagen fibers, revealing their shape and cross-sectional dimensions, which are ~2 by ~10 μm.

The defining small scale features of collagen fibers are more closely observed in Figure 4.6 by TEM. Figure 4.6a is a TEM of the highly ordered and aligned collagen fibrils within a fiber, in which the characteristic banding present on collagen fibrils is clearly visible. A cut nearly parallel to the skin surface (Figure 4.6b) reveals a variety of fibers with fibrils in various orientations, and a cut perpendicular to the surface (Figure 4.6c) shows fibers of ~2μm thickness stacked atop each other in the skin.

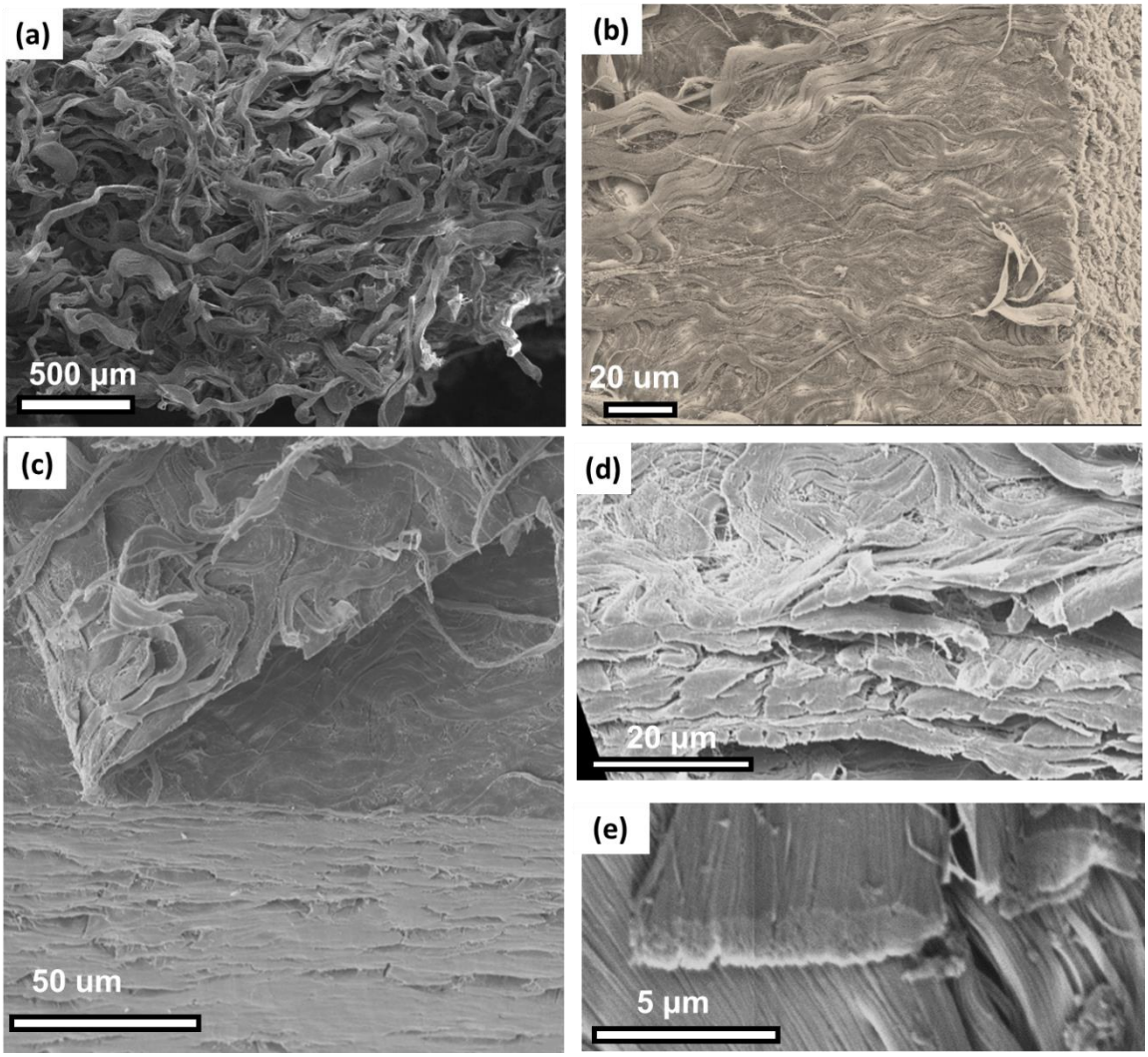

Figure 4.5: Observation of collagen in rabbit skin by SEM. (a) Fracture surface of skin frozen in liquid nitrogen reveals wavy fibers in apparent disorder. (b) Skin prepared through fixation and peeling: single layer of collagen fibers is observed in plane with the surface of the skin. (c) One single layer of collagen fibers is peeled from the stack of collagen layers comprise the thickness of the skin. (d) Several layers of collagen sheets atop each other. (e) Cross-section of single collagen fiber.

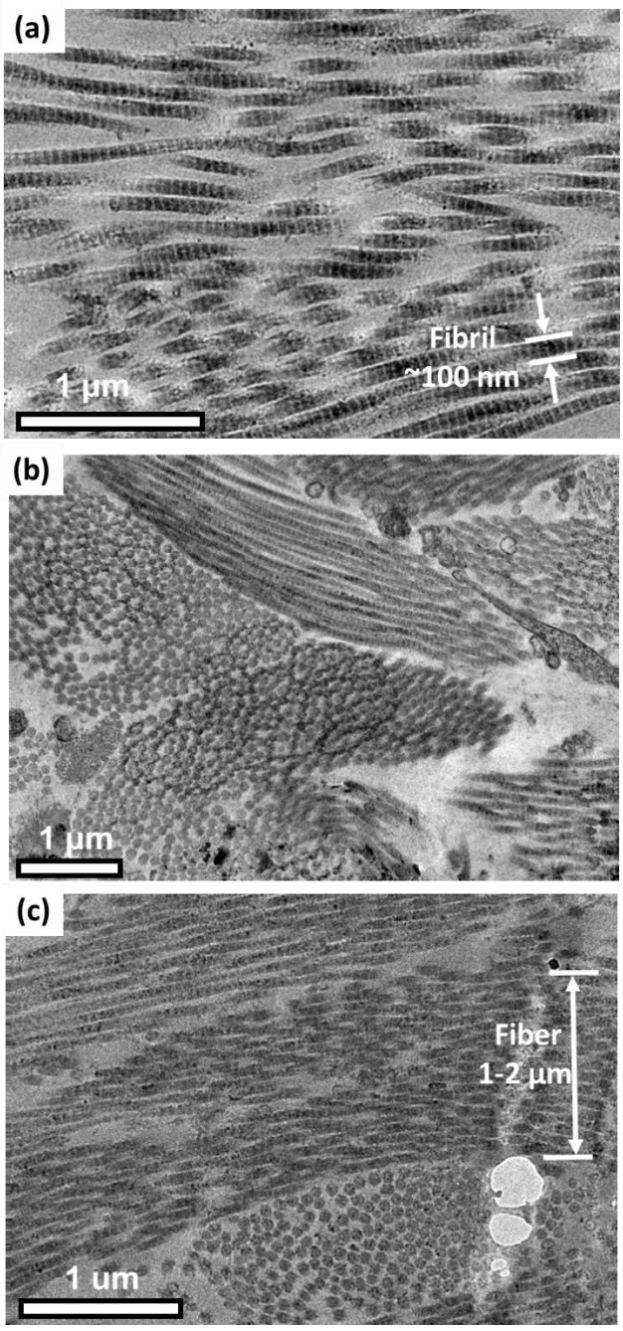

Figure 4.6: The fibers in skin observed by TEM. (a) TEM shows aligned collagen fibrils in one fiber. (b) TEM cross-section shows multiple collagen fibrils of different orientations. (c) TEM of three collagen fibers stacked vertically.

A full hierarchical description of skin is presented in Figure 4.7. Our understanding of the structure incorporates the presence of lamellae with preferred fiber orientations seen in Figure 4.5b; adjacent to the renderings of the hierarchical levels are transmission and

scanning electron microscopy images of each layer, down to the fibrillar level (Figure 4.7b-d).

The smallest spatial scale is well understood for collagen. Fibrils, as seen in Figure 4.7b, are approximately 50 nm in diamiter and form fibers. However, the organization of fibers into lamellae is less well characterized. We have identified that fibers assemble into lamellae parallel to the surface of the skin. The approximate cross-sectional dimensions of these 'flat fibers' or lamellae are ~2 um thickness and ~10 um in width. They form a wavy pattern which we model in Section 4.2.5 as consecutively connected circular segments, but it has also been described as sinusoidal and helical (although it is clear that these fibers are not helical). Figure 4.7c shows an SEM image in which multiple fibers are parallel to each other in the skin. These lamellae are arranged in distinct layers where each layer has a specific orientation. In Figure 4.7d, a cross-section of the dermis reveals many flat collagen fibers stacked upon each other. For the rabbit skin, the number of fiber/lamellae layers is obtained by dividing the dermis thickness (500 μm) by the thickness of each lamella: (2 μm); it is approximately 250. Non-collagenous elements, the most prominent of which is elastin, are not shown in Figure 4.7 because their relative contributions to the skin's mechanical properties is less important. Additionally, structural details of the elastin network in skin are currently not well defined.

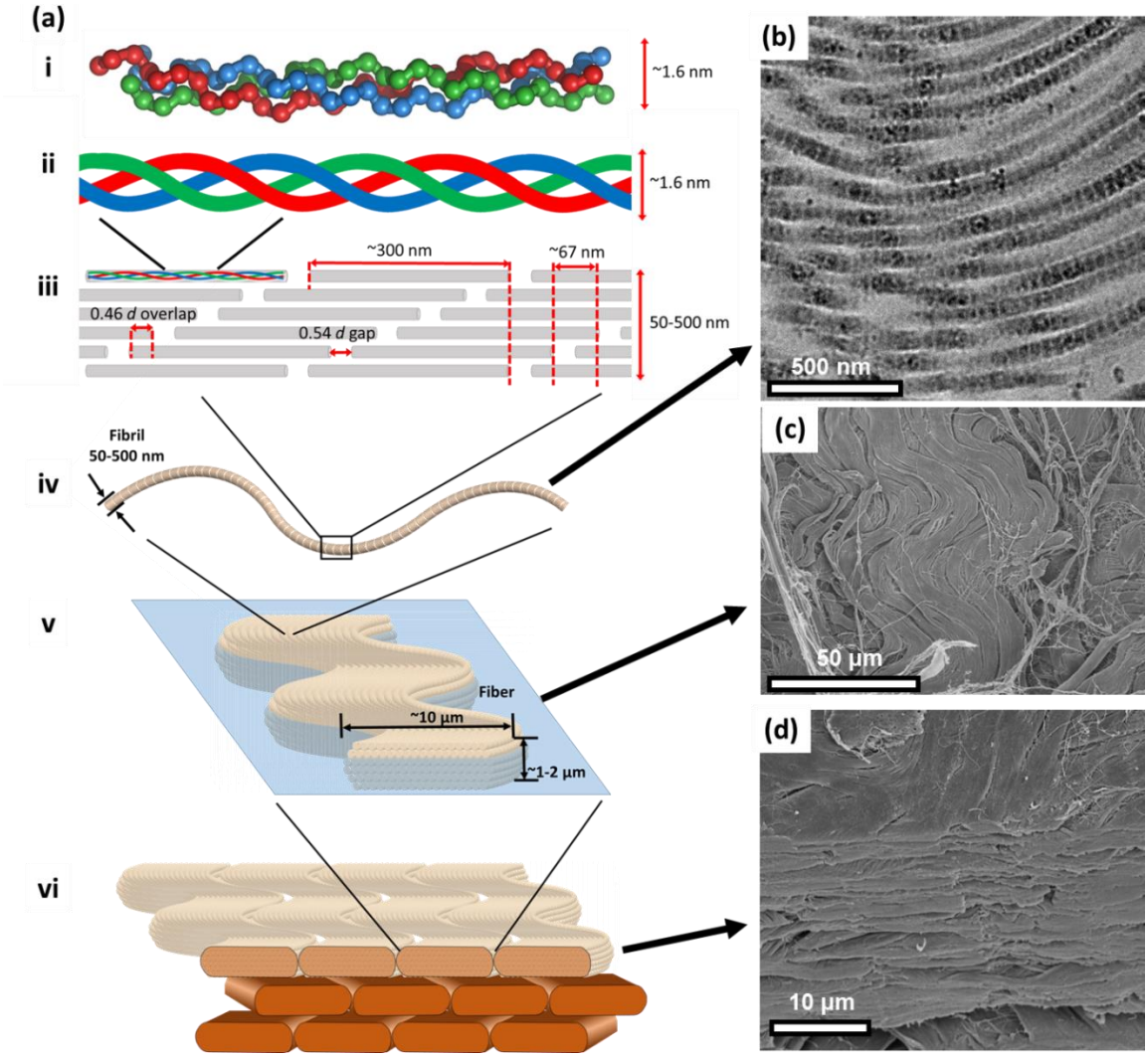

Figure 4.7: The full hierarchy of collagen in the dermis. (a) Schematic which represents the hierarchy of skin. The hierarchical order is: (i) Tropocollagen chains form right handed triple helices. (ii) Schematic of i. (iii) The fibril is formed through the quarter-staggered arrangement of tropocollagen molecules which leads to a gap region, an overlap region, and characteristic d-banding. (iv) Fibrils are long strands, and the d-banding is clearly evident. (v) Many fibrils are arranged to form wavy parallel fibers, which are flattened in the plane of the skin. (vi) Parallel fibrils form lamellae; these lamellae exist through the thickness of the skin. (b) Transmission electron micrograph of collagen fibrils that are curved and parallel, and form a fiber. (c) Parallel fibers in a single lamella of the skin. (d) Cross-section of skin with multiple lamellae

4.2.4 Deformation imaged by small angle x-ray scattering

Previous studies [58, 236] measured the degree of fibril orientation in rabbit skin under uniaxial tension using Small Angle X-ray Scattering (SAXS). Both studies used an orientation index and conclude that the fibrils align with the tensile direction under loading,

but information regarding the initial orientation is inconclusive due to the waviness of the skin which has a high influence on the initially recorded SAXS patterns. Therefore, two deformation paths, shown in Figure 4.8, were applied to the skin and analyzed by SAXS: uniaxial and biaxial extension. In uniaxial extension the progression of deformation was characterized along the stress-strain curve at the points marked. Four mechanisms of deformation were found to operate: straightening, rotation (toward the tensile axis), elastic extension of fibers, interfibrillar sliding, and finally fracture [58].

Two positions in the uniaxial extension are marked by open circles on the stress strain curve in Figure 4.8a. They correspond to the initial configuration and the one at the maximum load. The original curved configuration of the collagen fibers and multiple orientations of the lamellae result in an in-plane equiaxed structure, manifested in the SAXS pattern by circular rings which have an intensity that is independent of orientation (Figure 4.8b). As uniaxial deformation proceeds there is a gradual alignment of the fibers with the tensile axis. This is shown in Figure 4.8c: the SAXS pattern exhibits a higher intensity in the tensile direction (vertical axis).

Biaxial extension straightens the fibers and ideally should enable each lamella to retain its original orientation. Although the progression of biaxial stretching was not monitored, segments of skin subjected to biaxial stretch and then fixed were analyzed. Two representative scattering patterns are shown in Figure 4.8d,e. The intensity of the SAXS pattern across the circle corresponds to the fraction of the 250 (estimated) lamellae in this orientation. This radial intensity variation is plotted in Figure 4.8f for the four SAXS scans (b, c, d, e). The initial intensity is homogeneous and does not show much variation along the orientations. Uniaxial stretching dramatically changes the pattern and shows the

alignment of the collagen fibers with the tensile axis. Interestingly, biaxial stretching introduces some asymmetry in the orientation of the collagen, with an increased intensity in two directions. We attribute this to the preferential alignment of collagen fibers (shown by the analysis and a simplified schematic in Figure 4.8g), which is manifested by the Langer lines. Thus, similar to rhinoceros [105] and fish [237] skin, there is some anisotropy in the initial orientations of collagen fibers in the lamellae of rabbit skin.

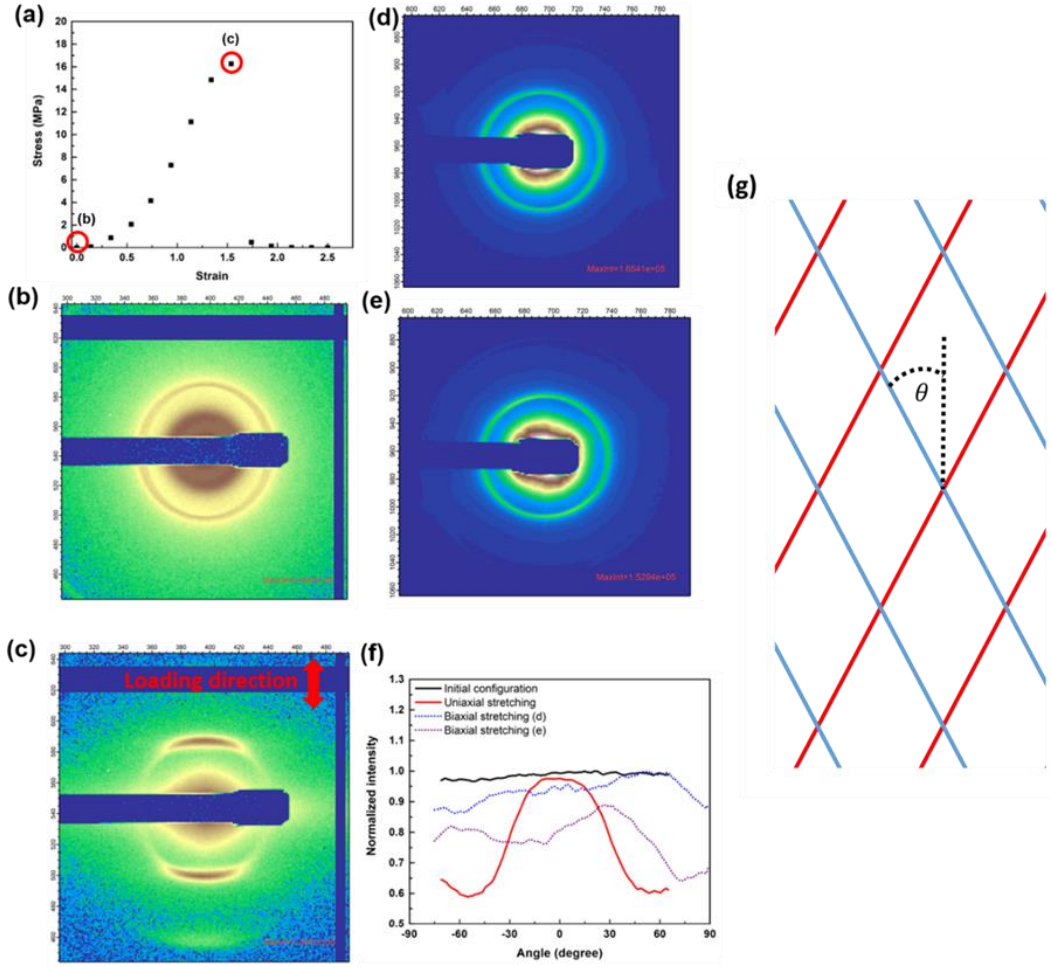

Figure 4.8: SAXS Results show skin has two principal orientations of fibers. (a) Stress-strain curve of the skin; (b) SAXS pattern of the natural skin before uniaxial stretching; (c) SAXS pattern of the skin at the maximum stress (direction of tension shown by arrow); (d, e) SAXS pattern of two fixed skin samples prepared by biaxial stretching; (f) Comparison of SAXS data showing two orientations with increased intensity in biaxially stretched skin, corresponding to two preferred collagen orientations, as seen in rhinoceros [105] and fish [237]. (f) Schematic showing two preferential lamellar directions; these are the two most common of many orientations.

4.2.5 The constitutive model

4.2.5.1 Elastic component: derivation

The stiffness of collagenous materials is a consequence of the arrangement of the collagen structures and their geometric distribution. For example, the toe region experienced by many biological materials corresponds to the straightening of the curved arrays of fibrils; when the fibrils are straight the stiffness increases drastically, although it rarely approaches that of the collagen constituents due to the sliding of collagen fibers and fibrils.

The strength of collagenous materials is lower than that of collagen fibrils, which are reported to vary from 200 MPa up to several GPa [238]. Because the strength of skin is well below this, reaching at most ~50 MPa (in rhinoceros), failure in tension is the consequence of interfibrillar and interfiber effects, namely the strength and viscoelasticity of bonds between fibrils. The viscoelastic contribution to the failure of skin is readily apparent when observing the fracture strength of rabbit skin measured at differing strain rates: only ~8 MPa at a strain rate of 10^{-3} s^{-1} compared to ~15 MPa at a strain rate of 10^{-1} s^{-1} [58].

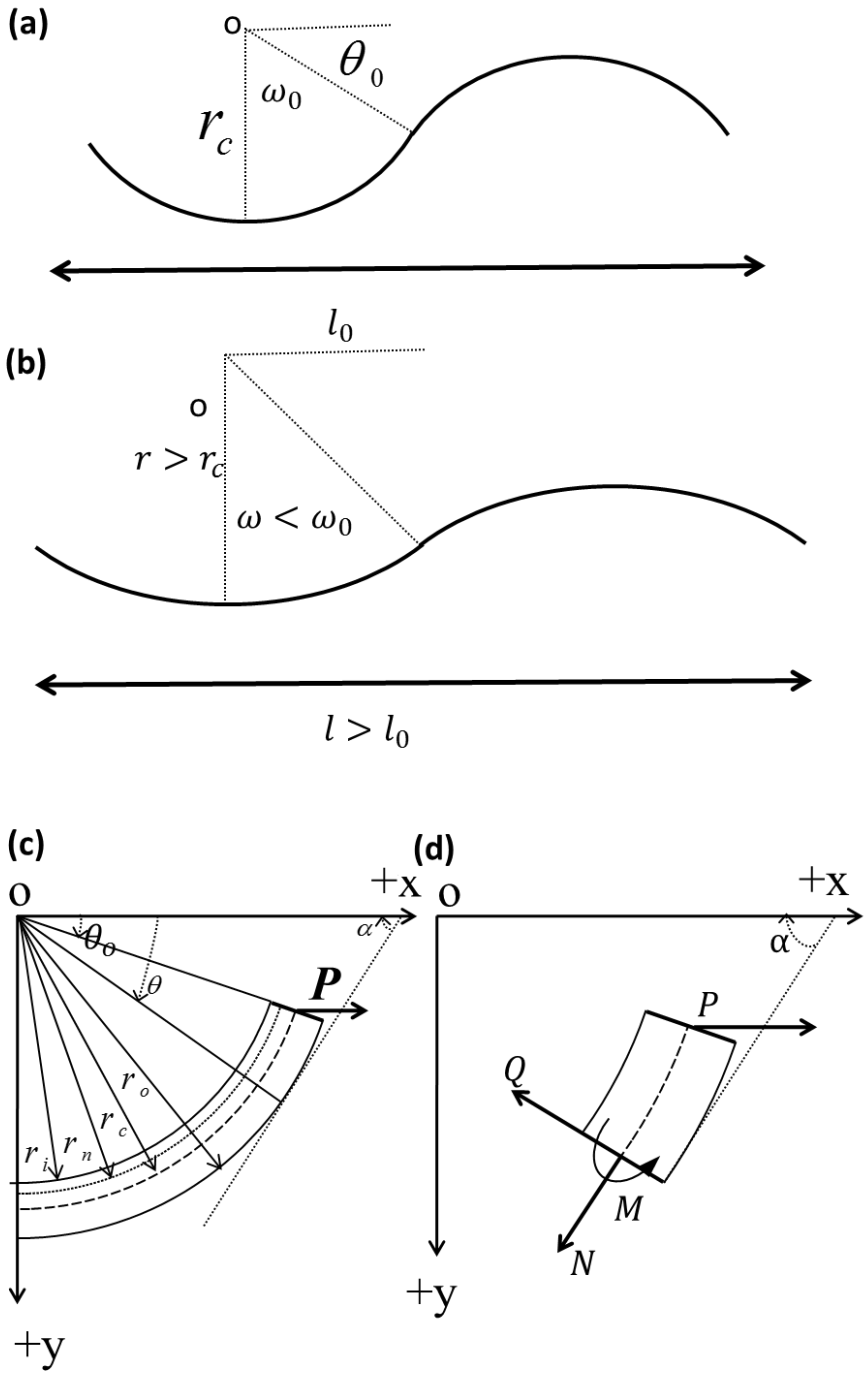

Figure 4.9: Circular segment model of collagen. (a-b) Behavior of model under extension. Initial curvature ω_0 decreases to ω. Initial radius r_c increases to r. Total length increases from l_0 to l. (c) A section of the circular segment collagen model, showing relevant parameters which are required for the strain energy and corresponding stress calculation using Castigliano's theorem. (d) Free body diagram of a wire segment showing P (applied force). The method-of-sections replaces the removed part with N (normal force), Q (shearing force), and M (bending moment).

In order to better understand the mechanical response of skin, we model the response of a single collagen fibril. The underlying assumption of this model is that these repeating units dictate the macroscopic material response; by quantitatively characterizing the elastic response of one fibril and the viscous interactions with the matrix we gain an understanding of the mechanical response. Materials consisting of collagen fibrils have been modeled using different shapes including zig zags [93], helices [61, 96], and a sine function [94, 95]. The limitations of these models were analyzed by Sherman et al. [238], and a circular segment model was suggested as an improved representation of the *in vivo* shape of collagen. Thus, these fibrils are modeled as circular segments, shown in Figure 4.9a.

In the circular segment model, adjacent segments connect with no discontinuities. Under applied strain, the radius of curvature increases, leading to a decreased segment arc, measured in degrees. One characteristic of these semicircular segments is that there are no discontinuities at their junction, independent of extension. The mechanism of deformation is graphically illustrated in Figure 4.9b. Based on the assumed shape and deformation method, the tensile response of a fibril may be calculated using Castigliano's theorem. The problem that must be solved is the following: if a curved beam is subjected to a force $\boldsymbol{P}$ at the ends; determine the load-displacement relationship. The required geometric measurements are schematically described in Figure 4.9c,d; Table 4.1 shows the parameters used in the derivation. In addition to these parameters, relationships between the force, shear force, and bending moment applied to the beam are necessary. These relationships are based on Figure 4.9d which shows a cut of the beam. Q is the shearing force acting on the cross-section:

$$Q = Psin\alpha \tag{43}$$

N is the normal force acting on the cross-section:

$$N = Pcos\alpha \tag{44}$$

and M is the bending moment:

$$M = -P\left(y - r_c \sin\theta_0\right) \tag{45}$$

The strain energy is expressed as the sum of components due to bending, normal force, and shear force, whose equations may be found in Beer [239]. The total strain energy is the sum of the three components of the strain energy obtained from Equations A16, A18, and A20 (details provided in Appendix A.3). From Castigliano's second theorem, the displacement at the point of application of an external force may be expressed as [239]:

$$u = \frac{\partial U}{\partial P} = \frac{\partial U_1}{\partial P} + \frac{\partial U_2}{\partial P} + \frac{\partial U_3}{\partial P} \tag{46}$$

The extension *u* in the direction of applied load P is determined using Equation 46. Since $l_0 = r_c \cos\theta_0$, strain is:

$$\varepsilon = \frac{u}{l_0} = \frac{u}{r_c \cos\theta_0} \tag{47}$$

From the definition of Young's modulus, strain may also be expressed by the ratio of stress/elastic modulus [240]. The modulus is replaced with a pseudo modulus, E', as it is not the material modulus, E, but the result of both structure and material modulus.

$$E' = \frac{P/A}{\varepsilon} = \frac{r_c \cos\left(\theta_0\right) P/A}{u} \tag{48}$$

Substituting Equation 46 into Equation 48:

$$E' = \frac{r_c \cos(\theta_0) P/A}{\frac{\partial U_1}{\partial P} + \frac{\partial U_2}{\partial P} + \frac{\partial U_3}{\partial P}} \tag{49}$$

Accounting for eccentricity and inserting the results into Equation 49 leads to a representation of the pseudo modulus in terms of various shape factors, where $\delta = \frac{H}{r_c}$, a_y=1.33, and E/G=2(1+υ):

$$E' = \frac{\mathrm{E} \cdot \cos\theta_0}{\phi_2(\theta_0) + \phi_3(\theta_0)\frac{a_y E}{G} + \phi_1(\theta_0)\frac{1}{\left(1 - \frac{\delta^2/4}{2\left(1 - \sqrt{\left(1-\frac{\delta}{2}\right)\left(1+\frac{\delta}{2}\right)}\right)}\right)}} \tag{50}$$

E’ is a function of the shape of the circular wire segment. Specifically, the shape parameters required to calculate E’ are thickness (H), the initial radius (r_c), initial degree of curvature ($\theta_0 = 90 - \omega_0$), and the material modulus E. Holding arc length constant, the relationship between the strain (ε), current radius (r), initial radius (r_c), current degree of curvature (ω), and initial degree of curvature (ω_0) is:

$$\varepsilon = \frac{l - l_0}{l_0} = \frac{r\sin\left(\frac{r_c}{r}\omega_0\right) - r_c\sin(\omega_0)}{r_c\sin(\omega_0)} \tag{51}$$

After several additional steps, one arrives at the relationship:

$$\sigma = \int E' \left\{ \frac{\csc\omega_0}{r_c r}\left[r\sin\left(\frac{r_c\omega_0}{r}\right) - r_c\varphi_0\cos\left(\frac{r_c\omega_0}{r}\right)\right]\right\} dr \tag{52}$$

Equation 52 is integrated from r_c to r to produce a stress vs strain relationship based on the initial circular shape.

Table 4.1: Parameters used in derivation of constitutive equation

Symbol	Parameter
ω_0	initial angle of waviness
ω	current angle of waviness
r_i	inner radius of curvature
r_o	outer radius of curvature
r_c	radius of curvature at the centroidal axis
r_n	initial radius of curvature for the neutral axis
e	eccentricity, $e= r_c- r_n$
A	cross-section area
H	height of the curved beam, $H=r_o- r_i$,
θ_0	description of degree of curvature
θ	description of location on the semicircular curve

4.2.5.2 Elastic component: comparison of experimental, analytical and computed results

In order to validate the model, macroscale tests described in Section 4.2.2 were performed. By comparing testing results to calculations, we confirm that our model is accurate. The tension setup and stress mapping from a simulation are also shown in Figure 4.10a. The results are illustrated in Figure 4.10b for three curves with 30 mm radius and $\omega_0=70^0$; one from calculations (solid line), one from tensile tests (dashed line), and one from simulations (dotted line). There is excellent agreement among them. Figure 4.10c shows the dramatic effect that varying the curvature can have on the elastic response, as larger values of ω_0 substantially increase strain achievable at low stresses. Similarly, calculations with a constant degree of curvature but different radii are shown in Figure 4.10d, indicating the profound effect that radius (more precisely, ratio of beam thickness to radius) can have on test results. In the biological context of collagen, this indicates the substantial effect that the thickening of fibrils (often associated with ageing) may have on the mechanical response of collagenous materials.

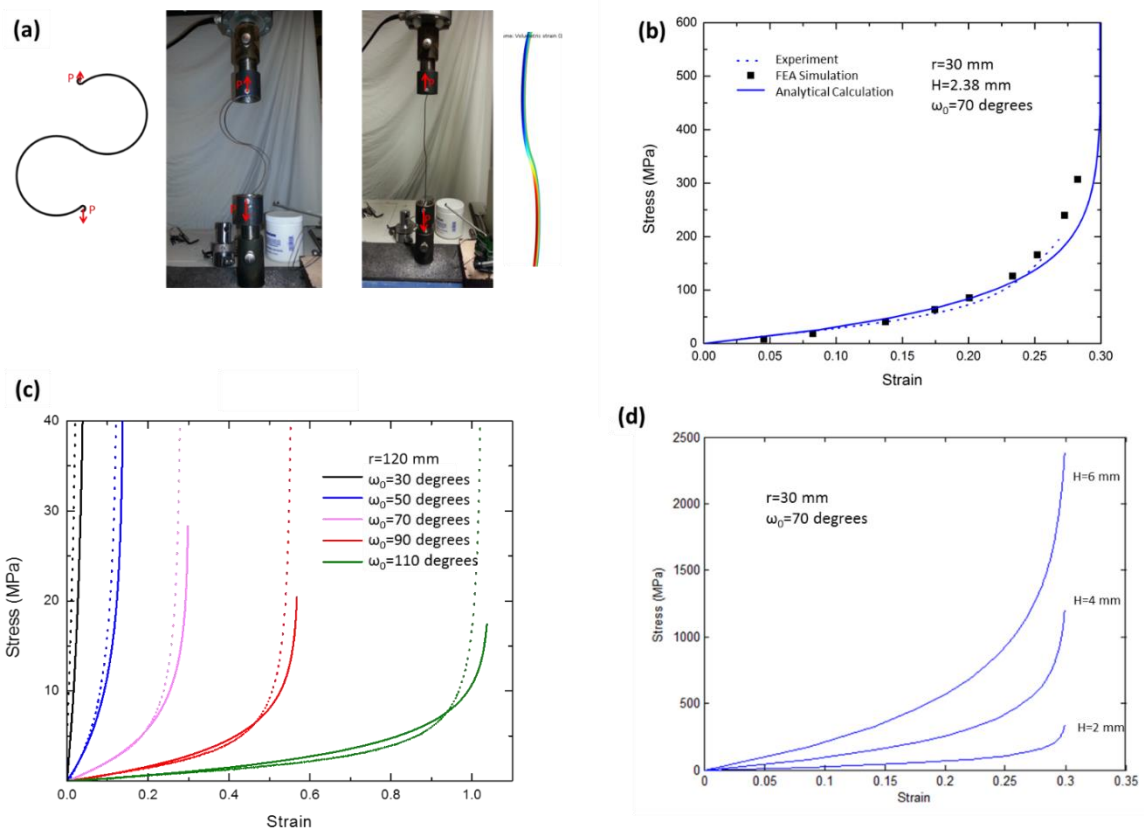

Figure 4.10: Validation of elastic model. (a) Tests performed by mechanical testing (left) and finite element analysis (right). (b) Comparison of results obtained by testing, calculations, and simulations for r=30 mm and ω_0=60 show close agreement. (c) Calculation and testing results from various degrees of curvature while holding r=30 constant show close agreement between calculations and tests, and illustrate the drastic effect that increasing the degree of curvature may have on both stress and strain. (d) Calculation results showing the effects increasing radius for $\omega_0=70^0$. Increasing radius reduces the ration of beam thickness to radius, which significantly reduces stress values.

4.2.5.3 Elastic component: application

The complete calculation of the elastic component of stress involves three stages:

1) Stress on a straightening circular segment is calculated. Fibril dimensions are applied, as estimated from SEM images. Strain is calculated using Equation 51, and stress is calculated using Equation 52.

2) The calculated strain from Equation 51 is divided by the cosine of the estimated average degree of misorientation from the tensile axis, determined by comparing the onset of the heel region of different orientations. This is based on the biaxial

SAXS data which suggests two preferred fibril directions, as shown in Figure 4.8f. This step accounts for the ability of fibrils to rotate.

$$\varepsilon = \frac{\varepsilon_{semicircular}}{\cos\left(\theta_{misorientation}\right)} \tag{53}$$

3) A maximum stiffness is applied which reflects the physical response of the skin [58], and is a property of collagen fibers in tension:

$$\sigma_{shape,orientation,\,fiber-stiffness} = \int \min\left(\frac{d\sigma_{shape,\mathrm{orientation}}}{d\varepsilon}, E_{\max}\right) d\varepsilon \tag{54}$$

This effect may be due to the stretching of the bonds between fibrils and fibers, and the continued recruitment of fibrils. These affect the true strength and stiffness of collagen fibrils, which are not reached in the skin, and leads to the presence of a linear region which is at a substantially decreased stiffness compared to that of a collagen fibril.

4.2.5.4 Incorporation of viscosity into the elastic model

Uniaxial tests show clear differences from the models which are attributable to the viscosity of skin [58]. The viscous effects of skin dissipate a large amount of energy, and lead to lower failure strengths, due to the larger sliding time. Previous descriptions of the elasticity and viscoelasticity of skin have resulted in a number of constitutive equations and mathematical curve fits. However, no relationship which directly considers the physical shape, viscosity, and orientation effects of skin has been successfully developed, other than the model by Yang et al [58]; it approximates the tensile response of the skin with circular segments in a Maxwell arrangement, and produces acceptable results for curves with a small toe region. This relationship, representative of a spring and dashpot in

series, leads to a large extension with low levels of stress at a sufficiently low strain rate, and decaying stress when strain is no longer applied. However, Shaw and MacKnight [241] suggested that the Maxwell model is a poor representation of viscoelastic bodies such as polymers.

In the case of rabbit skin, a low strain rate leads to reduced maximum stress levels; however, the amount of extension is not largely affected when the strain rate varies by a factor of 100. Therefore, we apply a Kelvin-Voigt model, which is better suited for use in a viscoelastic solid [241]. The spring, shaped as consecutively connected circular segments, is in parallel with a dashpot. As the parallel spring and dashpot experience equivalent strain, the total stress is equal to the sum of the elastic stress and viscous stresses.

The elastic stress is obtained from Equations 52 and 54. There are two regimes: straightening of the fibers (Equation 52) and their elastic extension; both are incorporated into Equation 54. For the viscous component, the general form is used (e. g., Meyers and Chawla [242]):

$$\eta = K\dot{\varepsilon}^n \tag{55}$$

Equation 55 adjusts viscosity based on strain rate; $n<0$ is shear thinning, $n=0$ is Newtonian viscosity, and $n>0$ is shear thickening. Shear thinning is a reduction in viscosity with increasing strain rate. Finlay [243] studied viscosity in human skin, and concluded that viscoelastic models of skin should account for shear thinning phenomenon if the theoretical results were to bear any relation to real life data under both static and dynamic conditions. The viscous stress occurs within the ground substance that connects fibers and fibrils of collagen. During the toe region of the curve, reorientation does not involve viscous effects in a significant manner. In the heel and linear region, the fibers are stretched

and the viscous effects become more prominent. Therefore, the viscous component of stress is applied proportionally to the ratio of current strain (ε) to the strain at the onset of the heel, (ε_{heel}), raised to the power of *a*; this is the fibril recruitment fitting parameter. Each viscoelasticity parameter (*a*, *K*, *n*) has a unique effect on the response. The parameter *a* effects the rate at which viscosity is applied to fiber recruitment; a value of 1 means that the fiber recruitment (and application of viscous stress) is proportional to the strain. As *a* increases above 1, low strain recruitment and corresponding viscous stress is reduced. *K* assigns a conventional viscosity value, which is adjusted by *n*, in order to account for the shear thinning. This describes the gradual recruitment of fibers which increases the viscous contribution throughout extension. The resulting equation is:

$$\sigma(\eta) = \left(\frac{\varepsilon}{\varepsilon_{heel}}\right)^{a} \eta\dot{\varepsilon} = \left(\frac{\varepsilon}{\varepsilon_{heel}}\right)^{a} K\dot{\varepsilon}^{n+1} \tag{14}$$

These required inputs are summarized in Table 4.2, which includes values from literature (a), estimated from microscopy and experimental results (b), and parameters which were estimated from fitting (c). Since there is so much variation in individual tests, the fitting can only be approximate.

The four mechanisms of deformation—elastic straightening, stretching, reorientation, and sliding are accounted for in the calculated response of the skin shown in Figure 4.11. It can be seen that the model accurately describes the response of transverse and longitudinal skin. These calculations show that the principal features of deforming skin are captured by the constitutive equation proposed, and are directly related its microstructure and mechanical response.

Table 4.2: Parameters used in elastic and viscoelastic models

Fitting parameters	Values
Modulus of collagen fibril	1 GPa[a]
Thickness of collagen fibril	0.13 μm[b]
Radius of curvature of collagen	7 μm[b]
Degree of curvature of collagen	70 degrees[b]
Average misorientation (from	70 degrees[b]
E_{max} (modulus)	10 MPa[c]
a (fiber recruitment parameter)	2[c]
K (viscosity coefficient)	25 Pa·s[c]
n (viscosity parameter)	-0.6[c]

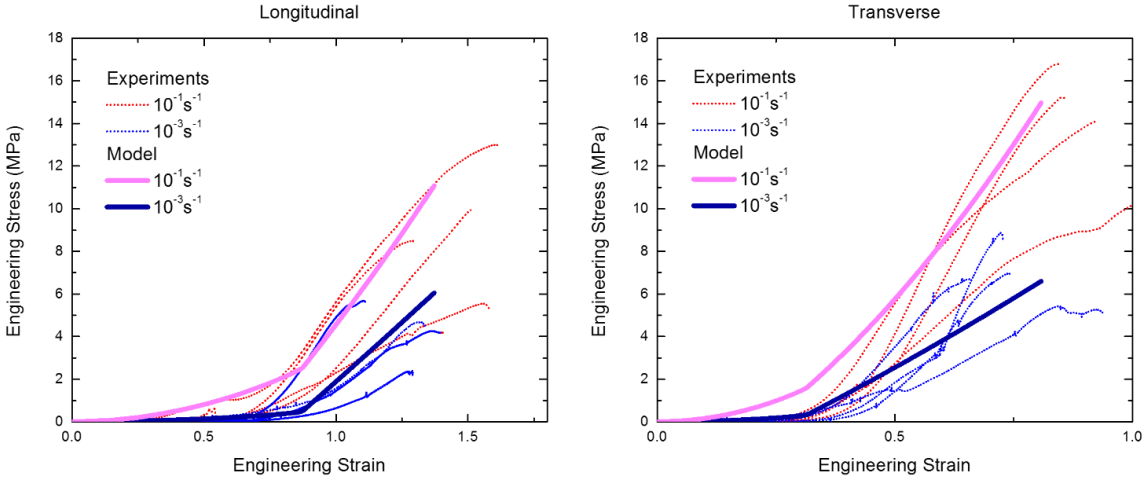

Figure 4.11: The model as applied to test results. Tensile engineering stress-engineering strain plots made using the constitutive model are shown with the solid lines, while physical tests are shown with the dotted lines. Experimental results on rabbit skin along two orientations: longitudinal (perpendicular to Langer lines) and transverse (parallel to Langer lines) [58]. Note considerable variability among experimental results, a characteristic of skin. The model is shown to match the experimental results reasonably well, and intrinsically all values are based in the physical processes that are occurring in the skin.

4.2.6 Summary

This investigation connects the mechanical response of rabbit skin in uniaxial extension to the changes in the structure by providing a new constitutive equation that captures the most important processes. The following principal results are obtained:

- The dermis of the rabbit is composed of sheets or lamellae which are assemblages of curved parallel collagen fibers. In these assemblages, each layer is comprised of curved fibers with a preferential direction, different layers having different orientations. It is estimated that 250 sheets with different orientations comprise the dermis of rabbit. The fibers are, in turn, composed of fibrils.
- In tension, the collagen in these sheets straightens and aligns with the tensile direction. This requires considerable interfiber shear and sliding, and generates viscous stress as alignment leads to high stress and strain values. The combined elastic and viscous effects lead to the unique tensile response of skin, as well as its strength, versatility, and tear resistance.
- The presence of some extremely wavy fibrils is responsible for the large amounts of strain that the skin can undergo before straightening. As the less curved fibrils straighten and align, the more curved remain non-aligned. As stretching continues, the previously straight fibrils break and misalign, transferring the load to the straightening curvier fibrils. The variance between fibrils results in a large heel region as certain fibers enter their linear region, and a large failure region due to the successive breaking of the most highly stressed fibrils.
- Processes that occur in the skin during tension are represented in a physically-based constitutive equation in which the waviness is modeled as circular segments whose radius increases with extension. By including the most important physical processes in our calculations, namely straightening, stretching, reorientation and sliding (through viscosity), the stress-strain response is successfully modeled.

- This knowledge has the potential to affect the development of new hyperplastic materials and synthetic skin. Biodegradable skin-like scaffolds are crucial for the improvement of integration and quality of healing; the large influence that material properties such as substrate stiffness can have on tissue growth is being increasingly recognized. By more precisely understanding the wavy structure and how it determines the stiffness of skin, biological elements of healing are likely to perform their functions more effectively, while the potential discomfort of having an inextensible or stiff synthetic skin attached to the body may be avoided.
- Our mechanical results are limited to uniaxial testing, in which most fibers reorient parallel to the loading direction. A future possibility is to apply the model to biaxial tension; this would reduce the tensile alignment, and result in a response dominated by the straightening and sliding of collagen, but with limited reorientation.

Additionally, understanding of the layered structure which leads to the response of skin may motivate the development of future engineering materials which mimic its anisotropic response, large extensibility, or tear resistance.

4.3 On the tear resistance of rabbit skin

4.3.1 Introduction

Vertebrates are covered with organ skin, which provides protection from the environment, temperature regulation, camouflage, thermal energy collection and a host for embedded sensors [213]. Skin consists of three layers, epidermis, dermis and endodermis, with mechanical properties dictated primarily by the dermis, the thickest layer. Its major constituents are type-1 collagen and elastin: collagen provides mechanical resistance to extension, whereas elastin accommodates the deformation [214]. To fulfill its

multifunctional role, skin must possess a tailored mechanical response to accommodate the body's flexibility and movement coupled with damage minimization strategies to prevent tearing.

Research into skin's mechanical properties began in 1831 when Guillaume Dupuytren [215] observed a patient who had stabbed himself over the heart three times with a stiletto having a circular cross-section. Doubting the patient's truthfulness due to the elliptical shape of the wounds, Dupuytren found that perforations made from an awl may either narrow or broaden depending on the tension of the skin across the wound. This led to Langer's proposal of lines representing the anisotropic nature of the skin that follow directions where the skin is under most tension [216]. The existence of Langer's lines is well recognized; indeed, surgeons find that incisions made along the lines close easily and heal rapidly, whereas incisions perpendicular to the lines tend to pull open, with prolonged healing and scarring [217].

Skin is often considered as a nonlinear-elastic material with low strain-rate sensitivity [80, 106]. Most work on its mechanical deformation has focused on the collagen, the main structural component of the dermis [198]. Deformation in collagen involves several distinct stages [220]. In arterial walls, for example, collagen fibril straightening, reorientation and elastic stretching have all been identified [197, 199, 221], akin to their alignment on stretching in tendons [51, 222]. Constitutive models are based on phenomenological curve-fitting [223], energy-based formulations [80] and physically based relationships [61, 94, 224].

Far less is known about the tearing of skin. Fracture-energy values have been measured for rhinoceros [105] and rat [244] skin, and the adherence of skin grafts estimated

during peeling from a wound surface [245]. Skin appears to have superior tear resistance to natural materials, for example, hevea plantations [246, 247] and wheat gluten [248], which are used in synthetic materials specifically to provide tear resistance. However, although the importance of tear strength and its dependence on fracture energy has been noted [230], there are few, if any, studies that directly relate tear resistance to the salient micro-mechanisms of deformation and fracture in the skin.

This study addresses skin's damage minimization strategies to prevent tearing. We attribute skin's tear resistance to the nano/micro-scale behavior of the collagen fibrils using mechanical and structural characterization involving *in situ* tension loading with small-angle X-ray scattering (SAXS) and scanning electron microscopy (SEM), together with ultrahigh-resolution SEM and transmission electron microscopy (TEM). As ~60% of skin is collagen [223], which is primarily responsible for its mechanical properties, the role of elastin is not considered as it is only relevant at low strains [249, 250]. Consequently, we validate our measurements using a constitutive equation derived from a physical analogue of skin's collagen fibrils, comprising steel wires shaped into a configuration that can be analyzed analytically. The tear resistance is due to the synergistic activation of four principal deformation mechanisms, which we identify and quantify the straightening and stretching of collagen fibrils, reorientation of fibrils towards the force application direction, and the sliding of fibrils by the deformation and reformation of bonds between them.

4.3.2 Results

4.3.2.1 Tensile Response of Skin

We first established the tensile stress-strain response of skin with hydrated edge-notched specimens to demonstrate its dramatic resistance to tearing (Figure 4.12a–d),

which we relate to synergistic structural changes occurring in the dermis during straining. Our experiments show that a notch in the skin did not propagate or induce fracture, it simply opened and blunted (Figure 4.12e). This response is distinct from that of bone and tooth dentin, which are also collagenous materials but with mineral crystals [75, 251, 252], where a notch can initiate cracking and failure (Figure 4.12f), and from natural rubber, where again a small cut can readily cause fracture. This experiment pertains to the opening of a tear at the edge of the skin. These experiments are done on hydrated specimens to reflect reality. However, the mechanical response is significantly altered by decreasing the water content, as described previously in Figure 2.11. The corresponding behavior of an internal tear (Figure 4.12g–j), which is more likely encountered in surgery, illustrates how an initially straight cut gradually deforms along a trajectory idealized by an ellipse that decreases its major axis ($2a$) and increases its minor axis ($2b$) until inversion occurs, as has been demonstrated computationally at the nanometer scale [253, 254]. This change in notch geometry, shown in Figure 4.12k-l, acts to diminish the stress concentration at the tip, as the local stress at the notch tip, σ_{tip}, is related to the globally applied stress, σ_{app}, by $\sigma_{tip}=\sigma_{app}(1+2a/b)$. When the minor axis is zero, the local stress is infinite; as the minor axis $2b$ increases and the major axis $2a$ decreases, this stress decreases. We show how this extraordinary flaw tolerance of skin is related to the reorganization of the collagen at any region of stress concentration.

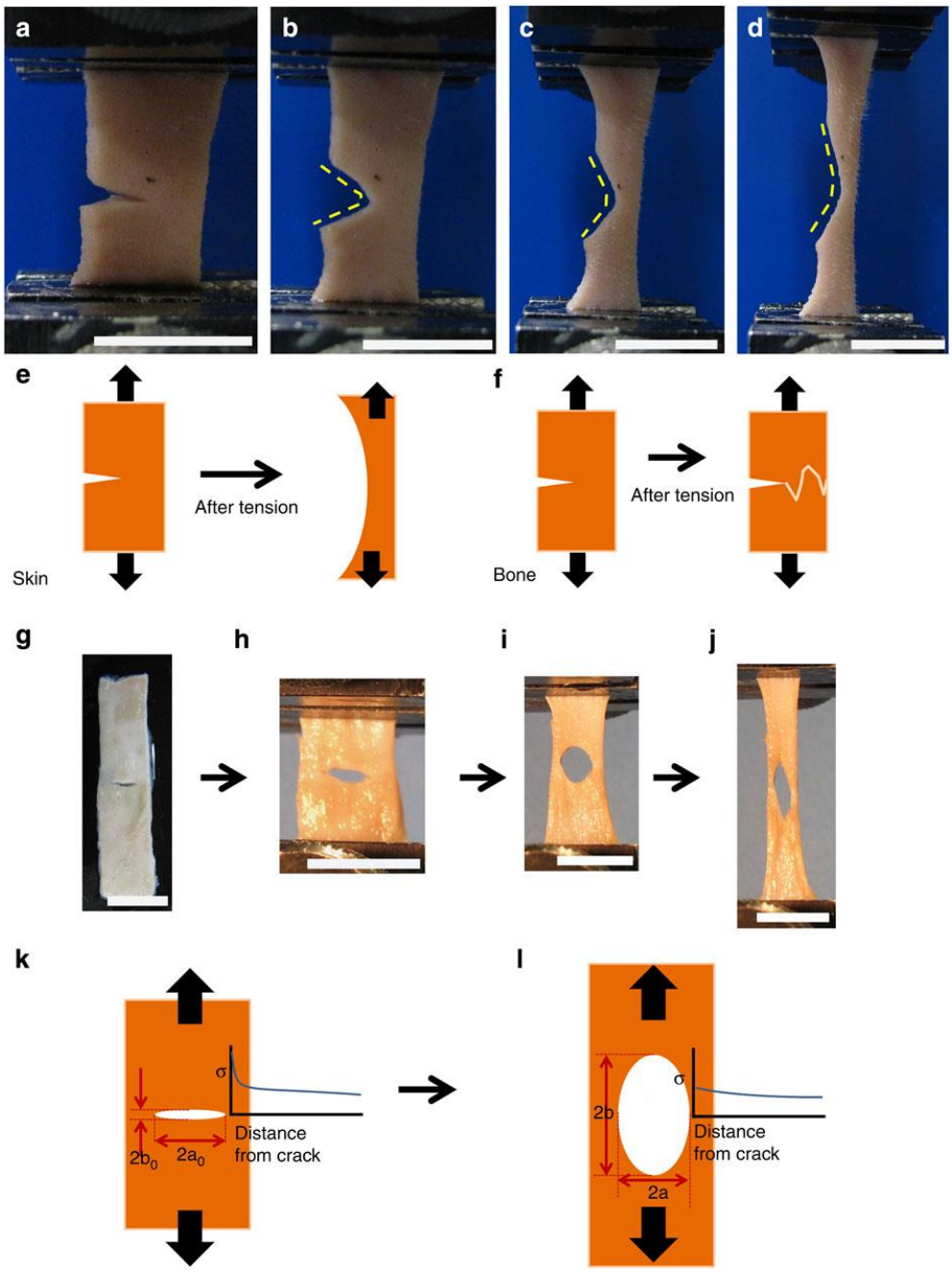

Figure 4.12: Tear resistance of skin in comparison to bone materials. (a–d) The sequence of events where rabbit skin, containing an edge notch or tear (of a length half the lateral specimen dimension), is strained under uniaxial tensile loading; the notch does not propagate but progressively yawns open under tensile loading. (e) Schematic illustration of skin with a pre-crack under loading; the crack does not propagate but instead blunts. (f) Corresponding schematic of bone (transverse orientation) with a notch under loading; the crack (white line) often propagates in a zig-zag pattern with multiple crack deflections. (g–j) The deformation of a central notch in skin loaded in tension. Distortion of a central notch as specimen of rabbit skin is extended uniaxially. There is no increase in the initial length of the cut. (k,l) The notch root radius increases with axial extension of the specimen, with a consequent decrease in stress concentration. This is enabled by local straightening and stretching of fibers and by interfibrillar sliding. Scale bar in (a–d), (g–j) is 10 mm.

Before testing, the collagen fibers show a disordered, curvy morphology (Figure 4.13a). Each fiber has a diameter of 5–10 μm and contains hundreds of ~50-nm diameter collagen fibrils (Figure 4.13b). TEM of the collagen fibrils reveals their principal orientations: nearly parallel and nearly perpendicular to the plane of the foil (Figure 4.13c), with a curved trajectory; their *d*-spacing, measured at 55 nm (Figure 4.13d), is lower than the actual value because the fibrils are inclined to the plane of observation. Under load, fiber straightening and reorientation occurs towards the direction of straining, as illustrated in Figure 4.13g–j. After loading, the collagen fibrils are aligned parallel, straightened and separated on the notched side, but relaxed from straightening and delamination on the unnotched side (Figure 4.13e-f). SEM images demonstrate that the collagen fibers straighten and reorient leading to their separation into fibrils from the action of the interfibrillar shear and tensile stresses (shown later).

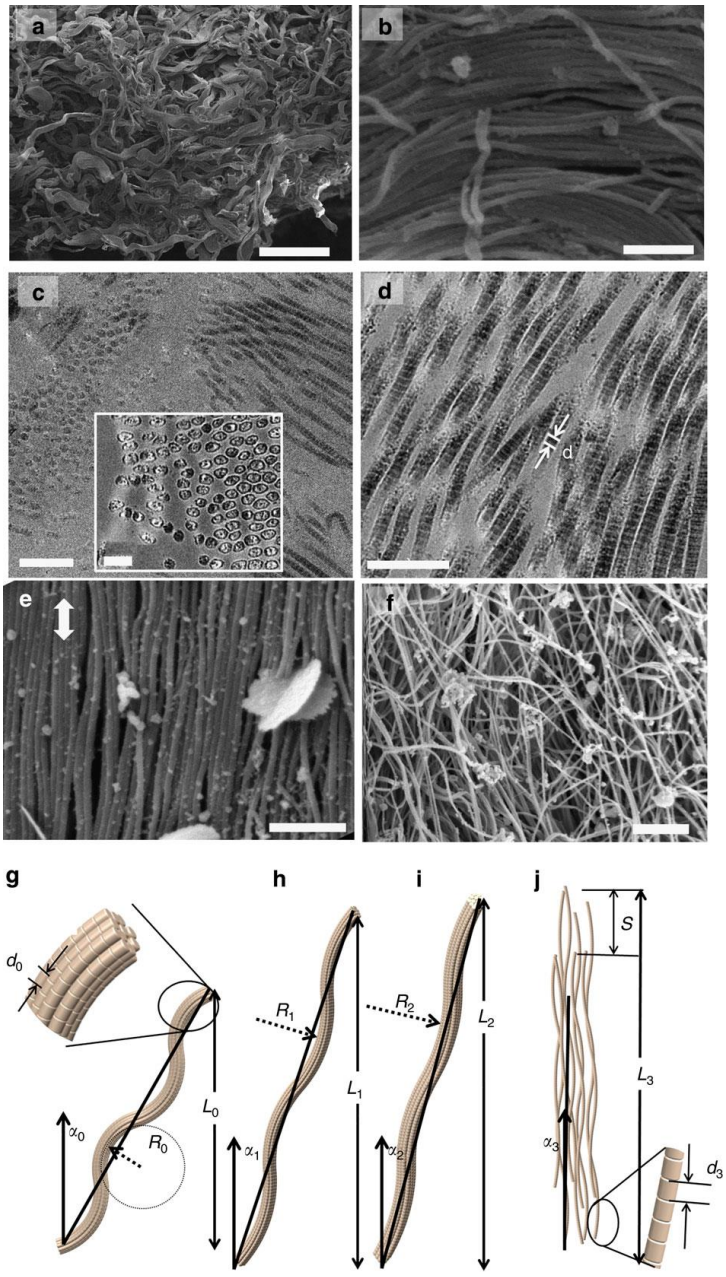

Figure 4.13: Evolution of fibril and fiber configuration during tensile extension. (a) Disordered arrangement of curved collagen fibers (SEM). (b) High magnification of a, collagen fibrils (~50 nm diameter) comprising each fiber (~1–10 μm diameter; SEM). (c,d) Collagen fibrils in section plane parallel to skin surface including detail of sectioned fibrils (inset in c) and wavy structure (TEM). (e) Collagen fibrils at notched side are delaminated, aligning close to the tension direction after loading. The loading direction is shown by the arrow, (f) collagen fibrils at unnotched side are delaminated/relaxed after loading/unloading. (g–j) Schematic of mechanisms of fibril deformation and failure under tension: (g) original configuration; (h,i) straightening and reorientation of fibers with projected length in tensile direction increasing from L_0 to L_1, and L_2 (j) separation into fibrils; elastic stretching through the increase in collagen d spacing from d_0 to d_3, and sliding (schematically shown by S), increasing length in tensile direction to L_3. R_0–R_2 are the radii of curvature of collagen during stretching. Scale bars in a–f and the picture inset in c are 50 μm, 500 nm, 500 nm, 500 nm, 1 μm, 2 μm and 200 nm, respectively.

4.3.2.2 Mechanisms of Deformation

The sequence of events can be analyzed in terms of four mechanisms (Figure 4.13g–j). One fiber with a reduced number of fibrils is used to schematically represent the process of deformation (Figure 4.13g). The fiber stretches and reorients itself, increasing its projected length in the tensile direction fromL_0 to L_1 and L_2 (Figure 4.13g–i). This takes place by increasing the radius of curvature of the initially curved fibers from R_0 to R_1 and R_2; due to stretching, the angle with the tensile axis decreases from α_0 to α_1, and α_2 (Figure 4.13g–i). As the fibers are straightened, shear strains develop between the fibrils because of kinematic requirements. At a critical juncture, the shear stresses at the interfaces exceed the interfacial cohesive strength and the separation of fibrils ensues, leading to the last stage of deformation in which extensive interfibrillar displacement occurs (Figure 4.13j). The displacement between two adjacent fibrils is indicated as S and the length along the tensile direction is now L_3 (Figure 4.13j). By the end of deformation, the d-spacing of collagen has increased from d_0 to d_3, as shown in Figure 4.13g–j. Separation of the fibers into fibrils is shown in Figure 4.13j.

Figure 4.14a shows the stress-strain curves of unnotched rabbit skin at two different strain rates, differing by a factor of 100: 10^{-1} and 10^{-3} s^{-1}. The plots represent a number of experiments (up to eight tests conducted for each condition) and the bands reflect the variation among individual results. The principal effect of increasing the strain rate is to increase the maximum stress, consistent with previous findings [80, 106], which we relate to the viscous effects of the extracellular matrix, including the sliding of collagen fibrils. Two orientations were tested: parallel and perpendicular to the backbone of the rabbit, which are, respectively, perpendicular to and along the Langer's lines [106]. The maximum

strains are lowest along Langer's lines, as expected. The tensile curves show three regions, characteristic of many collagenous materials [222, 255]: I–toe, II–heel and III–linear region. For comparison, the tensile response of isotropic, latex rubber is plotted in the inset of Figure 4.14a; this has a characteristic shape with an inflection point followed by a steep slope increase associated with entropic effects. In the dermis, collagen does not display this behavior; indeed, there are significant differences between the plots of the two materials. In the skin, the slope increases monotonically with increasing strain, until the linear region is reached. The skin shows higher strength (~15 MPa) at the strain rate of 10^{-1} s^{-1}, than at the strain rate of 10^{-3} s^{-1}(~8 MPa), the maximum stress decreasing from the prominence of interfibrillar sliding at low strain rates. Polymeric chains in rubber, conversely, are connected by strong bonds (for example, vulcanization) such that stretching of the structure is dictated by other mechanisms. In collagen, higher strain rates leave less time for interfibrillar sliding and owing to increased viscous forces, the fibers can carry more stress. These results are consistent with human skin tested parallel and perpendicular to Langer's lines [217, 256, 257]; the strength was also higher (~17–28 MPa) and the maximum strain lower (~0.5–0.6) parallel to the Langer's lines, compared with the corresponding strength (~10–16 MPa) and strain (~0.4) perpendicular to the lines.

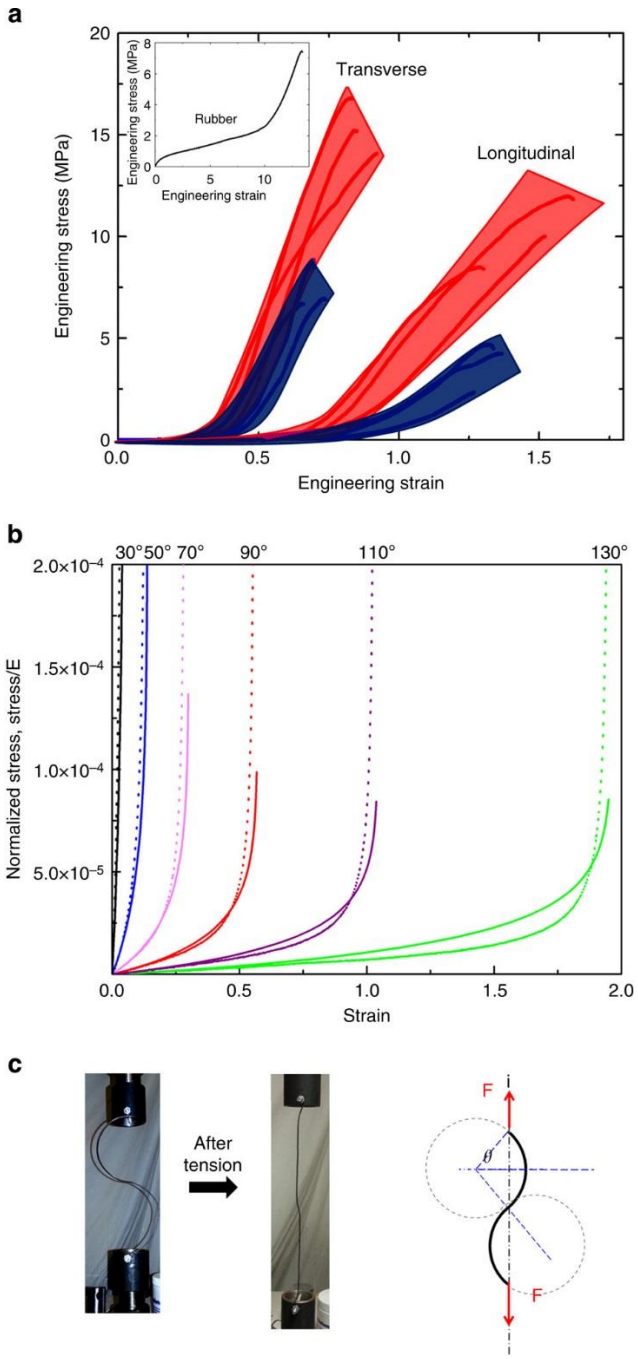

Figure 4.14: Experimental and predicted tensile response of a wavy structure simulating collagen in skin. (a) Stress-strain curves of rabbit skin in longitudinal (parallel to backbone, perpendicular to Langer's lines) and transverse (perpendicular to backbone) orientations, at strain rates of 10^{-1} (red band) and 10^{-3} s^{-1} (blue band). Skin displays higher strength at higher strain rates. Inset shows tensile response of latex, with much higher tensile strains determined by the degree of vulcanization. (b) Modelling of stress-strain curves of skin with Castigliano's theorem (dashed lines) and by experiments using steel wire, composed of segments of circles (full lines). (c) Steel wire before and after stretching. The wire curvature (shown in schematic drawing) is defined by the central angle θ_0 (~30° to 130°), which determines the maximum strain. Experimental and mathematical predictions indicate good agreement reflecting the characteristic response of skin.

4.3.2.3 Constitutive response and modelling

We modelled the tensile stress-strain response of skin by using a steel wire composed of circular segments. This new model is superior to the use of a sine-function [94, 250], zig-zag [93] or a helical shape [61, 224] because opposite segments are always continuous, independent of the radius; moreover, it enables analytical solutions to be derived. Sections of semicircles were connected consecutively, a geometry which is pertinent as there are no discontinuities in slope; this form accurately represents the *in vivo* arrangement of collagen. This is preferable to previous approaches because of its ability to control the maximum attained strain while maintaining an accurate representation of the skin. The plot shown in Figure 2.14 further justifies the selection of the chosen shape. Figure 4.14c shows one example of the collagen shape. The maximum strain is determined by the angle θ that defines the circular segments, increasing with rising θ. For instance, the maximum strain corresponding to a total rectification of the segments at an angle θ=90° is equal to 0.57. θ is the central angle of one quarter of the model; circular segments with central angles of 30°, 50°, 70°, 90°, 110° and 130° for a radius r of 120 mm were used to model the shapes of the collagen. Figure 4.14c shows the metal wire in the initial and fully stretched configurations. We used Castigliano's theorem [258] to derive the stress, σ_0 (normalized by the Young's modulus, E), which we compare with the experimental results from steel wires, shown by the solid lines in Figure 4.14b. Specifically, the extension of the steel spring was analyzed assuming a purely elastic response of circular beam segments in tension:

$$\frac{\sigma_0}{E} = \frac{1}{E} \cdot \int_{r_c}^{r} E' \left\{ \frac{\csc(\theta_0)}{r_c \cdot r} \left[r \sin\left(\frac{r_c}{r} \theta_0 \right) - r_c \theta_0 \cos\left(\frac{r_c \theta_0}{r} \right) \right] \right\} dr \qquad (56)$$

where E' is a pseudo-modulus (determined from the geometric shape of the wire), θ_0 is the initial central angle of the 1/4 circular segments (Figure 4.14b) and r_c is the initial circle radius. The strain increment, $d\varepsilon$, can be obtained directly from the change in radius r as the segment is stretched:

$$d\varepsilon = \left\{ \frac{\csc(\theta_0)}{r_c \cdot r} \left[r \sin\left(\frac{r_c}{r} \theta_0 \right) - r_c \theta_0 \cos\left(\frac{r_c \theta_0}{r} \right) \right] \right\} dr \qquad (57)$$

The dashed lines in Figure 4.14b show the model predictions from Equations 56 and 57.

The time-dependent component can be expressed by the Maxwell model, with the elastic spring (Equations 56 and 57) and a dashpot in series. The viscous contribution is due to hydrogen bonding between the fibrils, which, on being disrupted and reformed, allows their time-dependent sliding.

To include the non-elastic terms from interfibrillar sliding, we assume a simple spring/non-linear dashpot series model where the total strain ε_t is given as the sum of the elastic ε_{el} and viscous ε_η strains: $\varepsilon_t = \varepsilon_{el} + \varepsilon_\eta$. The viscous term can be represented by a simple Newtonian response: $\sigma = \eta \dot{\varepsilon}_t$, where η is the Newtonian viscosity, such that the viscous strain is given by:

$$\varepsilon_n = \frac{1}{\eta} \int \sigma dt \qquad (58)$$

It is simpler to use a polynomial fit to the elastic constitutive equation of the form $\sigma = A\varepsilon_{el} + B\varepsilon_{el}^{\,2} + C\varepsilon_{el}^{\,3} + D\varepsilon_{el}^{\,4}$, where A, B, C and D are fitting constants, leading to:

$$\varepsilon_\eta = \frac{1}{\eta} \int \left(A\varepsilon + B\varepsilon^2 + C\varepsilon^3 + D\varepsilon^4 \right) \dot{\varepsilon}^{-1} d\varepsilon \qquad (59)$$

where $\dot{\varepsilon}$ is the strain rate. We should emphasize that the viscous component comes from the breaking of interfibrillar bonds, which results in sliding between them. Thus, the fractional area where viscous flow takes place is a small number; as such, the viscosity used in equation 59 is an ‘effective’ viscosity. The resulting stress-strain response of the wire is modified as a function of viscosity (at a constant strain rate) in Figure 4.15a, and strain rate (at a constant viscosity) in Figure 4.15b. These calculations show in schematic manner how the viscosity influences the mechanical response. As the samples dry, the viscosity increases and the overall response is altered. This is predicted by the modelling of Gautieri *et al*. [79], and is shown previously in Figure 2.11.

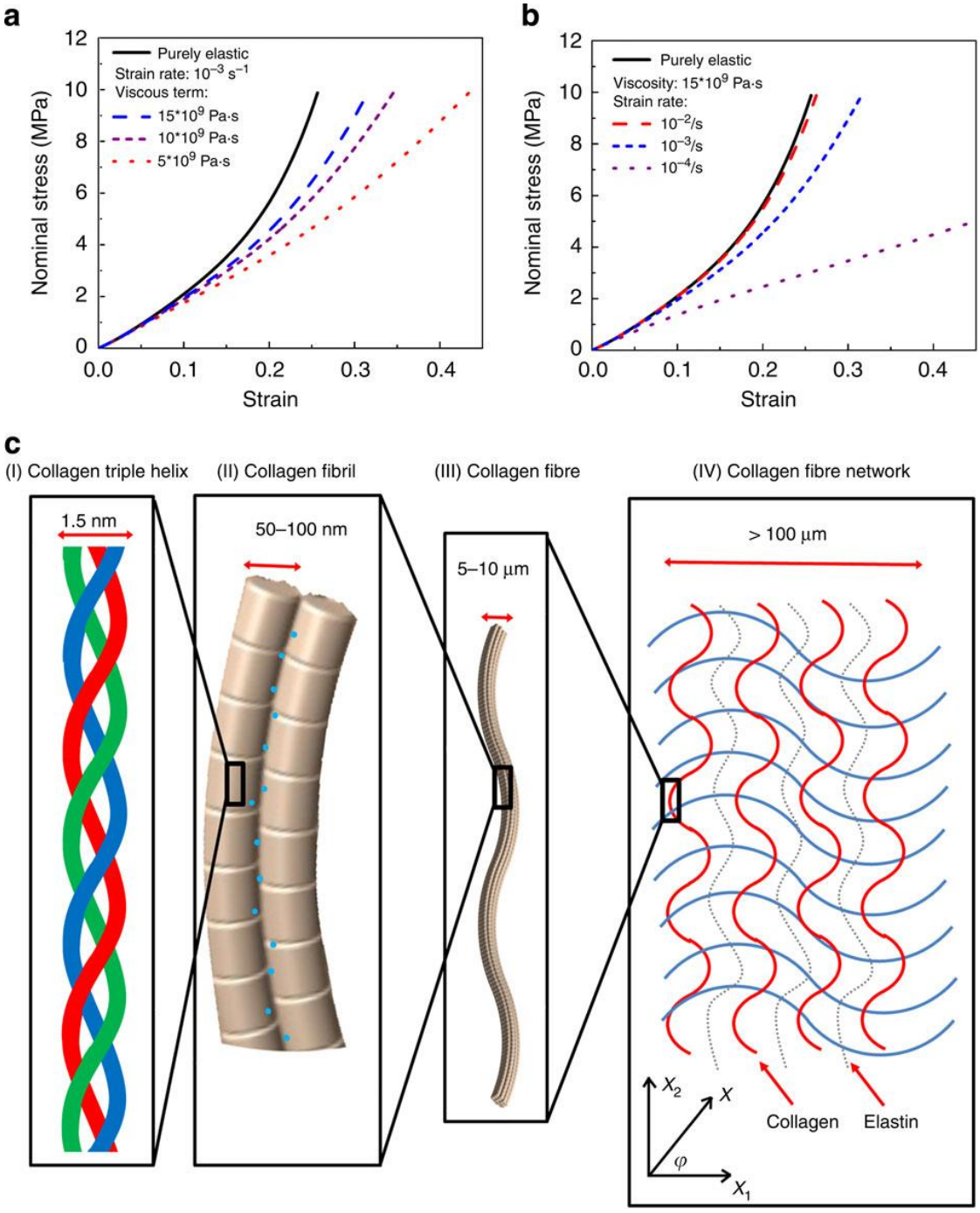

Figure 4.15: Viscosity and hierarchical structure. (a) Effect of viscosity on the stress-strain response of a non-linear elastic material. (b) Effect of strain rate, at a constant viscosity, purely elastic response at $10^{-3}\,s^{-1}$. (c) Actual skin has a hierarchical structure spanning the nanoscale of twisted peptide chains to the microscale of wavy collagen and elastin fibres. The proposed wire model only addresses structure at the ~50 nm to 10 µm dimensions, as depicted by levels II and III in the schematic. Blue dots in II represent hydrogen bonds and water molecules.

The wire model is a simple representation of almost two levels of the hierarchy of the skin. Figure 4.15c shows four levels of such hierarchy (considering primarily collagen), specifically: I (sub-nanometer) level—collagen molecule, II (nanometer) level—collagen fibrils, III (micrometer) level—collagen fibers, arranged in a 'curvy' geometry, and IV (mesoscale) level—collagen fibers with two orientations creating a fabric with orthotropic response. More complex models can be developed [259] but for the purposes of this analysis the one presented in Figure 4.15c suffices. The model focuses on levels II and III. Translating this to the mesoscale in level IV, and incorporating anisotropy, can provide the orientation-dependent mechanical response between the orthogonal axes ϕ=0 (direction of the Langer's lines) to 90° (perpendicular direction) in terms of the strains in directionsx_1 and x_2 by:

$$\sigma = \cos^2 \varphi \cdot f_1(\varepsilon_1) + \sin^2 \varphi \cdot f_2(\varepsilon_2) \tag{60}$$

where f_1 and f_2 are different functional dependencies of the stress. This leads to predictions of the stress-strain response as a function of the orientation in the skin, as described in Figure 4.16, which captures the essential features of the experimental data in Figure 4.14a.

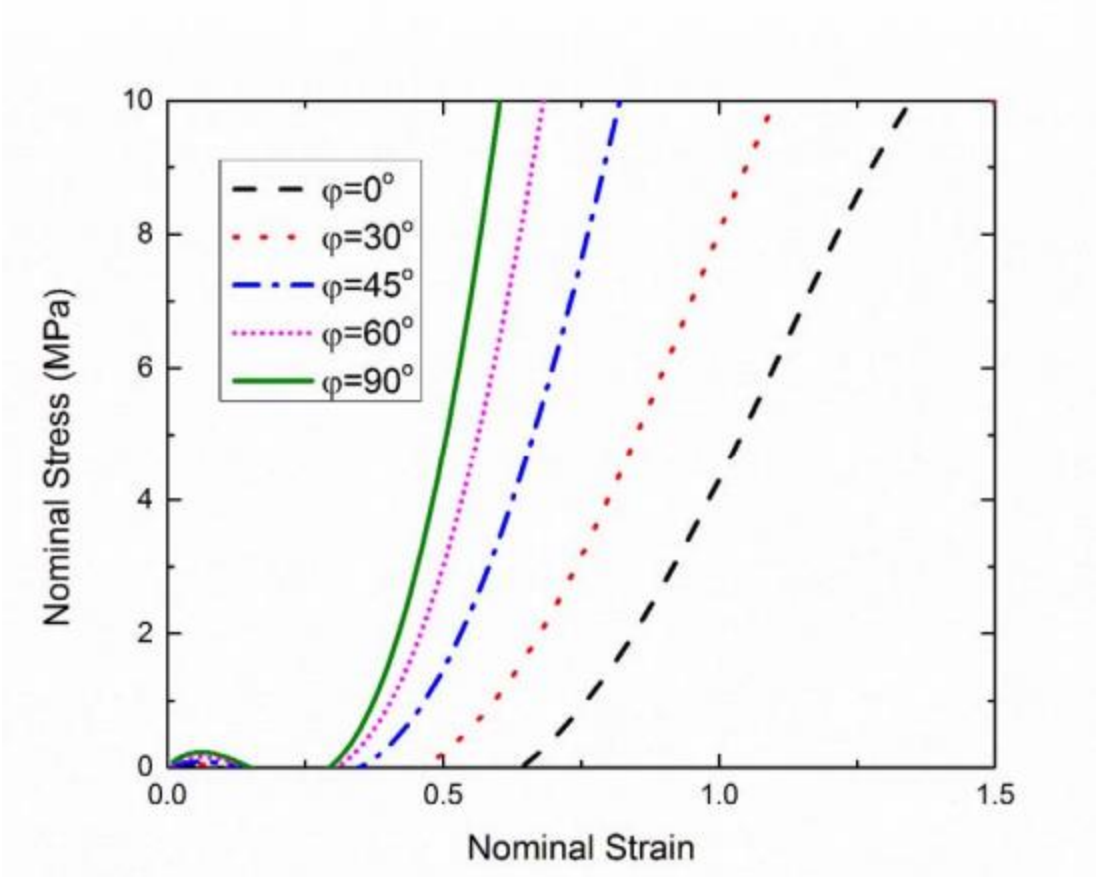

Figure 4.16: Calculated stress-strain curves incorporating anisotropy. Langer line orientation at φ = 90°; perpendicular orientation at φ = 0°. Orientations of 30°, 45° and 60° have correspondingly intermediate responses. Calculations used Equation 60 and best fit to experimental data for φ =0° and 90°

4.3.2.4 Synchrotron X-ray characterization

We used *in situ* SAXS [260] with a synchrotron X-ray source to investigate this reorganization of the collagen fibrils in the skin during tensile loading, combining these data with *in situ* structural observations of the collagen behavior in the environmental SEM under stretching. SAXS has been used previously to study collagen [94, 261, 262], specifically the uniaxial and biaxial directional stretch of bovine pericardium and the collagen structure at different temperatures and degrees of hydration. Here, we determined a stress-strain curve for skin exhibiting the three characteristic toe-, heel-, and linear-shaped regions [198, 222, 263] (stages I–III) with a stage IV representing failure (Figure

4.17a–e). The first three stages display a characteristic J-shape, which has been seen for collagen in other organs [198, 199, 221, 222]. Each point on the curve represents a SAXS measurement during tensile loading with 13 points exposed to X-rays. The four data points at the ends of the red dashed line arrows in Figure 4.17e are used to discuss the structural changes shown in Figure 4.17a–d. In the diffraction patterns of the four points (Figure 4.17a–d), the arcs represent the distributions of orientation of the collagen fibrils; the radii of the arcs indicate their *d*-spacing evolution. Figure 4.17f,g show, respectively, the evolution of the central angle of orientation of the collagen fibrils and their *d*-spacing. Evaluation of the results in Figure 4.17, combined with *in situ* SEM observations (Figure 4.18), permits the identification of the four salient mechanisms underlying the tear resistance of skin during tensile straining—in four stages marked I–IV in Figure 4.17f,g.

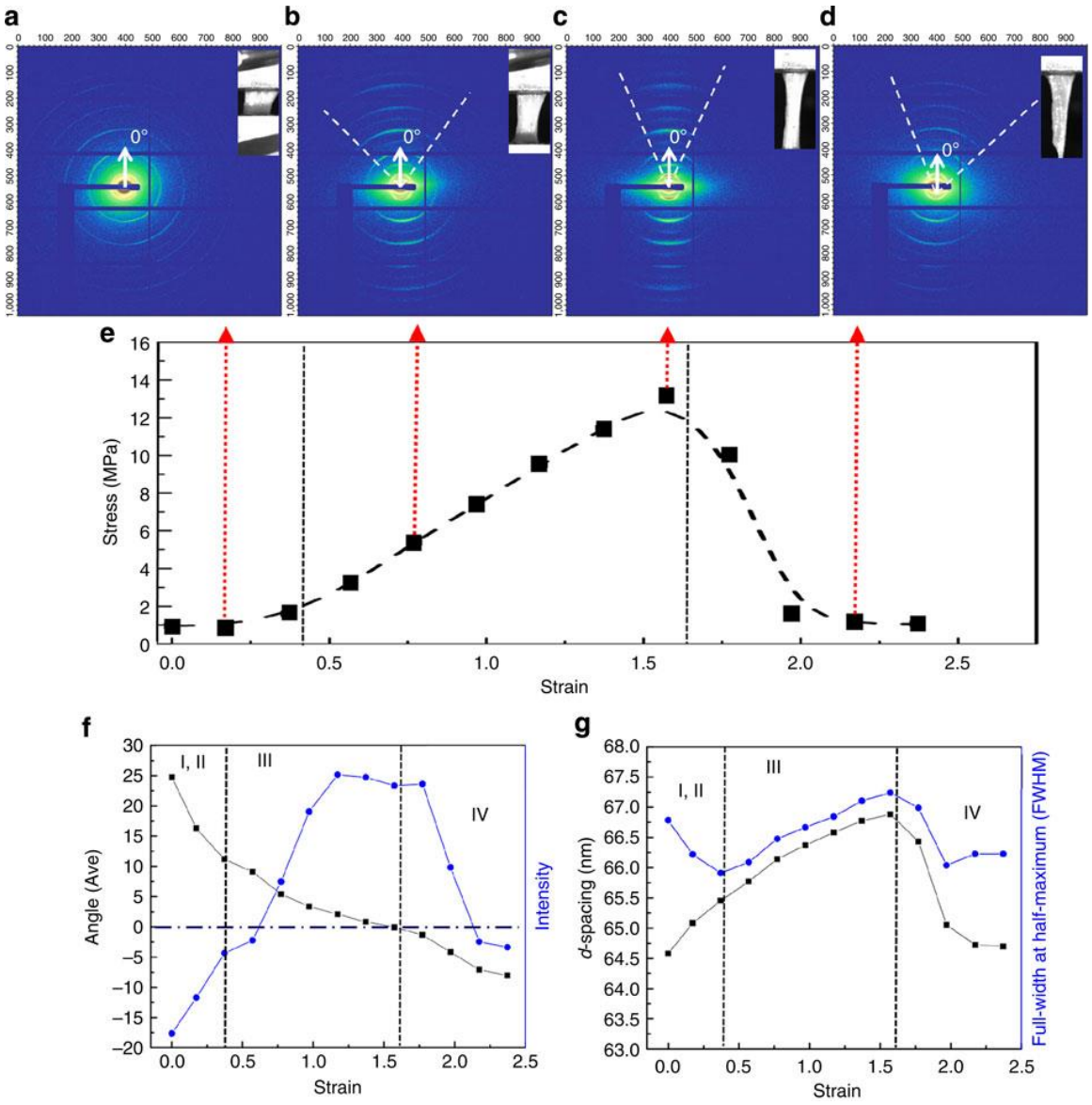

Figure 4.17: SAXS analysis of skin in tension. Variation in SAXS peak-intensity, orientation angle, collagen fibril *d*-spacing and full-width-at-half-maximum (FWHM), from tensile tests on rabbit skin. (a–d) Diffraction patterns: arcs show orientations of fibrils, images of the sample shown at top-right corners, (a) collagen fibrils randomly oriented to tensile axis, shown by constant intensity of diffraction pattern circles, (b) fibrils become gradually aligned in tension direction, (c) fibrils aligned along tensile axis, (d) fibrils fractured and relaxed. (e) During tensile test, 13 stress-strain data points (black dots) were recorded at 5 s intervals; four stages were identified. (f) Angle of normal to the tensile axis (black dots) versus intensity of fibrils (blue dots) as a function of strain, and (g) *d*-spacing (black dots) and FWHM (blue dots) of fibrils as a function of strain. Four stages: *I-toe* and *II-heel*, curved collagen fibrils straighten, rotate, stretch (*d*-spacing increases), *III-linear*, fibrils continue to rotate and stretch, orienting completely along tensile axis (angle=0°), but also slide and delaminate; *IV-fracture*, fibrils fracture and curl back (angle deviates from 0°, *d*-spacing, FWHM and intensity decrease).

4.3.2.4.1 Stage I and II (toe and heel)

The skin was moderately stretched before loading because of the gravity acting on the wet samples. No clear mechanistic distinction was observed in stages I and II, since due to the dose limit, only three data points were obtained. The diffraction pattern in Figure 4.17a (at the beginning of tensile testing) displays almost a continuous circle, suggesting that the collagen fibrils are arranged at widely varying angles. During these stages, the collagen fibrils straighten (Figure 4.18b,f) and rotate towards the tension axis (Figure 4.17f and Figure 4.18a,e). The fibrils also stretch, as the collagen *d*-spacing increases (Figure 4.17g). Despite the increasing strain, the toe and heel stages show little increase in stress, consistent with the wire model data, which suggest that during this period more strain is taken up by straightening than by stretching.

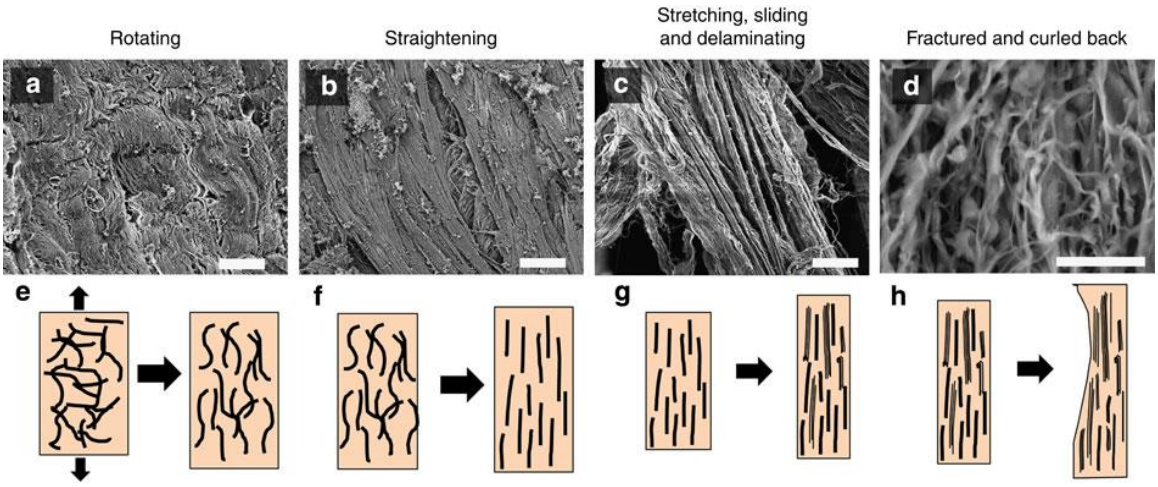

Figure 4.18: Mechanistic stages of the tensile loading of skin. SEM images (a–d) and schematic drawings (e–h) of the mechanisms during the four stages of tensile loading of rabbit skin, black arrows in a and e represent the direction of tension testing. (a,e) Curved collagen fibrils are oriented along the tensile axis; (b,f) collagen fibrils are straightening, larger and larger amount of the fibrils re-orient close to the tensile axis; (c,g) collagen fibrils are stretching, sliding, delaminating and orientated completely along the tensile axis; (d,h) collagen fibrils are fractured and curled back. Scale bars in a–d are 20, 20, 20, 50 μm, respectively.

4.3.2.4.2 Stage III (linear)

The collagen fibrils continue to rotate, as α (fibril angle with the tension axis) drops from ~10° to ~0°. The fibrils also become more uniformly aligned, with Herman's orientation factor increasing from 0.24 to 0.76 (data not shown). Herman's orientation factor defined as $\frac{1}{2}(3\cos^2\Phi-1)$, where Φ is the angle between the orienting entity and fibre axis, quantifies orientation on a scale from 0 (random distribution) to 1 (perfectly oriented/aligned). This is seen visually as the SAXS peak transforms from a circle to an oriented arc (Figure 4.17a–c). This peak correspondingly grows in intensity (Figure 4.17f), which also reflects the recruitment of greater numbers of fibrils into common alignment. The realignment of the collagen fibrils possibly increases the modulus locally, which would elevate local stress and precipitate failure at this stage. Simultaneously, the *d*-spacing of collagen fibrils increases from 64.5 to 66.9 nm, indicating that the collagen is still extending elastically. However, this small elastic strain of ~0.037 is not sufficient to accommodate the applied strain, which can be as high as 0.5 in this stage. Hence, the mechanisms of inter- and intrafibrillar sliding become major contributors to accommodate the imposed strain. Delamination of collagen fibrils is observed (Figure 4.18c), consistent with the SAXS peak becoming broader (full-width-at-half-maximum (FWHM) increases, Figure 4.17g), owing to the defects introduced into the previously well-ordered fibrils. In this stage, the main mechanisms are reorientation, stretching, sliding, and delamination of collagen fibrils (Figure 4.18e,g).

4.3.2.4.3 Stage IV (fracture)

In stage IV, the collagen fibrils fracture and curl back upon unloading (Figure 4.18d). The fibrils return to a wider range of orientations, so that the SAXS peak

concomitantly decreases in intensity, and the central angle of orientation drifts away from the axis of tension. Owing to unloading, the collagen *d*-spacing (Figure 4.17g) and the FWHM of the SAXS peak both decrease, as the fractured collagen returns to a shorter and more well-ordered *d*-spacing.

Thus, multiple mechanisms operate in the collagen under tensile loading to provide skin with its extraordinary tear resistance: rotation, straightening, stretching, sliding and delamination. The first three mechanisms provide the strain to induce large shape changes within the elastic regime; these mechanisms also permit the re-alignment of collagen around any tear in the skin to ensure its blunting.

In conclusion, we have shown the remarkable tear resistance of skin to be associated with specific mechanisms within the collagen. This behavior, especially the ability of collagen fibrils to slide past each other, contrasts with natural rubber vulcanizate, where 'nicked' specimens will readily tear at low loads [264]. Clearly, the role of collagen fibrils varies significantly in biological materials. In bone [252, 265], sliding between the collagen fibrils forms the basis of 'plasticity' and provides a bilinear uniaxial stress-strain response; indeed, collagen fibrils interact with cracks contributing to toughness. In certain fish scales [112, 153], the *Bouligand*-type structure, with collagen fibrils oriented in different directions, acts as a tough foundation to the highly mineralized surface to provide resistance to both penetration and fracture. In such biomaterials, the collagen fibrils are mineralized and initially straight. In contrast, the collagen fibrils in the skin are initially curvy and highly disordered. We have shown how these curvy collagen fibrils act to enhance skin's tear resistance through their rearrangement towards the tensile-loading direction, with rotation, straightening, stretching, and sliding/delamination before fracture.

The rotation mechanisms recruit collagen fibrils into alignment with the tension axis at which they are maximally strong or accommodate shape change (for example, blunting a tear); straightening allows strain uptake without much stress increase, sliding allows more energy dissipation during inelastic deformation. Such reorganization and sliding of the fibrils are responsible for stress redistribution (blunting) at the tips of tears and notches. It is the synergy of these four mechanisms that confers the extraordinary resistance to tearing in skin, which in itself is a requisite for the survival of organisms.

4.3.3 Methods

4.3.3.1 Materials

Sexually mature female New Zealand white rabbits (*Oryctolagus cuniculus*) were obtained from a breeder in Lake Elsinore, California (Da Le Ranch), USA. The animals were purchased and delivered as commercially available dead rabbits, in order to avoid the ethical implications of working with live animals. The hair was shaved carefully on the animal without damaging the skin before testing. The skin was pulled from the rabbit body with a minimum of cuts. Skin samples along both the transverse and longitudinal directions, with dimensions of 10–15 mm in width and 25 mm in length, were taken from the sides and back of the rabbit. The epidermis was not removed as it was presumed that the mechanical properties of the skin would not be affected by the very thin epidermis layer. Skin samples that were not tested immediately were stored in the frozen state, as prescribed by Marangoni *et al*. [266].

In total, three separate rabbits were examined. At least three unnotched and notched samples for each property measured were examined in both the longitudinal and transverse directions, specifically in tension both *ex situ* and *in situ* inside the synchrotron X-ray

source with real-time simultaneous SAXS measurements. For some conditions, up to eight experiments were conducted.

4.3.3.2 Uniaxial tensile tests

Using surgical blades, skin samples with dimensions of $20 \times 4 \times 0.6\ mm^3$ were cut along directions parallel and perpendicular to the backbone of the rabbit. Up to eight samples were tested in each orientation. Uniaxial tensile tests were carried out on an Instron 3342 mechanical testing machine (Instron Corp.) with a load cell of 500 N using the span of 12 mm at strain rates of 10^{-1} and $10^{-3}\ s^{-1}$. To keep the specimens hydrated during tests, phosphate-buffered saline solution was sprayed on to the skin samples periodically. The effects of dehydration are explored by reducing water content using a desiccator, and using weight measurements to quantify water loss.

4.3.3.3 SEM sample preparation

Strips of the rabbit skin were cut using surgical blade and a steel ruler (the latter to keep the cuts straight). The strips were first immersed in 2.5% glutaraldehyde for 3 h to fix the structure, and dehydrated with an ascending ethanol series (30, 50, 70, 90, 95 and 100 vol.% twice) while preventing shrinkage due to dehydration. The strips were fractured using forceps immediately after being immersed in liquid nitrogen. The fractured samples were immersed in ethanol and dried in a critical point dryer (Auto Samdri 815A, Tousimis). The dried fracture surfaces were then sputter coated with iridium using an Emitech K575X sputter coater (Quorum Technologies Ltd.) and examined by FEI SFEG ultra-high resolution SEM (FEI, Hillsboro).

Samples were also observed under wet conditions using an *in situ* SEM (Hitachi S-4300SE/N SEM (Hitachi America) during the tension testing. However, owing to the wet

condition of the skin sample, high resolution could not be obtained. Some stretched samples in different tensile stages (toe, heel, linear and fracture) were prepared using the similar SEM sample preparation procedure (structure fixing, dehydration and critical point drying) and observed using FEI SFEG ultra-high-resolution SEM. All structure-fixed samples, which were tensile tested, were subsequently characterized in the SEM.

4.3.3.4 TEM sample preparation

For TEM observation, the skin was cut using a scalpel into 5 mm thick strips. A primary fixation was performed by immersing the tissue sections in 2.5% paraformaldehyde, 2.5% glutaraldehyde in 0.1 M cacodylate buffer for 2 h, and post-fixation was done in 1% osmium tetroxide in 0.15 M cacodylate buffer for 12 h. The specimens were then stained in 1% uranyl acetate for 12 h and dehydrated with an ascending ethanol series, followed by a 1:1 ratio of 100% ethanol and 100% acetone, and finally 100% acetone. Samples were then embedded in Spurr's low-viscosity resin and polymerized at 48 °C for 48 h. Samples were subsequently sectioned parallel to the skin surface, generating usable samples 70-100 nm thick using a Leica Ultracut UCT ultramicrotome (Leica) and a Diatome diamond knife (Diatome). Ultramicrotomed sections were then placed on copper grids for TEM observation, and post stained with Sato lead for 1 min. The glutaraldehyde, which was used to prepare SEM and TEM samples, is a cross-linking agent to fix the structure, which can alter the original orientation of the collagen fibrils; however, the altered angle is within the standard error in this work and did not affect the mechanisms involved.

4.3.3.5 Steel model tensile tests

Steels with a circular section (2.38 mm diameter) were used to model the tensile behaviour of a single collagen fibril. The steel wires were shaped into circular segments with radius of 120 mm; the maximum strain capability was prescribed by using different angles of the segments (as shown in Figure 4.14b): θ=30°, 50°, 70°, 90°, 110° and 130°. The macroscopic strain rate (crosshead velocity divided by total specimen length) was $10^{-3}\,s^{-1}$.

4.3.3.6 Calculation method

Castigliano's theorem was used in the derivation for the straightening of an initially circular segment of a steel wire under tension. The strain can be obtained as a function of the change in radius *r*, by simultaneously solving Equations 56 and 57.

4.3.3.7 Small-angle X-ray scattering

Skin samples with dimensions of $20 \times 4 \times 0.6\,mm^3$ were prepared using surgical blade and sprayed by phosphate-buffered saline solution before testing. A minimum of six hydrated samples were loaded in uniaxial tension at 25 °C at a displacement rate of $40\,\mu m\,s^{-1}$ with a span of 4 mm, and exposed to X-rays at beamline 7.3.3 at the Advanced Light Source synchrotron at the Lawrence Berkeley National Laboratory. The mechanical tests were performed with a custom-made rig using a 10-mm displacement stage and an Omega LC703-10 load cell, calibrated to 45 N; this setup permits SAXS data collection to be recorded in real time with the simultaneous measurement of the load-displacement curve. The samples were sprayed by phosphate-buffered saline just before testing, and the entire tensile procedure of one sample took ~4 min.

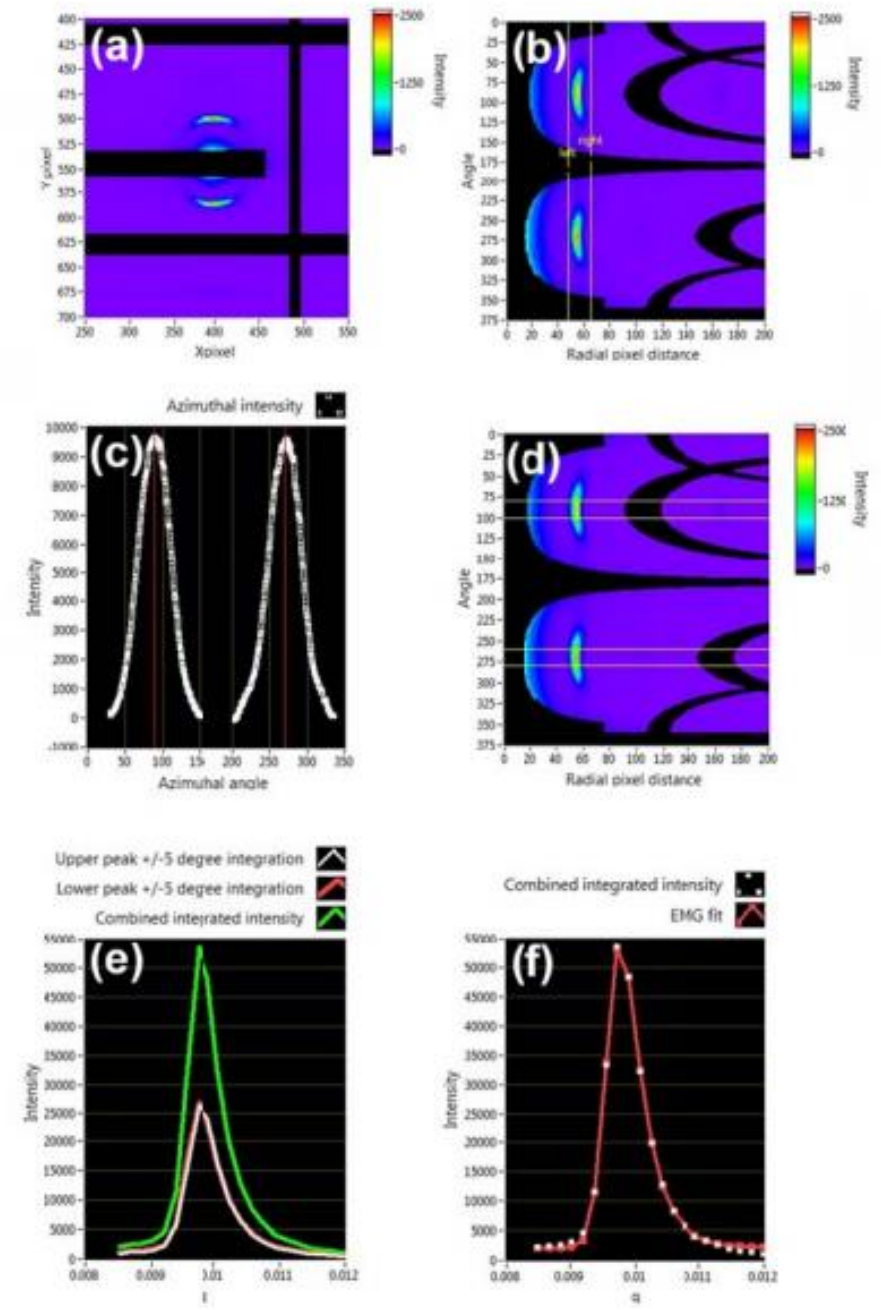

Figure 4.19: SAXS analyzing process with pictures. 1) Image was obtained from Plilatus X-ray detector. 2) The image was remapped from Cartesian plot to polar coordinates. The background intensity was subtracted. The area between yellow cursors was integrated to create plot of integrated intensity vs. angle shown in Step 3. 3) Peaks are fitted with Gaussian functions to find the central angles of orientation (marked by red cursors). Herman's orientation parameter is calculated to quantify the degree of orientation. 4) Areas between yellow cursors (±5° around orientation central angles found in previous step) are integrated to yield two curves of intensity vs. q. 5) The two scattering curves of intensity vs. q are added to create one curve. 6) The final curve is fitted with an exponentially modified Gaussian and measurements are made of peak location, height, integrated area and FWHM.

A Pilatus 1 M detector (Dectris Ltd.), used to collect the SAXS data, was located at the largest allowable distance from the sample (~4 m) to permit detection of the fine changes in the collagen peak positions. The sample was exposed to 10 keV X-rays for 0.5 s at ~5 s intervals during mechanical testing. The SAXS data reduction software Nika was used to calibrate the sample-to-detector distance and beam center from an X-ray exposure of a silver behenate standard sample. Following this, software written in Labview was used to transform all exposures to polar coordinates (maps of azimuthal angle versus q). For the analysis, the first-order peak of intensity versus q ($q=2\pi/d$) was analyzed, where d is the spacing of the peak being diffracted.

Diffuse scattering near the beam center was removed by fitting a weighted spline function to the scattering curve at each azimuthal angle (the area containing the first-order collagen peak being weighted lightly, and the remainder of the curve weighted heavily), and subtracting this fit from the curve. Azimuthal peaks were then detected and fitted with Gaussian functions to locate the angle of orientation of the collagen. Herman's orientation factor, also known as $P2$, the second Legendre polynomial, and equal to $\frac{1}{2}(3\cos^2\Phi-1)$, where Φ is the angle between the orienting entity and fiber axis, was used to quantify the degree to which the azimuthal signal was oriented. Scattering curves were made by integrating the data ±5° from the angle of orientation. The first-order peak of collagen, which had already had background scattering subtracted in a previous step, was then fitted to an exponentially modified Gaussian function, from which peak location, height, area and FWHM were measured. This procedure is given by the sequence of six steps (which are given in Figure 4.19a–f): (i) image is obtained from Pilatus X-ray detector. (ii) The image is remapped from Cartesian plot to polar coordinates. The background intensity is

subtracted with a weighted spline fit. The area between yellow cursors is integrated to create plot of integrated intensity versus angle shown in Step iii. (iii) Peaks are fitted with Gaussian functions to find the central angles of orientation (marked by red cursors). Herman's orientation parameter, that is, the second Legendre polynomial coefficient P2, is calculated to quantify the degree of orientation. (iv) Areas between yellow cursors (±5° around orientation central angles found in previous step) are integrated to yield two curves of intensity versus q, where q is defined (in units of $Å^{-1}$) as $2\pi/d$, where d here is 67 nm, the spacing of the peak being diffracted. (v) The two scattering curves of intensity versus q are added to create one curve. (vi) The final curve is fitted with an exponentially modified Gaussian and measurements are made of peak location, height, integrated area and 'FWHM'.

Chapter 4, in part, is under peer review for publication with coauthors Y. Tang, S. Zaho, W. Yang and M. Meyers. The dissertation author is the first author of this work.

Chapter 4, in part, is published as "On the tear resistance of skin" Nature Communications, vol 6, 2015. This work was coauthored by W. Yang, B. Gludovatz, E. Schaible, P. Stewart, R. Ritchie and M. Meyers. The dissertation author is the second author of this work.

CHAPTER 5: CONCLUSIONS

Collagen is a protein of crucial importance. Starting from the molecular level, a complex and refined hierarchal structure leads to a plethora of natural and synthesized materials with a broad range of mechanical properties. Through advanced characterization methods these structures are becoming better understood, clarifying the essential connection between structure and function. Nevertheless, in spite of many years of research, there are still many aspects of this material which are not fully understood and instances where conflicting views have not been resolved. This work aimed to provide insight and clarification to the use of collagen in dermal protection, specifically with mammalian skin and fish scales. This work presents constitutive equations based in structural observations which fully incorporate anisotropy and viscoelasticity in skin. The contributions of key features of naturally designed scales are understood and some features are incorporated into a flexible armor.

5.1 Scales

In our work, we have investigated the armored scales of three large fish: the *Arapaima gigas* (arapaima), *Latimeria chalumnae* (coelacanth) and *Atractosteus spatula* (alligator gar). Each of these fish utilize a different class of scales for protection, respectively cycloid, ctenoid, and ganoid. These finely tuned dermal armors have protected these fish for millions of years, and barring direct or indirect human intervention, will likely continue to do so. Like most armors, these scales are designed with a hard outer surface to resist penetration and a tough inner foundation to accommodate excessive strains.

However, each type of scale owes its effectiveness to specific features which are related to the fish's main predators:

- The elasmoid (cycloid) scale of the arapaima enables flexibility in spite of a highly mineralized exposed surface and substantial overlap to effectively resist the penetration of piranha teeth. The ridges on the surface enable the mineral to effectively flex, minimizing the tensile stresses acting on it.
- The elasmoid (ctenoid) scale of the coelacanth has a much lower stiffness but higher ultimate strength (40–60 MPa) than that of the arapaima (30 MPa), with a considerably higher work-of-fracture (9–10 MJ m^{-3} vs. 1–1.5 MJ m^{-3}). Although the coelacanth scale uses similar mechanisms to the arapaima, the interfibrillar collagen struts between the collagen bundles in the structure contribute significantly to the energy dissipation.
- The ganoid scale of the alligator gar resists the extreme bite forces of its predators by having a highly mineralized, tough and strong foundation beneath a hard and stiff ganoine outer layer. The wet gar scales dissipate energy as the water molecules act as a plasticizer to promote ductility while in the dry scales the tubules provide toughening through crack deflection and meandering.

Each type of scale has unique and fascinating features in its nano-, micro-, and meso-structure which lead to its capacity to prevent failure when under attack by either sharp teeth or crushing force of predators. If placed in alternative environments, each fish would be likely to suffer as the minimally overlapped gar scales may provide regions where a piranha's sharp teeth can penetrate into the fish's connective tissue and flesh, while the cycloid scales of the arapaima may not resist the powerful bite of the alligator. The

understanding of these dermal armors and their effectiveness in protecting these three fish may inspire the production of novel designs for flexible body armor which provides superior safety and protection from physical threats.

Our research on the scales of the alligator gar reveals important features that can be incorporated into synthetic scale-inspired flexible designs. The following are the principal findings:

- The arrangement of scales in the quasi-cylindrical body of the gar makes an angle of $\gamma=55^{o}$ with the longitudinal axis. Upon flexing, one side of the gar is stretched while the other is compressed. Both sliding and rotation, necessary to permit the length changes, are quantitatively expressed as a function of the flexing radius of the fish. Calculations show that the angle $\gamma=55^{0}$ is a compromise between coverage area per tile and sliding/rotation on stretching.
- The scale, placed on a muscle simulant, was subjected to the increasing force of an alligator tooth. The scale resisted a bite force of 500 N, and the tooth broke. The radius of the tooth and maximum bite force depend on the mass and nature of the predator, but it is clear that the hard ganoine layer is effective in producing fracture of the tooth. Bending tests show that the flexural strength shows a considerable asymmetry; the orientation corresponding to attack (compressive force by an external load) is significantly enhanced.
- Toughening features exist in each layer of the scale. In the outer ganoine, twisted cross-plied mineral enhances fracture toughness and arrests cracks. The microstructural arrangement of the composite bone lengthens crack paths and

utilizes the tough collagen fibrils. The saw-tooth interface between the two layers is designed to deflect and arrest cracks.

The penetration response and tensile behavior of the *Arapaima gigas* scales were investigated, with particular attention to the mechanisms of damage in the individual collagen layers. This was achieved experimentally through the use of tensile tests on hydrated scales and indentation experiments, analytically by predicting the various mechanisms that retard damage in the scales, and computationally with MD calculations performed to understand the response of collagen fibrils to tensile loading. Based on these studies, the following specific conclusions can be made:

- TEM and AFM confirm that the collagen fibrils have diameters of ~100 nm and are parallel in one lamella. The d band spacing of the collagen is clearly revealed by AFM and is equal to 67 nm, characteristic of type I collagen.
- The scales act to efficiently resist bites from other fish. As a tooth attempts to penetrate the scale, first the brittle external layer is placed under compression and would eventually crack due to the stress concentration and gradients, exposing the collagen layers beneath. As the penetrator enters more deeply into the scale, the collagen fibrils are pushed apart and separated. Since it has to traverse several lamellae with different orientations, no macroscopic cracks are formed. In an extreme case, eventually, individual collagen fibers fail in tension, exhibiting necking which is characteristic of considerable permanent deformation.
- We confirm and quantify earlier conclusions by Zimmermann et al. [153], namely that the stretching, rotation, delamination and fracture of collagen fibrils are the principal mechanisms of energy dissipation in the flexible foundation. Under

tensile loading, most of the collagen fibrils are stretched and rotate toward the tension direction; the collagen fibrils with a large angle to the loading (closer to 90°) delaminate as portions can rotate away or towards the tensile direction. An analytical model predicts the rotation of the collagen fibers toward the tensile axis; the model is in good agreement with measurements by SAXS.

- MD calculations of interfibril separations yield results that match quantitatively the experimental measurements, with interaction energy between microfibrils of 1 J m^{-2} being assumed. The calculations correctly predict the separation of fibrils and angular rotation toward and away from the tensile axis for large angles, and rotation of fibrils toward the tensile axis for small angles. Since only three lamellae are used in the computation, their splitting is accompanied by significant load drops; the drop at a stress of 26.4 MPa corresponds closely to the maximum stress of 30–40 MPa experimentally observed.

5.2 Skin

This investigation connects the mechanical response of rabbit skin in uniaxial extension to the changes in the structure by providing a new constitutive equation that captures the most important processes. The following principal results are obtained:

- The dermis of the rabbit is composed of sheets or lamellae which are assemblages of curved parallel collagen fibers. In these assemblages, each layer is comprised of curved fibers with a preferential direction, different layers having different orientations. It is estimated that 250 sheets with different orientations comprise the dermis of rabbit. The fibers are, in turn, composed of fibrils.

- In tension, the collagen in these sheets straightens and aligns with the tensile direction. This requires considerable interfiber shear and sliding, and generates viscous stress as alignment leads to high stress and strain values. The combined elastic and viscous effects lead to the unique tensile response of skin, as well as its strength, versatility, and tear resistance.
- Under tension, Herman's orientation factor increases from 0.24-0.76, which indicates that even at maximum stress (and maximum alignment) there remains a significant degree of misalignment. This is due the presence of some extremely wavy fibrils which can undergo large amounts of strain before straightening. As the less curved fibrils straighten and align, the more curved remain non-aligned. As stretching continues, the previously straight fibrils break and misalign, transferring the load to the straightening curvier fibrils. The variance between fibrils results in a large heel region as certain fibers enter their linear region, and a large failure region due to the successive breaking of the most highly stressed fibrils.
- A representation of what occurs in the skin during tension is presented in a physically based constitutive equation. By including the most important physical processes in our calculations, namely straightening, stretching, reorientation and sliding, the stress-strain response is successfully modeled. However, there is a large amount of variance between tests and in the microstructure of skin; numbers included in our calculation are representative of what is found in the skin. In reality, not all fibers are oriented in one of two directions, and the degree of curvature varies among fibers and between different layers. Nonetheless, the essence of what occurs in skin and how this leads to the mechanical response has been described.

- Our mechanical results are limited to uniaxial testing, in which most fibers reorient parallel to the loading direction. A future possibility is to apply the model to biaxial tension; this would reduce the tensile alignment, and result in a response dominated by the straightening and sliding of collagen, but with limited reorientation.

This knowledge of the structure of natural skin has the potential to affect the development of new hyperplastic materials and synthetic skin. Biodegradable skin-like scaffolds are crucial for the improvement of integration and quality of healing; the large influence that material properties such as substrate stiffness can have on tissue growth is being increasingly recognized. By more precisely understanding the wavy structure and how it determines the stiffness of skin, biological elements of healing are likely to perform their functions more effectively, while the potential discomfort of having an inextensible or stiff synthetic skin attached to the body may be avoided.

APPENDIX

A.1 Matlab code for model integration

These results of the strain energy circular model derivation may be solved and plotted using the following matlab functions. “splot” plots the stress versus strain relationship, which based on inputs including initial radius, and initial degree of curvature. Many other factors which are accounted for in the program include wire thickness, Young’s modulus, shear modulus, and correctional area. The integration is performed using the built in matlab function “quad”.

Function: splot

```
% splot plots a wire stress versus strain relationship. Inputs rc (initial radius of
curvature) and theta0. Other parameters are accounted for in functions called in splot.

function splot=splot(rc,w0)
%maxe is the maximum achievable strain using this method.
maxe=(w0/sin(w0))-1

for n=a:b
 r=rc*(1+(n/5)-(1/5));
% radius of curvature (r) is increased from original radius (rc)
  strain(n)=e(r,rc,w0);
% strain is calculated from new r, and inputs rc, and theta0
  stress(n)=sig(r,rc,w0);
% stress is calculated from inputs r, rc, and theta0
end

plot(strain,stress);
maxe

%stress/strain is plotted, and maximum strain level displayed.
end
```

Function:sig

```
% sig defines remaining parameters, and calls a built in matlab function to
integrate the function myfun, which returns stress values.

function sig= sig(r,rc,w0)
E=1000;
G=400;
ay=1.33;
h=50;

sig = quad(@(r)myfun(r,h,rc,E,ay,G,w0),rc,t)
%integrate from rc (initial radius) to r (current radius) to determine stress levels,
using quad method and calling function myfun
end
```

Function: e

```
% e calculates strain level, based on inputs r, rc, and theta0.
function e=e(r,rc,w0)
e=((r*sin(rc*w0/r))-(rc*sin(w0)))/(rc*sin(w0))
end
```

Function: myfun

```
function [ y ] = myfun( r,h,rc,E,ay,G,w0 )
%the following theta0 is for dr tang's E' calculation
theta0=(pi/2-rc.*power(r,-1).*w0);
delta2=power(h,2).*power(r,-2);
box=(csc(w0).*power(r,-1).*power(rc,-1)).*(r.*sin(rc.*w0.*power(r,-1))-
rc.*w0.*cos(rc.*w0.*power(r,-1)))
triangle=power((1-(delta2.*power((8.*(1-power((1-delta2/4),.5))),-1))),-1)
term2=((1/2.*cos(theta0).*sin(theta0)-(theta0)/2+pi/4))
term3=((-1/2.*cos(theta0).*sin(theta0)-(theta0)/2+pi/4).*ay.*E/G)
term1=((-3/2).*cos((theta0)).*sin((theta0))-((theta0))/2-
power(sin((theta0)),2).*(theta0)-
pi/2.*power(cos((theta0)),2)+3.*pi/4).*(triangle)

y=(E.*(box).*cos(theta0)).*power(((term2)+(term3)+(term1)),-1)
end
```

A.2 Strain energy derivation

The derivatives of the strain energy (or Helmholtz free energy per unit volume, in the case where the volume is constant) with respect to stretch is equal to:

$$\sigma_1 = \frac{\partial W}{\partial \lambda_1} \tag{A1}$$

$$\sigma_2 = \frac{\partial W}{\partial \lambda_2} \tag{A2}$$

$$\sigma_3 = \frac{\partial W}{\partial \lambda_3} \tag{A3}$$

where σ_1, σ_2, σ_3 are the principal stresses and λ_1, λ_2, λ_3 are the principal stretches. Here, assuming constancy of volume:

$$\lambda_1\lambda_2\lambda_3 = 1 \tag{A4}$$

If λ_1 and λ_2 are considered independent variables (for a sheet being stretched in plane OX_1X_2):

$$\lambda_3 = \frac{1}{\lambda_1\lambda_2} \tag{A5}$$

$$\partial\lambda_3 = \frac{1}{\lambda_1^2\lambda_2}\partial\lambda_1 + \frac{1}{\lambda_2^2\lambda_1}\partial\lambda_2 \tag{A6}$$

Inserting the constancy of volume and equilibrium condition:

$$\delta W = \sigma_1\lambda_2\lambda_3\delta\lambda_1 + \sigma_2\lambda_3\lambda_1\delta\lambda_2 + \sigma_3\lambda_1\lambda_2\delta\lambda_3 \tag{A7}$$

we obtain:

$$\delta W = \left(\frac{\sigma_1 - \sigma_3}{\lambda_1}\right)\delta\lambda_1 + \left(\frac{\sigma_1 - \sigma_3}{\lambda_2}\right)\delta\lambda_2 \tag{A8}$$

When stretches change by $\partial\lambda_1$ and $\partial\lambda_2$, the Helmholtz free energy changes by:

$$\delta W = \frac{\partial W\left(\lambda_1, \lambda_2\right)}{\partial \lambda_1}\delta\lambda_1 + \frac{\partial W\left(\lambda_1, \lambda_2\right)}{\partial \lambda_2}\delta\lambda_2 \tag{A9}$$

Comparing the two previous equations, we obtain:

$$\sigma_1 - \sigma_3 = \lambda_1 \frac{\partial W\left(\lambda_1, \lambda_2\right)}{\partial \lambda_1} \tag{A10}$$

$$\sigma_2 - \sigma_3 = \lambda_2 \frac{\partial W\left(\lambda_1, \lambda_2\right)}{\partial \lambda_2} \tag{A11}$$

Equation A10 is Equation 2 in the text. It enables obtaining the difference in stresses from the strain energy derivative with respect to the stretch ratios. This is the foundation of hyperelastic macroscopic models based on strain energy.

A.3 Complete derivation of circular segment elastic response.

These relationships are based on Figure 4.9d of the main text which shows a section of the beam, and are presented. Q is the shearing force acting on the cross section:

$$Q = Psin\alpha \tag{A12}$$

N is the normal force acting on the cross-section:

$$N = Pcos\alpha \tag{A13}$$

and M is the bending moment:

$$M = -P\left(y - r_c \sin\theta_0\right) \tag{A14}$$

For a circular beam with round cross-section, the strain energy is expressed as the sum of components due to bending, normal force, and shear force, whose equations may be found in Beer [239]. The strain energy due to bending is given by Gavin [267]. Applied to our problem, it is:

$$U_1 = \int_0^s \frac{M^2}{2EAr_c e} ds \tag{A15}$$

Substituting Equation A14:

$$U_1 = \frac{P^2}{2EAr_c e} \int_{\theta_0}^{\pi/2} r_c^2 \left(\sin\theta - \sin\theta_0\right)^2 r_c d\theta = \frac{P^2 r_c^2}{2EAe} \varphi_1(\theta_0) \tag{A16}$$

where:

$$\varphi_1(\theta_0) = -\frac{3}{2}\cos\theta_0 \sin\theta_0 - \frac{\theta_0}{2} - \theta_0 \sin^2\theta_0 - \frac{\pi}{2}\cos^2\theta_0 + \frac{3\pi}{4} \tag{A17}$$

Similarly, the strain energy due to normal force is:

$$U_2 = \frac{P^2 r_c}{2EA}\varphi_2(\theta_0) \tag{A18}$$

$$\varphi_2(\theta_0) = \frac{1}{2}\cos\theta_0 \sin\theta_0 - \frac{\theta_0}{2} + \frac{\pi}{4} \tag{A19}$$

The strain energy due to shearing force is:

$$U_3 = \frac{a_y P^2 r_c}{2GA}\varphi_3(\theta_0) \tag{A20}$$

$$\varphi_3(\theta_0) = -\frac{1}{2}\cos\theta_0 \sin\theta_0 - \frac{\theta_0}{2} + \frac{\pi}{4} \tag{A21}$$

The total strain energy is the sum of the three components of the strain energy obtained from Equations. A16, A18, and A20:

$$U = U_1 + U_2 + U_3 \tag{A22}$$

Based on Castigliano's second theorem, the displacement at the point of application of an external force may be expressed as [239]:

$$u = \frac{\partial U}{\partial P} = \frac{\partial U_1}{\partial P} + \frac{\partial U_2}{\partial P} + \frac{\partial U_3}{\partial P} \tag{A23}$$

The extension is *u*. Therefore, strain may be expressed by:

$$\varepsilon = \frac{u}{l_0} = \frac{u}{r_c \cos\theta_0} \tag{A24}$$

since $l_0 = r_c \cos\theta_0$. From the definition of Young's modulus, strain may also be expressed by the ratio of stress/elastic modulus [240]. The modulus is replaced with a pseudo

modulus, E', as it is not the material modulus, E, but the result of both structure and material modulus.

$$E' = \frac{P/A}{\varepsilon} = \frac{r_c \cos(\theta_0) P/A}{u} \tag{A25}$$

Substituting Equation A23 (defined by Castigliano's second theorem):

$$E' = \frac{r_c \cos(\theta_0) P/A}{\frac{\partial U_1}{\partial P} + \frac{\partial U_2}{\partial P} + \frac{\partial U_3}{\partial P}} \tag{A26}$$

The eccentricity of a round cross-section beam is needed to calculate the strain energy due to bending, and is expressed by [268]:

$$e = r_c - \frac{(r_o - r_i)^2 / 4}{2r_c - 2\sqrt{r_o r_i}} \tag{A27}$$

Inserting values into Equation A26 and simplifying leads to a representation of the pseudo modulus in terms of various shape factors, where $\delta = \frac{H}{r_c}$, a_y=1.33 for round cross-section, and E/G=2(1+υ):

$$E' = \frac{\mathrm{E} \cdot \cos\theta_0}{\phi_2(\theta_0) + \phi_3(\theta_0)\frac{a_y E}{G} + \phi_1(\theta_0)\left(\frac{1}{1 - \frac{\delta^2/4}{2\left(1 - \sqrt{\left(1 - \frac{\delta}{2}\right)\left(1 + \frac{\delta}{2}\right)}\right)}}\right)} \tag{A28}$$

E' now is described as a function of the shape of the circular wire segment. Specifically, the shape parameters required to calculate E' are thickness (H), the initial radius (r_c), initial

degree of curvature ($\theta_0 = 90 - \omega_0$), and the material modulus E. Holding the arc length constant, one arrives at the relationship between the decrease in curvature as the applied strain straightens the circular segments, causing a corresponding increase in radius of curvature.

$$\omega = \left(\frac{r_c}{r} \omega_0 \right) \tag{A29}$$

As described in Figure 4.9a-b of the main text, strain is applied by decreasing ω while holding the arc length constant, and substitution of l_0 and l

$$l_0 = r_c \sin \omega_0 \tag{A30}$$

$$l = r \sin \omega \tag{A31}$$

Through substitution of Equations A29-A31, strain is described as a function of current radius (r), initial radius (r_c), and initial degree of curvature (ω_0).

$$\varepsilon = \frac{l - l_0}{l_0} = \frac{r \sin\left(\frac{r_c}{r} \omega_0 \right) - r_c \sin\left(\omega_0 \right)}{r_c \sin\left(\omega_0 \right)} \tag{A32}$$

Relationships between strain and radius may be further described by solving the derivative of strain with respect to the radius:

$$d\varepsilon = \left\{ \frac{\csc\left(\omega_0 \right)}{r_c r} \left[r sin\left(\frac{r_c \omega_0}{r} \right) - r_c \omega_0 \cos\left(\frac{r_c \omega_0}{r} \right) \right] \right\} dr \tag{A33}$$

But,

$$d\sigma = E' d\varepsilon \tag{A34}$$

thus:

$$\mathrm{d}\sigma = \mathrm{E}' d\varepsilon = E' \left\{ \frac{\csc \omega_0}{r_c r} \left[r \sin\left(\frac{r_c \omega_0}{r} \right) - r_c \omega_0 \cos\left(\frac{r_c \omega_0}{r} \right) \right] \right\} dr \qquad \text{(A35)}$$

integrating:

$$\sigma = \int E' \left\{ \frac{\csc \omega_0}{r_c r} \left[r \sin\left(\frac{r_c \omega_0}{r} \right) - r_c \varphi_0 \cos\left(\frac{r_c \omega_0}{r} \right) \right] \right\} dr \qquad \text{(A36)}$$

Equation A36 is integrated from r_c to r to produce a stress vs strain relationship based on the initial circular shape.

REFERENCES

[1] R. Sadeghi. The Stone Age, The Bronze Age, The Composite Age. <simulatemore.mscsoftware.com/the-stone-age-the-bronze-age-the-composite-age>, 2009 (accessed December 15 2014).

[2] D.A.W. Thompson. On growth and form, Cambridge University Press, Cambridge, United Kingdom, 1917.

[3] M.A. Meyers and P.-Y. Chen. Biological Materials Science: Biological Materials, Bioinspired Materials, and Biomaterials, 1 ed., Cambidge University Press, Cambridge, United Kingdom, 2014.

[4] K. Gelse, E. Poschl, T. Aigner. Collagens - structure, function, and biosynthesis. Adv Drug Deliver Rev 2003; 55:1531-1546.

[5] D.J.S. Hulmes. Collagen Diversity, Synthesis and Assembly, in: P. Fratzl (Ed.), Collagen: Structure and Mechanics, Springer, New York, New York, 2008, pp. 15-27.

[6] J.W. Smith. Molecular Pattern in Native Collagen. Nature 1968; 219:157-158.

[7] J.P.R.O. Orgel, J.D.S. Antonio, O. Antipova. Molecular and structural mapping of collagen fibril interactions. Connect Tissue Res 2011; 52:2-17.

[8] J.W. Smith. Packing Arrangement of Tropocollagen Molecules. Nature 1965; 205:356-358.

[9] B.R. Olsen. Electron Microscope Studies on Collagen I. Native Collagen Fibrils. Z Zellforsch Mik Ana 1963; 59:184-198.

[10] E. Vuorio and B. Decrombrugghe. The Family of Collagen Genes. Annu Rev Biochem 1990; 59:837-872.

[11] J.P.R.O. Orgel, T.C. Irving, A. Miller, T.J. Wess. Microfibrillar structure of type I collagen in situ. P Natl Acad Sci USA 2006; 103:9001-9005.

[12] J.J. Wu, P.E. Woods, D.R. Eyre. Identification of Cross-Linking Sites in Bovine Cartilage Type-Ix Collagen Reveals an Antiparallel Type-Ii-Type-Ix Molecular Relationship and Type-Ix to Type-Ix Bonding. J Biol Chem 1992; 267:23007-23014.

[13] M. Vanderrest and R. Mayne. Type-Ix Collagen Proteoglycan from Cartilage Is Covalently Cross-Linked to Type-Ii Collagen. J Biol Chem 1988; 263:1615-1618.

[14] H.P. Bächinger, K. Mizuno, J.A. Vranka, S.P. Boudko. Collagen Formation and Structure, in: L.N. Mander, H.-W. Liu, J.C. Vederas (Eds.), Comprehensive Natural Products II: Chemistry and Biology Elsevier Ltd2010, pp. 469-530.

[15] J. Myllyharju and K.I. Kivirikko. Collagens and collagen-related diseases. Ann Med 2001; 33:7-21.

[16] K.E. Kadler, C. Baldock, J. Bella, R.P. Boot-Handford. Collagens at a glance. J Cell Sci 2007; 120:1955-1958.

[17] C.W. Franzke, P. Bruckner, L. Bruckner-Tuderman. Collagenous transmembrane proteins: Recent insights into biology and pathology. J Biol Chem 2005; 280:4005-4008.

[18] R.A. Gelman, B.R. Williams, K.A. Piez. Collagen Fibril Formation - Evidence for a Multistep Process. J Biol Chem 1979; 254:180-186.

[19] M. Leslie. Making tendons. The Journal of cell biology 2006; 172:167.

[20] R.L. Trelstad, K. Hayashi, J. Gross. Collagen Fibrillogenesis - Intermediate Aggregates and Supra-Fibrillar Order. P Natl Acad Sci USA 1976; 73:4027-4031.

[21] D.E. Birk and R.L. Trelstad. Extracellular Compartments in Tendon Morphogenesis - Collagen Fibril, Bundle, and Macroaggregate Formation. J Cell Biol 1986; 103:231-240.

[22] B. Brodsky and A.V. Persikov. Molecular structure of the collagen triple helix. Adv Protein Chem 2005; 70:301-339.

[23] M. Leighton and K.E. Kadler. Paired basic/furin-like proprotein convertase cleavage of pro-BMP-1 in the trans-Golgi network. J Biol Chem 2003; 278:18478-18484.

[24] W.M. Wang, S. Lee, B.M. Steiglitz, I.C. Scott, C.C. Lebares, M.L. Allen, M.C. Brenner, K. Takahara, D.S. Greenspan. Transforming growth factor-beta induces secretion of activated ADAMTS-2 - A procollagen IIIN-proteinase. J Biol Chem 2003; 278:19549-19557.

[25] E.G. Canty, Y.H. Lu, R.S. Meadows, M.K. Shaw, D.F. Holmes, K.E. Kadler. Coalignment of plasma membrane channels and protrusions (fibripositors) specifies the parallelism of tendon. J Cell Biol 2004; 165:553-563.

[26] D.R. Eyre and J.-J. Wu. Collagen Cross-Links, in: J. Brinckmann, H. Notbohm, P.K. Müller (Eds.), Collagen: Primer in Structure, Processing and Assembly, Springer Berlin Heidelberg, Berlin, Heidelberg, Germany, 2005, pp. 207-229.

[27] G. Pasquinelli. Fibrohistiocytic Tumors Containing Zebra Body-like Inclusions and Fibripositors. Ultrastruct Pathol 2010; 34:366-370.

[28] A.P. Bhole, B.P. Flynn, M. Liles, N. Saeidi, C.A. Dimarzio, J.W. Ruberti. Mechanical strain enhances survivability of collagen micronetworks in the presence of collagenase: implications for load-bearing matrix growth and stability. Philos T R Soc A 2009; 367:3339-3362.

[29] R.L. Trelstad. The Bilaterally Asymmetrical Architecture of the Sub-Mammalian Corneal Stroma Resembles a Cholesteric Liquid-Crystal. Dev Biol 1982; 92:133-134.

[30] J.W. Ruberti and J.D. Zieske. Prelude to corneal tissue engineering - Gaining control of collagen organization. Prog Retin Eye Res 2008; 27:549-577.

[31] E.D. Hay and J.P. Revel. Fine structure of the developing avian cornea. Monogr Dev Biol 1969; 1:1-144.

[32] C. Cintron, H. Covington, C.L. Kublin. Morphogenesis of Rabbit Corneal Stroma. Invest Ophth Vis Sci 1983; 24:543-556.

[33] R.C. Haut. The Influence of Specimen Length on the Tensile Failure Properties of Tendon Collagen. J Biomech 1986; 19:951-955.

[34] A. Gautieri, S. Vesentini, A. Redaelli, M.J. Buehler. Hierarchical Structure and Nanomechanics of Collagen Microfibrils from the Atomistic Scale Up. Nano Lett 2011; 11:757-766.

[35] K. Okuyama, X.Z. Xu, M. Iguchi, K. Noguchi. Revision of collagen molecular structure. Biopolymers 2006; 84:181-191.

[36] A.C. Lorenzo and E.R. Caffarena. Elastic properties, Young's modulus determination and structural stability of the tropocollagen molecule: a computational study by steered molecular dynamics. J Biomech 2005; 38:1527-1533.

[37] M.J. Buehler. Atomistic and continuum modeling of mechanical properties of collagen: Elasticity, fracture, and self-assembly. J Mater Res 2006; 21:1947-1961.

[38] S. Vesentini, C.F.C. Fitie, F.M. Montevecchi, A. Redaelli. Molecular assessment of the elastic properties of collagen-like homotrimer sequences. Biomech Model Mechan 2005; 3:224-234.

[39] A. Gautieri, A. Russo, S. Vesentini, A. Redaelli, M.J. Buehler. Coarse-Grained Model of Collagen Molecules Using an Extended MARTINI Force Field. J Chem Theory Comput 2010; 6:1210-1218.

[40] A. Gautieri, M.J. Buehler, A. Redaelli. Deformation rate controls elasticity and unfolding pathway of single tropocollagen molecules. J Mech Behav Biomed 2009; 2:130-137.

[41] S. Pradhan, D. Katti, K. Katti. Steered Molecular Dynamics Study of Mechanical Response of Full Length and Short Collagen Molecules. J Nanomech Micromech 2011; 1:104-110.

[42] N. Sasaki and S. Odajima. Stress-strain curve and Young's modulus of a collagen molecule as determined by the X-ray diffraction technique. J Biomech 1996; 29:655-658.

[43] R. Harley, D. James, A. Miller, J.W. White. Phonons and the elastic moduli of collagen and muscle. Nature 1977; 267:285-287.

[44] S. Cusack and A. Miller. Determination of the Elastic-Constants of Collagen by Brillouin Light-Scattering. J Mol Biol 1979; 135:39-51.

[45] H. Hofmann, T. Voss, K. Kuhn, J. Engel. Localization of Flexible Sites in Thread-Like Molecules from Electron-Micrographs - Comparison of Interstitial, Basement-Membrane and Intima Collagens. J Mol Biol 1984; 172:325-343.

[46] F.H.M. Nestler, S. Hvidt, J.D. Ferry, A. Veis. Flexibility of Collagen Determined from Dilute-Solution Viscoelastic Measurements. Biopolymers 1983; 22:1747-1758.

[47] Y.L. Sun, Z.P. Luo, A. Fertala, K.N. An. Direct quantification of the flexibility of type I collagen monomer. Biochem Bioph Res Co 2002; 295:382-386.

[48] S.J. Eppell, B.N. Smith, H. Kahn, R. Ballarini. Nano measurements with micro-devices: mechanical properties of hydrated collagen fibrils. J Roy Soc Interface 2006; 3:117-121.

[49] Z.L. Shen, M.R. Dodge, H. Kahn, R. Ballarini, S.J. Eppell. Stress-strain experiments on individual collagen fibrils. Biophys J 2008; 95:3956-3963.

[50] H.S. Gupta, P. Messmer, P. Roschger, S. Bernstorff, K. Klaushofer, P. Fratzl. Synchrotron diffraction study of deformation mechanisms in mineralized tendon. Phys Rev Lett 2004; 93:

[51] N. Sasaki and S. Odajima. Elongation mechanism of collagen fibrils and force-strain relations of tendon at each level of structural hierarchy. J Biomech 1996; 29:1131-1136.

[52] J.A.J. van der Rijt, K.O. van der Werf, M.L. Bennink, P.J. Dijkstra, J. Feijen. Micromechanical testing of individual collagen fibrils. Macromol Biosci 2006; 6:697-702.

[53] M.J. Buehler. Nanomechanics of collagen fibrils under varying cross-link densities: atomistic and continuum studies. J Mech Behav Biomed 2008; 1:59-67.

[54] M.J. Buehler. Nature designs tough collagen: explaining the nanostructure of collagen fibrils. P Natl Acad Sci USA 2006; 103:12285-12290.

[55] E. Gentleman, A.N. Lay, D.A. Dickerson, E.A. Nauman, G.A. Livesay, K.C. Dee. Mechanical characterization of collagen fibers and scaffolds for tissue engineering. Biomaterials 2003; 24:3805-3813.

[56] Y.P. Kato, D.L. Christiansen, R.A. Hahn, S.J. Shieh, J.D. Goldstein, F.H. Silver. Mechanical-Properties of Collagen-Fibers - a Comparison of Reconstituted and Rat Tail Tendon Fibers. Biomaterials 1989; 10:38-41.

[57] H. Miyazaki and K. Hayashi. Tensile Tests of Collagen Fibers Obtained from the Rabbit Patellar Tendon. Biomed Microdevices 1999; 2:151-157.

[58] W. Yang, V.R. Sherman, B. Gludovatz, E. Schaible, P. Stewart, R.O. Ritchie, M.A. Meyers. On the tear resistance of skin. Nat Commun 2015; 6:

[59] B.J. Rigby, N. Hirai, J.D. Spikes, H. Eyring. The Mechanical Properties of Rat Tail Tendon. J Gen Physiol 1959; 43:265-283.

[60] G.J. Orssengo and D.C. Pye. Determination of the true intraocular pressure and modulus of elasticity of the human cornea in vivo. B Math Biol 1999; 61:551-572.

[61] A.D. Freed and T.C. Doehring. Elastic model for crimped collagen fibrils. J Biomech Eng-T Asme 2005; 127:587-593.

[62] S.J. Marrink, H.J. Risselada, S. Yefimov, D.P. Tieleman, A.H. de Vries. The MARTINI force field: Coarse grained model for biomolecular simulations. J Phys Chem B 2007; 111:7812-7824.

[63] S. Vesentini, A. Redaelli, A. Gautieri. Nanomechanics of collagen microfibrils. Muscles Ligaments Tendons J 2013; 3:23-34.

[64] I.V. Yannas and C. Huang. Fracture of Tendon Collagen. J Polymer Sci 2 Polymer Phys 1972; 10:577-584.

[65] J.V. Benedict, L.B. Walker, E.H. Harris. Stress-strain characteristics and tensile strength of unembalmed human tendon. J Biomech 1968; 1:53-63.

[66] M.R. Bryant, K. Szerenyi, H. Schmotzer, P.J. Mcdonnell. Corneal Tensile-Strength in Fully Healed Radial Keratotomy Wounds. Invest Ophth Vis Sci 1994; 35:3022-3031.

[67] W.J. Landis, K.J. Hodgens, J. Arena, M.J. Song, B.F. McEwen. Structural relations between collagen and mineral in bone as determined by high voltage electron microscopic tomography. Microsc Res Techniq 1996; 33:192-202.

[68] W.J. Landis, K.J. Hodgens, M.J. Song, J. Arena, S. Kiyonaga, M. Marko, C. Owen, B.F. McEwen. Mineralization of collagen may occur on fibril surfaces: Evidence from

conventional and high-voltage electron microscopy and three-dimensional imaging. J Struct Biol 1996; 117:24-35.

[69] S.A. Wainwright. Mechanical design in organisms, Princeton University Press, Princeton, New Jersey, 1982.

[70] C. Rey, J.L. Miquel, L. Facchini, A.P. Legrand, M.J. Glimcher. Hydroxyl-Groups in Bone-Mineral. Bone 1995; 16:583-586.

[71] G.Y. Cho, Y.T. Wu, J.L. Ackerman. Detection of hydroxyl ions in bone mineral by solid-state NMR spectroscopy. Science 2003; 300:1123-1127.

[72] J.D. Pasteris, C.H. Yoder, M.P. Sternlieb, S. Liu. Effect of carbonate incorporation on the hydroxyl content of hydroxylapatite. Mineral Mag 2012; 76:2741-2759.

[73] P. Fratzl, H.S. Gupta, E.P. Paschalis, P. Roschger. Structure and mechanical quality of the collagen-mineral nano-composite in bone. J Mater Chem 2004; 14:2115-2123.

[74] M.J. Buehler. Molecular nanomechanics of nascent bone: fibrillar toughening by mineralization. Nanotechnology 2007; 18:

[75] K.J. Koester, J.W. Ager, 3rd, R.O. Ritchie. The true toughness of human cortical bone measured with realistically short cracks. Nat Mater 2008; 7:672-677.

[76] S. Lees. A model for the distribution of HAP crystallites in bone-an hypothesis. Calcif Tissue Int 1979; 27:53-56.

[77] H.S. Gupta, J. Seto, W. Wagermaier, P. Zaslansky, P. Boesecke, P. Fratzl. Cooperative deformation of mineral and collagen in bone at the nanoscale. P Natl Acad Sci USA 2006; 103:17741-17746.

[78] H.S. Gupta, U. Stachewicz, W. Wagermaier, P. Roschger, H.D. Wagner, P. Fratzl. Mechanical modulation at the lamellar level in osteonal bone. J Mater Res 2006; 21:1913-1921.

[79] A. Gautieri, M.I. Pate, S. Vesentini, A. Redaelli, M.J. Buehler. Hydration and distance dependence of intermolecular shearing between collagen molecules in a model microfibril. J Biomech 2012; 45:2079-2083.

[80] Y.C. Fung. Biomechanics: Mechanical Properties of Living Tissues, Springer-Verlag, New York, New York, 1981.

[81] P.J. Blatz, B. Mae Chu, H. Wayland. On the Mechanical Behavior of Elastic Animal Tissue. T Soc Rheol 1969; 13:83-102.

[82] D.R. Veronda and R.A. Westmann. Mechanical Characterization of Skin-Finite Deformations. J Biomech 1970; 3:111-122.

[83] R.W. Ogden. Non-linear elastic deformations, Dover Publications, Mineola, New York, 1997.

[84] P. Tong and Y.C. Fung. Stress-Strain Relationship for Skin. J Biomech 1976; 9:649-657.

[85] K.C. Valanis and R.F. Landel. Strain-Energy Function of a Hyperelastic Material in Terms of Extension Ratios. J Appl Phys 1967; 38:2997-3002.

[86] G. Wertheim. Mémoire sur l'élasticité et la cohésion des principaux tissus du corps humain. Ann Chim Phys 1847; 21:385-414.

[87] Y.C. Fung. Biomechanics: Mechanical Properties of Living Tissues, Second edition. ed., Springer New York, New York, NY, 1993.

[88] F.R. Morgan. The mechanical properties of collagen fibres: stress-strain curves. J Soc Leather Trades' Chem 1960; 44:170-182.

[89] M.D. Ridge and V. Wright. The description of skin stiffness. Biorheology 1964; 2:67-74.

[90] Y.C.B. Fung. Elasticity of Soft Tissues in Simple Elongation. Am J Physiol 1967; 213:1532-1544.

[91] T.C. Doehring, E.O. Carew, I. Vesely. The effect of strain rate on the viscoelastic response of aortic valve tissue: A direct-fit approach. Ann Biomed Eng 2004; 32:223-232.

[92] P.Y. Chen, J. McKittrick, M.A. Meyers. Biological materials: Functional adaptations and bioinspired designs. Prog Mater Sci 2012; 57:1492-1704.

[93] J. Diamant, R.G.C. Arridge, E. Baer, M. Litt, A. Keller. Collagen - Ultrastructure and Its Relation to Mechanical Properties as a Function of Aging. Proc R Soc Lond B 1972; 180:293-315.

[94] M. Comninou and I.V. Yannas. Dependence of Stress-Strain Nonlinearity of Connective Tissues on Geometry of Collagen-Fibers. J Biomech 1976; 9:427-433.

[95] Y. Lanir. Structure-Strength Relations in Mammalian Tendon. Biophys J 1978; 24:541-554.

[96] D.E. Beskos and J.T. Jenkins. Mechanical Model for Mammalian Tendon. J Appl Mech 1975; 42:755-758.

[97] J. Kastelic, I. Palley, E. Baer. A Structural Mechanical Model for Tendon Crimping. J Biomech 1980; 13:887-893.

[98] M.A. Meyers, Y.Z. Tang, S. Zhao, W. Yang, V.R. Sherman. Structural characterization and viscoelastic constitutive modeling of skin. 2016;

[99] C. Bustamante, J.F. Marko, E.D. Siggia, S. Smith. Entropic Elasticity of Lambda-Phage DNA. Science 1994; 265:1599-1600.

[100] W.C. Dale, E. Baer, A. Keller, R.R. Kohn. On the ultrastructure of mammalian tendon. Experientia 1972; 28:1293-5.

[101] R. Puxkandl, I. Zizak, O. Paris, J. Keckes, W. Tesch, S. Bernstorff, P. Purslow, P. Fratzl. Viscoelastic properties of collagen: synchrotron radiation investigations and structural model. Philos T Roy Soc B 2002; 357:191-197.

[102] O. Franke, M. Goken, M.A. Meyers, K. Durst, A.M. Hodge. Dynamic nanoindentation of articular porcine cartilage. Mater Sci Eng C 2011; 31:789-795.

[103] R.B. Svensson, T. Hassenkam, P. Hansen, S.P. Magnusson. Viscoelastic behavior of discrete human collagen fibrils. J Mech Behav Biomed 2010; 3:112-115.

[104] F.H. Silver, A. Ebrahimi, P.B. Snowhill. Viscoelastic properties of self-assembled type I collagen fibers: Molecular basis of elastic and viscous behaviors. Connect Tissue Res 2002; 43:569-580.

[105] R.E. Shadwick, A.P. Russell, R.F. Lauff. The Structure and Mechanical Design of Rhinoceros Dermal Armor. Philos T Roy Soc B 1992; 337:419-428.

[106] Y. Lanir and Y.C. Fung. Two-dimensional mechanical properties of rabbit skin. II. Experimental results. J Biomech 1974; 7:171-82.

[107] W. Yang, B. Gludovatz, E.A. Zimmermann, H.A. Bale, R.O. Ritchie, M.A. Meyers. Structure and fracture resistance of alligator gar (Atractosteus spatula) armored fish scales. Acta Biomater 2013; 9:5876-5889.

[108] W. Yang, I.H. Chen, B. Gludovatz, E.A. Zimmermann, R.O. Ritchie, M.A. Meyers. Natural Flexible Dermal Armor. Adv Mater 2013; 25:31-48.

[109] D.J. Zhu, C.F. Ortega, R. Motamedi, L. Szewciw, F. Vernerey, F. Barthelat. Structure and Mechanical Performance of a "Modern" Fish Scale. Adv Eng Mater 2012; 14:B185-B194.

[110] Y.S. Lin, C.T. Wei, E.A. Olevsky, M.A. Meyers. Mechanical properties and the laminate structure of Arapaima gigas scales. J Mech Behav Biomed 2011; 4:1145-1156.

[111] A.K. Dastjerdi and F. Barthelat. Teleost fish scales amongst the toughest collagenous materials. J Mech Behav Biomed 2015; 52:95-107.

[112] W. Yang, V.R. Sherman, B. Gludovatz, M. Mackey, E.A. Zimmermann, E.H. Chang, E. Schaible, Z. Qin, M.J. Buehler, R.O. Ritchie, M.A. Meyers. Protective role of Arapaima gigas fish scales: Structure and mechanical behavior. Acta Biomater 2014; 10:3599-3614.

[113] Z. Qin and M.J. Buehler. Impact tolerance in mussel thread networks by heterogeneous material distribution. Nat Commun 2013; 4:

[114] Z. Qin and M.J. Buehler. Flaw Tolerance of Nuclear Intermediate Filament Lamina under Extreme Mechanical Deformation. Acs Nano 2011; 5:3034-3042.

[115] M.M. Giraud, J. Castanet, F.J. Meunier, Y. Bouligand. The fibrous structure of coelacanth scales: a twisted 'plywood'. Tissue Cell 1978; 10:671-686.

[116] H. Quan, W. Yang, M.A. Meyers. The Relationship between Structure and Properties in Coelacanth Scales. Submitted for publication 2016;

[117] L. Knott and A.J. Bailey. Collagen cross-links in mineralizing tissues: A review of their chemistry, function, and clinical relevance. Bone 1998; 22:181-187.

[118] F. Nudelman, K. Pieterse, A. George, P.H.H. Bomans, H. Friedrich, L.J. Brylka, P.A.J. Hilbers, G. de With, N.A.J.M. Sommerdijk. The role of collagen in bone apatite formation in the presence of hydroxyapatite nucleation inhibitors. Nat Mater 2010; 9:1004-1009.

[119] G.L. Lucas, F.W. Cooke, E.A. Friis. A primer of biomechanics, Springer, New York Berlin Heidelberg Barcelona Budapest Hong Kong London Milan Paris Singapore Tokyo, 1998.

[120] R.O. Ritchie, M.J. Buehler, P. Hansma. Plasticity and toughness in bone. Phys Today 2009; 62:41-47.

[121] M.E. Launey, M.J. Buehler, R.O. Ritchie. On the Mechanistic Origins of Toughness in Bone. Annual Review of Materials Research 2010; 40:25-53.

[122] R.O. Ritchie. The conflicts between strength and toughness. Nat Mater 2011; 10:817-822.

[123] P. Zioupos. Ageing human bone: Factors affecting its biomechanical properties and the role of collagen. J Biomater Appl 2001; 15:187-229.

[124] P. Zioupos, J.D. Currey, A.J. Hamer. The role of collagen in the declining mechanical properties of aging human cortical bone. J Biomed Mater Res 1999; 45:108-116.

[125] R.K. Nalla, J.J. Kruzic, J.H. Kinney, M. Balooch, J.W. Ager, R.O. Ritchie. Role of microstructure in the aging-related deterioration of the toughness of human cortical bone. Mater Sci Eng C 2006; 26:1251-1260.

[126] X. Wang, X. Shen, X. Li, C.M. Agrawal. Age-related changes in the collagen network and toughness of bone. Bone 2002; 31:1-7.

[127] J.D. Currey. Role of collagen and other organics in the mechanical properties of bone. Osteoporosis Int 2003; 14:S29-S36.

[128] R.O. Ritchie. How does human bone resist fracture? Ann N Y Acad Sci 2010; 1192:72-80.

[129] M.E. Launey, M.J. Buehler, R.O. Ritchie. On the Mechanistic Origins of Toughness in Bone. Annu Rev Mater Res 2010; 40:25-53.

[130] M.E. Launey, P.Y. Chen, J. McKittrick, R.O. Ritchie. Mechanistic aspects of the fracture toughness of elk antler bone. Acta Biomater 2010; 6:1505-1514.

[131] F.H. Silver and Y.P. Kato. Synthetic collagen orthopaedic structures such as grafts, tendons and other structures, Google Patents, 1992.

[132] B.A. Roeder, K. Kokini, J.E. Sturgis, J.P. Robinson, S.L. Voytik-Harbin. Tensile mechanical properties of three-dimensional type I collagen extracellular matrices with varied microstructure. J Biomech Eng-T Asme 2002; 124:214-222.

[133] G.D. Pins, D.L. Christiansen, R. Patel, F.H. Silver. Self-assembly of collagen fibers. Influence of fibrillar alignment and decorin on mechanical properties. Biophys J 1997; 73:2164-2172.

[134] M.S. Sacks and W. Sun. Multiaxial mechanical behavior of biological materials. Annu Rev Biomed Eng 2003; 5:251-284.

[135] M.A. Meyers, P.Y. Chen, A.Y.M. Lin, Y. Seki. Biological materials: Structure and mechanical properties. Prog Mater Sci 2008; 53:1-206.

[136] B.H. Ji and H.J. Gao. Mechanical Principles of Biological Nanocomposites. Annu Rev Mater Res 2010; 40:77-100.

[137] P.Y. Chen, J. Schirer, A. Simpson, R. Nay, Y.S. Lin, W. Yang, M.I. Lopez, J.A. Li, E.A. Olevsky, M.A. Meyers. Predation versus protection: Fish teeth and scales evaluated by nanoindentation. J Mater Res 2012; 27:100-112.

[138] R.K. Chintapalli, M. Mirkhalaf, A.K. Dastjerdi, F. Barthelat. Fabrication, testing and modeling of a new flexible armor inspired from natural fish scales and osteoderms. Bioinspir Biomim 2014; 9:036005.

[139] M.M. Porter, M. Yeh, J. Strawson, T. Goehring, S. Lujan, P. Siripasopsotorn, M.A. Meyers, J. McKittrick. Magnetic freeze casting inspired by nature. Mater Sci Eng A 2012; 556:741-750.

[140] S. Deville, E. Saiz, R.K. Nalla, A.P. Tomsia. Freezing as a path to build complex composites. Science 2006; 311:515-518.

[141] E. Munch, M.E. Launey, D.H. Alsem, E. Saiz, A.P. Tomsia, R.O. Ritchie. Tough, Bio-Inspired Hybrid Materials. Science 2008; 322:1516-1520.

[142] U.G.K. Wegst, H. Bai, E. Saiz, A.P. Tomsia, R.O. Ritchie. Bioinspired structural materials. Nat Mater 2015; 14:23-36.

[143] J.Y. Sire and A. Huysseune. Formation of dermal skeletal and dental tissues in fish: a comparative and evolutionary approach. Biol Rev 2003; 78:219-249.

[144] G.S. Helfman, B.B. Collette, D.E. Facey. The Diversity Of Fishes-Biology, Evolution, and Ecology, 2 ed., Wiley-Blackwell, Oxford, United Kingdom, 2009.

[145] J.Y. Sire, P.C.J. Donoghue, M.K. Vickaryous. Origin and evolution of the integumentary skeleton in non-tetrapod vertebrates. J Anat 2009; 214:409-440.

[146] M.K. Vickaryous and J.Y. Sire. The integumentary skeleton of tetrapods: origin, evolution, and development. J Anat 2009; 214:441-464.

[147] B.J.F. Bruet, J.H. Song, M.C. Boyce, C. Ortiz. Materials design principles of ancient fish armour. Nat Mater 2008; 7:748-756.

[148] J. Song, C. Ortiz, M.C. Boyce. Threat-protection mechanics of an armored fish. J Mech Behav Biomed 2011; 4:699-712.

[149] D.J. Zhu, L. Szewciw, F. Vernerey, F. Barthelat. Puncture resistance of the scaled skin from striped bass: Collective mechanisms and inspiration for new flexible armor designs. J Mech Behav Biomed 2013; 24:30-40.

[150] F.G. Torres, O.P. Troncoso, J. Nakamatsu, C.J. Grande, C.M. Gomez. Characterization of the nanocomposite laminate structure occurring in fish scales from Arapaima Gigas. Mater Sci Eng C 2008; 28:1276-1283.

[151] P.G. Allison, M.Q. Chandler, R.I. Rodriguez, B.A. Williams, R.D. Moser, C.A. Weiss, A.R. Poda, B.J. Lafferty, A.J. Kennedy, J.M. Seiter, W.D. Hodo, R.F. Cook.

Mechanical properties and structure of the biological multilayered material system, Atractosteus spatula scales. Acta Biomater 2013; 9:5289-5296.

[152] F.J. Vernerey and F. Barthelat. On the mechanics of fishscale structures. Int J Solids Struct 2010; 47:2268-2275.

[153] E.A. Zimmermann, B. Gludovatz, E. Schaible, N.K.N. Dave, W. Yang, M.A. Meyers, R.O. Ritchie. Mechanical adaptability of the Bouligand-type structure in natural dermal armour. Nat Commun 2013; 4:

[154] G. Roux. The microscopic anatomy of the Latimeria scale. S Afr J Med Sci 1942; 7:1-18.

[155] M.M. Smith, W.A. Miller, M.H. Hobdell. Structure of Scales of Latimeria-Chalumnae. J Zool 1972; 167:501-509.

[156] A. Marino Cugno Garrano, G. La Rosa, D. Zhang, L.N. Niu, F.R. Tay, H. Majd, D. Arola. On the mechanical behavior of scales from Cyprinus carpio. J Mech Behav Biomed 2012; 7:17-29.

[157] S. Murcia, M. McConville, G.H. Li, A. Ossa, D. Arola. Temperature effects on the fracture resistance of scales from Cyprinus carpio. Acta Biomater 2015; 14:154-163.

[158] N. Geographic. Arapaima. <http://environment.nationalgeographic.com/environment/freshwater/arapaima/>, (accessed August 22 2016).

[159] M.A. Meyers, Y.S. Lin, E.A. Olevsky, P.Y. Chen. Battle in the Amazon: Arapaima versus Piranha. Adv Eng Mater 2012; 14:B279-B288.

[160] J.L.B. Smith. A living fish of Mesozoic type. Nature 1939; 143:455-456.

[161] H. Fricke, J. Schauer, K. Hissmann, L. Kasang, R. Plante. Coelacanth Latimeria Chalumnae Aggregates in Caves: first Observations on Their Resting Habitat and Social Behavior. Environ Biol Fish 1991; 30:281-285.

[162] D.R. Huber, J.M. Claes, J. Mallefet, A. Herrel. Is Extreme Bite Performance Associated with Extreme Morphologies in Sharks? Physiol Biochem Zool 2009; 82:20-28.

[163] K.R. Mara, P.J. Motta, D.R. Huber. Bite Force and Performance in the Durophagous Bonnethead Shark, Sphyrna tiburo. J Exp Zool A Ecol Genet Physiol 2010; 313:95-105.

[164] T.L. Ferrara, P. Clausen, D.R. Huber, C.R. McHenry, V. Peddemors, S. Wroe. Mechanics of biting in great white and sandtiger sharks. J Biomech 2011; 44:430-435.

[165] N. Geographic. Alligator gar. <http://environment.nationalgeographic.com/environment/freshwater/alligator-gar/>, Accessed 2016).

[166] S. Potts. The American Alligator, Capstone Books, Mankato, Minnesota, 1998.

[167] G.M. Erickson, A.K. Lappin, K.A. Vliet. The ontogeny of bite-force performance in American alligator (Alligator mississippiensis). J Zool 2003; 260:317-327.

[168] G.M. Erickson, A.K. Lappin, T. Parker, K.A. Vliet. Comparison of bite-force performance between long-term captive and wild American alligators (Alligator mississippiensis). J Zool 2004; 262:21-28.

[169] B. Wang, W. Yang, V.R. Sherman, M.A. Meyers. Pangolin armor: overlapping, structure, and mechanical properties of the keratinous scales. Acta Biomater 2016; 16:S1742-7061.

[170] P. Erdkamp. A companion to the Roman army, Paperback ed., Wiley-Blackwell, Oxford ; Malden, MA, 2011.

[171] A. Bigi, M. Burghammer, R. Falconi, M.H.J. Koch, S. Panzavolta, C. Riekel. Twisted plywood pattern of collagen fibrils in teleost scales: An X-ray diffraction investigation. J Struct Biol 2001; 136:137-143.

[172] V.R. Sherman, H. Quan, W. Yang, R.O. Ritchie, M.A. Meyers. A comparative study of piscine defense: The scales of *Arapaima gigas*, *Latimeria chalumnae* and *Atractosteus spatula*. J Mech Behav Biomed Mater 2016;

[173] A. Browning, C. Ortiz, M.C. Boyce. Mechanics of composite elasmoid fish scale assemblies and their bioinspired analogues. J Mech Behav Biomed 2013; 19:75-86.

[174] J. Daget, M. Gayet, F.J. Meunier, J.Y. Sire. Major discoveries on the dermal skeleton of fossil and Recent polypteriforms: a review. Fish Fish 2001; 2:113-124.

[175] G. Wulff. On the question of speed of growth and dissolution of crystal surfaces. Z Krystallogr Minera 1901; 34:449-530.

[176] I.H. Chen, W. Yang, M.A. Meyers. Leatherback sea turtle shell: A tough and flexible biological design. Acta Biomater 2015; 28:2-12.

[177] A.G. Evans and E.A. Charles. Fracture Toughness Determinations by Indentation. J Am Ceram Soc 1976; 59:371-372.

[178] B.R. Lawn, A.G. Evans, D.B. Marshall. Elastic-Plastic Indentation Damage in Ceramics - the Median-Radial Crack System. J Am Ceram Soc 1980; 63:574-581.

[179] G.M. Pharr. Measurement of mechanical properties by ultra-low load indentation. Mater Sci Eng A 1998; 253:151-159.

[180] R. Hassan, A.A. Caputo, R.F. Bunshah. Fracture-Toughness of Human-Enamel. Journal of Dental Research 1981; 60:820-827.

[181] H. Kessler, R. Ballarini, R.L. Mullen, L.T. Kuhn, A.H. Heuer. A biomimetic example of brittle toughening (1) Steady state multiple cracking. Comp Mater Sci 1996; 5:157-166.

[182] J. Dundurs. Edge-Bonded Dissimilar Orthogonal Elastic Wedges under Normal and Shear Loading. J Appl Mech 1969; 36:650-652.

[183] V. Imbeni, J.J. Kruzic, G.W. Marshall, S.J. Marshall, R.O. Ritchie. The dentin-enamel junction and the fracture of human teeth. Nat Mater 2005; 4:229-232.

[184] M.E. Launey, E. Munch, D.H. Alsem, H.B. Barth, E. Saiz, A.P. Tomsia, R.O. Ritchie. Designing highly toughened hybrid composites through nature-inspired hierarchical complexity. Acta Materialia 2009; 57:2919-2932.

[185] E.S. Goodrich. On the scales of fish, living and extinct, and their importance in classification. Proc Zool Soc Lond 1907; 77:751-774.

[186] T. Ørvig. Remarks on the vertebrate fauna of the Lower Upper Devonian of Escuminac Bay, P. Q., Canada, with special reference to the Porolepiform Crossopterygians. Ark Zool 1957;

[187] F.J. Meunier and L. Zylberberg. The structure of the outer components of the scales of Latimeria chalumnae (Sarcopterygii : Actinistia : Coelacanthidae) revisited using scanning and transmission electron microscopy. Proceedings of 5th Indopacific Fish Conference Noumea 1997 1999; 109-116.

[188] H. Onozato and N. Watabe. Studies on fish scale formation and resorption. III. Fine structure and calcification of the fibrillary plates of the scales in Carassius auratus (Cypriniformes: Cyprinidae). Cell Tissue Res 1979; 201:409-422.

[189] T. Ikoma, H. Kobayashi, J. Tanaka, D. Walsh, S. Mann. Microstructure, mechanical, and biomimetic properties of fish scales from Pagrus major. J Struct Biol 2003; 142:327-333.

[190] T. Orvig. Phylogeny of tooth tissues: Evolution of some calcified tissues in early vertebrates, in: A.E.W. Miles (Ed.), Structural and chemical organization of teeth, Academic Press, New York/London, 1967, pp. 45-110.

[191] D. Gur, Y. Politi, B. Sivan, P. Fratzl, S. Weiner, L. Addadi. Guanine-Based Photonic Crystals in Fish Scales Form from an Amorphous Precursor. Angew Chem Int Ed 2013; 52:388-391.

[192] L. Zylberberg, J. Bonaventure, L. Cohen-Solal, D.J. Hartmann, J. Bereiterhahn. Organization and characterization of fibrillar collagens in fish scales in situ and in vitro. J Cell Sci 1992; 103:273-285.

[193] S. Weiner and H.D. Wagner. The material bone: Structure mechanical function relations. Annu Rev Mater Sci 1998; 28:271-298.

[194] H.D. Barth, M.E. Launey, A.A. MacDowell, J.W. Ager, R.O. Ritchie. On the effect of X-ray irradiation on the deformation and fracture behavior of human cortical bone. Bone 2010; 46:1475-1485.

[195] V. Burdak. Functional morphology of scale cover in fish, Naukova Dumka, Kyiv, Ukraine, 1979.

[196] Bouligan.Y. Twisted Fibrous Arrangements in Biological-Materials and Cholesteric Mesophases. Tissue Cell 1972; 4:189-217.

[197] F. Schmid, G. Sommer, M. Rappolt, C.A. Schulze-Bauer, P. Regitnig, G.A. Holzapfel, P. Laggner, H. Amenitsch. In situ tensile testing of human aortas by time-resolved small-angle X-ray scattering. J Synchrotron Radiat 2005; 12:727-733.

[198] P. Fratzl. Collagen: Structure and Mechanics, Springer, New York, New York, 2008.

[199] G.A. Holzapfel. Collagen in Arterial Walls: Biomechanical Aspects, in: P. Fratzl (Ed.), Collagen: Structure and Mechanics, Springer, New York, New York, 2008, pp. 285-324.

[200] W. Ramberg and W.R. Osgood. Description of stress-strain curves by three parameters. Tech. Note 902, National Advisory Committee for Aeronautics, Washington, D.C., 1943.

[201] T.K. Hight and J.F. Brandeau. Mathematical-Modeling of the Stress-Strain Strain Rate Behavior of Bone Using the Ramberg-Osgood Equation. J Biomech 1983; 16:445-450.

[202] Z. Qin, A. Gautieri, A.K. Nair, H. Inbar, M.J. Buehler. Thickness of Hydroxyapatite Nanocrystal Controls Mechanical Properties of the Collagen-Hydroxyapatite Interface. Langmuir 2012; 28:1982-1992.

[203] A.K. Nair, A. Gautieri, S.W. Chang, M.J. Buehler. Molecular mechanics of mineralized collagen fibrils in bone. Nat Commun 2013; 4:1724.

[204] S. Varshney, E. Zolotovsky, Y.N. Li, M.C. Boyce, N. Oxman, C. Ortiz. Morphometric origins of biomechanical flexibility in fish armor. Integr Comp Biol 2013; 53:E218.

[205] S. Sudo, K. Tsuyuki, Y. Ito, T. Ikohagi. A study on the surface shape of fish scales. Jsme Int J C-Mech Sy 2002; 45:1100-1105.

[206] F.J. Vernerey and F. Barthelat. Skin and scales of teleost fish: Simple structure but high performance and multiple functions. J Mech Phys Solids 2014; 68:66-76.

[207] S. Rudykh, C. Ortiz, M.C. Boyce. Flexibility and protection by design: imbricated hybrid microstructures of bio-inspired armor. Soft Matter 2015; 11:2547-2554.

[208] N. Funk, M. Vera, L.J. Szewciw, F. Barthelat, M.P. Stoykovich, F.J. Vernerey. Bioinspired Fabrication and Characterization of a Synthetic Fish Skin for the Protection of Soft Materials. Acs Appl Mater Inter 2015; 7:5972-5983.

[209] R. Martini and F. Barthelat. Stability of hard plates on soft substrates and application to the design of bioinspired segmented armor. J Mech Phys Solids 2016; 92:195-209.

[210] R. Martini and F. Barthelat. Stretch-and-release fabrication, testing and optimization of a flexible ceramic armor inspired from fish scales. Bioinspir Biomim 2016;

[211] S. Rudykh and M.C. Boyce. Analysis of elasmoid fish imbricated layered scale-tissue systems and their bio-inspired analogues at finite strains and bending. Ima J Appl Math 2014; 79:830-847.

[212] D. Bajaj and D.D. Arola. On the R-curve behavior of human tooth enamel. Biomaterials 2009; 30:4037-46.

[213] N.G. Jablonski. Skin: a natural history, University of California Press, Berkeley, California, 2006.

[214] H. Oxlund, J. Manschot, A. Viidik. The Role of Elastin in the Mechanical-Properties of Skin. J Biomech 1988; 21:213-218.

[215] G. Dupuytren, C.F. Gräfe, M. Kalisch. Dupuytren theoretisch-praktische Vorlesungen über die Verletzungen durch Kriegswaffen, Veit, Berlin, Germany, 1836.

[216] K. Langer. On the anatomy and physiology of the skin. I. The cleavability of the cutis. (Translated from Langer, K. (1861). Zur Anatomie und Physiologie der Haut. I. Uber die Spaltbarkeit der Cutis. Sitzungsbericht der Mathematisch-naturwissenschaftlichen Classe der Kaiserlichen Academie der Wissenschaften. Br J Plast Surg 1978; 31:3-8.

[217] M.D. Ridge and V. Wright. The directional effects of skin. A bio-engineering study of skin with particular reference to Langer's lines. J Invest Dermatol 1966; 46:341-346.

[218] A. Rauber and F. Kopsch. Rauber's Lehrbuch der Anatomie des Menschen, Georg Thieme, Leipzig, Germany, 1908.

[219] S. Inc. Spa Candle Treatment. <http://www.sophis-inc.jp/eng/candle/candle.html>, 2015 (accessed 05/07 2015).

[220] P. Fratzl, K. Misof, I. Zizak, G. Rapp, H. Amenitsch, S. Bernstorff. Fibrillar structure and mechanical properties of collagen. J Struct Biol 1998; 122:119-122.

[221] G.A. Holzapfel, T.C. Gasser, R.W. Ogden. A new constitutive framework for arterial wall mechanics and a comparative study of material models. J Elasticity 2000; 61:1-48.

[222] A. Masic, L. Bertinetti, R. Schuetz, L. Galvis, N. Timofeeva, J.W.C. Dunlop, J. Seto, M.A. Hartmann, P. Fratzl. Observations of Multiscale, Stress-Induced Changes of Collagen Orientation in Tendon by Polarized Raman Spectroscopy. Biomacromolecules 2011; 12:3989-3996.

[223] M.D. Ridge and V. Wright. The rheology of skin. A bio-engineering study of the mechanical properties of human skin in relation to its structure. Br J Dermatol 1965; 77:639-649.

[224] R. Grytz and G. Meschke. Constitutive modeling of crimped collagen fibrils in soft tissues. J Mech Behav Biomed 2009; 2:522-533.

[225] J.H. Connell. Home Range and Mobility of Brush Rabbits in California Chaparral. J Mammal 1954; 35:392-405.

[226] J. Biniok. Rabbits, Eldorado Ink, Pittsburgh, Pennsylvania, 2009.

[227] G. Ritchison. Avian Integument. <http://people.eku.edu/ritchisong/avian_integument.htm>, (accessed December 1 2014).

[228] R.O. Prum and R. Torres. Structural colouration of avian skin: convergent evolution of coherently scattering dermal collagen arrays. J Exp Biol 2003; 206:2409-2429.

[229] G. Schwinger, K. Zanger, H. Greven. Structural and mechanical aspects of the skin of Bufo marinus (Anura, Amphibia). Tissue Cell 2001; 33:541-547.

[230] I.V. Yannas and J.F. Burke. Design of an Artificial Skin. 1. Basic Design Principles. J Biomed Mater Res 1980; 14:65-81.

[231] J.F. Burke, I.V. Yannas, W.C. Quinby, C.C. Bondoc, W.K. Jung. Successful Use of a Physiologically Acceptable Artificial Skin in the Treatment of Extensive Burn Injury. Ann Surg 1981; 194:413-428.

[232] B.D. Ratner. Biomaterials science: an introduction to materials in medicine, 3rd ed., Elsevier Academic Press, Amsterdam, Netherlands, 2013.

[233] B.C.K. Tee, C. Wang, R. Allen, Z.N. Bao. An electrically and mechanically self-healing composite with pressure- and flexion-sensitive properties for electronic skin applications. Nat Nanotechnol 2012; 7:825-832.

[234] Y. Gao, A.M. Waas, J.A. Faulkner, T.Y. Kostrominova, A.S. Wineman. Micromechanical modeling of the epimysium of the skeletal muscles. J Biomech 2008; 41:1-10.

[235] G.D. Weinstein and R.J. Boucek. Collagen and Elastin of Human Dermis. J Invest Dermatol 1960; 35:227-229.

[236] K.H. Sizeland, R.L. Edmonds, M.M. Basil-Jones, N. Kirby, A. Hawley, S. Mudie, R.G. Haverkamp. Changes to Collagen Structure during Leather Processing. J Agr Food Chem 2015; 63:2499-2505.

[237] I.C. Smith. I.—The Structure of the Skin and Dermal Scales in the Tail of Acipenser ruthenus L. Transactions of the Royal Society of Edinburgh 1956; 63:1-14.

[238] V.R. Sherman, W. Yang, M.A. Meyers. The materials science of collagen. J Mech Behav Biomed Mater 2015; 52:22-50.

[239] F.P. Beer, E.R. Johnston, J.T. DeWolf, D.F. Mazurek. Mechanics of materials, 5 ed., McGraw-Hill Higher Education, Boston, Massachusetts, 2009.

[240] T. Young. A course of lectures on natural philosophy and the mechanical arts, Printed for Joseph Johnson by William Savage, London, United Kingdom, 1807.

[241] M.T. Shaw and W.J. MacKnight. Introduction to polymer viscoelasticity, 3 ed., Wiley, Hoboken, New Jersey, 2005.

[242] M.A. Meyers and K.K. Chawla. Mechanical behavior of materials, Prentice Hall, Upper Saddle River, New Jersey, 1999.

[243] J.B. Finlay. Thixotropy in human skin. J Biomech 1978; 11:333-42.

[244] P.P. Purslow. Measurement of the Fracture-Toughness of Extensible Connective Tissues. J Mater Sci 1983; 18:3591-3598.

[245] C. Dong, E. Mead, R. Skalak, Y.C. Fung, J.C. Debes, R.L. Zapatasirvent, C. Andree, G. Greenleaf, M. Cooper, J.F. Hansbrough. Development of a Device for Measuring Adherence of Skin-Grafts to the Wound Surface. Ann Biomed Eng 1993; 21:51-55.

[246] A.K. Wong. Orthodontic Elastic-Materials. Angle Orthod 1976; 46:196-205.

[247] S.C. Chen, S.Q. Peng, G.X. Huang, K.X. Wu, X.H. Fu, Z.Q. Chen. Association of decreased expression of a Myb transcription factor with the TPD (tapping panel dryness) syndrome in Hevea brasiliensis. Plant Mol Biol 2003; 51:51-58.

[248] A. Gennadios, C.L. Weller, R.F. Testin. Property Modification of Edible Wheat, Gluten-Based Films. T Asae 1993; 36:465-470.

[249] G.C. Wood. Some Tensile Properties of Elastic Tissue. Biochim Biophys Acta 1954; 15:311-324.

[250] J.F. Manschot and A.J. Brakkee. The measurement and modelling of the mechanical properties of human skin in vivo--II. The model. J Biomech 1986; 19:517-521.

[251] J.D. Currey, K. Brear, P. Zioupos. The effects of ageing and changes in mineral content in degrading the toughness of human femora. J Biomech 1996; 29:257-60.

[252] R.K. Nalla, J.H. Kinney, R.O. Ritchie. Mechanistic fracture criteria for the failure of human cortical bone. Nat Mater 2003; 2:164-8.

[253] T. Ackbarow, D. Sen, C. Thaulow, M.J. Buehler. Alpha-helical protein networks are self-protective and flaw-tolerant. Plos One 2009; 4:e6015.

[254] M.J. Buehler and S. Keten. Colloquium: Failure of molecules, bones, and the Earth itself. Rev Mod Phys 2010; 82:1459-1487.

[255] A. Viidik. Functional properties of collagenous tissues. Int Rev Connect Tissue Res 1973; 6:127-215.

[256] A. Ní Annaidh, M. Ottenio, K. Bruyère, M. Destrade, M.D. Gilchrist. Mechanical Properties of Excised Human Skin, in: C.T. Lim, J.C.H. Goh (Eds.), 6th World Congress of Biomechanics (WCB 2010), Springer Berlin Heidelberg, Singapore, 2010, pp. 1000-1003.

[257] A. Ní Annaidh, K. Bruyere, M. Destrade, M.D. Gilchrist, M. Ottenio. Characterization of the anisotropic mechanical properties of excised human skin. J Mech Behav Biomed 2012; 5:139-148.

[258] E.P. Popov and T.A. Balan. Engineering mechanics of solids, 2 ed., Prentice Hall, Upper Saddle River, New Jersey, 1999.

[259] M.J. Buehler and R. Ballarini. Materiomics multiscale mechanics of biological materials and structures, Courses and lectures, Springer, Vienna; New York, 2013.

[260] A. Hexemer, W. Bras, J. Glossinger, E. Schaible, E. Gann, R. Kirian, A. MacDowell, M. Church, B. Rude, H. Padmore. A SAXS/WAXS/GISAXS Beamline with Multilayer Monochromator. J Phys Conf Ser 2010; 247:1-11.

[261] J. Liao, L. Yang, J. Grashow, M.S. Sacks. Molecular orientation of collagen in intact planar connective tissues under biaxial stretch. Acta Biomater 2005; 1:45-54.

[262] M.M. Basil-Jones, R.L. Edmonds, G.E. Norris, R.G. Haverkamp. Collagen Fibril Alignment and Deformation during Tensile Strain of Leather: A Small-Angle X-ray Scattering Study. J Agr Food Chem 2012; 60:1201-1208.

[263] O.P. Reuterwall. Über die Elastizität der Gefässwände und die Methoden ihrer näheren Prüfung. Acta med scand 1921; 2:7-175.

[264] A.G. Thomas. Rupture of Rubber. V. Cut Growth in Natural Rubber Vulcanizates. J Polym Sci 1958; 31:467-480.

[265] E.A. Zimmermann, H.D. Barth, R.O. Ritchie. The Multiscale Origins of Fracture Resistance in Human Bone and Its Biological Degradation. Jom-Us 2012; 64:486-493.

[266] R.D. Marangoni. Effect of storage and handling techniques on skin tissue properties, New York Academy of Sciences, New York, New York, 1966.

[267] H.P. Gavin. Strain Energy in Linear Elastic Solids, Department of Civil and Environmental Engineering, Duke University, Durham, North Carolina, 2015.

[268] R. Beardmore. Curved Beams. <www.roymech.co.uk/Useful_Tables/Beams/Curved_beams.html>, 2013 (accessed August 22 2016).